

On the interrelation of
fluid-induced seismicity and crustal deformation
at the Columbo Submarine Volcano
(Aegean Sea, Greece)

Dissertation zur Erlangung des
Doktorgrades der Naturwissenschaften
im Department Geowissenschaften
der Universität Hamburg

vorgelegt von

Martin Hensch

aus Koblenz

Hamburg

2009

Als Dissertation angenommen vom Department Geowissenschaften
der Universität Hamburg

auf Grund der Gutachten von
und

Prof. Dr. Torsten Dahm
Prof. Dr. Matthias Hort

Hamburg, den 11. Januar 2010,

Prof. Dr. Jürgen Oßenbrügge
Leiter des Departments Geowissenschaften

ABSTRACT

Joint seismological and deformation studies are a mighty tool to study the dynamics of magmatic systems at active volcanoes. While GPS measurements and InSAR are successfully applied at onshore volcanoes, the monitoring of submarine volcanoes is mostly restricted to island based or temporary seismological measurements. We therefore developed a free fall, self leveling Ocean Bottom Tiltmeter (OBT) to observe ground deformation on the seafloor, using a two component tilt sensor with a resolution of about 15 nrad . The tiltmeter is mounted on the preexisting Hamburg Ocean Bottom Seismometer (OBS) carrier system. It is additionally equipped with a hydrophone to assess seismic data and an absolute pressure sensor to observe uplift and subsidence.

Between June 2006 and March 2007, four of these OBT systems were deployed along a profile over the slopes and on top of the Columbo Submarine Volcano. The network was completed by four OBSs in the vicinity of the seamount and additional seismometers on the surrounding islands. Columbo is part of the Santorini volcanic complex, located in the center of the Hellenic Volcanic Arc, Aegean Sea (Greece), approximately 8 km north-east of Thira island (Santorini). The volcano has attracted attention since island based monitoring indicates a high seismicity rate clustering around the seamount and possible crustal deformation. Both might represent fluid migration in the subsurface.

Through this 10 months long local experiment, azimuthal gaps between the islands were closed and the magnitude threshold of the permanent network was significantly decreased. The installation of zero offset seismic stations on top of the volcano enabled us to derive high precise depth locations of earthquakes. Purpose of the study was to find evidences for swarm triggers, such as possibly fluid migration, by precisely relocating the events by means of multiple events methods. About 4000 events have been manually picked and six earthquake swarms directly occurring at Columbo have been analyzed for migration velocities of seismic fronts. Four of these swarms were classified as supposedly dike-induced, the two remaining swarms as the expression of increased hydrothermal activity. Moment tensor solutions of stronger earthquakes ($M_W > 3$) were calculated to evidence our findings in terms of possible stress field perturbations induced by the postulated triggers.

Simultaneously to the seismological observations, general unrest in terms of noise increase was found on the tiltmeters for all earthquake swarms, predominantly oriented radial to the

earthquake cluster centroid. For one swarm occurring close to the tiltmeter profile, strong near-field terms were observed and successfully modeled as an ascending volume source. Both findings are discussed extensively with respect to a possible linkage between the seismic cluster and the origin of the deformation signals. Further points of discussion are the general technical functionality of the newly developed OBT as well as additional findings like long period deformation signals and trends suggesting the uplift of the complete region between Columbo and Santorini.

We conclude with a hypothetical model on deformation signals accompanying the ascent of a volumetric source. This hypothesis is based on our preexisting model about the pattern of dike-induced earthquake swarms. We show, that the same migration velocities found by seismological observations can be independently derived by analyzing the change of the deformation signal of a propagating volumetric source. Finally, we evidence that our approach is sufficient to estimate source depth, ascent velocity and a crude source volume by analyzing spatial and temporal tilt maxima, as well as their amplitudes.

CONTENTS

Abstract	iii
Table Of Contents	v
List Of Figures	ix
List Of Tables	xv
 Chapters	
1 Introduction	1
1.1 Outline	1
1.1.1 State of the art	1
1.1.2 Goal	3
1.2 Geology of the Eastern Mediterranean	5
1.2.1 Regional settings	5
1.2.2 Local settings and monitoring networks	8
1.3 The Columbo Experiment	10
1.4 Structure of the thesis	11
 2 Data acquisition	 13
2.1 Passive measurements	14
2.1.1 The Columbo OBS/OBT Experiment	14
2.1.2 The EGELADOS Experiment	17
2.2 Active measurements	18
2.2.1 Reflection seismic profiling	19
2.2.2 Gravimetric and magnetic profiling	20

3	The new Hamburg Ocean Bottom Tiltmeter (OBT)	23
3.1	Technical description	23
3.2	First experiences in practical use	25
3.2.1	Calibration in the laboratory	25
3.2.2	Test measurements in the Black Forest Observatory (BFO)	27
3.2.3	Overview on signals observed at Columbo	28
4	Theory of seismic and deformation sources	35
4.1	Seismic sources	35
4.1.1	Earthquake mechanism	35
4.1.2	The Earthquake Moment Tensor	37
4.2	Deformation sources	39
4.2.1	The Fault Source Model	40
4.2.2	The Mogi Source Model for spheric volumes	47
4.2.3	The Lenticular Volume Source for dike intrusions	54
5	Methods and Results 1	
	Seismological analysis	57
5.1	Precise relative earthquake relocation	57
5.1.1	SEISAN: Picking and further parameterization	57
5.1.2	Velocity model	61
5.1.3	3 component cross correlation	63
5.1.4	HYPOSAT single event location	65
5.1.5	HYPODD relative earthquake relocation	67
5.2	Moment Tensor Inversion	70
5.2.1	Moment Tensor solutions	73
5.2.2	Stress inversion	78
6	Methods and Results 2	
	Cluster and deformation analysis	81
6.1	Analysis of earthquake swarms	81
6.1.1	Estimation of cluster migration velocities	81

6.1.2	Results for cluster migration velocities at Columbo	83
6.2	Additional findings	87
6.2.1	Further swarm parameters	87
6.2.2	Magnitude distribution	87
6.2.3	Activation of adjacent faults	88
6.3	Analysis of deformation data	89
6.3.1	Re-orientation of freefall tiltmeters	89
6.3.2	Removal of levelling- and high frequency jumps	92
6.3.3	Results of tilt measurements	94
6.3.4	Absolute pressure data	101
7	Discussion	105
7.1	Classification of earthquake swarms	105
7.2	Correlation of deformation signals and short lasting swarms	107
7.2.1	Model for dike-induced earthquake swarms	107
7.2.2	Accompanying deformation	110
7.2.3	Joint hypothetical model for dike-induced earthquake swarms and accompanying deformation signals	119
7.3	Global trends and aseismic deformation signals	121
7.4	Possible technical improvements of the OBT	123
8	Conclusions	125
 Appendices		
A	Sensor parameters and velocity models	127
A.1	Seismic stations	127
A.2	Instrumentation	129
A.3	Bandpass filters	131
B	Correlation Coefficients	133
B.1	Correlation coefficients of the Columbo Experiment	133

C Instrument calibration	137
C.1 Seismometer calibration	138
C.1.1 PMD sensor	139
C.1.2 EP300 sensor	140
C.1.3 Comparison	140
C.2 Tiltmeter calibration	143
D Synopsis of earthquake swarms	149
D.1 Swarm on 28th of July 2006 (CS-1)	150
D.2 Swarm from 23rd Sept. until 1st of Oct. 2006 (CL-1)	154
D.3 Swarm from 6th until 8th of December 2006 (CL-2)	158
D.4 Swarm on 10th of January 2007 (CS-2)	162
D.5 Swarm on 18th of February 2007 (CS-3)	166
D.6 Swarm on 26th of February 2007 (AS-1)	170
D.7 Swarm on 1st of March 2007 (CS-4)	174
E Synopsis of focal mechanisms	179
F The EGELADOS working group	207
Acknowledgements	209
References	210

FIGURES

1.1	Overview map of the Hellenic Subduction Zone	6
1.2	Target area: The Santorini-Amorgos Fault	7
1.3	Combined bathymetry and lower sediment layers: The Santorini-Anafi Basin	8
1.4	Recent seismicity and deformation at Santorini	9
1.5	3D view of the Columbo bathymetry	11
2.1	Experimental setup around Columbo Seamount	15
2.2	Tiltmeter profile over Columbo Seamount	15
2.3	Scientific crew of the recovery cruise (RV Aegaeo)	17
2.4	The EGELADOS network	18
2.5	Profile lines of active measurements (RV Poseidon)	19
2.6	Joint seismic and magnetic profile over Columbo	20
2.7	Magnetic heterogeneity around Santorini and Columbo	21
3.1	Sketch and photo of the OBT sensor sphere	24
3.2	Photos of absolute pressure gauge and OBT deployment	25
3.3	Tilt-table used for tiltmeter calibration	26
3.4	Example for tiltmeter calibration	26
3.5	Regional earthquake observed at the BFO	27
3.6	OBT traces of BFO measurement	28
3.7	Noise comparison: BFO vs. Columbo	29
3.8	Local earthquake on OBT54 and OBS50	30
3.9	Teleseismic event on OBTs and STS2	31
3.10	Short period tilt-signal simultaneous to an earthquake	31
3.11	Long period tilt-signal simultaneous to an earthquake swarm	32

3.12	Global trend of OBT 57	33
3.13	Tiltmeter powerspectrum (OBT 54)	33
4.1	Defining parameters of a fault	36
4.2	Equivalent body forces and force couples	37
4.3	Example for a high frequency tilt signal	40
4.4	Rectangular source model	41
4.5	Displacement- and tilt-fields for typical faults	43
4.6	Minimum moment over depth and distance to trigger deformation sensors	44
4.7	Minimum moment over depth and distance for a strike-slip event	45
4.8	The Mogi point source model	47
4.9	The Mogi Model: Displacement and tilt	51
4.10	The Mogi Model: Amplitude distribution on X- and Y-components	51
4.11	The Mogi Model: Volume- and depth-dependencies	52
4.12	Threshold-Volume depending on depth and distance to trigger the OBT	53
4.13	Gridded volume threshold over depth and distance	53
4.14	Deformation due to magmatic diking	54
5.1	Overview: STA/LTA triggered and picked events	58
5.2	Typical event at Columbo seamount (OBS 50 and IOSI)	59
5.3	Earthquake swarm at Columbo	60
5.4	Velocity model for v_P and v_S	61
5.5	Wadati diagram based on SEISAN picks	62
5.6	Example for time windows cut off continuous data	64
5.7	Station corrections for P- and S-phases	66
5.8	Comparison of original HYPO71 and improved HYPOSAT locations	67
5.9	Structogram of data processing and moment tensor inversion	72
5.10	Focal mechanisms of all events $M_L \geq 3.5$	73
5.11	Focal mechanisms of events $3.5 > M_L \geq 3.0$	74
5.12	Example for a cross checked moment tensor solution	75
5.13	Comparison of average focal mechanisms	76

5.14	Result plot of stress inversion	78
6.1	From zt-distribution to gridded event density	82
6.2	Centroid depth estimation with Gaussian curve fit	82
6.3	Example of migration velocities for both swarm types	86
6.4	Magnitude-time distribution for all earthquake swarms	87
6.5	Time dependence of average and maximum magnitudes	88
6.6	Activation of adjacent faults	89
6.7	Correlation coefficients between OBT 54 and land seismometers	90
6.8	Rose diagrams of OBS orientations	91
6.9	Example for the removal of a leveling event on OBT 54	92
6.10	Correction example for a jump due to an earthquake on OBT 54	93
6.11	Location of potential deformation sources	95
6.12	Tilt-walk of the tiltmeter pendulum during an earthquake swarm	96
6.13	Tiltmeter traces rotated in back-azimuth direction	97
6.14	Tilt traces for two months of sparse activity	100
6.15	Trends of OBTs over the complete experiment	102
6.16	Results of absolute pressure measurements	103
6.17	Comparison: Tilt measurement on a point and over distance	104
7.1	Result-Plot for swarm CS-1 close to OBTs 54 and 55	108
7.2	Hypothetical model for short lasting earthquake swarms	110
7.3	Unrest and inflation-deflation signal on OBTs during the CS-1 swarm	111
7.4	Depth dependency of the tilt amplitude	114
7.5	Distance dependency of the tilt amplitude	115
7.6	Tilt amplitude over epicentral distance, depth and time	117
7.7	Spatial and temporal tilt maxima	118
7.8	Tilt amplitude versus epicentral distance	118
7.9	Hypothetical model for deformation signals accompanying short swarms	120
7.10	Reflection seismic profile over elevated region between Santorini and Columbo	122
A.1	Powerspectra of STS2 landstation IOSI	131

A.2	Powerspectra of EP300/DPG offshore station OBS50	132
B.1	Analysis of correlation curves	133
B.2	Correlation coefficients 1	134
B.3	Correlation coefficients 1	135
B.4	Correlation coefficients 1	136
C.1	Tilt-table for instrument calibration	137
C.2	Instrument spheres of PMD end EP300 seismometer	138
C.3	Calibration curves of PMD s/n 512 seismometer	139
C.4	Calibration curves of PMD s/n 4 seismometer	140
C.5	Calibration curves of EP300 s/n 10535 seismometer	140
C.6	Calibration curves of EP300 s/n 10536 seismometer	141
C.7	Comparison of PMD and EP300 sensors	141
C.8	Back-shift velocity according to immersion depth of the sensor (Stokes)	142
C.9	Calibration measurements of tiltmeter 1	144
C.10	Calibration measurements of tiltmeter 3	145
C.11	Calibration measurements of tiltmeter 4	146
C.12	Calibration measurements of tiltmeter 5	147
D.1	Swarm CS-1: lat-lon, lat-z, lon-z, map	150
D.2	Swarm CS-1: zt-distribution	151
D.3	Swarm CS-1: Tilt traces	152
D.4	Swarm CS-1: Tilt orientation	153
D.5	Swarm CL-1: lat-lon, lat-z, lon-z, map	154
D.6	Swarm CL-1: zt-distribution	155
D.7	Swarm CL-1: Tilt traces	156
D.8	Swarm CL-1: Tilt orientation	157
D.9	Swarm CL-2: lat-lon, lat-z, lon-z, map	158
D.10	Swarm CL-2: zt-distribution	159
D.11	Swarm CL-2: Tilt traces	160
D.12	Swarm CL-2: Tilt orientation	161

D.13 Swarm CS-2: lat-lon, lat-z, lon-z, map	162
D.14 Swarm CS-2: zt-distribution	163
D.15 Swarm CS-2: Tilt traces	164
D.16 Swarm CS-2: Tilt orientation	165
D.17 Swarm CS-3: lat-lon, lat-z, lon-z, map	166
D.18 Swarm CS-3: zt-distribution	167
D.19 Swarm CS-3: Tilt traces	168
D.20 Swarm CS-3: Tilt orientation	169
D.21 Swarm AS-1: lat-lon, lat-z, lon-z, map	170
D.22 Swarm AS-1: zt-distribution	171
D.23 Swarm AS-1: Tilt traces	172
D.24 Swarm AS-1: Tilt orientation	173
D.25 Swarm CS-4: lat-lon, lat-z, lon-z, map	174
D.26 Swarm CS-4: zt-distribution	175
D.27 Swarm CS-4: Tilt traces	176
D.28 Swarm CS-4: Tilt orientation	177
D.29 Tilt traces over event rate	178
E.1 Focal mechanism of event 2006.07.28 12:11:14.5	180
E.2 Focal mechanism of event 2006.07.28 12:24:29.4	181
E.3 Focal mechanism of event 2006.07.28 12:26:48.0	182
E.4 Focal mechanism of event 2006.08.24 09:28:25.4	183
E.5 Focal mechanism of event 2006.09.03 15:34:29.3	184
E.6 Focal mechanism of event 2006.09.27 01:23:24.4	185
E.7 Focal mechanism of event 2006.10.11 20:33:21.0	186
E.8 Focal mechanism of event 2006.10.22 20:48:52.2	187
E.9 Focal mechanism of event 2006.10.22 20:50:04.2	188
E.10 Focal mechanism of event 2006.11.11 11:26:45.6	189
E.11 Focal mechanism of event 2006.11.13 08:04:24.2	190
E.12 Focal mechanism of event 2006.11.13 08:49:50.7	191
E.13 Focal mechanism of event 2006.11.14 12:42:33.9	192

E.14 Focal mechanism of event 2006.11.14 12:45:29.7	193
E.15 Focal mechanism of event 2006.12.06 10:24:37.9	194
E.16 Focal mechanism of event 2007.01.10 17:22:16.4	195
E.17 Focal mechanism of event 2007.02.18 17:23:34.1	196
E.18 Focal mechanism of event 2007.02.26 13:24:51.1	197
E.19 Focal mechanism of event 2007.03.01 11:48:25.4	198
E.20 Focal mechanism of event 2007.03.01 11:48:42.7	199
E.21 Focal mechanism of event 2007.03.01 11:53:41.2	200
E.22 Focal mechanism of event 2007.03.01 12:46:15.6	201
E.23 Focal mechanisms of events $M_L < 3.5$ (plot 1)	202
E.24 Focal mechanisms of events $M_L < 3.5$ (plot 2)	203
E.25 Focal mechanisms of events $M_L < 3.5$ (plot 3)	204
E.26 Focal mechanisms of events $M_L < 3.5$ (plot 4)	205

TABLES

2.1	List of automatic triggers of different networks	14
5.1	Velocity models for v_P and v_S	62
5.2	hypoDD initial control parameters	68
5.3	List of Moment Tensor solutions	77
6.1	Results: Migration velocities	85
6.2	Further swarm parameters	87
6.3	Orientation of ocean bottom sensors	91
6.4	List of cluster centroids and other possible deformation sources	98
6.5	Results: Deformation	99
6.6	Results: Long period trends	101
6.7	Results: Absolute pressure data	103
A.1	List of seismic stations	127
A.2	List of station corrections	128
A.3	Instrumentation	129
A.4	Data loggers and sampling rates	130
A.5	Poles and zeros of seismic sensors	130
A.6	Bandpass filters applied to seismic data	131
C.1	Tilt-steps for seismometer calibration	139
C.2	Tilt-steps for tiltmeter calibration	143
C.3	Tilt-steps for tiltmeter 1 (OBT54)	144
C.4	Tilt-steps for tiltmeter 3 (OBT55)	145
C.5	Tilt-steps for tiltmeter 4 (OBT56)	146

C.6	Tilt-steps for tiltmeter 5 (OBT57)	147
D.1	Deformation of the 28th of July 2006 swarm (CS-1)	152
D.2	Deformation of the 23rd of Sept.-1st of Oct. 2006 swarm (CL-1)	156
D.3	Deformation of the 6th-8th of December 2006 swarm (CL-2)	160
D.4	Deformation of the 10th of January 2007 swarm (CS-2)	164
D.5	Deformation of the 18th of February 2007 swarm (CS-3)	168
D.6	Deformation of the 1st of March 2007 swarm (CS-4)	176

CHAPTER 1

INTRODUCTION

1.1 Outline

The assessment of volcanic hazards in populated regions is the main goal of all volcanological disciplines, whereas volcano seismology mostly deals with the location and tracing of magmatic and other volcanic fluid reservoirs and their migration in the subsurface, based on seismological observations. Therefore, fundamental studies at active volcanoes are as indispensable as the monitoring itself, because they have the potential to improve permanent surveys and the general knowledge on volcanic processes. In case of the Santorini-Columbo Volcanic Complex, located in the Hellenic Volcanic Arc (Aegean Sea, Greece), a dense population, increased by tourists during summer on Santorini and the surrounding islands, and, of much greater impact in case of a volcanic hazard in this region, the possible cut off of the Northern Aegean and thus the Black Sea (Turkey, Bulgaria, Ukraine etc.) from international sea routes make a duly preparation on a possible eruption necessary. The Columbo project was a completely fundamental research project, using data of an amphibian seismic network, including seismometers on the adjacent islands, Ocean-Bottom-Seismometers and newly developed Ocean-Bottom-Tiltmeters to assess submarine deformation data.

1.1.1 State of the art

Magma propagation at depth, such as dike ascent, is often accompanied by volcanic earthquake swarms (e.g. Rubin and Gillard, 1998b; Battaglia et al., 1999). The complexity of the hypocenter patterns and migration paths has been intensively discussed for several types of earthquake swarms and today it is known, that despite of magma movement also other origins have to be considered as swarm triggers: Tectonic mainshock-aftershock sequences (e.g. Hauksson et al., 2001) and increased hydrothermal activity due to volcanic unrest (e.g. Lupi et al., 2007).

While the separation of purely tectonic earthquake sequences is relatively simple due to their hyperbolic decrease of the event rate predicted by Omori's law (Lay and Wallace, 1995),

the classification of different types of volcanic earthquake swarms is rather complicated. It is exhaustively discussed in Hensch (2005) for earthquake swarms offshore North Iceland, by regarding vertical migration velocities and the depth over time pattern (z -distribution) of these swarms: Supposedly dike-induced earthquake swarms show clear seismicity fronts which resemble the propagation of local stress accumulation. A fast migrating front during the initial phase of the swarm is discussed to be caused by crack opening and/or degassing. A second front is supposed to reflect the actual position of the head region of the ascending dike. This backfront is ascending much slower than the initial front and marks the boundary to the region below, where seismicity is lacking. Result of both fronts is the typical triangular shape of the z -distribution of this type of earthquake swarm. In opposite to magma induced earthquake swarms, hydrothermally triggered swarms or swarms due to gas propagation are more scattered and of a less structured shape. These swarms are supposed to be triggered by the wide spread unrest of hydrothermal fluids and thus do not show characteristic fronts of seismicity.

Similar studies led to comparable results, e.g. for the Izu (Japan) swarm in 2000 (Ukawa and Tsukahara, 1996) or an earthquake swarm heralding the 2001 Mt. Etna eruption (Patané et al., 2002), which are both discussed to be linked to dike ascent. In both cases, fast migration paths during the initial phase of the swarm and the triangular shape of the z -distribution due to a seismic backfront were observed. Additionally, these swarms ended within a few days. Fluid- or gas-induced earthquake swarms have been discussed by e.g. Fischer (2003) or Fischer and Horálek (2003) for a cluster in NW-Bohemia (Czech Republic). These swarms are comparable with hydrothermally induced clusters, the structure of their z -distribution is more complicated, often without clear migration paths and the temporal length of these swarms is much longer, partly a week and more.

The observation of varying temporal lengths for both types of volcanic earthquake swarms fits well with our results of recent studies. A maximum length of $2d$ for supposedly dike induced swarms in contrast to durations up to a week for hydrothermally triggered swarms is a general finding for swarms offshore North Iceland (Hensch et al., 2008). Both, magma intrusion and increased hydrothermal activity, must be considered as possible trigger mechanisms for earthquake swarms measured at Columbo.

A second important expression of magma propagation in shallow depths is local crustal deformation. It can be caused directly by a volume source, such as a magma reservoir or an ascending dike, or by near-field terms of shallow volcano-tectonic earthquakes. Early approaches on modeling these sources have been done e.g. by Mogi (1958) for a spheric volume source or Okada (1992) for point and rectangular fault sources. With today's technical opportunities, InSAR and GPS measurements, large areas and volcanoes are successfully monitored in terms of deformation (e.g. Sturkell et al., 2006) and the propagation of more complex sources,

such as lenticular volumes which are more comparable with dikes are modeled and observed (e.g. Pollard et al., 1983; Hautmann et al., 2009). While both techniques, InSAR and GPS, are mighty tools in surveying onshore volcanoes, they fail for offshore observations. Assessments of the state of activity of submarine volcanoes is still mainly restricted to seismological measurements, mostly even limited to temporary amphibian networks.

Only very few studies tackled the field of submarine deformation measurements up to now. Already in the late 1980s, Fox (1990) installed absolute pressure sensors at the summit of the axial volcano (central Juan de Fuca Ridge, Pacific Ocean) and successfully measured deflation after an active episode in 1998 in the range of a few meters (Fox, 1999). Tolstoy et al. (1998) developed short- and long-baseline tiltmeters with resolutions of 50 nrad that were deployed as freefall instruments. Those instruments partly worked successfully in another deployment at the Juan de Fuca Ridge. The most recent approach by Fabian and Villinger (2007) and Fabian and Villinger (2008), University of Bremen (Germany), was to study deformations caused by hydrothermal activity at the Logatchev Vent Field at the southern Mid-Atlantic Ridge: A single prototype was successfully recovered after a long term deployment and proved the possibility to measure tilt in the range of some μrad on the seafloor.

Restrains of already developed Ocean-Bottom-Tiltmeters (OBTs) were their poor resolution for absolute pressure sensors, their limited operating time of only some weeks or in case of the Bremen OBT the fact that it has to be deployed and recovered by a Remote Operating Vehicle (ROV). But the studies cited above have all shown that submarine deformation measurements are in principle possible and that it is worth to advance investigations on this field. Thus, we developed a freefall OBT system for longterm deployments (up to 10 months), with theoretical resolutions of 15 nrad for tilt and 1 mm or 0.1 mbar for absolute pressure to measure uplift and subsidence. Additionally, it is equipped with a hydrophone to record seismic signals. These sensors were mounted on the pre-existing Hamburg Ocean-Bottom-Seismometer (OBS) frame.

1.1.2 Goal

Aim of this study is to perform deformation measurements at an active submarine volcano and to study correlations between possible deformation signals and the occurrence of earthquake swarms. Columbo was chosen because of its recent and continuous seismic and possibly deformation activity, because of its favorable position between many islands to mount onshore seismometers and due to the excellent cooperation and data-exchange with our colleagues of the EGELADOS project (Friederich and Meier, 2008), another amphibian network installed parallelly in the whole Aegean region (see Ch. 2.1.2). This study solely deals with basic and technical aspects of offshore volcano seismology and first steps in submarine deformation measurements with the new Hamburg OBT system.

The main technical innovation of this work was the development of the prototype of an offshore deformation sensor and its successful test in a pilot experiment at a submarine volcano. A basic question was, whether this instrument is in principle working and capable for submarine deformation measurements.

The most important scientific innovations of my work despite of technical developments can be summarized as follows:

- The improvement of our hypothetical models for volcanic earthquake swarms, which were derived from recent studies
- The first assessment of moment tensor solutions for earthquakes including hydrophone data of our OBS/OBT system
- The first submarine deformation measurement using the preexisting carrier system of the Hamburg Ocean Bottom Seismometer
- The investigation of 10 months long tilt time series for trends and short period deformation signals in a joint analysis with earthquake swarm data

Scope and complexity of the following investigations using the obtained data required exhaustive theoretic and methodic works, which are sorted as three recurrent themes in the same order as given below (swarm behaviour, source mechanisms and deformation) for each chapter, to increase the readability of the thesis and to allow skipping of specific sections. From Chapter 4 on, chapters are thus subdivided each into the main goals of this thesis:

- **Classification of earthquake swarms** by the parameterization of cluster pattern and migration velocities, with the background to conclude for trigger mechanisms of earthquake swarms occurring in the Columbo region and to generally affirm similar findings of recent studies in other regions.
- **Estimation of focal mechanisms including hydrophone data** to draw conclusions on the regional stress regime and possible local perturbations by inverting for the stress tensor. The knowledge of the stress field is of great importance for the discussion of geometry and orientation of possibly ascending dikes.
- **Study of accompanying submarine deformation signals** and finding possible interrelations to simultaneously occurring seismic activity is the final purpose of the thesis. The objective is to substantiate previous findings, such as migration velocities of seismic clusters, as well as the evaluation of a general approach to measure submarine deformation signals.

1.2 Geology of the Eastern Mediterranean

The European Mediterranean Sea has been built up by the opening of Pangea during the Triassic rifting about 220-230 Ma ago and the later northwards motion of the African plate caused by the sea-floor spreading geometry of the North and South Atlantic ocean during the Cretaceous and Tertiary (Gealey, 1988). Strong reduction of the northward motion of the African plate after the collision with Eurasia 30-35 Ma ago initiated Mediterranean extension and a southward retreat of the oceanic slab that is subducting below the European plate. This retreat is suggested to have caused the formation of several extensional basins within the Mediterranean Sea, one of which is now known as the **Aegean Sea**, which has been further opened by recent slab rollback of the **Hellenic Subduction Zone** (Pichon and Angelier, 1979; Kahle et al., 1998; Jolivet and Faccenna, 2000).

1.2.1 Regional settings

Fig. 1.1 gives an overview on the regional tectonic settings of the Aegean Sea, positions of sedimentary arc and volcanic arc and the five volcanic centers. The Hellenic Subduction Zone (HSZ) is the seismically most active region in Europe (Bohnhoff et al., 2006). Due to slab rollback, it is a typically extended subduction zone: The convergent plate boundary between the Aegean microplate and the African plate is placed in the Lybian Sea, around 100-150 km south of the Hellenic Arc. The sedimentary arc is located (from west to east, see Fig. 1.1) between the Peloponessus peninsula, Kythera, Crete and Rhodos (Papazachos and Panagiotopoulos, 1993; Meier et al., 2004). The overall rate of convergence of the HSZ is about 3.5-4 cm/a, split into a major contribution of the Aegean plate with about 3 cm/a SW-ward propagation and 0.5-1 cm/a N-ward migration of the African plate, the dip angle of the subducting lithosphere is on average 30 – 40° (Papazachos and Panagiotopoulos, 1993; Knapmeyer, 1999; Jolivet and Faccenna, 2000; Bohnhoff et al., 2001). Following the subducting lithosphere around 150-200 km to the north, it reaches a depth of 100-150 km (e.g. Meier et al., 2004) and the absence of strong earthquakes below 150 km is assumed to be linked to the high temperature of the material in this region (Papazachos and Panagiotopoulos, 1993). Hot material ascends from these deep zones and possibly intrudes into the crust along the fracture zones. Extensional faults open the pathways for these magmatic intrusions (Papazachos and Panagiotopoulos, 1993; Dimitriadis et al., 2009). This assumption is supported by the occurrence of volcanism along the Hellenic Volcanic Arc (HVA) directly above this region, separated into five seismovolcanic clusters (from west to east): Sousaki, Methana, Milos, Santorini and Nysiros.

The most prominent and recently most active one is the **Santorini Volcanic Complex (SVC)**, known due to the globally impacting Minoan eruption about 3500-3650 years b.p.

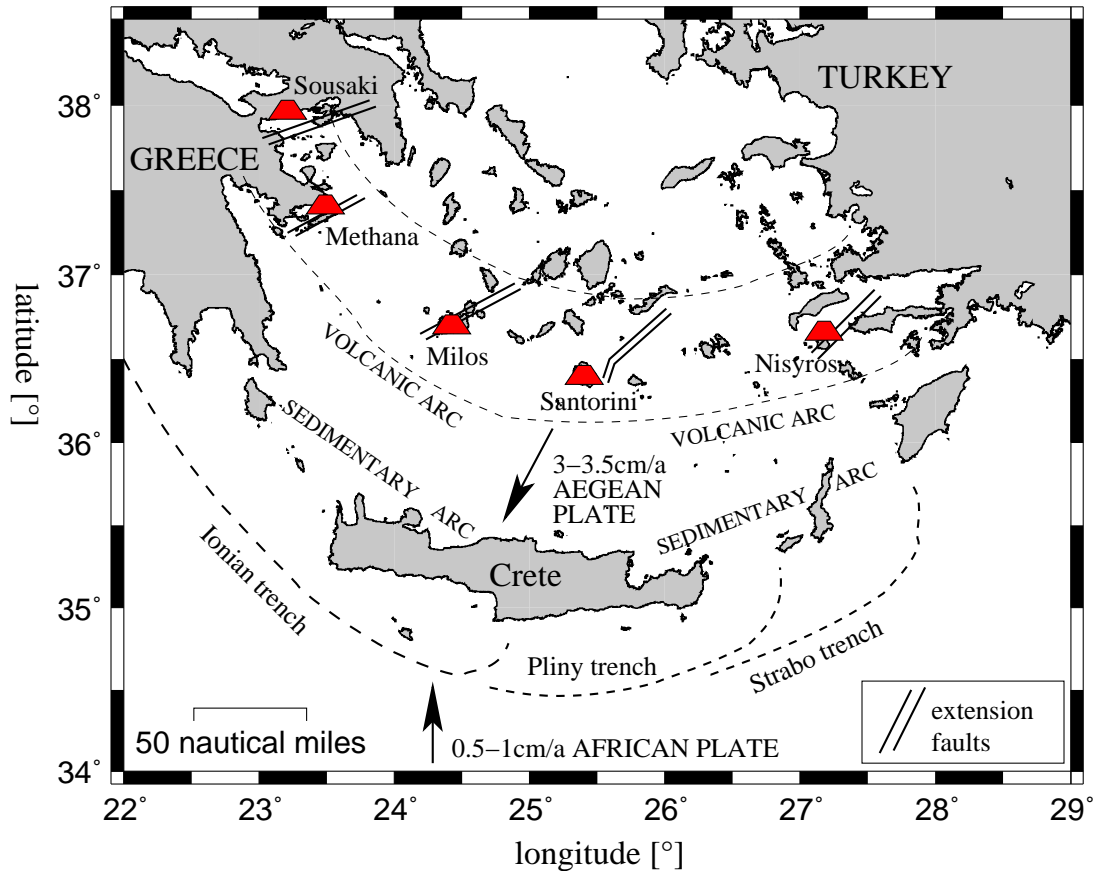


Figure 1.1: **Overview map of the Hellenic Subduction Zone:** Subduction of African lithosphere south of Crete leads to a sedimentary arc and further northwards to a typical volcanic arc with the known volcanic centers of Sousaki, Methana, Milos, Santorini and Nisyros. Target area of our studies is the Santorini Volcanic Complex and its adjacent region to the north east, the Santorini-Amorgos fault zone. (Locations of extension faults taken from Papazachos and Panagiotopoulos (1993)).

(Heiken and McCoy, 1984), and its adjacent extensional fault system, the **Santorini Amorgos Fault (SAF)**. Both, volcanic and tectonic activity are observed in this region: At least nine recent eruptions of Santorini have been proven for the last 600 years, the last one in 1950 (Dimitriadis et al., 2009) and furthermore strong and shallow earthquakes occur along the extensional faults, such as the 1956 events at the SAF: Two M 7.5 and M 6.9 normal faulting events (location see Fig. 1.2) within 13 minutes on 9th of July 1956, accompanied by a tsunami. Fault planes of the 1956 earthquakes clearly fit with the assumed stress model (Papazachos and Panagiotopoulos, 1993).

The target area of our study is located between $36.3^{\circ} N - 36.9^{\circ} N$ and $25.25^{\circ} E - 26.15^{\circ} E$, see Fig. 1.2. The dominant tectonic feature is the Santorini-Amorgos Fault with a couple of minor faults in its vicinity and around the Columbo Seamount. The SAF is slightly bended from SSW-NNE striking east of Santorini to WSW-ENE striking south of Amorgos due to perturbations of the local stress field (Dimitriadis et al., 2005). Smaller seamounts are also

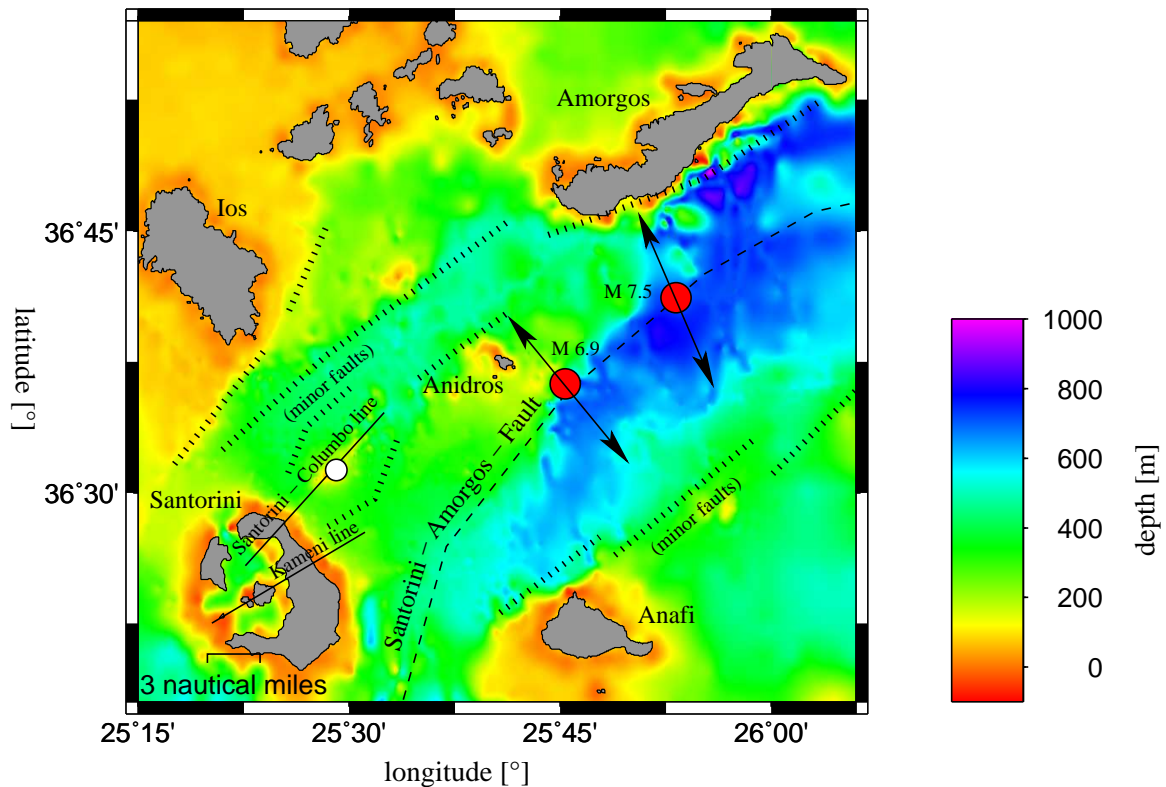


Figure 1.2: **Bathymetry map of target area - The Santorini-Amorgos Fault:** The dashed line marks the dominant tectonic feature, the Santorini-Amorgos-Fault. Dotted lines mark adjacent minor faults. The 1956 earthquakes are given with red dots, direction of extension is marked with arrows (a slight bending of the stress axis is visible). Data on faults and the earthquakes are taken from Dimitriadis et al. (2009). Main volcanic features around Santorini are given with solid lines: The Santorini-Columbo line and the Kameni line (taken from the Volcanic Hazard Zonation Map of the Institute for the Study and Monitoring of the Santorini Volcano (ISMOSAV), <http://ismosav.santorini.net>). Additional small seamounts around Anidros island are visible in the bathymetry. The Columbo caldera is marked by a white dot.

found around Anidros island on an elongated axis Santorini-Columbo-Anidros, parallel to the SAF, which indicates the occurrence of volcanic activity along a fault parallel belt and not only at one spot at Santorini. A very important feature of this volcanic belt is the **Columbo Submarine Volcano** (white dot in Fig. 1.2), which is the focus of this study.

A cross section derived of reflection seismic profiling is given in Fig. 1.3 (Note: View from NE!). The SAF is directly located SE of the escarpment between Santorini, Anidros and Amorgos. Lateral tilting of the sediment layers suggest sudden stress releases in form of large earthquakes in frequent intervals and underlines the existence of the above mentioned extensional stress regime.

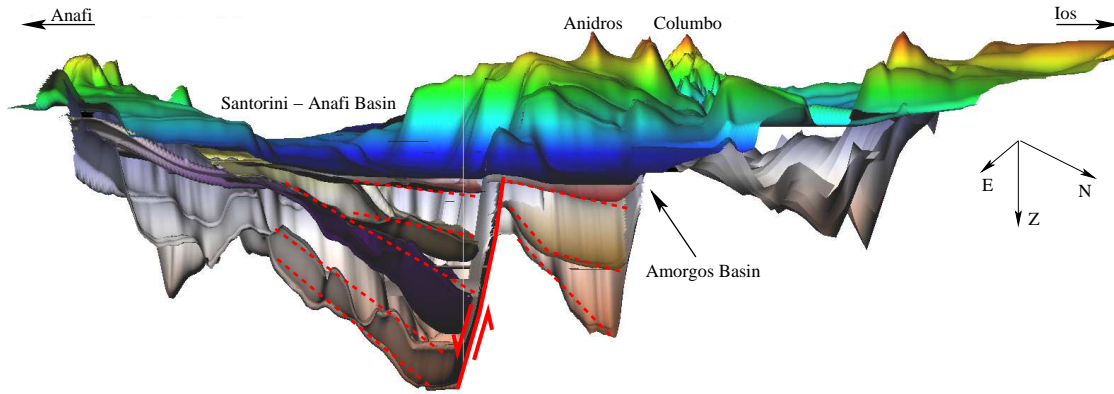


Figure 1.3: **Combined bathymetry and lower sediment layers** measured by reflection seismic profiling of the Santorini-Anafi and the Amorgos Basins. The depth scale is ten times exaggerated, the maximum depth range of the used high frequent seismic waves is about 2 km. The main tectonic feature, normal faulting at the Santorini-Amorgos Escarpment, is marked by a red line. Dashed lines mark sedimentary layers, supposedly tilted by several strong normal faulting earthquakes due to the extensional stress regime. The view is from NE, seamounts around Anafi, the Columbo volcano in the background and another smaller basin caused by adjacent minor faults are visible.

1.2.2 Local settings and monitoring networks

The Columbo Submarine Volcano is located about 8 km northeast of Santorini at $36.55^\circ N$ and $25.45^\circ E$. It has a well defined caldera of about 1500 m diameter, a maximum depth inside the caldera of about 500 m and a minimum depth of the crater rim (the Columbo Reef) as shallow as 17 m (Sigurdsson et al., 2006; Dimitriadis et al., 2009). The most recent eruption of Columbo is documented to have happened on 26th of September 1650, lasting until December of the same year and causing a tsunami on Thera island (Santorini). Since geological and other observations were thoroughly documented in Greece already at that time, it is known that earthquake activity increased about two weeks before the eruption. Furthermore, the occurrence of a small islet during the initial phase of the eruption has been reported (Dominey-Howes et al., 2000, and references therein).

Currently, Columbo shows seismic and geothermal activity: Sigurdsson et al. (2006) observed widespread hydrothermal vents, emission plumes of 10 m and more and fluid temperatures of up to $220^\circ C$ from vent chimneys of up to 4 m height. Hydrothermal activity is mainly concentrated on the northern part of the inner Columbo caldera. In contrast to Columbo, only low-temperature venting is observed inside the Santorini caldera with temperatures of about $15 - 17^\circ C$ during the same marine survey (Sigurdsson et al., 2006).

Local seismicity is also suggested to derive mainly from a volcanic origin: Fig. 1.4 is an overview on seismic activity and observed deformation. While some events are scattered along the known faults and have already been described to be linked to extension of the basins NE of Santorini (Dimitriadis et al., 2005, 2009), a large seismic cluster is also observed at Columbo volcano and in its vicinity. These events have already been discussed by Dimitriadis

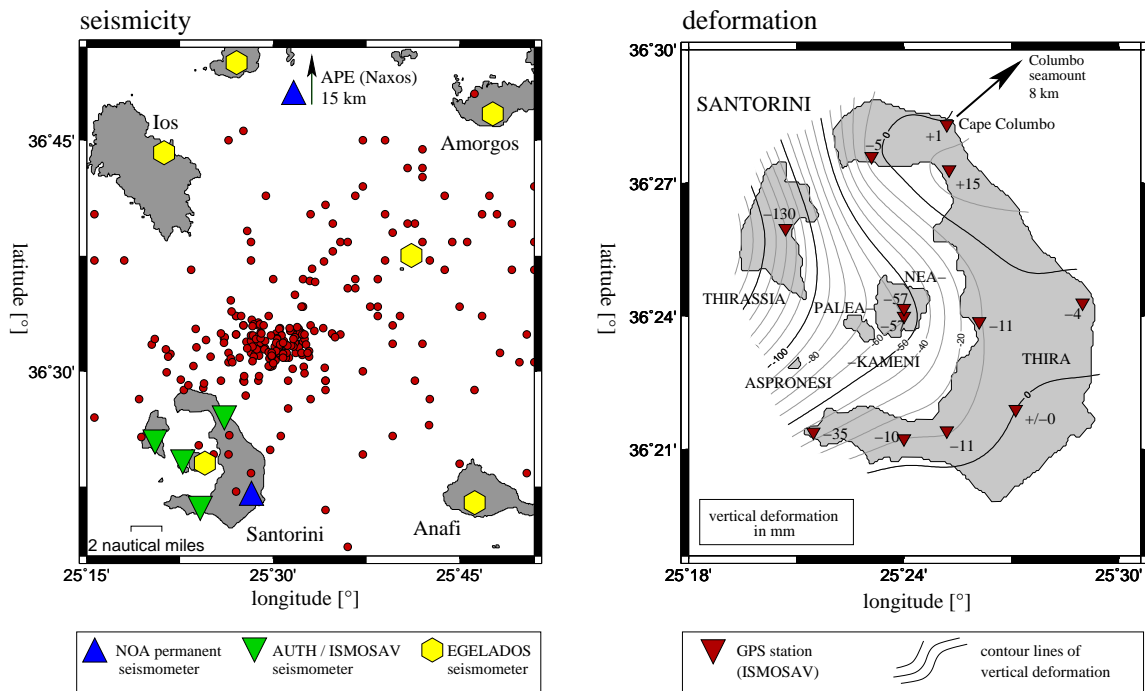


Figure 1.4: **Recent seismicity and deformation at Santorini.** Joint catalogue data of the National observatory Athens (NOA, www.gein.noa.gr) and the Institute for the Study and Monitoring of the Santorini volcano (ISMOSAV, ismosav.santorini.net) for the year 2006 (left hand side plot). Red dots mark single events, yellow diamonds EGELADOS temporary landstations, green inverse triangles stations run by the Aristotle University Thessaloniki and ISMOSAV, blue triangles mark permanent NOA stations, of which the second closest on Naxos is slightly outside the map. While the seismicity rate at Santorini is relatively low, events occur along the Santorini-Amorgos escarpment and a large cluster is observed about 8 km NE, around the Columbo Submarine Volcano. Parallel (plot on the right hand side), GPS measurements (ISMOSAV) suggest tilting of Santorini with highest uplift rates a few km east of Cape Columbo. Brown inverse triangles mark positions of GPS stations. Deformation data here shown is of the period from 1994 to 2001 (taken from ismosav.santorini.net).

et al. (2009) to be related to volcanic, possibly hydrothermal, activity. The occurrence of earthquakes before the 1650 eruption (Dominey-Howes et al., 2000) also suggests magma ascent as a possible trigger of such events. However, an investigation on temporal clustering, such as typical for volcanically induced earthquake swarms, has not been carried out yet.

A permanent seismic network is run by the National Observatory Athens (NOA, for parameter data see www.gein.noa.gr), with one station on Santorini which is mostly shut down or noisy and a sparse net of stations on the surrounding islands. The second closest station is Naxos at a distance of about 50 km, which is definitely insufficient to analyze weak volcanotectonic earthquakes. The magnitude threshold of the NOA network to successfully locate events around Santorini is about $M_L = 3$. Recently, an additional network is being established on Santorini and the surrounding islands to better locate events offshore Santorini and to decrease the magnitude threshold to about $M_L = 1.5$ (for parameter data see ismosav.santorini.net).

Parallel to seismic observations, the Institute for the Study and Monitoring of the Santorini

Volcano (ISMOSAV, ismosav.santorini.net) is running an onshore GPS network on Santorini that is permanently installed to measure possible deformation signals. Here shown data (Fig. 1.4) suggests slight uplift of two spots on Thira (main island of Santorini): One spot in the northeast, close to Cape Columbo, and possibly another one in the southeast. The overall uplift near Cape Columbo was 15 *mm* for the period from 1994-2001, while for the same time subsidence of Thirassia island of about 130 *mm* was observed. But also for these deformation signals, no further investigations on short-term behaviour or relation to the seismic activity have been carried out until now.

1.3 The Columbo Experiment

To study the temporal behaviour of volcanic earthquake clusters, a much denser network and seismic stations in closer epicentral distance, some preferably near zero-offset, are necessary. Similar experiments at offshore volcanoes (e.g. Hensch et al., 2008) have already shown that an improvement of the event location residuals by a factor of 10-20 is possible, once azimuthal gaps around the source region are closed. Hypocentral depths can be estimated more precisely using zero-offset stations and events are relatively relocated using waveform-correlation techniques.

We therefor installed a network of 4 Ocean-Bottom-Seismometers (OBS) and 4 of the new OBTs on top of the Columbo Reef and its vicinity between 10th of June 2006 and 27th of March 2007. Fig. 1.5 shows the bathymetry and the positions of the OBT profile over Columbo and the closest OBSs. For a detailed description of the amphibian network and station positions see chapter 2. OBTs were additionally equipped with hydrophones to record seismic signals. Technical details of the new Hamburg OBT system are given in chapter 3. The tiltmeter profile (Fig. 1.5) was deployed along the third principal stress axis σ_3 , since possible intrusions such as a dike would open along an axis perpendicular to σ_3 (Rubin and Gillard, 1998a). The smallest deformation wavelength and thus largest tilt gradients are thus expected along σ_3 . Even the shape of the Columbo volcano is clearly elongated perpendicular to σ_3 , indicating the predominance of NE-SW orientation of dikes.

Parallel to our experiment, the EGELADOS experiment, another amphibian network with a large number of landseismometers and additional 24 OBSs (see chapter 2.1.2), was performed in the complete Aegean Sea region. In collaboration with our German, Greek and Turkish partners, all networks were joint to a large database for several subprojects and thus we had access to much more seismic data of the surrounding islands to complete our data set.

These temporal improvements enabled us to precisely investigate six earthquake swarms that occurred during our experiment and investigate their behaviour in terms of possible migration paths or repeating patterns of event distributions.

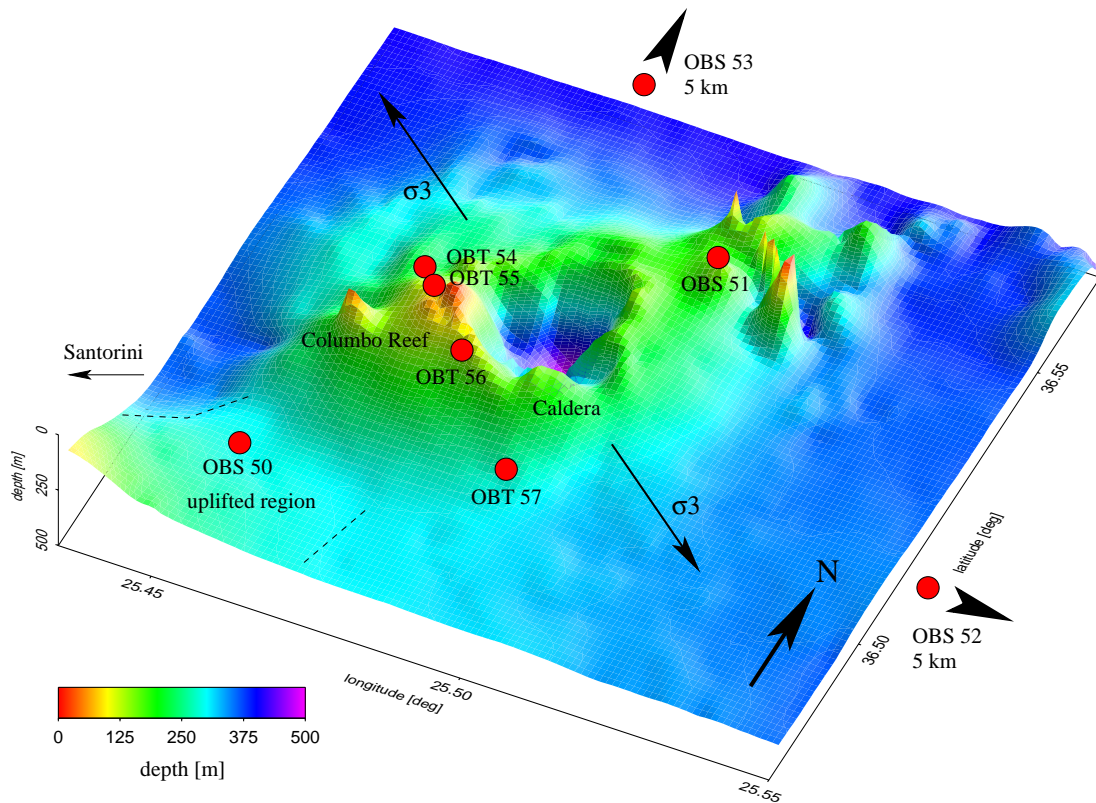


Figure 1.5: **3D view of the Columbo bathymetry:** Bathymetry plot of Columbo derived from ship echo sounder data of RV Poseidon, view with an azimuth of 135° and a plunge of 40° . Highest elevation is the Columbo reef, located between the caldera and an uplifted region between Columbo and Santorini. An OBS with an absolute pressure sensor was located on top of the uplifted region, another OBS on the opposite site of the caldera. A profile of 4 OBTs was deployed over the Columbo Reef and perpendicular to an axis Santorini-Columbo, parallel to the lowest principle stress axis σ_3 . Two additional OBSs slightly outside this map section closed azimuthal gaps between the surrounding islands.

1.4 Structure of the thesis

The complete Columbo experiment, active measurements parallel to the OBS/OBT deployment and the partner project EGELADOS are introduced in Chapter 2, followed by a detailed technical description of our newly developed Ocean-Bottom-Tiltmeter in Chapter 3. Within this OBT chapter, questions on the technical functionality will be cleared based on test measurements in the laboratory, in a mine and finally the practical test at Columbo.

An exhaustive introduction on seismic and especially deformation sources is given in Chapter 4: Despite the seismic moment tensor inversion, predominantly the theory of near-field terms of rectangular fault sources and volume sources is shown. Deformation sources are introduced very detailed, including modelings on their shape and range.

Chapter 5 summarizes all methods and results of the seismological analysis (earthquake relocation and moment tensor inversion). All methods and result concerning the earthquake swarm and deformation data analysis are given in chapter 6. Both chapters give detailed

overviews on data-processing steps.

All observations are finally discussed together with modelling approaches and other findings of all main topics in Chapter 7. Results of active measurements during the Columbo deployment cruise in June 2006, active seismic and magnetic profiling, and additional findings beside the main topics are taken into account to discuss our findings.

CHAPTER 2

DATA ACQUISITION

The Columbo Seamount Ocean-Bottom-Seismometer (OBS) and Ocean-Bottom-Tiltmeter (OBT) Experiment took place at and around the Columbo submarine volcano between 10th of June 2006 and 27th of March 2007. The data set is composed of own OBS/OBT data and passive seismic data of the amphibian EGELADOS network (see section 2.1.2), which covered the whole Aegean Sea, major Aegean islands and Greek and Turkish mainland in the vicinity of the Aegean Sea during the same time. We also had access to data of the permanent network of the National Observatory of Athens (NOA). Parallel to the deployment of 4 OBSs and 4 newly developed OBTs (for technical details see chapter 3), 1.500 km of high frequency reflection seismic, magnetic and gravimetric profiles were measured.

While the installation of onshore stations was organized by the EGELADOS project partners of Bochum, Thessaloniki and Istanbul, the deployment of offshore stations and active measurements was carried out during three ship cruises:

- 18th - 30th of May 2006: Heraklion (Crete) - Piraeus
deployment of EGELADOS OBSs in the southern Aegean Sea
RV Poseidon, cruise P337, chief scientist Prof. Dr. Wolfgang Friederich
- 1st - 12th of June 2006: Piraeus - Piraeus
deployment of Hamburg OBSs/OBTs at Columbo and active measurements
RV Poseidon, cruise P338, chief scientist PD Dr. Christian Hübscher
- 27th of March - 11th of April 2007: Piraeus - Piraeus
recovery of EGELADOS and COLUMBO OBSs/OBTs in a joint cruise
RV Aegaeo (Hellenic Center of Marine Research), chief scientist Prof. Dr. Torsten Dahm

I took part in all three cruises, on the 2nd and 3rd cruise I was responsible for the Hamburg OBS/OBT deployment and recovery. This chapter gives an overview on the different legs and methods of the joint experiments.

2.1 Passive measurements

Different types of offshore seismic and deformation sensors have been deployed around Columbo to better analyze seismicity and to get close enough to potential deformation sources.

2.1.1 The Columbo OBS/OBT Experiment

Recent studies on the seismicity of the Columbo seamount and the tectonic faults in its vicinity were based on data recorded on islands (e.g. Bohnhoff et al., 2006; Dimitriadis et al., 2009). Although the area allowed the installation of dense networks on the surrounding islands, these experiments had to deal with large uncertainties in location, especially depth, of the events due to partly large azimuthal gaps and missing zero-offset stations. With the deployment of seismic sensors in the direct vicinity of the seamount and even on its top, azimuthal gaps between the surrounding islands were closed and the sensitivity of the network, i.e. the magnitude threshold of detectable events significantly decreased (see Tab. 2.1):

<i>network</i>	<i>remarks</i>	<i>3 closest stations</i>	<i>automatic triggers</i>	<i>M_L threshold</i>
NOA	permanent	SANT, APE, AMOE	4	3.5
EGELADOS	temporary	NEAK, ANID, IOSI	800	2.0
COLUMBO	temporary	all OBSs/OBTs	14.000	0.5

Table 2.1: List of automatic triggers of different networks. The sparse permanent NOA network triggered only events above magnitude 3.5. The denser the temporary networks are, the more the number of triggers increased, while the magnitude threshold sank. For the Columbo network, these were over 14.000 triggers of which around 90% were "real" events and only 10% mistriggers or noise, the threshold could be decreased to $M_L = 0.5$.

Ocean bottom stations were installed as shown in Fig. 2.1: OBSs between the islands of Ios, Anidros and Anafi, between Columbo and Santorini as well as on the back side of the Columbo caldera towards the Santorini Amorgos Fault. Furthermore, all OBTs were equipped with hydrophones in order to measure seismic signals. Differential Pressure Gauges (DPGs, Scripps Institution of Oceanography, for technical details see Cox et al., 1984) to measure long period relative pressure signals from 60 s up to 5 Hz were mounted on OBSs 50 and 51, i.e. those OBSs closest to the seamount.

The Tiltmeter stations were deployed directly on top of the seamount (see Fig. 2.2), since crustal deformation due to magmatic ascent is best recorded locally. The profile is designed asymmetric due to unknown depth and size of a possible migrating fluid batch: A deep source causes slight deformation of a larger region, while a shallow source causes stronger deformation of a much smaller region. Depth and volume dependencies of the deformation signal are modeled in Chapter 4.2.2. Furthermore, the OBT profile was deployed along the weakest stress axis σ_3 . The strongest tilt signal occurs in the inflexion points of uplift (or

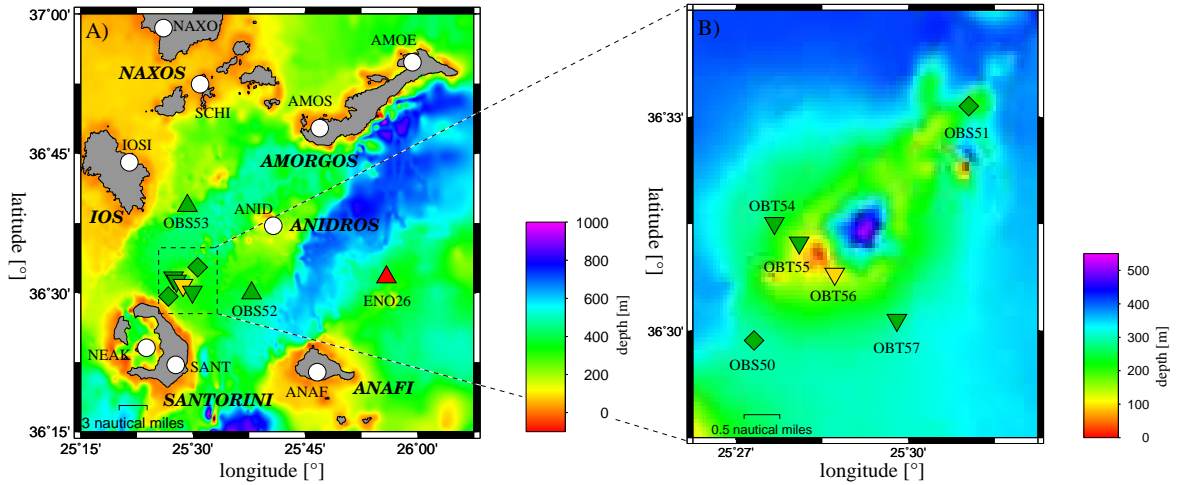


Figure 2.1: **Experimental setup around Columbo Seamount.** A) Seismic network at Columbo and the surrounding islands: triangles mark OBSs with OAS-hydrophone, diamonds OBSs with DPG; inverse triangles mark OBTs, white circles NOA and EGELADOS landstations. Colors of OBSs/OBTs stand for green = permanently running, yellow = incomplete data, red = no data. B) Dense network at Columbo Seamount, symbols and colors same as graphic A.

subsidence). A dike is supposed to have its smallest extension and thus the tilt signal with the shortest wave length in direction of σ_3 (e.g. Rubin and Gillard, 1998a). Thus, an asymmetric profile along σ_3 allows the largest coverage of possible depths and sizes of an intrusion, even with only four tiltmeters.

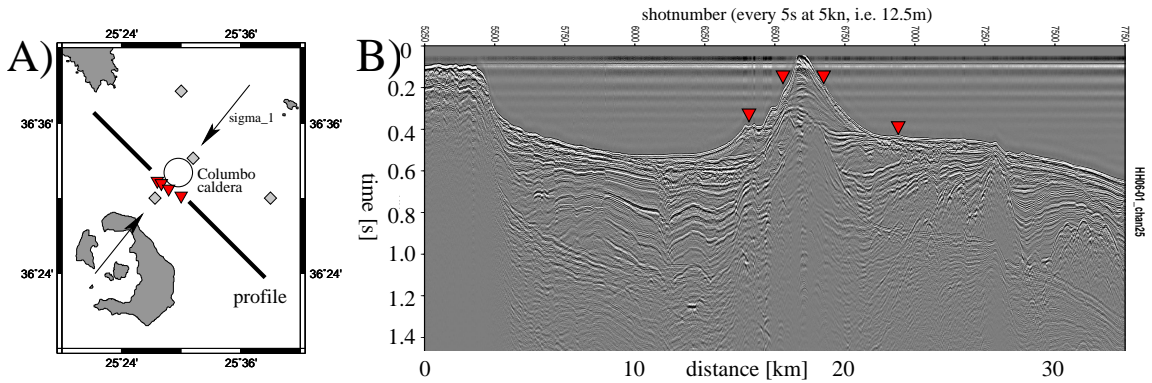


Figure 2.2: **Tiltmeter profile over Columbo Seamount.** A) Asymmetric profile over Columbo Seamount along σ_3 . Tiltmeters are marked with red triangles, gray symbols mark OBSs. B) Reflection seismic cross section over the tiltmeter profile (red triangles), 10-times exaggerated. Despite the topography of the seamount, both, volcanic deposits and possible intrusions are visible and will be discussed in chapter 2.2.1.

Additionally, all OBTs and OBS50 (between Columbo and Santorini island, see Fig. 2.1) were equipped with absolute pressure sensors to measure uplift and subsidence. This was deemed important in case of having placed the sensor on top of the possibly inflating region, where the vertical signal reaches its maximum, but tilt becomes zero.

A detailed description of all instruments, including individual equipment with sensors,

positions, poles and zeros etc. is given in Appendix A.

The deployment campaign started on 1st of June 2006 from the harbour of Piraeus with the German research vessel RV Poseidon. The first week of the expedition was used for active measurements (see chapter 2.2), while OBSs and OBTs were assembled on board. The final deployment took place on the 10th of June.

The recovery cruise finally started on midnight of 26th/27th of March 2007 from Piraeus with the Greek research vessel RV Aegaeo of the Hellenic Center of Marine Research (HCMR), in collaboration with the EGELADOS OBS recovery of the RUB. The target area around Columbo was reached during the evening of the 27th. During an overnight recovery, all Hamburg OBSs/OBTs could be recovered within less than 12 hours.

Except for OBT 56, all OBSs/OBTs could be synchronized with GPS to interpolate their clock-drift over the complete data set. All synchronized recorders showed drifts smaller than 0.8 s and an average drift of around $0.05 \frac{s}{month}$. OBT 56 shut down only 35 days after its deployment due to a water leakage in the battery cylinder which affected both, tilt and seismic recording as well as the absolute pressure sensor and its logger. All stations were showing unusual strong corrosion damages, such as rusty screws and critically corroded releaser housings. The so called "stainless"-steel of the absolute pressure sensors was partly dissolved so that water ran into the sensors and destroyed them.

Another interesting aspect was, that there was strong lime-accretion on all OBS frames if they were deployed above the critical depth where lime becomes completely dissolved in water (the lysocline for carbonate dissolution can be expected at about 3.500-4.000 m depth according to Berger, 1973). This accretion was observed for all Hamburg OBSs, OBTs 54 and 57 and most EGELADOS OBSs despite of those deployed in the deep-sea trench south of Crete. But for both OBTs 55 and 56 which were standing closest to the caldera rim of Columbo, no accretion, but strongest corrosion damages were observed after deployment. This might indicate an acidic chemical regime due to fumarole activity inside the caldera.

Since active levelling of the OBTs was executed the first time on 11th of June and one re-levelling (every 48 hours) was awaited as well as the passive levelling of the OBSs requires several hours to reach its perfect vertical adjustment, we used data between the 1st of July 2006, 00:00 UTC, and 27th of March 2007, 12:00 UTC, for processing. Smooth nonlinear trends on the tiltmeters for the first days of data collection suggested an initial phase of sinking and setting of the instrument frame of about 3 weeks after deployment. This period was not used for data interpretation.

All results presented in this thesis correspond to the time window 1st of July 2006 00:00 UTC - 27th of March 12:00 (269.5 days).



Figure 2.3: **Scientific crew of the recovery cruise (RV Aegaeo)**. Research vessel AEGAEO (Hellenic Center of Marine Research, Athens) in the harbour of Piraeus (left-hand side photo) and the scientific crew of the recovery cruise: Upper row, from left to right, Torsten Dahm, Martin Hensch and Sven Winter (all University of Hamburg, UHH), Wolfram Geissler (AWI), Kasper Fischer (Ruhr-University Bochum, RUB), Tuncay Taymaz (Istanbul Technical University), Reinhard Schrotzky (SEND GmbH), mid row, Wolfgang Friederich (RUB), Erik Labahn (KUM Kiel), Mechita Schmidt-Aursch (AWI), front row, Celia Rios (UHH), Domenicos Vamvakaris (Aristotle University of Thessaloniki), Andreas Schmidt (RUB).

2.1.2 The EGELADOS Experiment

The EGELADOS experiment ("Exploring the **GE**odynamics of subducting **L**ithosphere using an **A**mphibian **D**eployment **O**f **S**eismographs", (Friederich and Meier, 2008)) was a passive seismic experiment in the Hellenic Subduction Zone, conducted within the framework of the Collaborative Research Center CRC526 "Rheology of the Earth" at the Ruhr University Bochum (RUB), funded by the German Research Foundation (DFG).

The COLUMBO project is carried out in close cooperation with EGELADOS, both experiments were performed parallel and data is exchanged between all participating institutions (see Appendix F). Between autumn 2005 and spring 2007, 51 broadband seismometers of the RUB and the German pool of amphibian seismographs (DEPAS) were mounted in addition to the existing NOA network on the Aegean islands and the adjacent Greek and Turkish mainland. By the middle of May 2006, the densified network was completed with 24 DEPAS OBSs between the Aegean islands and south of Crete along the Hellenic trench. The offshore deployment was also carried out by RV Poseidon, shortly before the Columbo expedition and the recovery was done in cooperation with the Columbo project with RV Aegaeo (27th of March - 11th of April 2007).

A station map of EGELADOS is given in Fig. 2.4, a list of stations is given in App. A.1. For our relocation and moment tensor inversion routines, we only used EGELADOS stations being less than 80 km away from Columbo for two reasons: Limited disk space (the complete SEISAN setup for the complete Columbo network including 15 landstations over the complete time is about 400 GB) and variations of the velocity model outside the Hellenic Volcanic Arc

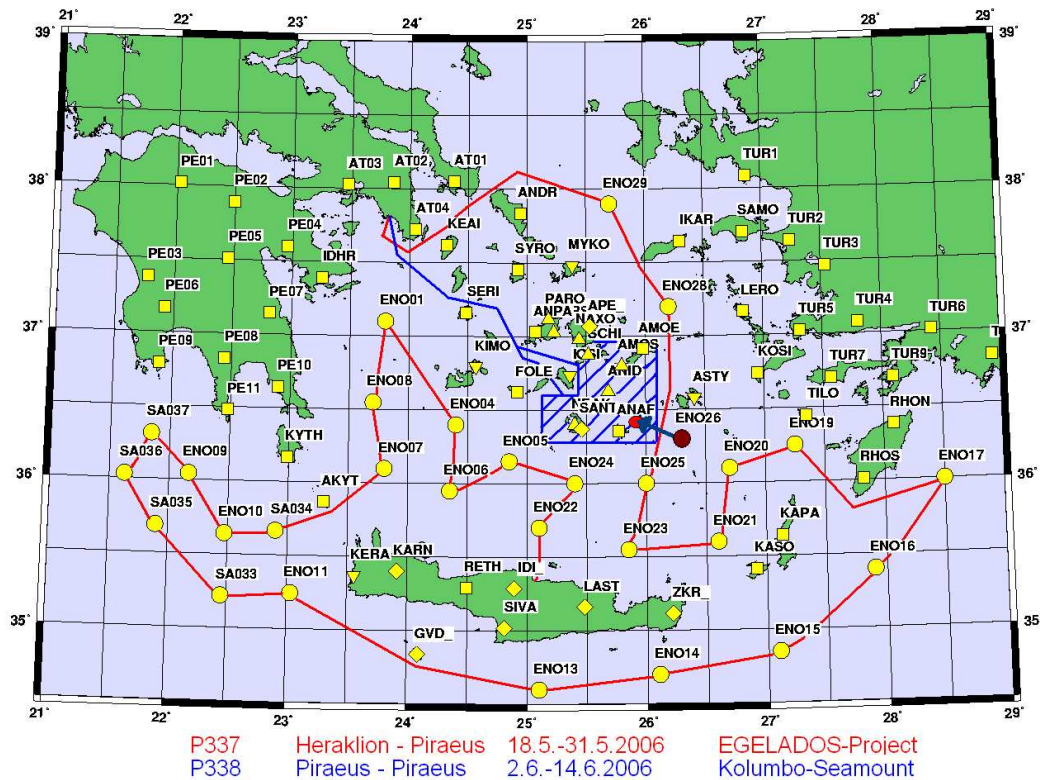


Figure 2.4: The **EGELADOS network** consisted of 104 seismic stations, of which 24 were installed offshore in the entire Aegean Sea between latitudes $34.5^{\circ}N$ and $38^{\circ}N$ and longitudes $21.5^{\circ}E$ and $29^{\circ}E$. In addition to offshore stations, the Aegean islands, as well as Greek and Turkish mainland were covered with seismometers.

(a 1D model of the Santorini-Columbo volcanic complex was used, the regional model for the Aegean Sea is faster and thus led to differences in picked and calculated traveltimes up to 3 s for stations > 200 km away). SEISAN and MTInvers are not able to handle a more dimensional velocity model.

2.2 Active measurements

While passive seismic measurements as described above deliver an image of present activity of the target area (location, frequency and strength of activity), active measurements were used to image the subsurface (sediment thickness, layers of former eruptions etc.). The investigation of the active data is the task of two diploma students at the Institute of Geophysics at the University of Hamburg and will only be shortly introduced here; already existing results will be included in the discussion of the passive data.

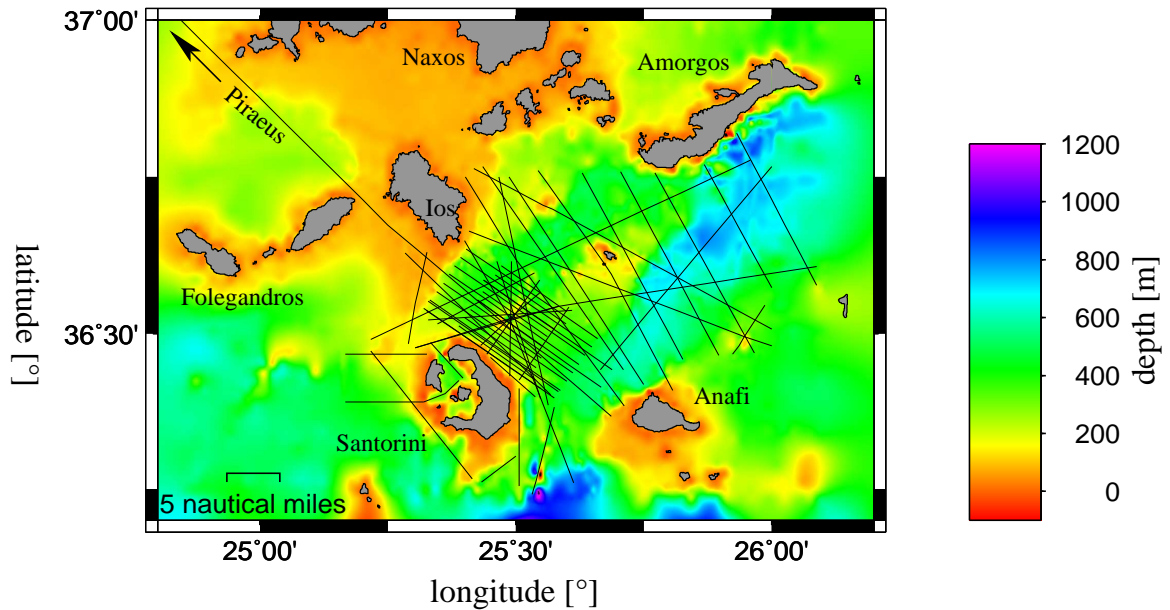


Figure 2.5: **Profile lines of active measurements (RV Poseidon)**. Tracklines (black) of active profiling (reflection seismic, magnetic and gravimetry, plotted over the bathymetry of the target region. Dense profiles (500 m distance) were shot over the Columbo volcano, a sparser net of profiles over the Santorini-Amorgos-Zone. Additional profiles around and through the Santorini caldera complete the dataset.

2.2.1 Reflection seismic profiling

To investigate shallow expressions of tectonic processes and/or magmatic intrusions, that might result in active faulting, the Columbo volcano itself and the adjacent Santorini-Amorgos-Zone were mapped in detail by means of multichannel reflection seismic. The complete profile length of the experiment is about 1.500 km (Fig. 2.5). For this active measurement, a GI-Airgun with a main frequency of 100 Hz was used as the seismic source. Data were recorded by two seismic streamers (sensor cables) of 150 m and 600 m length.

Fig. 2.6 shows a joint plot of a magnetic and a seismic profile, measured directly over the Columbo caldera. A reflection-free spot underneath the caldera is interpreted to be caused by gas and/or hydrothermal fluids in shallow depths. The distribution of volcanoclastic deposits, especially stacked cones beneath the present caldera rim, suggest at least two eruptions of Columbo in the past.

Scope of the reflection seismic experiment is to identify active tectonics as well as to budget pyroclastic and other volcanic deposits around Columbo, Santorini and the Santorini-Amorgos-Zone (see Ruhnau, 2009).

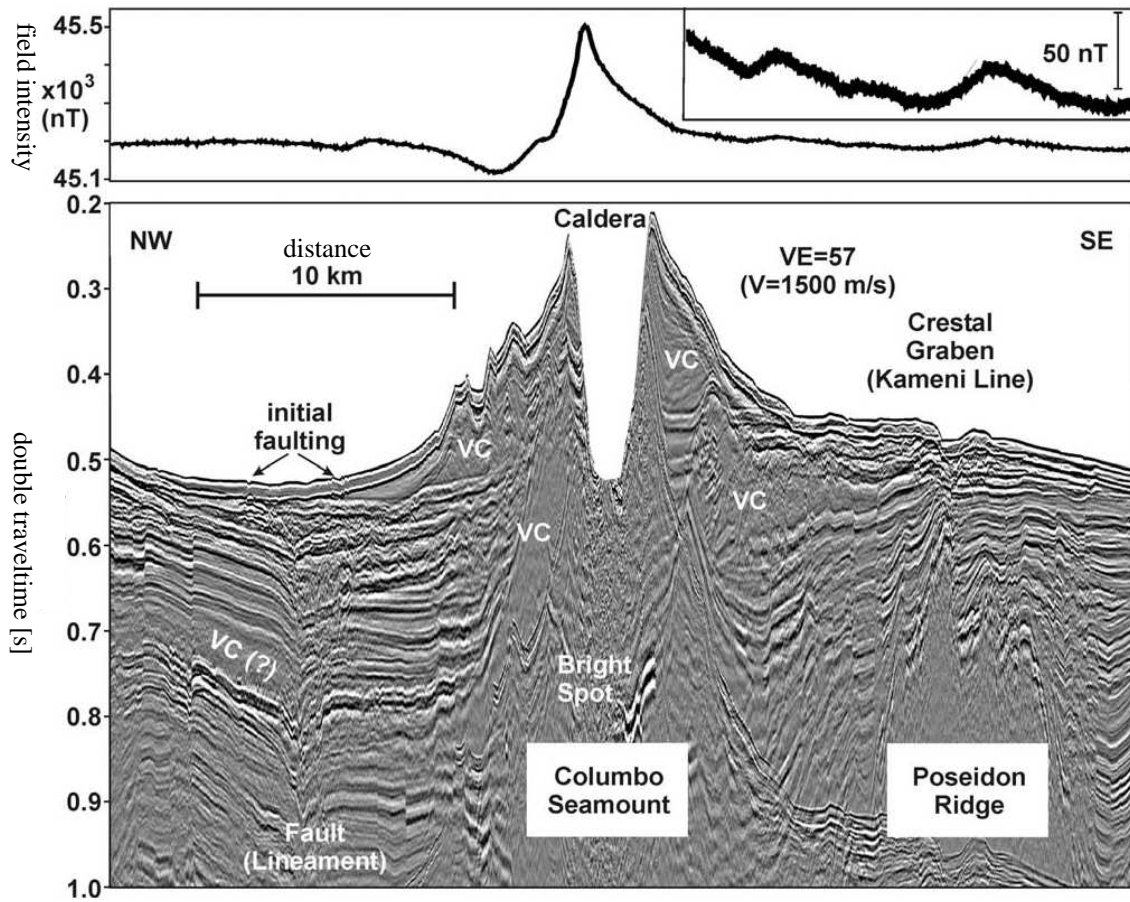


Figure 2.6: **Joint seismic and magnetic profile over Columbo.** Seismic (time-migrated section) and magnetic (gradiometer) data across the Columbo submarine volcano. Volcanoclastic (VC) deposits are characterized by weak and chaotic reflections. The so called Poseidon Ridge aligns along the Kameni line. Strongest signals of the magnetic field are found directly above the Caldera (Hübscher et al., 2006).

2.2.2 Gravimetric and magnetic profiling

The Hamburg Sea Gravimeter was running during the complete deployment cruise, including reference measurements onshore in Piraeus at the beginning and at the end of the cruise, all in all around 2.500 km. Magnetometer profiles (gradiometer) have been carried out parallel to the seismic profiling, which led to about 1.500 km of magnetic profiles.

The detection of magnetic heterogeneities can help to model size and depth of possible former intrusions, which makes it an interesting parallel tool to study present and recent activity at a volcano, especially when depth and spatial extension of possible deformation sources are unsure before the experiment, as it was the case for Columbo.

Fig. 2.7 shows magnetic anomalies around the Santorini-Columbo volcanic complex. Despite of a large dipole underneath Santorini, many small anomalies are found at Columbo and the seamounts in its vicinity (see Landschulze, 2009). Shallow magnetic anomalies are

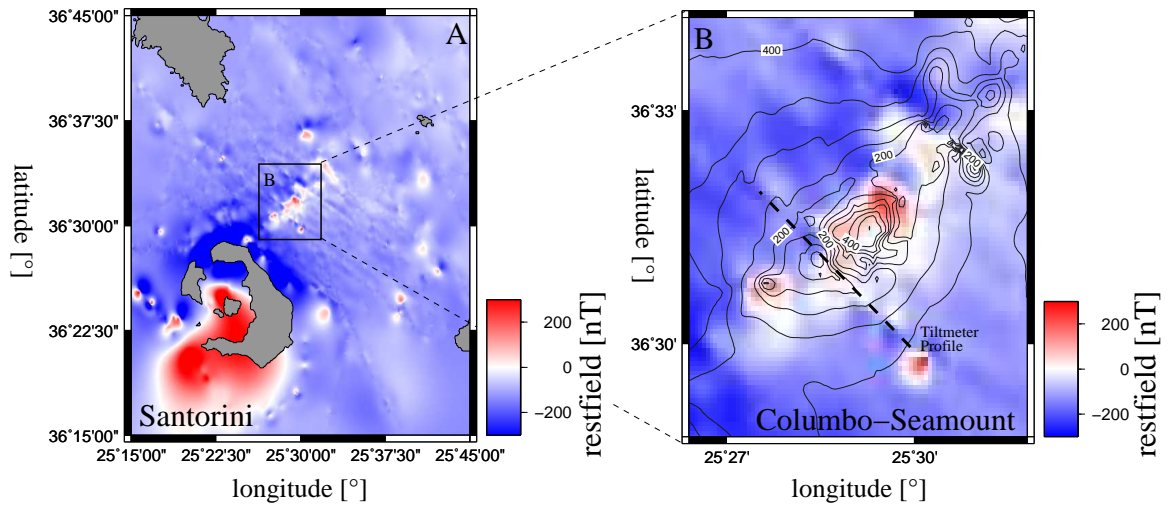


Figure 2.7: **Magnetic heterogeneity around Santorini and Columbo.** Magnetic restfield once the international geomagnetic reference field (IGRF) has been subtracted from the data. A large dipole underneath Santorini and several small anomalies concentrated at Columbo and the surrounding seamounts are observed. These anomalies are suggested to reflect former intrusions.

suggested to derive from former magmatic intrusions, which intensify the reference field due to their ferromagnetic susceptibility once they cool below the Curie-Temperature. Results of the magnetic measurements will be partly included in our final discussion. Additionally, based on onboard preprocessing, gravimetric and magnetic data helped to find and optimize locations for OBSs and OBTs on the deployment cruise.

THE NEW HAMBURG OCEAN BOTTOM TILTMETER (OBT)

While common techniques, such as InSAR or GPS measurements, have already been proven to be valuable in monitoring onshore deformation signals due to magmatic recharging, both methods are not applicable to assess the state of activity for submarine volcanoes or the submarine slopes of volcanic islands. A first step towards measuring deformation related tilt of the seafloor is the development of the Hamburg Ocean Bottom Tiltmeter (OBT), whose four prototypes have been deployed in the pilot-experiment at Columbo. This chapter summarizes technical details of the OBT and first experiences in practical use.

3.1 Technical description

Core of the new Hamburg OBT is a highly sensitive 2 component tiltmeter, manufactured by *Lippmann Geophysikalische Messgeräte* (Germany). Each component of the tiltsensor is a pendulum which is kept at the zero-position in an electric field. Once the instrument is tilted, this causes a slight horizontal acceleration (as a small component of the gravity) on the pendulum. To maintain the pendulum at its zero-position, the instrument adjusts the electric field accordingly. The change in voltage used to keep the pendulum at its zero-position is the measured variable to calculate for tilt.

The instrument including a gimbal system is mounted in a 17" glass sphere which are also used for the Hamburg Ocean-Bottom-Seismometer (Dahm et al., 2002) and thus can be deployed using the standard Hamburg OBS-frame. The tiltmeter has a theoretical resolution of 2 nrad. Recording the data with the SEND Geolon MLS (SEND GmbH Hamburg, Germany) with a sampling rate of 50 Hz (18 bits resolution), results in a final resolution of about 15nrad. The range of the sensor is ± 4 mrad (4000 μ rad), but the range is extended to several tens of degrees through mechanically relevering the sensor platform (external gimbaling, see Fig. 3.1).

Because this highly sensitive sensor is mounted on a freefall ocean bottom instrument frame, the instrument design called for certain requirements:

- A tilt of the terrain of up to 45° should be accommodated by the external gimbal system
- The system should level the tiltmeter sensor platform to better than $\pm 50 \mu rad$
- During operation, the sensor is mounted on the bottom of the glass sphere at 3 points by gravity, i.e. it stands free on the bottom of the sphere

Those requirements were obtained by developing a two phases leveling process: The external gimbaling system of made cardanic aluminium rings is fixed to the lower half of the glass sphere. A highly sensitive leveling stage of the sensor platform (manufactured by *Quante*) is fixed below the center of the external gimbaling's aluminium rings (see Fig. 3.1). The sensor platform is connected to the external gimbal system through three nylon strings that are length controlled by a small electric motor. This allows to lower and raise the sensor platform with an accuracy of better than $\pm 5^\circ$. Once the platform rests on the bottom of the sphere, the internal leveling device of *Quante* levels the sensor down to an accuracy of about $10 \mu rad$.

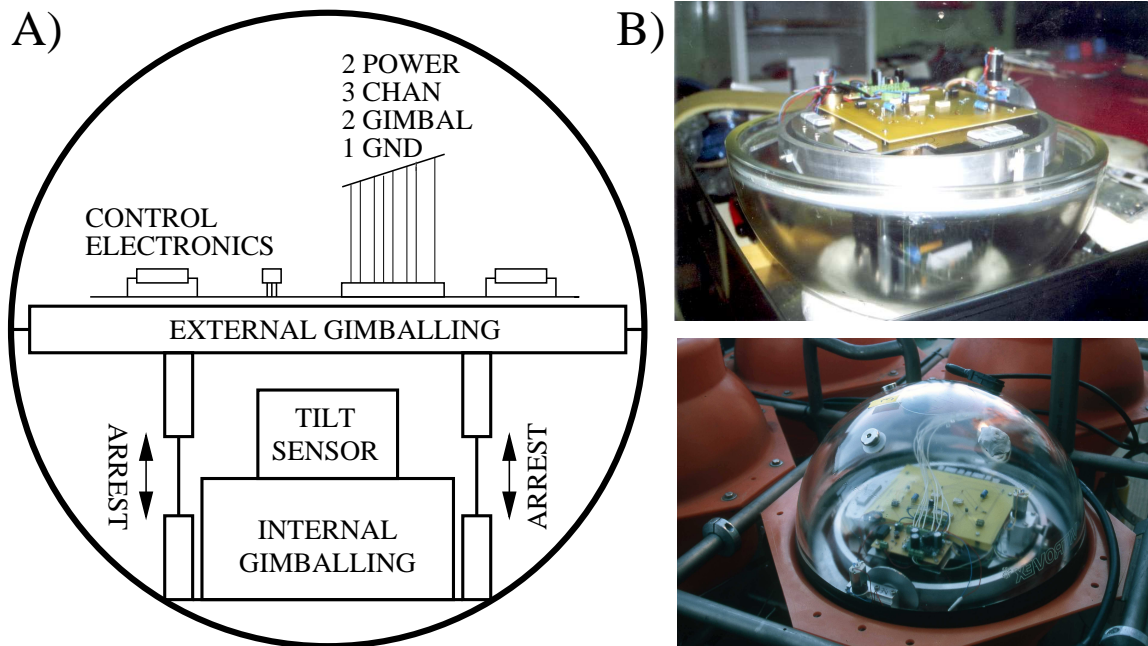


Figure 3.1: **Sketch and photo of the OBT sensor sphere.** A) Sketch of the sensor sphere of the OBT: The internal gimbaling system is hosting the tiltmeter and is hanging in the external cardanic gimbaling. Nylon strings enable to mount and unmount the sensor. B) The aluminium rings of the external gimbaling and how they are mounted to the sphere are shown in the upper photo. On top, the steering electronics are visible, through the glass sphere, the leveling stage hosting the tiltmeter can be crudely seen. The lower photo shows, how the sensor sphere is mounted on the ocean bottom frame (other spheres are for floatation only).

Once the system is deployed, it can be programmed to rest for a given number of days before the first leveling of the system is carried out. Afterwards, the system is leveled on a regular basis (in our case every 48 hours, since it was unclear how fast the signals could reach the limits of the instrument's dynamic range during this pilot experiment). One disadvantage of the system is that tilt steps caused by leveling of the sensor platform (internal and external gimbaling) are not measured by an independent sensor and have to be estimated and removed from data during postprocessing.

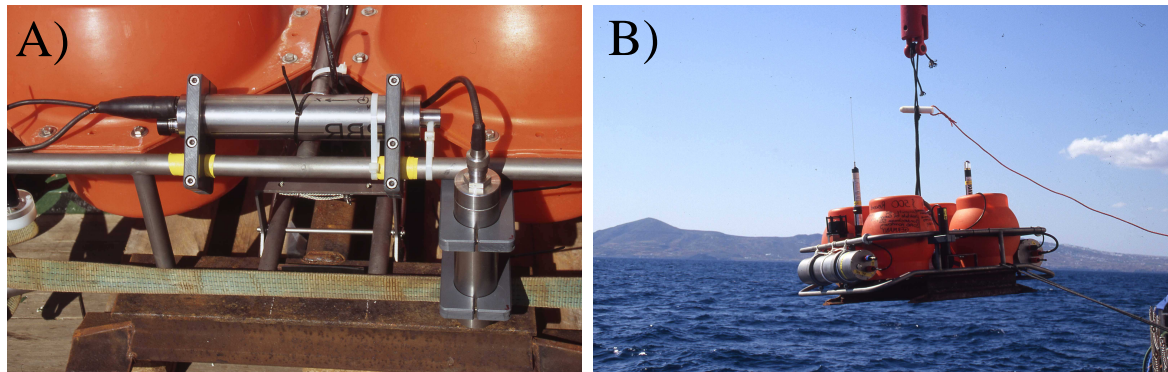


Figure 3.2: **Photos of absolute pressure gauge and OBT deployment** A) The absolute pressure gauge (vertical cylinder) is mounted at the side of the OBS/OBT-frame. It uses a power supply independent from the tiltmeter and MLS data logger, its data is recorded on a separate logger (horizontal cylinder). B) Deployment of the OBT system at Columbo seamount (Santorini island in the background). The instrument sinks to the sea bottom using an anchor-weight (iron rails), it can be recovered by releasing the weight and ascending due to its own buoyancy. Once it reaches the sea surface, radio beacon and flash light help to find it even in rough sea or during the night. The batteries and the MLS data logger are stored in the large pressure tubes on the beside of the frame.

In addition to the two tilt traces, we also recorded the temperature inside the sphere in order to detect a possible temperature dependence of the tilt signals. The instrument frame also hosts a OAS-hydrophone to collect seismic data (lower corner frequency is $f_c = 0.3 \text{ Hz}$) and a highly sensitive absolute pressure sensor (see Fig. 3.2) manufactured by *Paroscientific* to observe possible uplift and subsidence with a resolution of $0.1 \text{ mbar} = 10 \text{ Pa}$ which corresponds to a vertical displacement of 1 mm .

3.2 First experiences in practical use

Following subsections give a short overview what kinds of signals can be measured with the OBT - from its first steps in the laboratory to its pilot-deployment in the Aegean Sea.

3.2.1 Calibration in the laboratory

The tiltsensor was calibrated in the laboratory using a tilt-table as shown in Fig 3.3 by splitting the gravity g into accelerations normal z'' and parallel x'' to the table.

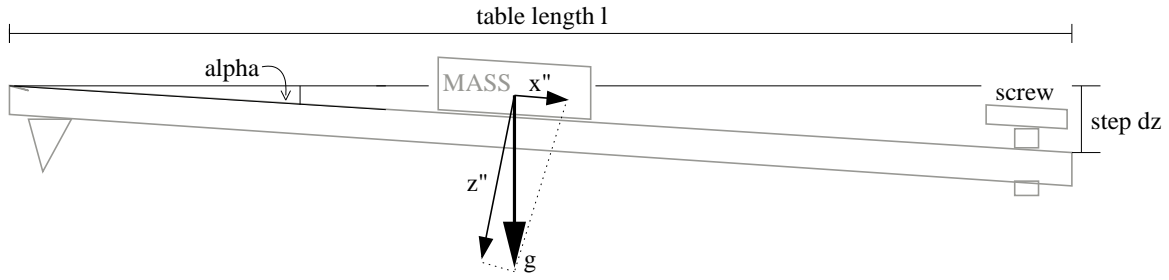


Figure 3.3: **Tilt-table used for tiltmeter calibration:** Raising and lowering the tilt table at one side using a micrometer screw causes a tilt α . Gravity g is thus splitted in two components normal and parallel to the table. The table-parallel component acts as a horizontal acceleration component x'' of the gravity g .

The calibration itself is relatively simple: By applying a pre-defined step dz on a table with the length l using a micrometer screw (see Fig. 3.4), the sensor measures a step-like tilt signal of $\alpha = (\frac{dz}{l})$.

For each sensor and each component, several steps of varying size are measured, a constant $k = \alpha/A$ [rad/count] with A as the amplitude of measured counts and α as the tilt angle can be derived through linear regression.

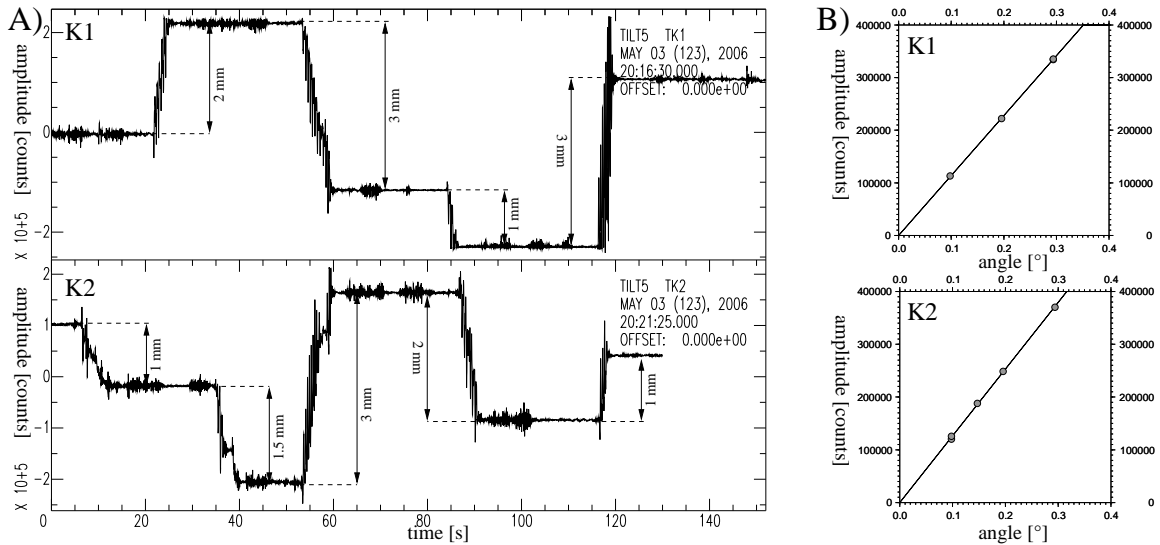


Figure 3.4: **Example for tiltmeter calibration.** A) shows both traces of a tiltmeter (here: s/n 5, OBT57). Jumps within these traces mark tiltsteps given with the tilt-table. The linear regression over these steps is given in B) and leads to the calibration constant k .

The calibration of all used sensors leads to an average calibration value of:

$$k = 14.5 \pm 0.7 \frac{\mu\text{rad}}{\text{count}} \quad (3.1)$$

This value is used from here on to convert the digitized signal into a tilt signal. Calibration plots and tables for all used sensors can be found in Appendix C.

3.2.2 Test measurements in the Black Forest Observatory (BFO)

To better understand the first data measured outside the laboratory, two OBT systems were installed in the mining shaft of the Black Forest Observatory (BFO) in southern Germany for 4 weeks in March/April 2008. The originally planned "huddle-test" to analyze possible deviations between two sensors that are operating directly next to each other failed due to a shut-down of one of the OBT systems due to battery problems. The test was also intended to see if there were constructionally caused deformation signals, such as e.g. deflection of the frame. The BFO was chosen because of low noise conditions inside the mine to better study the characteristics of the instrument.

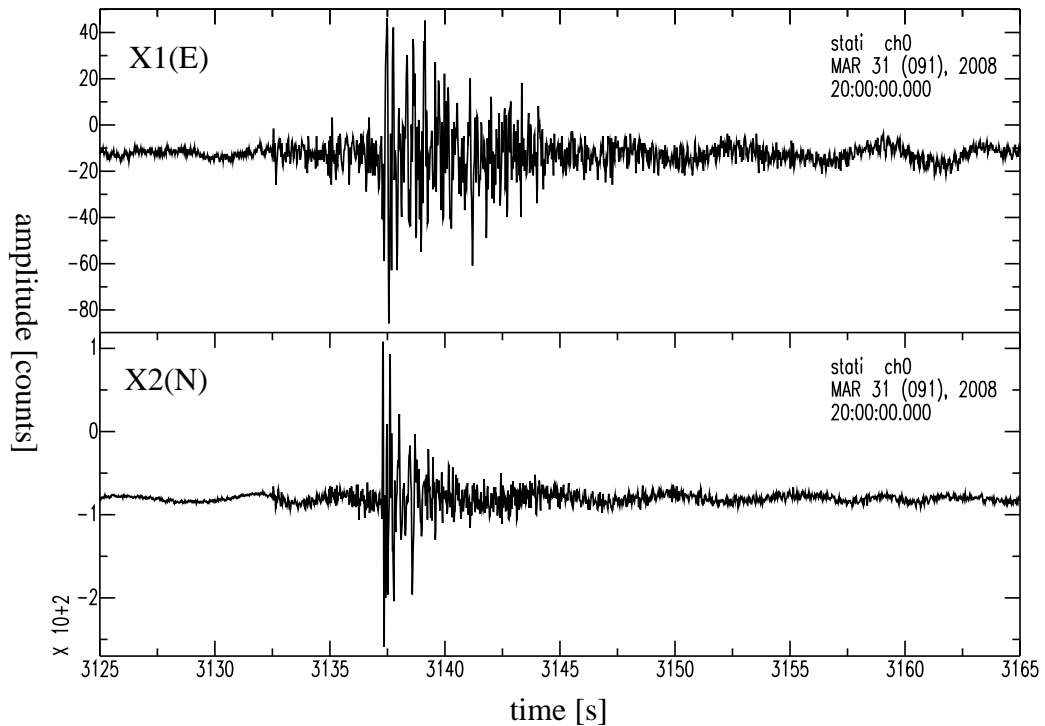


Figure 3.5: **Regional earthquake observed at the BFO.** Unfiltered rawdata of a local earthquake at about 50 km epicentral distance was observed on 31st of March 2008 during the test measurement at the BFO.

A local seismic earthquake was recorded on 31st of March 2008 (Fig. 3.5). Without any filtering, this event is clearly separated from noise and thus proves the functionality of the tiltmeter for high frequencies. A long period signal measured during the test period of 22 days was an exponential decreasing trend or drift. It is unsure whether these strong, but quickly reducing trends derive from sensor drifts or the complete tiltmeter setup of the OBS/OBT frame, e.g. due to relaxation of screws or yielding of the underground. A similar drift for the initial phase has been observed on the 4 OBTs at the Columbo seamount and as a consequence, the first 3 weeks of data were cut off.

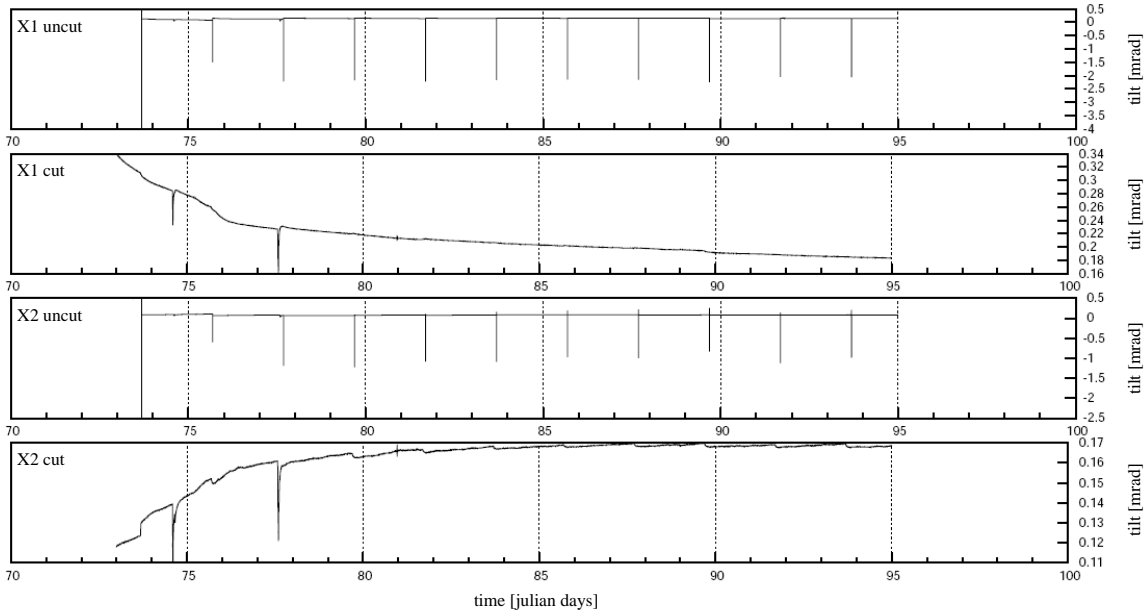


Figure 3.6: **OBT traces of BFO measurement.** Traces for both components of a tiltmeter running in the BFO mine. The first trace of each component is unprocessed. It includes levelling events (peaks), the second trace is cut for these events and the trend becomes visible showing an exponential decay.

Unfortunately, due to the unexpected strong initial drift and because of the relatively short test period, we were not able to resolve the week tilt signals caused by solid earth tides at the BFO. A long period functionality test on the resolution of tides with periods of about 12.5-13 hours is still open.

3.2.3 Overview on signals observed at Columbo

Compared to offshore measurements, where noise is induced due to sea waves, currents and ship traffic, noise at the BFO was smaller by a factor of up to 30 (see Fig. 3.7). This effect is also supported by the coupling of the instrument: While a concrete block on a fundament of bedrock is the optimal setup to couple our OBT frame to the ground, the reality at the seamount looks different. There, the instrument is dropped onto unconsolidated volcanic deposits (sediments). Coupling to the seafloor is only granted by the anchor weight of 120 kg mounted to the OBT-frame (the weight of the complete system under water is 20 kg).

Similar to the recordings at the BFO, high frequency earthquake signals are well resolved on the OBT at Columbo (see Fig. 3.8). Although the upper corner frequency of the tiltmeter is about 3 Hz, local events at Columbo with dominant frequencies between 3-10 Hz are still recorded by the system. Onsets of arriving waves are not as sharp as they are on a seismometer, but can be used to pick onset times. Low frequency earthquake data, as generated by teleseismic events, have been observed very clear by the OBTs (see Fig. 3.9 for the $M_W = 8.3$ Kuril islands earthquake, 15th of November 2006). Compared to a STS2 seismometer (station

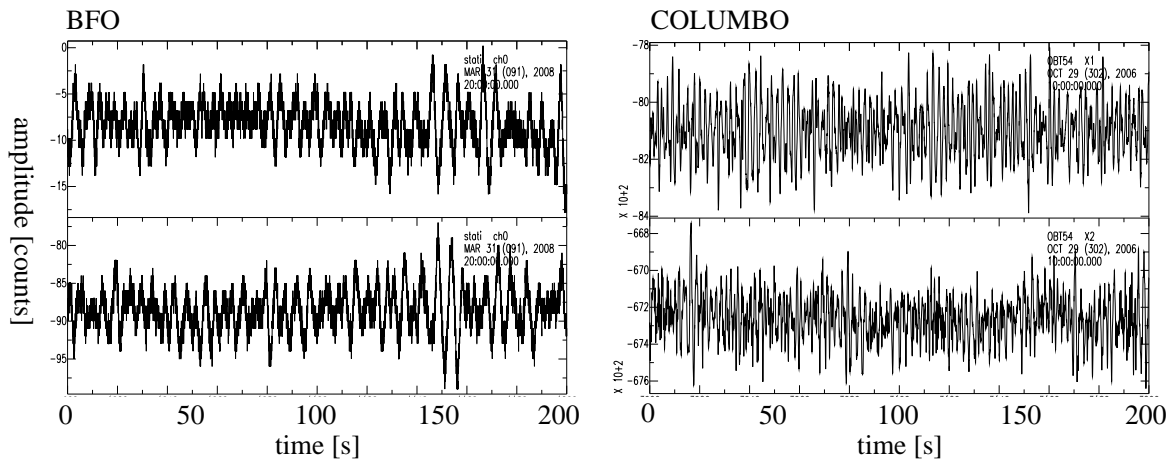


Figure 3.7: **Noise comparison: BFO vs. Columbo.** Timetraces of 200 s each for noise in the BFO mine and offshore at Columbo. Noise amplitudes at Columbo is up to 30 times higher than for the BFO. Further, the noise frequency seems to be higher at Columbo.

IOSI, lower traces), the tiltmeter (upper traces) nicely resolves long period seismic signals, here bandpass filtered between $0.01 - 0.1$ Hz to analyze periods below 10 s. Although teleseismic events were not further investigated in this work, this plot evidences the successful observation of broadband seismic signals on the seafloor with our OBT.

Fig. 3.10 shows a high frequency tilt step that occurred simultaneously to the arrival of S-waves at a small epicentral distance. The low frequency coda of the horizontal components of the seismometers indicate that in fact a tilting of the instrument occurred. These tilt steps could be interpreted as near-field displacement of the earthquake source, which was only about 1 km away from the closest OBT. Similar high frequency tilt signals were observed several times over the complete experiment. They will be discussed in the chapter on source theory (see chapter 4.2.1), where near-field terms are modelled.

Further signals of interest are trends or step-like transients lasting over hours and days. These transients are mostly found simultaneously to earthquake swarms and radial to the cluster centroid. They are suspected to be related to tectonic and/or volcanic activity. An example for such a signal is given in Fig. 3.11: During a 22 hours long earthquake swarm on 28th of July 2006 at the south-western flank of Columbo, about 1 km away from OBTs 54 and 55, a scatter of the tilt component radial to the cluster centroid can be observed (tiltmeter traces were rotated in direction of the cluster centroid to derive a radial and a transversal component of tilt). The sensor is first tilted away (i.e. it measures subsidence in direction of the source epicenter), before a strong signal with a period of around 4 hours and a maximum positive tilt in direction of the cluster is observed. (see modelling in Chapter 4.2 and discussion Chapter 7).

A last signal of interest are global trends, i.e. trends or possibly drifts of the instrument over the entire time of the experiment. Although these trends can be easily removed during

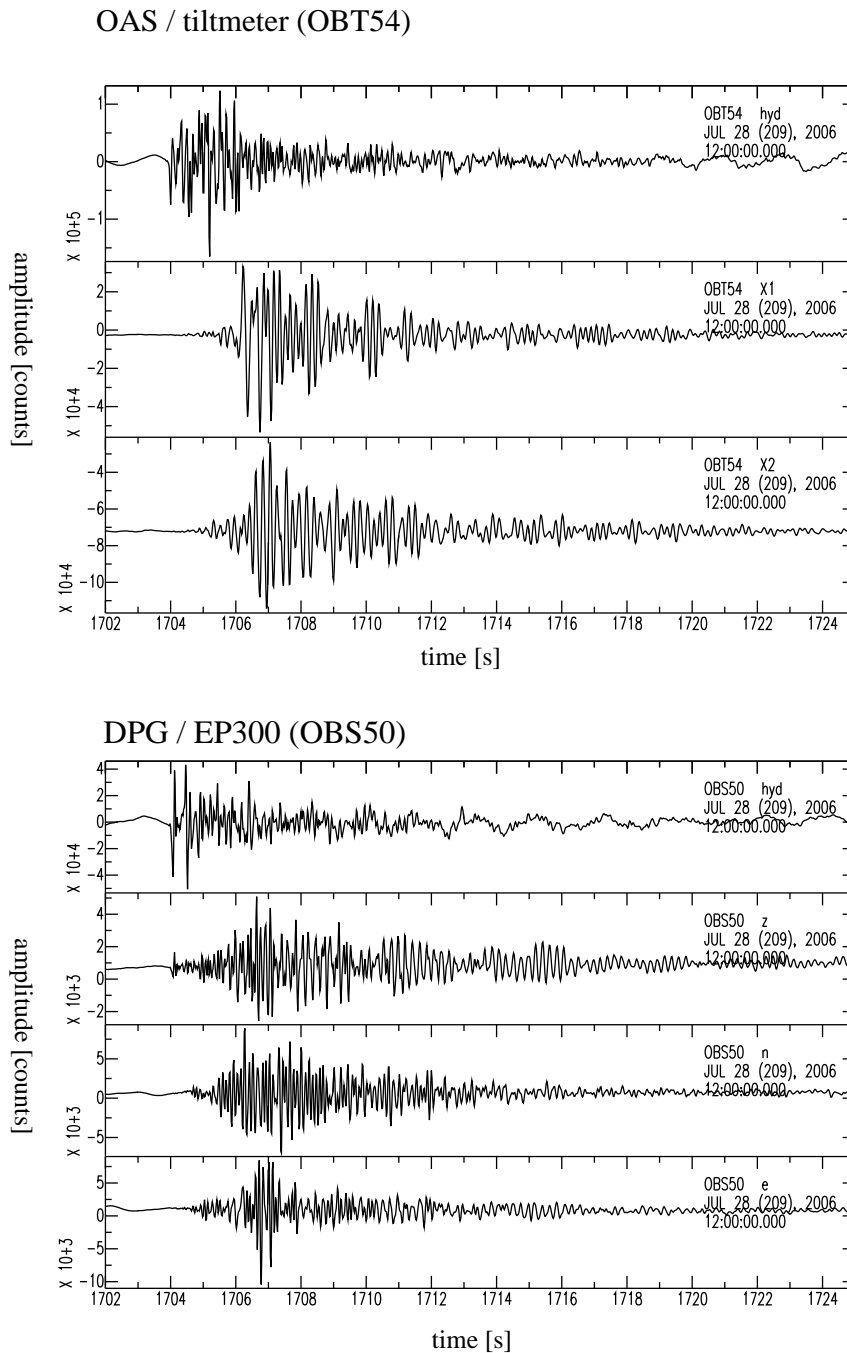


Figure 3.8: **Local earthquake on OBT54 and OBS50.** High frequent local events are detected on both, the tiltmeter (upper plot, trace 1 is an OAS-hydrophone) and the standart OBS system using a DPG relative pressure gauge (trace 1) and an EP300 seismometer (traces 2-4).

processing, they might shed light on constructional deficiencies of our system or sensitivity to temperature changes. Fig. 3.12 shows both traces of OBT 57 for the complete time of the Columbo experiment. Trends seem to be varying, which argues for the superposition of two or more trends rather than a constructional or temperature caused drift. The general trends observed on the different tiltmeters are discussed in chapter 6.3.

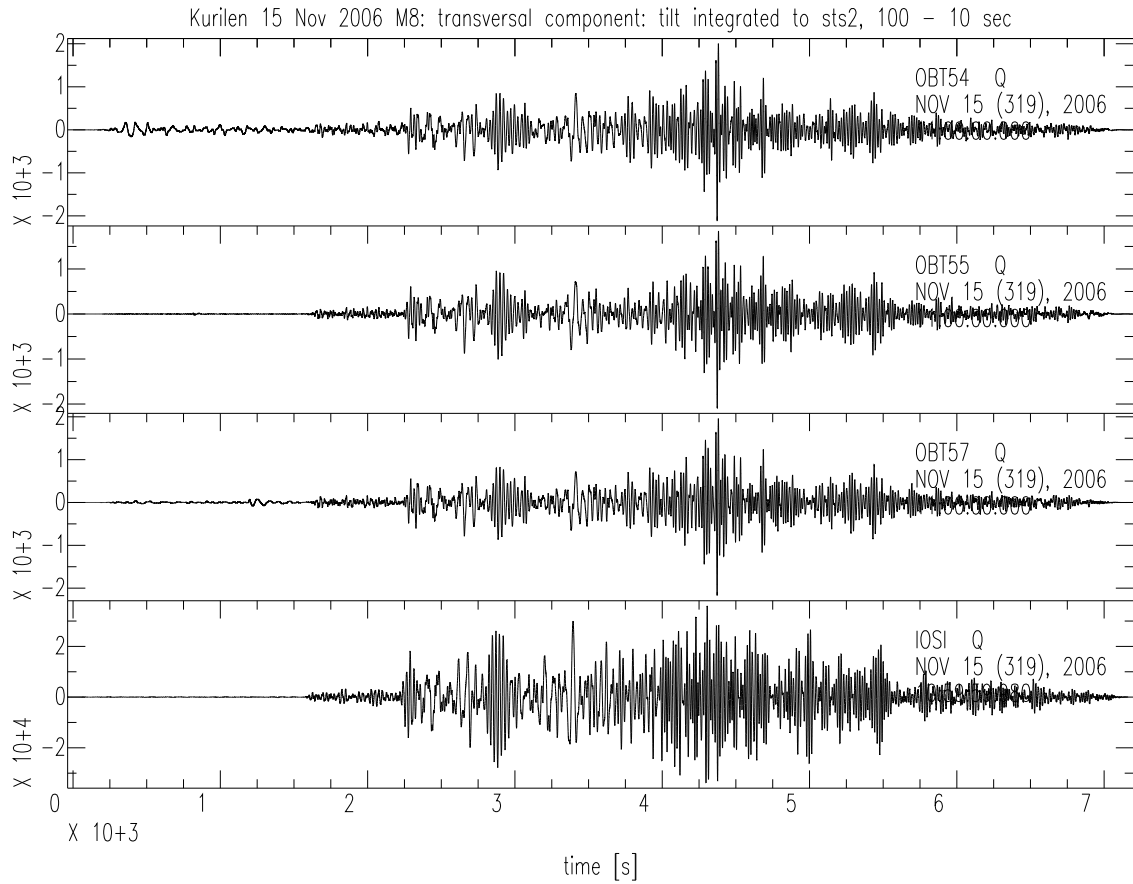


Figure 3.9: **Teleseismic event on OBTs and STS2.** The $M_W 8.3$ Kuril Islands earthquake of 15th of November 2006. Plotted traces are transversal component of the tiltmeters (first three traces) and of an onshore STS2 seismometer (station IOSI, fourth trace). Tilt traces have been integrated to compare them with the velocity traces of the STS2.

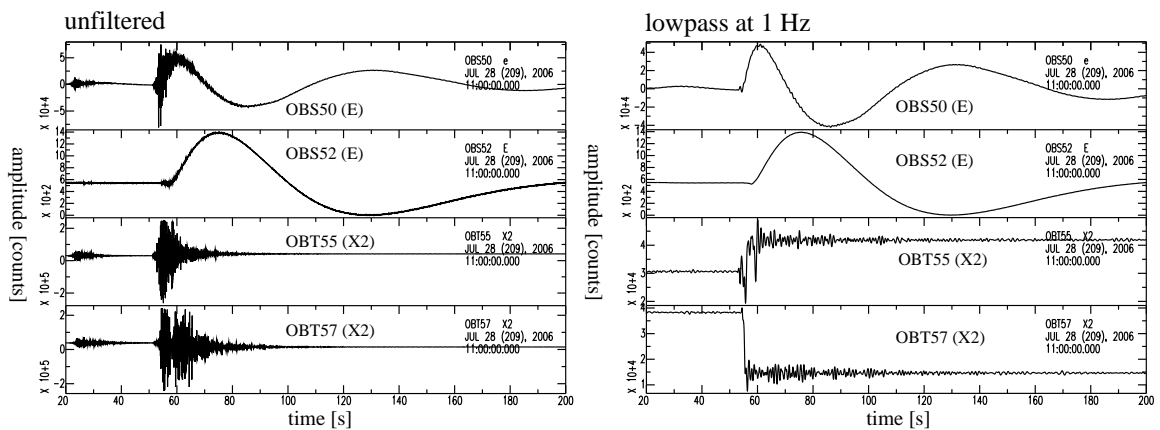


Figure 3.10: **Short period tilt-signals simultaneous to an earthquake of $M_L \geq 3$.** The left hand plot shows rawdata, the right hand plot lowpass filtered data at 1 Hz. On tiltmeters (both lower traces), this is a static step that occurs crudely parallel to the S- or surface wave onset.

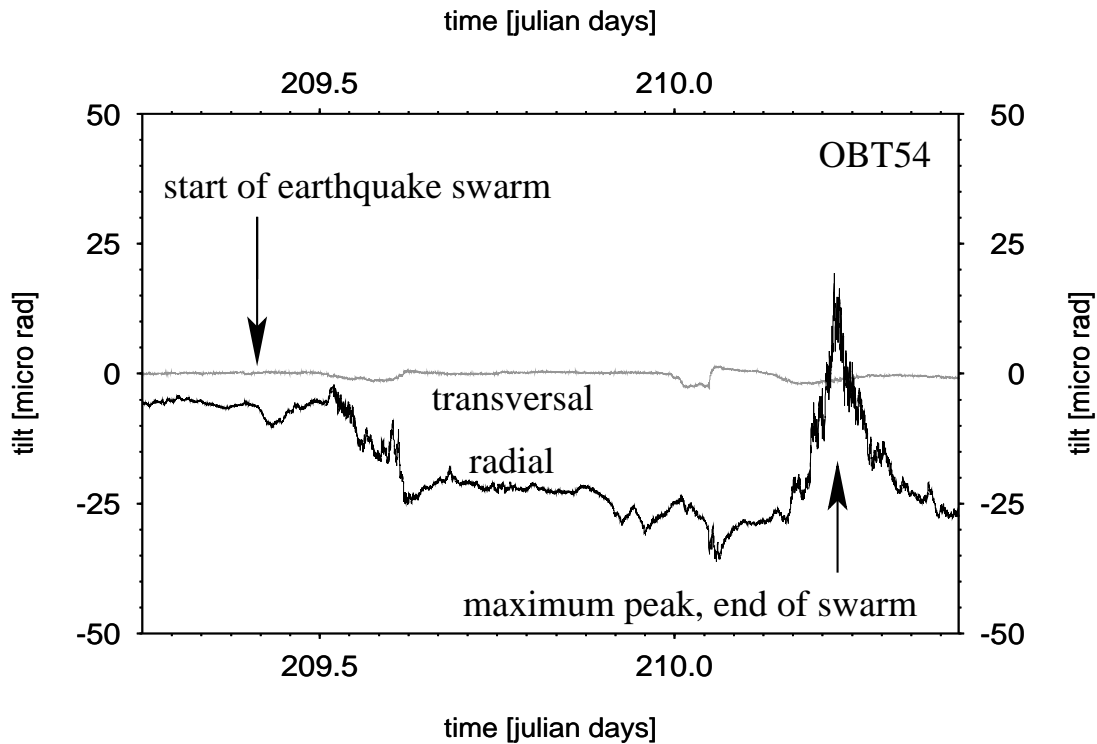


Figure 3.11: **Long period tilt-signal simultaneous to an earthquake swarm.** The black curve is the trace radial to the centroid, the grey curve the transversal. Arrows mark start and end of an simultaneously occurring earthquake swarm with a distance of about 1 km between the OBT and the earthquake cluster centroid.

We finally investigated the spectral content of a one week period of the Columbo dataset for solid earth tides. Fig. 3.13 shows the power spectrum of OBT 54 for this period. Time series were lowpass filtered at 0.5 Hz. While typical features like microseismicity and the low noise notch can be clearly resolved, we do not resolve a clear tidal-related peak at about 1/12 hours. The power spectral density curve scatters a bit in the range of typical tidal periods, but no clear amplitude increase could be observed. Equivalent observations with a permanently installed tiltmeter in the BFO mine indicate amplitudes of the solid earth tides of about 10-20 nrad (Forbriger pers. comm.), i.e. they probably disappear in the noise using our OBT system.

A further description on technical details and experiences in practical use of the Hamburg OBT is given in Hort and Hensch (2009).

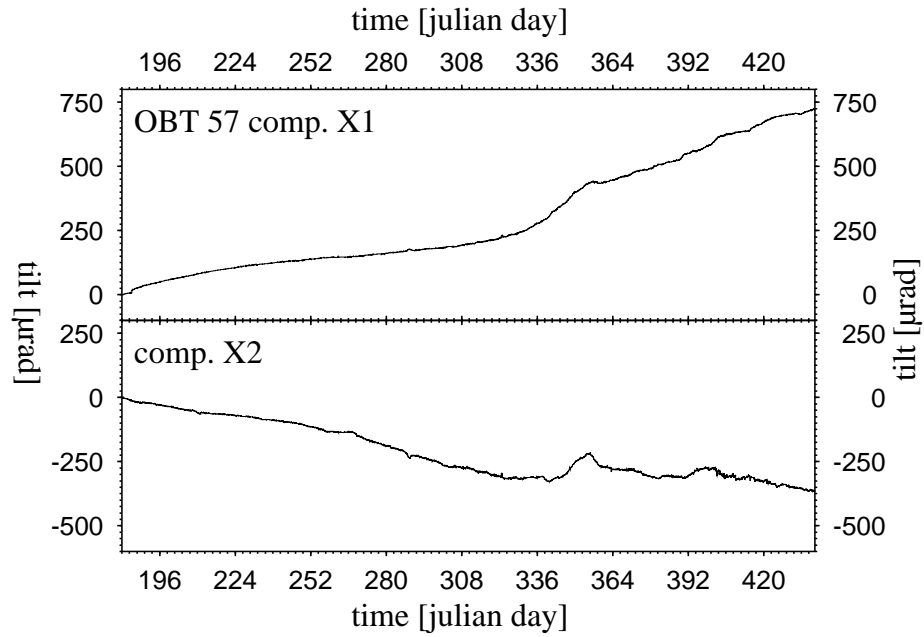


Figure 3.12: **Global trend of OBT 57.**

Traces X1 and X2 of OBT 57 over the complete time of the Columbo experiment show varying trends in terms of amplitude, orientation and permanence: While the trend of X1 suddenly increases around Julian day 340, it slightly decreases on X2.

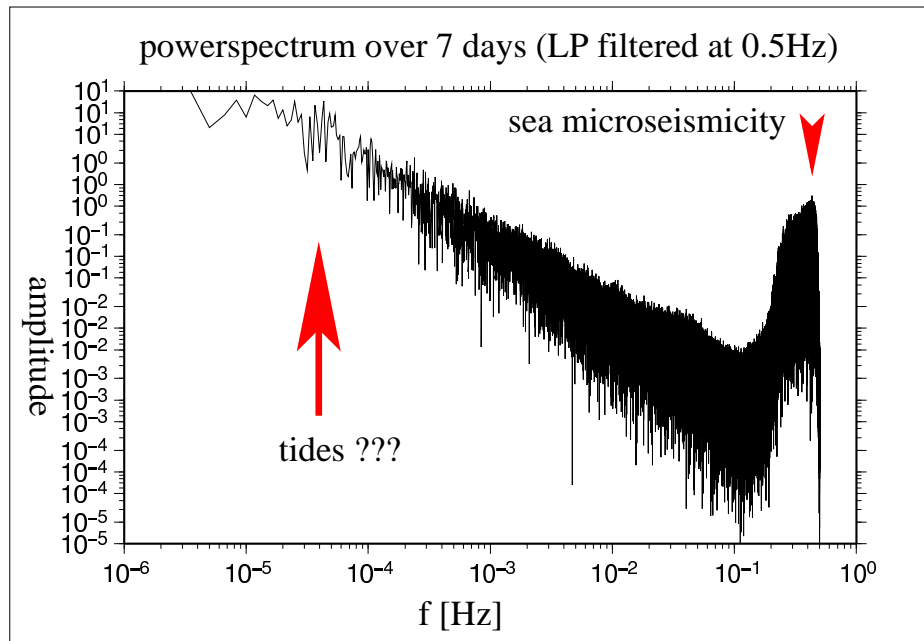


Figure 3.13: **Powerspectrum of OBT 54 E component at Columbo over 7 days, lowpass filtered at 0.5 Hz.** Red arrows indicate frequencies of expected solid earth tides and microseismic peaks.

THEORY OF SEISMIC AND DEFORMATION SOURCES

This chapter introduces earthquake mechanisms and three types of deformation sources: The fault source model as well as two volume source models, the Mogi model for spheric volumes and the Dike model. Section 4.2.2 is of great importance for the later following modeling of a propagating Mogi source.

4.1 Seismic sources

Volcanotectonic earthquakes at Columbo were all of Magnitude $M_L \leq 4.6$, maximum spatial fault plane dimensions are smaller than a few hundred meters and radiated energetic waves have wavelengths from tens of meters to some km. We use the point source approximation that is valid for source dimension smaller than the wavelengths of interest ($\lambda_{min} \simeq 135 \text{ m}$ for $f_{max} = 20 \text{ Hz}$ and $v_S = 2.7 \text{ km/s}$ for the shallowest layer).

4.1.1 Earthquake mechanism

A rupture starts at a nucleation point, the hypocenter, and slips rapidly over a fault surface. Both velocities, rupture and slip velocity, are in the range of seismic waves which makes them capable to radiate free waves. The pattern of this radiation is controlled by the fault plane orientation which itself is a result of the lithostatic stress regime (a 3D stress ellipsoid). The radiation pattern leads to two possible fault solutions, which are orthogonal to each other. From low frequency wave observations only, it is not possible to distinguish between the actual and the auxiliary fault plane (see Fig. 4.1). A common way to illustrate fault plane solutions is the projection of P-wave nodal planes onto the lower or backward focal hemisphere (e.g. Stein and Wysession, 2003; Lay and Wallace, 1995), see Fig. 4.2. The nodal planes represent the possible fault planes, while nodal points indicate pressure axis (P) and tension axis (T) of the strain release tensor. The intersection point of the potential faults indicates the null

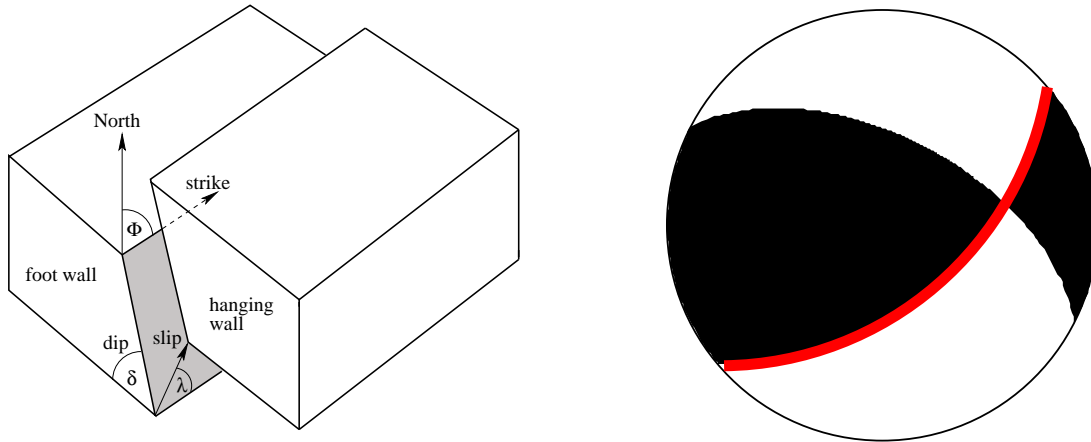


Figure 4.1: **Defining parameters of a fault**, here oblique thrust faulting, with Φ as the strike, δ as the dip and λ as the rake or slip angle. The resulting focal mechanism is given on the right hand side of the plot. The actual fault plane is marked red. For other focal solution types see Stein and Wysession (2003).

axis (B). Principle axes of the stress tensor are similar, but not necessarily identical to the principle axes of the strain release tensor.

The geometrical description of a fault plane is given by the strike ($0^\circ < \Phi < 360^\circ$, azimuth from north), the dip ($0^\circ < \delta < 90^\circ$, angle from horizontal) and the rake or slip angle ($-180^\circ < \lambda < 180^\circ$, angle between strike direction and the slip vector).

Techniques to determine fault mechanisms are analysis of P-wave polarity and SV-P amplitude ratios (Snoke et al., 1984), or the inversion for the moment tensor when comparing theoretical with observed waveforms.

Fig. 4.2 gives an overview on single, single couple and double couple forces, as well as the nine force couples representing the components of the seismic moment tensor. A force couple can have two forms: M_{xy} has two forces normal to an offset d and thus a torque and M_{xx} as a force dipole without torque. Slip on a fault is equivalently described as the superposition of either a double couple like M_{xy} or M_{yx} or dipoles $M_{x'x'}$ and $-M_{y'y'}$. Each moment tensor component consists of two opposite forces separated by an offset. The net force and net torque of the moment tensor is zero.

Seismic wave radiation due to single force sources are found for example for land slides. Probably because of the generation of torques, no geophysical processes have been found which are best modeled using single force couples (Stein and Wysession, 2003), with one exception: Earthquakes due to cavity collapses might reflect a torqueless single force couple (M_{zz} , see Fig. 4.2 and Hasegawa et al. (1989)). A pair of force couples as shown in Fig. 4.2-A, i.e. a double couple force system, is sufficient to give a point source representation of a shear

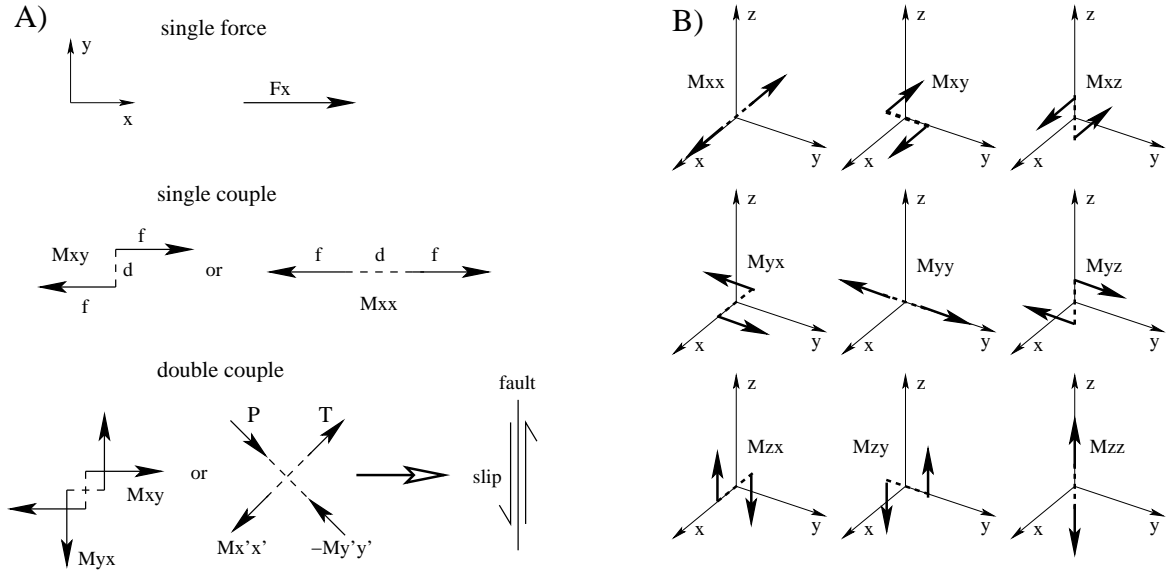


Figure 4.2: **Equivalent body forces and force couples.** A) illustration of single force, single couple and double couple.

B) The nine force couples: Components of the seismic Moment tensor.

fracture. The example in Fig. 4.2 shows a left lateral strike-slip in the $\pm y$ direction on a fault in the $y - z$ plane, the equivalent body forces $M_{xy} + M_{yx}$ form the double-couple source. While M_{yx} points in slip direction, M_{xy} is needed to cancel the torque. Body forces would be the same for a slip in the $x - z$ plane (auxiliary plane of the given solution).

4.1.2 The Earthquake Moment Tensor

The nine force couples are the components of the moment tensor \mathbf{M} . The seismic moment M_0 is defined as the scalar magnitude of the equivalent bodyforces, $M_0 = \sqrt{\frac{\sum M_{ij}^2}{2}}$ [Nm] or [dyn-cm] (Jost and Hermann, 1989). The moment magnitude is given with $M_W = \frac{2}{3} \log_{10} M_0 - 10.73$ (Hanks and Kanamori, 1979) for M_0 in *dyn cm*. The moment tensor can be decomposed into an isotropic and a deviatoric component using its eigenvalues e_i (Jost and Hermann, 1989):

$$\mathbf{M} = \begin{pmatrix} e_1 & 0 & 0 \\ 0 & e_2 & 0 \\ 0 & 0 & e_3 \end{pmatrix} = \underbrace{\begin{pmatrix} tr & 0 & 0 \\ 0 & tr & 0 \\ 0 & 0 & tr \end{pmatrix}}_{\text{isotropic component}} + \underbrace{\begin{pmatrix} e_1 - tr & 0 & 0 \\ 0 & e_2 - tr & 0 \\ 0 & 0 & e_3 - tr \end{pmatrix}}_{\text{deviatoric component}} \quad (4.1)$$

whereas the trace $tr = \frac{e_1 + e_2 + e_3}{3}$ is the **isotropic component** of the moment tensor and

$e'_1 = e_i - tr$ the eigenvalues of the **deviatoric component**. The isotropic component is represented by 3 orthogonal vector dipoles and indicates volumetric changes of the source (Müller, 2007). The deviatoric component can be further decomposed into a pure **double couple** and a **compensated linear vector dipole (CLVD)**. As it represents a pure shear fracture, the double couple component is of most interest to analyze tectonic earthquakes. It is defined as follows:

$$M_{ij} = \mu A(u_i \nu_j + u_j \nu_i) \quad (4.2)$$

with μ as the shear modulus and A as the fault plane area. $\vec{\nu}$ is the normal vector of the fault, \vec{u} the slip vector. The term in brackets describes the moment tensor of a double couple source \mathbf{M}_{DC} . Due to the required symmetry of the tensor, $\vec{\nu}$ and \vec{u} can be interchanged without altering the radiation pattern, which leads to the ambiguity of the real fault plane and the auxiliary plane. The moment tensor of a pure double couple source is then defined in the principal axis coordinate system as:

$$\mathbf{M}_{\text{DC}} = M_0 \begin{pmatrix} 1 & 0 & 0 \\ 0 & -1 & 0 \\ 0 & 0 & 0 \end{pmatrix} \quad (4.3)$$

The moment tensor of the example in Fig. 4.2 (lower left) is:

$$\mathbf{M} = \begin{pmatrix} M_{xx} & M_{xy} & M_{xz} \\ M_{yx} & M_{yy} & M_{zy} \\ M_{zx} & M_{zy} & M_{zz} \end{pmatrix} = \begin{pmatrix} 0 & M_0 & 0 \\ M_0 & 0 & 0 \\ 0 & 0 & 0 \end{pmatrix} = M_0 \begin{pmatrix} 0 & 1 & 0 \\ 1 & 0 & 0 \\ 0 & 0 & 0 \end{pmatrix} \quad (4.4)$$

The Tensor of the CLVD component, \mathbf{M}_{CLVD} (Knopoff and Randall, 1970), is interpreted as a linear vector dipole compensated for a volumetric change:

$$\mathbf{M}_{\text{CLVD}} = M_0 \begin{pmatrix} -1 & 0 & 0 \\ 0 & -1 & 0 \\ 0 & 0 & 2 \end{pmatrix} = M_0 \left(\underbrace{\begin{pmatrix} 0 & 0 & 0 \\ 0 & 0 & 0 \\ 0 & 0 & 3 \end{pmatrix}}_{\text{linear dipole vector}} + \underbrace{\begin{pmatrix} -1 & 0 & 0 \\ 0 & -1 & 0 \\ 0 & 0 & -1 \end{pmatrix}}_{\text{volumetric change}} \right) \quad (4.5)$$

A characteristic CLVD tensor consists of two equal eigenvalues and a third one that is twice their negative value. E.g. for volcanic earthquakes, Cesca et al. (2007) discuss tensile cracks due to ascending magma dikes.

Assuming the DC and CLVD components to be caused by the same stress field, also P-, T- and Null-axes are the same for both components. The full moment tensor \mathbf{M} is therefore given by (see Jost and Hermann, 1989; Dahm et al., 2004):

$$\frac{\mathbf{M}}{M_0} = \underbrace{tr \begin{pmatrix} 1 & 0 & 0 \\ 0 & 1 & 0 \\ 0 & 0 & 1 \end{pmatrix}}_{\text{isotropic}} + (e_2 - tr) \underbrace{\begin{pmatrix} 1 & 0 & 0 \\ 0 & 1 & 0 \\ 0 & 0 & -2 \end{pmatrix}}_{\text{CLVD}} + (e_1 - e_2) \underbrace{\begin{pmatrix} 1 & 0 & 0 \\ 0 & -1 & 0 \\ 0 & 0 & 0 \end{pmatrix}}_{\text{DC}} \quad (4.6)$$

Solving the isotropic component for volcanic earthquakes is difficult. Since most of the Columbo seamount events are associated with tectonic earthquakes, we only inverted seismic waveforms in the far-field for their deviatoric component and its double couple percentage. i.e. the last term in Eq. 4.6.

4.2 Deformation sources

The filling of a magma chamber, magmatic diking, aseismic creep on preexisting faults and/or tectonic events may have caused static deformation and tilt at Columbo. This section is on the theory of the three possible sources of static deformation that are regarded in this study, i.e.:

- The Fault Source Model (near-field terms of strike-slip-, normal- and reverse-faulting)
- The Volume Source Model for a spherical volume (Mogi-Model)
- The Volume Source Model for a dike (lenticular volume)

4.2.1 The Fault Source Model

Static ground deformation and tilt in a seismically active region may be caused by near-field terms of the radiated waves of earthquakes. In opposite to continuous volume increase as it is expected for loading of a magma reservoir, earthquakes cause sudden and rapid displacement and thus a high frequency deformation signal. An example for that is given in Fig. 4.3 for a $M_L = 3.7$ earthquake during a swarm on 28th of July 2006, directly underneath the volcano. Both instruments show their expected reaction during a static horizontal acceleration: While it is a step on the tiltmeter traces, seismometers start swinging with their lower corner frequency and quickly become attenuated. There is no doubt that this deformation signal is definitely linked to the accompanying earthquake, but it might reflect both, near-field terms or tilting of the complete instrument or its carrier system due to ground vibration.

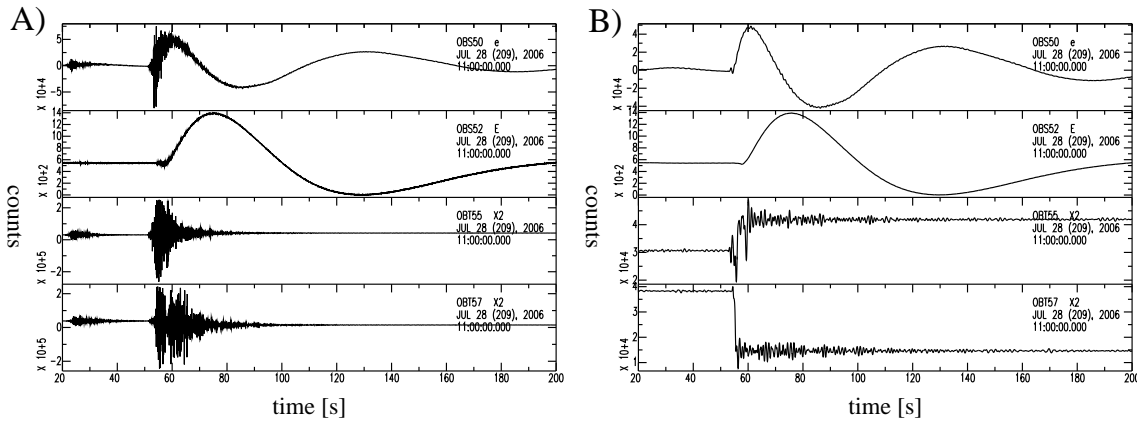


Figure 4.3: **Example for a high frequency tilt signal.** 4 traces horizontal components of seismometers (OBS50 and OBS52, both upper traces) and tiltmeters (OBT55 and OBT57, both lower traces) of a $M_L = 3.7$ earthquake on 28th of July 2006, directly underneath Columbo seamount. A) shows rawdata and B) lowpass filtered data at 1 Hz. The response of both instruments differs: While seismometers start swinging at their lower corner frequency, tiltmeters show a static offset.

Theory and software of the now following modelling correspond to the work of Yoshimitsu Okada, "Internal deformation due to shear and tensile faults in a half space" (Okada, 1992), developed for a finite rectangular source. This section concentrates on the modelling of the minimum seismic moment M_0 that is needed to trigger a visible signal on both deformation sensors, tiltmeter and absolute pressure gauge. Theory is shortened to its basics:

Fig. 4.4 shows the definition of a rectangular source as it was used for modelling. L is defined as the length of the fault, W as its width and δ as the dip angle.

The initial approach starts with a **single force \mathbf{F} in a homogeneous half-space**: At the point of observation (x_1, x_2, x_3) , $w_i^j(x_1, x_2, x_3; \xi_1, \xi_2, \xi_3)$ is the i -th component of the displacement caused by the j -th direction of force \mathbf{F} at its point of occurrence (ξ_1, ξ_2, ξ_3) (Press, 1965).

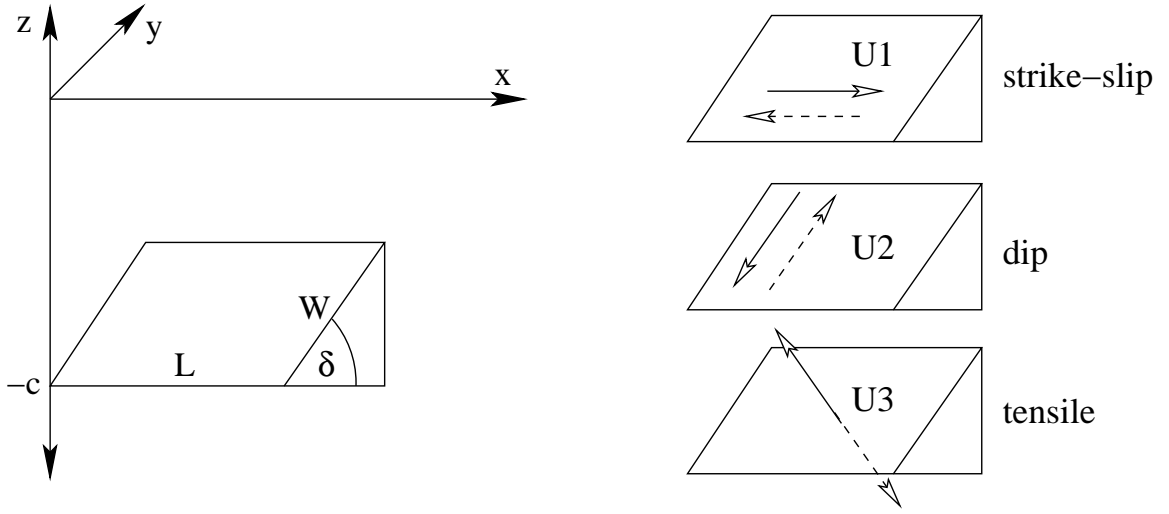


Figure 4.4: **Rectangular source model.** Geometry of finite rectangular sources for strike-slip, dip and tensile faults. (Okada, 1992)

Written in equation form:

$$\begin{aligned}
 u_i^j(x_1, x_2, x_3) = & u_{iA}^j(x_1, x_2, -x_3) - u_{iA}^j(x_1, x_2, x_3) \\
 & + u_{iB}^j(x_1, x_2, x_3) + x_3 u_{iC}^j(x_1, x_2, x_3)
 \end{aligned} \tag{4.7}$$

The first term in equation 4.7, $u_{iA}^j(x_1, x_2, -x_3)$, represents the displacement field due to a single force at (ξ_1, ξ_2, ξ_3) in an infinite medium. The second term, $u_{iA}^j(x_1, x_2, x_3)$, corresponds to a contribution of an image source of F at $(\xi_1, \xi_2, -\xi_3)$ in the same medium. The polarity of the image source is switched from one to the other component, so that the surface displacement vanishes when both terms are combined.

The third term, $u_{iB}^j(x_1, x_2, x_3)$, and the part $u_{iC}^j(x_1, x_2, x_3)$ of the fourth term are depth dependent. For an observation at the surface of a half-space, $x_3 = 0$, the fourth term becomes zero, terms one and two eliminate each other and the remaining term is $u_{iB}^j(x_1, x_2, x_3)$. Eq. 4.7, the fundamental equation for the internal displacement field due to a single source in a half-space consists of two infinite medium terms (A), a term related to the surface deformation (B) and a depth multiplied term (C).

To get equations for displacement fields caused by nucleation points of strain, i.e. a **double-couple point source**, ξ_k derivatives of Eq. 4.7 are needed:

$$\begin{aligned} \frac{\partial u_i^j}{\partial \xi_k}(x_1, x_2, x_3) &= \frac{\partial u_{iA}^j}{\partial \xi_k}(x_1, x_2, -x_3) - \frac{\partial u_{iA}^j}{\partial \xi_k}(x_1, x_2, x_3) \\ &\quad + \frac{\partial u_{iB}^j}{\partial \xi_k}(x_1, x_2, x_3) + x_3 \frac{\partial u_{iC}^j}{\partial \xi_k}(x_1, x_2, x_3) \end{aligned} \quad (4.8)$$

For practical use, three typical sources are considered, the strike-slip, the dip-slip and the tensile point source. For the following equations, sources are placed at $(0, 0, -d)$ of a (x, y, z) coordinate system, with $-d$ as the depth, the fault strike is parallel to x and the slip is dextral for $-\pi < \delta < 0$ and sinistral for $0 < \delta < \pi$. The sense of dip slip is normal for $(\pi/2 < \delta < \pi$ or $-\pi/2 < \delta < 0)$ and reverse for $(0 < \delta < \pi/2$ or $-\pi < \delta < \pi/2)$.

A dislocation $\Delta u_j(\xi_1, \xi_2, \xi_3)$ across a surface Σ in an isotropic medium causes a dislocation field $u_i(x_1, x_2, x_3)$, which can be described using summation convention (Steketee, 1958):

$$u_i = \frac{1}{F} \int \int_{\Sigma} \Delta u_j \left[\lambda \delta_{ij} \frac{\partial u_i^n}{\partial \xi_n} + \mu \left(\frac{\partial u_i^j}{\partial \xi_k} + \frac{\partial u_i^k}{\partial \xi_j} \right) \right] \nu_k d\Sigma \quad (4.9)$$

with λ and μ as Lamé parameters and ν_k as the direction cosine of the normal to the surface element $d\Sigma$. The displacement field \vec{u} can now be synthesized using the displacement field due to strain nucleation points, $\partial \vec{u}^j / \partial \xi_k$.

- Strike-Slip point source (moment = M_0):

$$\vec{u} = \frac{M_0}{F} \left[- \left(\frac{\partial \vec{u}^1}{\partial \xi_2} + \frac{\partial \vec{u}^2}{\partial \xi_1} \right) \sin \delta + \left(\frac{\partial \vec{u}^1}{\partial \xi_3} + \frac{\partial \vec{u}^3}{\partial \xi_1} \right) \cos \delta \right] \quad (4.10)$$

- Dip-Slip point source (moment = M_0):

$$\vec{u} = \frac{M_0}{F} \left[\left(\frac{\partial \vec{u}^2}{\partial \xi_3} + \frac{\partial \vec{u}^3}{\partial \xi_2} \right) \cos 2\delta + \left(\frac{\partial \vec{u}^3}{\partial \xi_3} + \frac{\partial \vec{u}^2}{\partial \xi_2} \right) \sin 2\delta \right] \quad (4.11)$$

- Tensile point source (intensity = $2M_0$ for the uniaxial part and $(\lambda/\mu)M_0$ for the isotropic part):

$$\vec{u} = \frac{M_0}{F} \left[\frac{2\alpha - 1}{1 - \alpha} \frac{\partial \vec{u}^n}{\partial \xi_n} + 2 \left(\frac{\partial \vec{u}^2}{\partial \xi_2} \sin^2 \delta + \frac{\partial \vec{u}^3}{\partial \xi_3} \cos^2 \delta \right) - \left(\frac{\partial \vec{u}^2}{\partial \xi_3} + \frac{\partial \vec{u}^3}{\partial \xi_2} \right) \sin 2\delta \right] \quad (4.12)$$

In a next step, the internal deformation field is derived for a finite rectangular source, introducing fault length L along the fault direction, width W along the perpendicular direction of the strike and a dislocation Δd . To derive tilt from the displacement field \vec{u} , the derivative of the vertical displacement u_z over distance x , $\partial u_z / \partial x$, is calculated. Both steps end in exhaustive tables of equations given in Okada (1992).

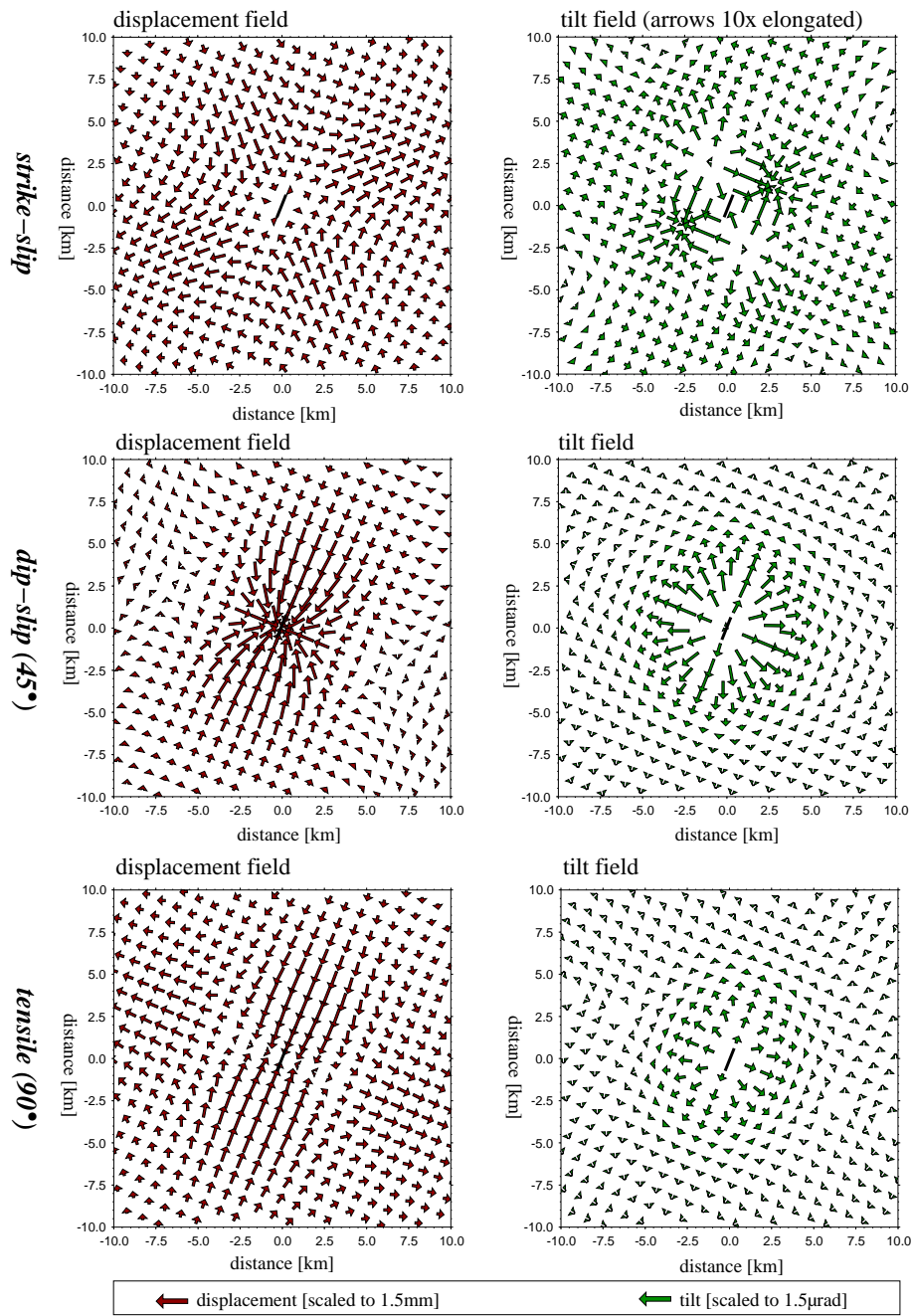


Figure 4.5: **Displacement- and tilt-fields for strike-slip and normal faulting, as well as vertical tensile opening** of a M_W 5 event (fault length $L = 1.2$ km, width $W = 1.0$ km and dislocation $\Delta d = 9.6$ cm) at $x=y=0$ in 5 km depth. Faults are given with fat black lines. The strike angle is 22.5° for each fault in this model. Red arrows mark displacement, green arrows tilt of the respective fault type. Strongest signals are observed for normal and tensile faulting. For the displacement field, the arrow points in direction of the mass movement, for tilt it points in direction of the uplift gradient.

The Okada Fortran routines allow the choice of size and depth of the source as well as the control of dislocation of the strike-slip, dip and tensile component. In this work, the Okada equations (routines) have been implemented in a Fortran program to simulate and plot different types of dislocation sources and their displacement and deformation or tilt at

the seafloor. As the shear traction at the seafloor is zero (shear modulus $\mu = 0$ and Poisson's ratio $\nu = 0.5$ in water), half space solutions have been applied as a first approximation to the seafloor problem. The aim was to reconstruct the faultplanes of the observed earthquakes and to estimate the minimum seismic moment M_0 to cause a signal of 50 nrad on the tiltmeters and 1 mm uplift or subsidence on the absolute pressure gauges. A gridsearch over epicentral distances and hypocentral depths was performed. All sources were of finite rectangular shape.

Absolute displacement and tilt fields for typical fault types are given in Fig. 4.5. Strongest vertical deformation is found for normal faulting and tensile opening. Even strike-slip faulting causes slight vertical deformation due to volume shift and thus also small tilt signals, but strongest deformation is found in horizontal direction for this fault type.

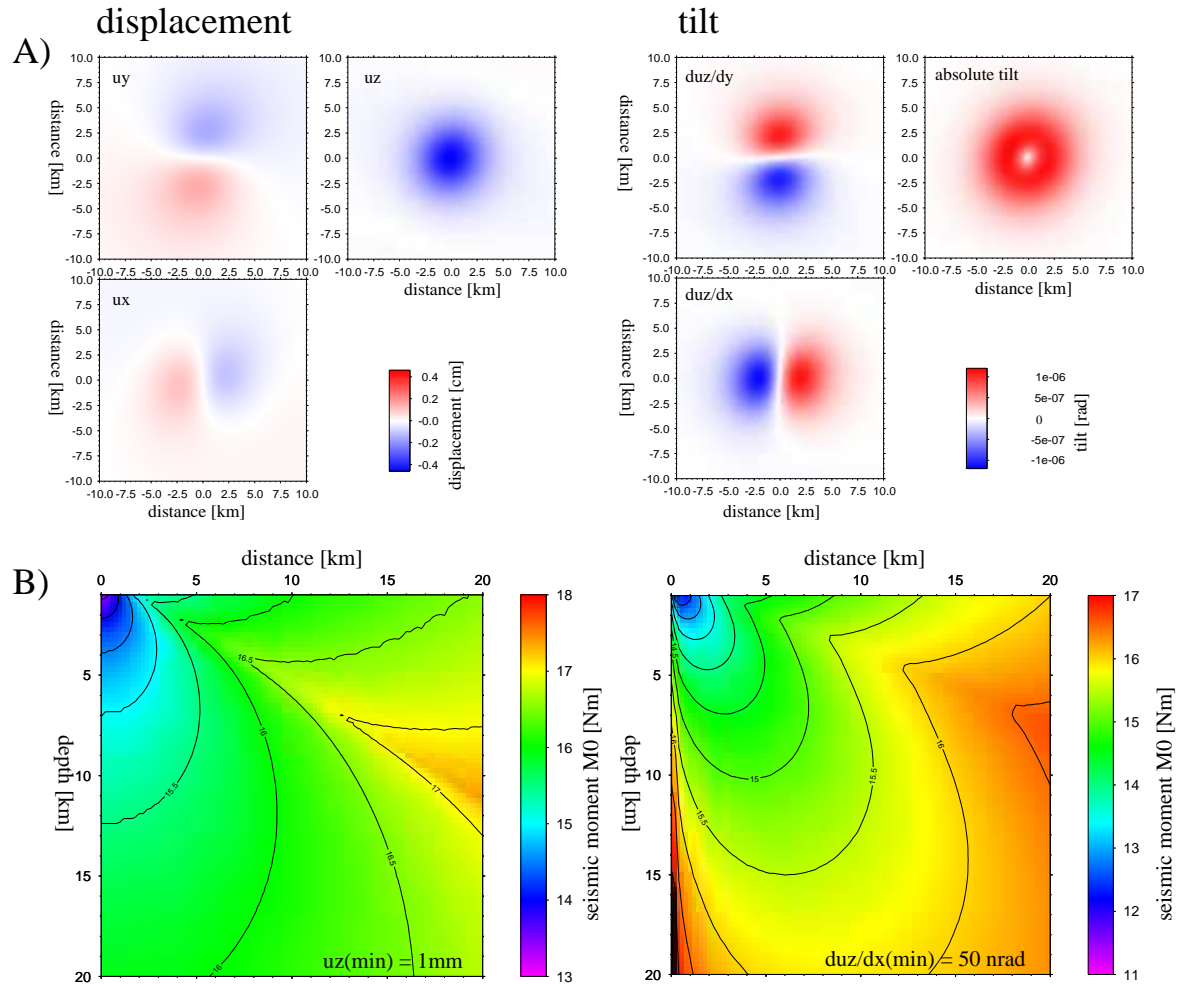


Figure 4.6: **Displacement and tilt fields, minimum moment over depth and distance to be solved on deformation sensors.** A) Displacement and tilt fields of a M_W 5 normal faulting ($dip = 45^\circ$) event in 5 km depth, decomposed for their components, how they are measured on a two component tiltmeter. B) Minimum moment over source depth and distance. As resolution thresholds, $\Delta u_z = 1 \text{ mm} \equiv 0.1 \text{ mbar}$ for the absolute pressure sensor and $\alpha = 50 \text{ nrad}$ for the tiltmeter were used. Slight deformation signals could even be measured for weak shallow events in close epicentral distances with seismic moments of $M_0 = 1 \cdot 10^{14} \text{ Nm}$, which corresponds to a magnitude of about $M_W = 2$.

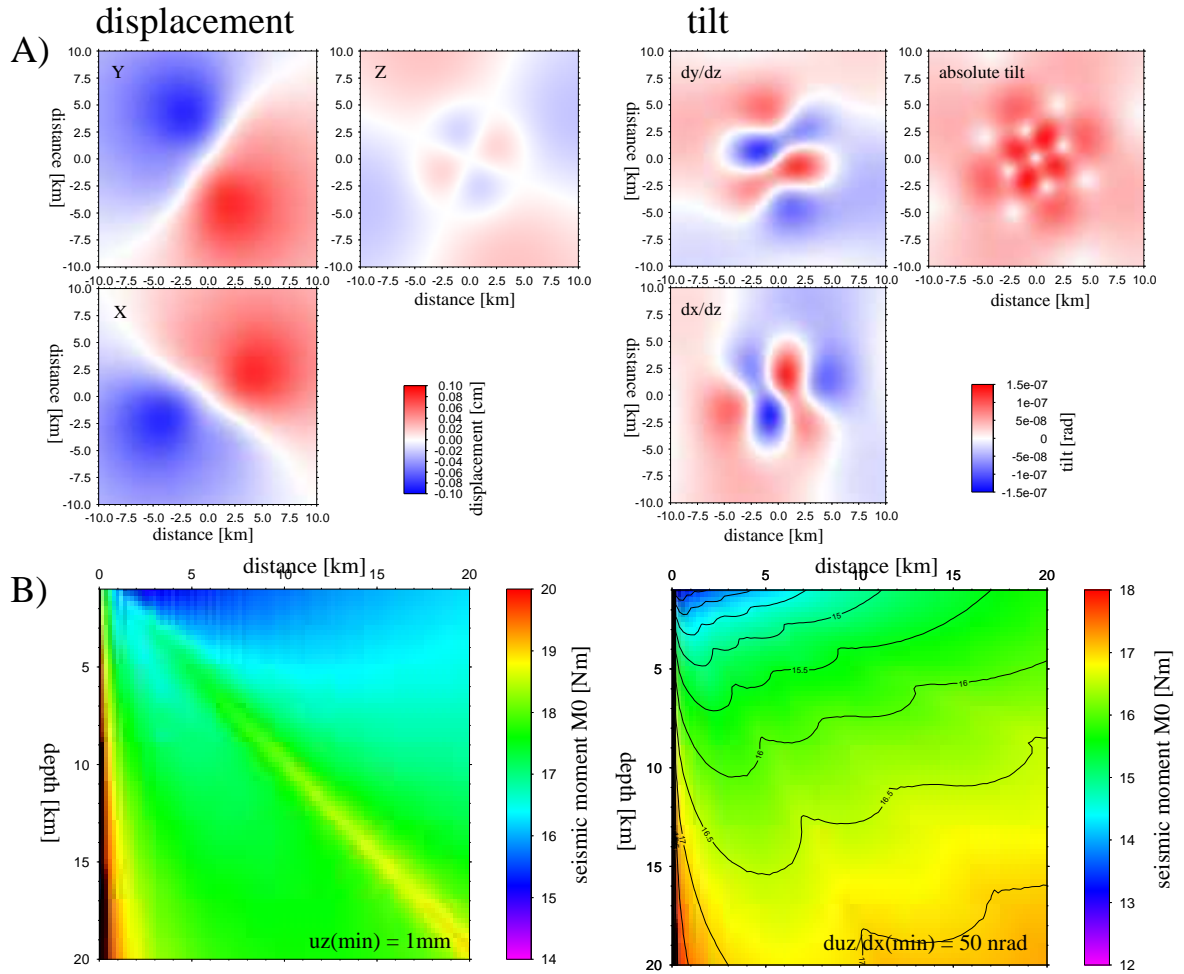


Figure 4.7: **Displacement and tilt fields, minimum moment over depth and distance to trigger deformation sensors.** A) Displacement and tilt fields of a M_W 5 strike-slip faulting event in 5 km depth, decomposed for their components. As expected, horizontal displacement is larger for strike-slip, while vertical displacement is nearly zero. B) Minimum moment over source depth and distance, that is needed to trigger our deformation sensors. Because u_z is small, both sensors would require a relatively large earthquake to be triggered for near-field terms.

To model for possible deformations due to fault sources, tilt and deformation for a master event of M_W 5 in a depth of 5 km, fault extensions $1.2 \cdot 1.0$ km (NE strike of 22.5°) and a slip of 9.6 cm were modeled and decomposed for their x and y components. In a further step, the minimum moment depending on hypocentral depth and epicentral distance was modeled, that is needed to be resolved on our sensors. As thresholds, 50 nrad for the tiltmeter and a vertical deformation of $1 \text{ mm} \equiv 0.1 \text{ mbar}$ were assumed.

Results are given in Figs. 4.6 and 4.7: The complete displacement and tilt fields are superpositions of the 3D displacement or 2D tilt field, respectively. A normal fault (and nearly equivalent tensile opening) are indeed able to trigger measurable deformation signals, if shallow near events are assumed with moments of about $1 \cdot 10^{14}$ Nm which corresponds to

$M_W = 2$ (Hanks and Kanamori, 1979). For strike-slip faulting, these minimum moments are significantly larger due to the fact that horizontal mass movement indeed causes vertical deformation due to volume increases and decreases due to its shift, but of much lower amplitude than vertical mass movements do.

The most important result is that abrupt tilt steps with amplitudes of some hundreds of μrads , as observed for stronger earthquakes at Columbo (e.g. Fig. 4.3), can not be explained by near-field terms. The modeling assumes a homogeneous half space with a Poisson ratio of 0.25 and a shear modulus of 30 GPa (ideal elastic medium). These steps must be the result of either tilting of the complete OBT frame or of the sensor within the glass sphere. Since this has not been investigated further, abrupt steps observed on the tiltmeters simultaneously to earthquakes are not further discussed in this work.

4.2.2 The Mogi Source Model for spheric volumes

Another cause of static deformation and tilt are volumetric sources. The following section is based on the scriptum "*Basics of the volume-source model and its application in volcano seismology*" by Erhard Wielandt, University of Stuttgart, Germany (Wielandt, 2001).

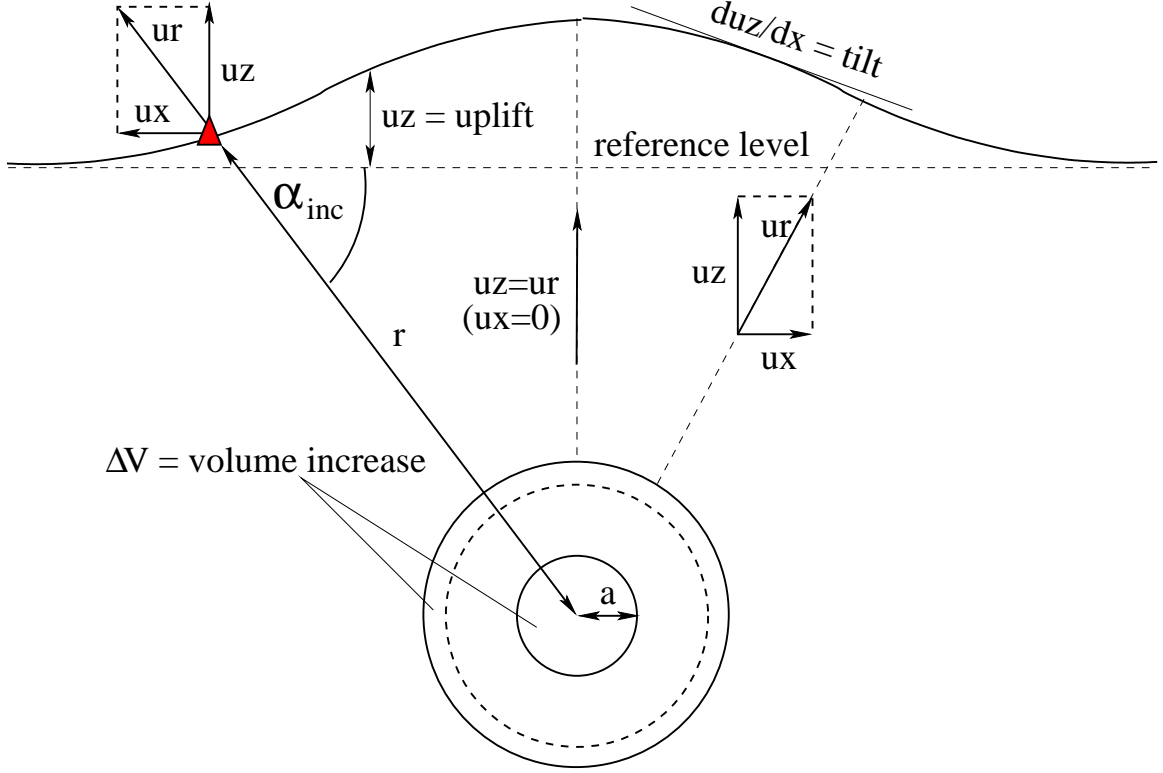


Figure 4.8: **Geometry of the Mogi point source model** (spheric volume increase). Nomenclature: a =equivalent radius of volume increase ($\Delta V = \frac{4}{3}\pi a^3$), u_r =radial displacement, u_z =vertical displacement, u_x =horizontal displacement, r =distance between source and observation point, z =source depth, x =epicentral distance. The solid rings mark the radius increase caused by ΔV in case of the absence (small ring) and the presence (largest ring) of a possibly preexisting volume V_0 (dashed ring). The relative displacements u_r , u_z and u_x only depend on the volume increase ΔV and are independent of V_0 , illustrated by a varying size of the source (solid rings).

The Mogi point source is here defined to represent an expansive or explosive spherical source, characterized by the volume of displaced material and causing a seismic and/or deformation signal. It can be described as a function of time or as an absolute value.

With $\vec{u}(\vec{x}(t))$ as the time-dependent displacement and σ as the stress tensor, the elastic wave equation is given by:

$$\rho \vec{\ddot{u}} = \vec{\nabla} \sigma[\vec{u}] \quad (4.13)$$

Decomposition of the displacement into rotation- and divergence-free parts, with Φ as the compressional- (scalar potential) and \vec{A} as the shear-potential (vector potential), delivers

(Müller, 2007):

$$\vec{u} = \nabla\Phi + \nabla \times \vec{A} \quad (4.14)$$

For infinite homogeneous media, Φ and \vec{A} are uncoupled. Thus, a purely radial displacement, as it is induced by a spherical volume source embedded in an elastic medium with P-wave velocity v_p , can be described by Φ alone:

$$\vec{u} = \nabla\Phi \quad (4.15)$$

with

$$\Phi(r, t) = -\frac{1}{r}f\left(t - \frac{r}{v_p}\right) \quad (4.16)$$

The compressional potential is decaying with r^{-1} , the term $f\left(t - \frac{r}{v_p}\right)$ describes the v_p dependent time between volume change of the source and occurrence of the changes effect at a sensor in distance r .

This leads to the radial displacement u_r that consists of the sum of near- and far-field terms u_n and u_f :

$$u_r = u_n + u_f \quad (4.17)$$

$$u_r = \frac{1}{r^2}f\left(t - \frac{r}{v_p}\right) + \frac{1}{rv_p}f'\left(t - \frac{r}{v_p}\right) \quad (4.18)$$

The relation between both terms is given by:

$$u_f = \frac{r}{v_p}\dot{u}_n \quad (4.19)$$

$$u_n = \frac{v_p}{r} \int_{-\infty}^t u_f(t') dt' \quad (4.20)$$

Harmonic time dependence, $u_n = u_0 e^{i\omega t}$, leads to

$$u_f = \frac{r}{v_p} i\omega u_n \quad (4.21)$$

and thus with the wavelength $\lambda := \frac{2\pi v_p}{\omega}$ to

$$\frac{|u_f|}{|u_n|} = \frac{\omega r}{v_p} = \frac{2\pi r}{\lambda} \quad (4.22)$$

It follows, that the near-field term is dominating for $r < \frac{1}{2}\pi\lambda$. This is insofar important, since for a quasistatic deformation (long period and thus long wavelength radiation), such as a slowly loading reservoir, only the near-field term is relevant. The existence of a far-field term requires the initiation of a free propagating wave. An initialization velocity (here radial expansion velocity) $v_i \rightarrow 0$ is slow enough to cause near-field terms only.

The source volume $V(t)$ can be derived from the near-field term of equation 4.18, with $4\pi a^2$ as the point source strength (equivalent radius a):

$$V(t) = 4\pi a^2 u_n(a, t) = 4\pi f\left(t - \frac{a}{v_p}\right) \quad (4.23)$$

It follows for the source function $f(t) = V(t)/4\pi$. The complete wavefield can then be calculated, assuming that the source volume is known:

$$u_r = \frac{1}{4\pi r^2} V\left(t - \frac{r - a}{v_p}\right) \quad (4.24)$$

This equation is independent of the total radius of the source, its pressure and the elastic moduli of the medium, except for their presence in v_p . Apart from the delay a/v_p , the source is the same for each choice of a and can be measured at any distance from the source within the near-field.

With the following slight simplifications, a static solution for the displacement field of a spherical volcanic pressure source, buried in an elastic half-space was derived from Eq. 4.24 (Mogi, 1958):

- $\lambda = \mu$
- source radius much smaller than depth, $a \ll z$

With P as the pressure, this leads to the radial displacement at the free surface:

$$u_r = \frac{3a^3 P}{4\mu r^2} = \frac{3V}{4\pi r^2} \quad (4.25)$$

Obviously, the static displacement at the free surface differs from that in a fullspace by nothing else than a constant factor of 3, actually proven with a finite element method (Kirchdörfer, 1999).

Horizontal and vertical displacement can be derived by:

$$u_x = u_r \cos(\alpha_{inc}) = u_r \cdot \frac{x}{\sqrt{(x^2 + z^2)}} = \frac{3V}{4\pi r^2} \cdot \frac{x}{\sqrt{(x^2 + z^2)}} \quad \text{and} \quad (4.26)$$

$$u_z = u_r \sin(\alpha_{inc}) = u_r \cdot \frac{z}{\sqrt{(x^2 + z^2)}} = \frac{3V}{4\pi r^2} \cdot \frac{z}{\sqrt{(x^2 + z^2)}} \quad (4.27)$$

With u_r , u_z and u_x as the displacement in vertical (z) and horizontal (x) directions, $T(x, z) = \frac{\partial u_z}{\partial x}$ as the amplitude of tilt, x as the epicentral distance and z as the hypocentral depth, it follows:

$$\begin{aligned} T(x, z) &= \frac{\partial u_z}{\partial x} = \frac{\partial u_r \cdot \sin(\alpha)}{\partial x} \\ &= \frac{3V}{4\pi(x^2 + z^2)} \cdot \frac{z}{\sqrt{x^2 + z^2}} = \frac{9Vxz}{4\pi(x^2 + z^2)^5} \\ &= 3 \cdot \underbrace{\frac{3V}{4\pi r^2}}_{=u_r} \cdot \frac{xz}{(x^2 + z^2)^3} = 3 \cdot u_r \cdot \underbrace{\frac{z}{\sqrt{x^2 + z^2}}}_{=\sin(\alpha)} \cdot \frac{x}{(x^2 + z^2)} \\ &= 3u_z \cdot \frac{x}{(x^2 + z^2)} = \frac{3u_z}{x} \cdot \left(\frac{x}{\sqrt{x^2 + z^2}} \right)^2 \\ &= \frac{3u_z}{x} \cdot (\cos(\alpha))^2 = \frac{3u_z}{x} \cdot \left(\frac{u_r \cdot \cos(\alpha)}{u_r} \right)^2 \\ &= \frac{3u_z}{x_s} \left(\frac{u_x}{u_r} \right)^2 \end{aligned} \quad (4.28)$$

x and z are known, T is measured or modeled, u_r can be derived by the Mogi equation (see Eq. 4.25), u_x and u_z are calculated of u_r and the incidence angle α_{inc} :

Fig. 4.9 gives an overview on the distributions vertical $u_z(x)$ and horizontal $u_x(x)$ displacement, as well as tilt $T(x, z)$. The maximum radial deformation is found directly above the Mogi source. At this epicentral point, the deformation is purely vertical. Thus, horizontal deformation is zero above the source and finds its maximum at the inflexion points of the radial deformation curve. The tilt signal, as it is the derivative of vertical deformation with respect to the epicentral distance, $\partial u_z / \partial x$, finds its maximum at the inflexion points of $u_z(x)$ and is zero at (0;0). The absolute tilt signal of a Mogi source is of circular shape around the epicenter of the source. The absolute amplitude and the distribution on X and Y components of a tiltmeter are given in Fig. 4.10.

The volume- and depth-dependencies of deformation due to a Mogi source can be derived

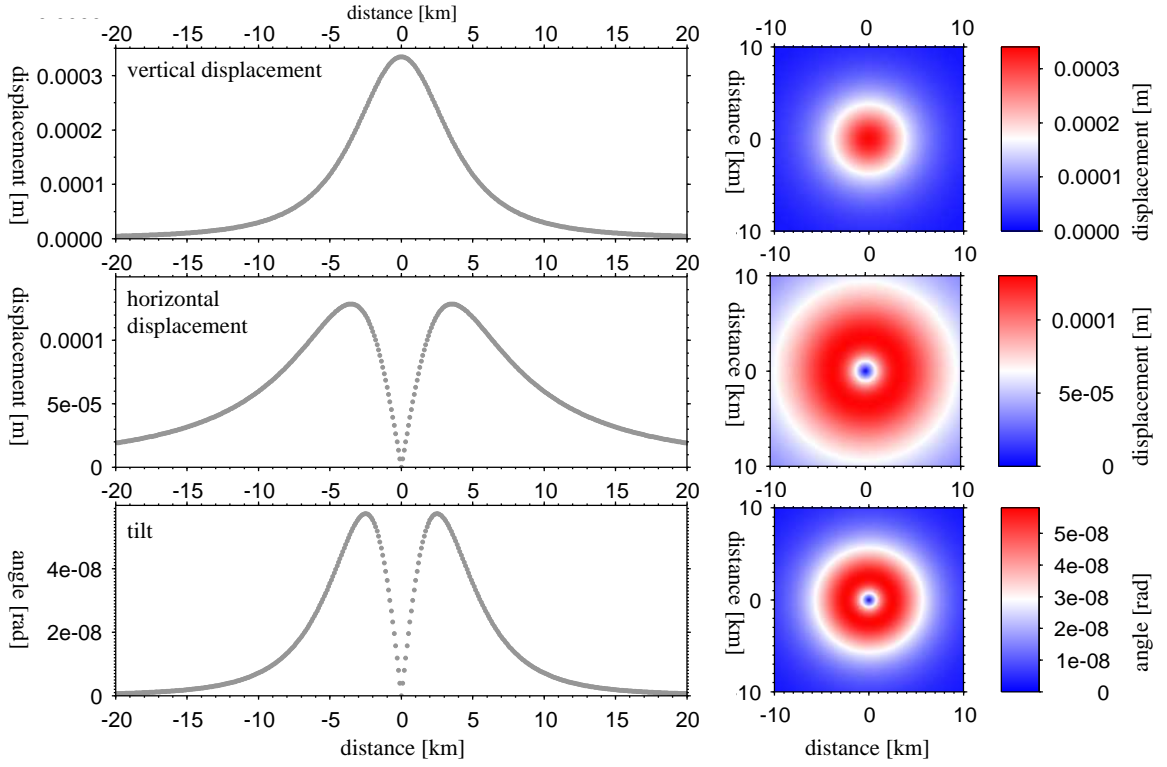


Figure 4.9: **The Mogi Model:** Vertical and horizontal displacement as well as tilt for a 35.000 m^3 source ($a = 20 \text{ m}$) at 5 km depth. Profiles over the source on the left hand side, 2D grids on the right hand side. While the uplift signal is dominating in the center of the deformation pattern, horizontal deformation finds its maximum at the inflexion points of the radial deformation curve and tilt is maximal at the inflexion points of the vertical deformation curve. T and u_z are zero on the direct top of the source.

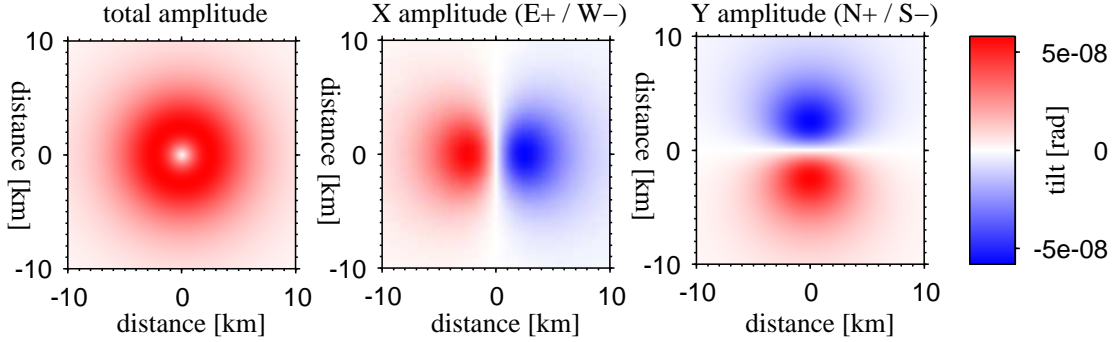


Figure 4.10: **Amplitude distribution on X- and Y-components of a Mogi source:** Total tilt amplitude and amplitude distributions for X and Y components of a tiltmeter for a Mogi source ($V = 35.000 \text{ m}^3$, $z = 5 \text{ km}$).

from equation 4.27:

$$u_z \propto \frac{1}{r^2} \sin(\alpha_{inc}) \quad \text{and} \quad u_z \propto V \sin(\alpha_{inc}) \quad (4.29)$$

Deformation amplitudes depend linear on the source volume. For the case of a fixed volume and a varying depth, strongest deformations are found for shallow depths and are rapidly

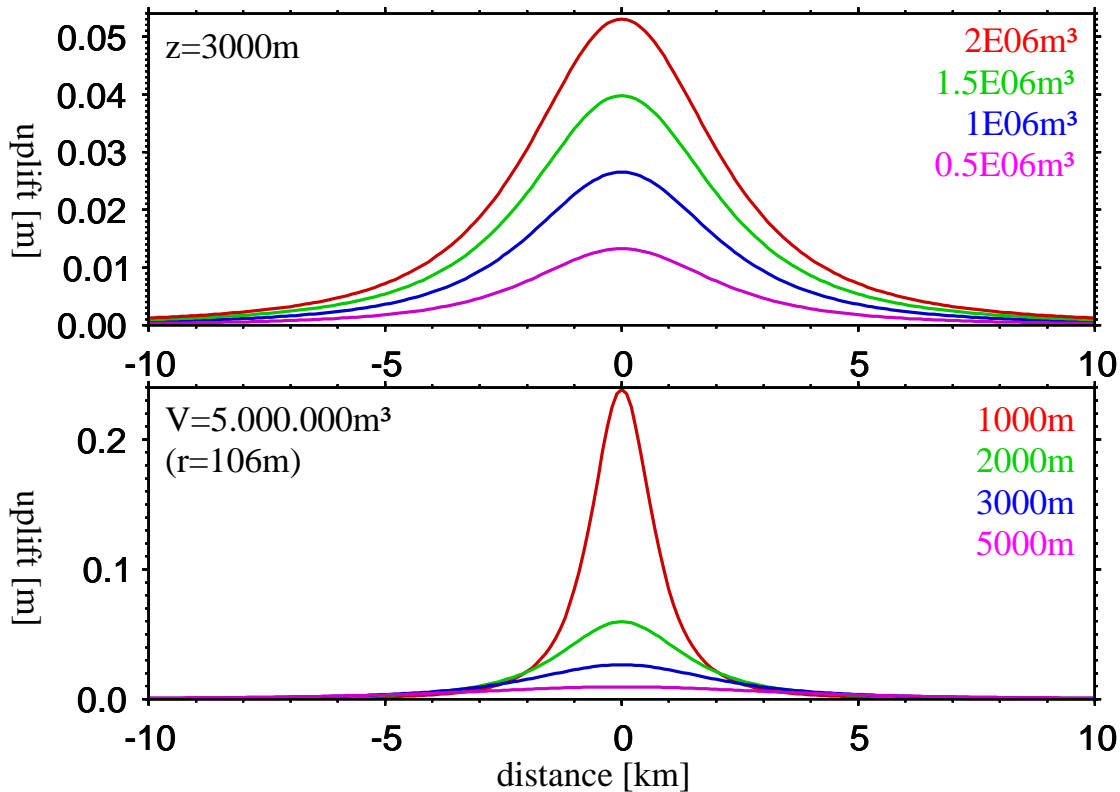


Figure 4.11: **The Mogi Model: Volume- and depth-dependencies.** Variation of u_z due to volume increase (upper plot) assuming a fixed depth, and due to increasing depth assuming a fixed volume (lower plot). While for a fixed depth, a volume increase of the source causes a linear increase of the amplitude, the amplitude decreases nonlinear with an increasing depth, while the wavelength of the signal increases linear with depth.

decreasing with depth. Also the wavelength of the deformation signal and thus the epicentral distance of the maximum of the tilt signal increases with the source depth. This leads to an important fact: A slowly upward migrating Mogi source leads to a surface deformation with exponentially increasing amplitudes and linearly decreasing wavelength. The maximum of the related tilt signal occurs time-shifted on tiltmeters with different epicentral distances.

Decreasing wavelength of the uplift for an upwards migrating source leads to a sourcewards migration of the inflexion points of the vertical deformation field. Thus, the maximum of the related tiltsignal is shifting towards the epicenter of the source, i.e. the maximum tilt will be approaching time-shifted on stations with varying epicentral distance.

Fig. 4.12 illustrates the volume threshold for a Mogi source depending on depth and distance, assuming a minimal tilt signal of 50 nrad . The visible effect of varying depths show the same trend: Strong tilt for shallow sources and an increase of the signal's wavelength for deeper sources.

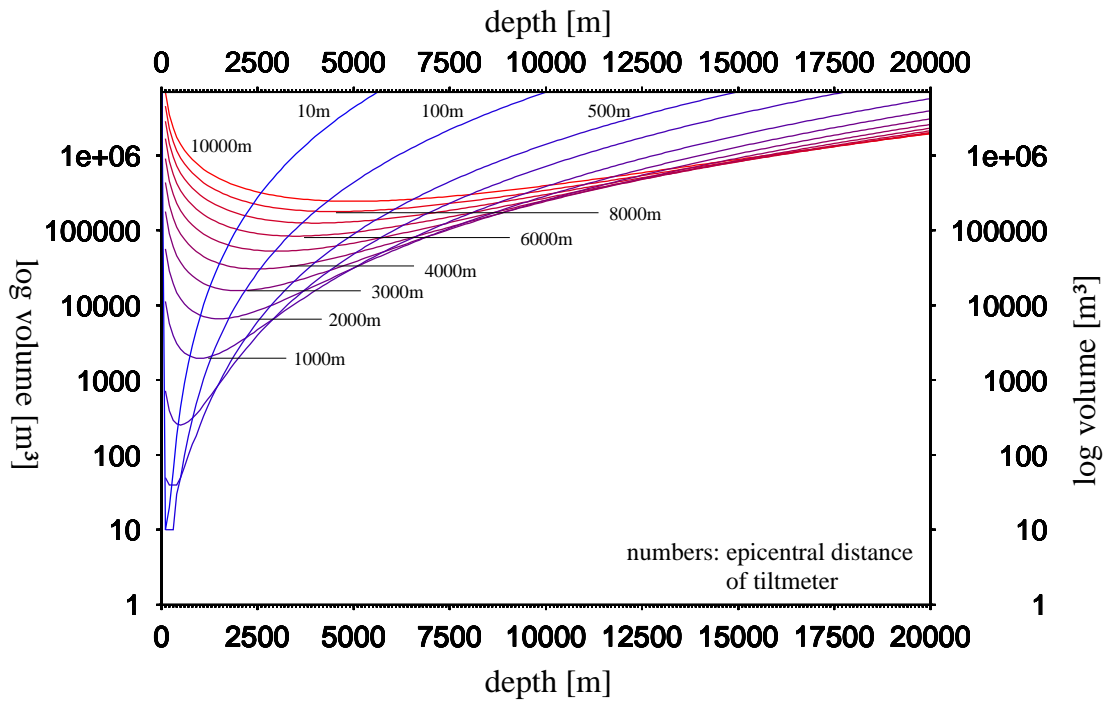


Figure 4.12: **Threshold-Volume** depending on depth and distance to trigger the OBT. Distribution of the minimum volumina depending on depth and distance of the source to trigger a visible signal on the Hamburg OBT. The threshold is here set to 50 *nrad*.

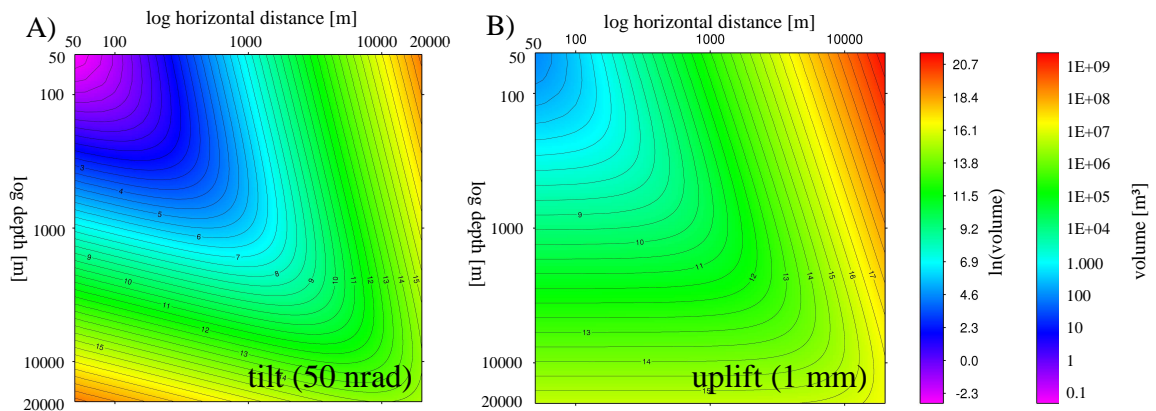


Figure 4.13: **Gridded volume threshold over depth and distance** Volume thresholds for A) a minimum tilt signal of 50 *nrad* on the tiltmeter and B) a minimum uplift of 1 *mm* of the absolute pressure sensor. Depth and distance are scaled with a common logarithm (\log_{10}), the volume scale (colours) is a natural logarithm (\ln). This was the only way to break down the effect to a colour scale, since the fastest threshold increase takes place in the direct vicinity of the source.

4.2.3 The Lenticular Volume Source for dike intrusions

A magmatic intrusion, a dike, has a lenticular shape parallel to the first principal stress axis σ_1 and is opening in direction of σ_3 . Its planar shape directly suggests a more complicated deformation field than compared to the Mogi source, which also makes it much more difficult to model it.

Vertical surface displacement, as modeled for example by Hautmann et al. (2009) for the shallow magmatic feeder system of the dome forming eruption of Soufrière Hills, Montserrat, suggests uplift maxima beside the dike in σ_3 -direction and not directly on top of it. As a consequence, a much more difficult deformation pattern can be assumed: E.g. tilt between the epicenter of the deformation source and the actual uplift maximum becomes negative compared to a Mogi source, tilt in σ_1 -direction remains nearly zero (Pollard et al., 1983; Rubin, 1992).

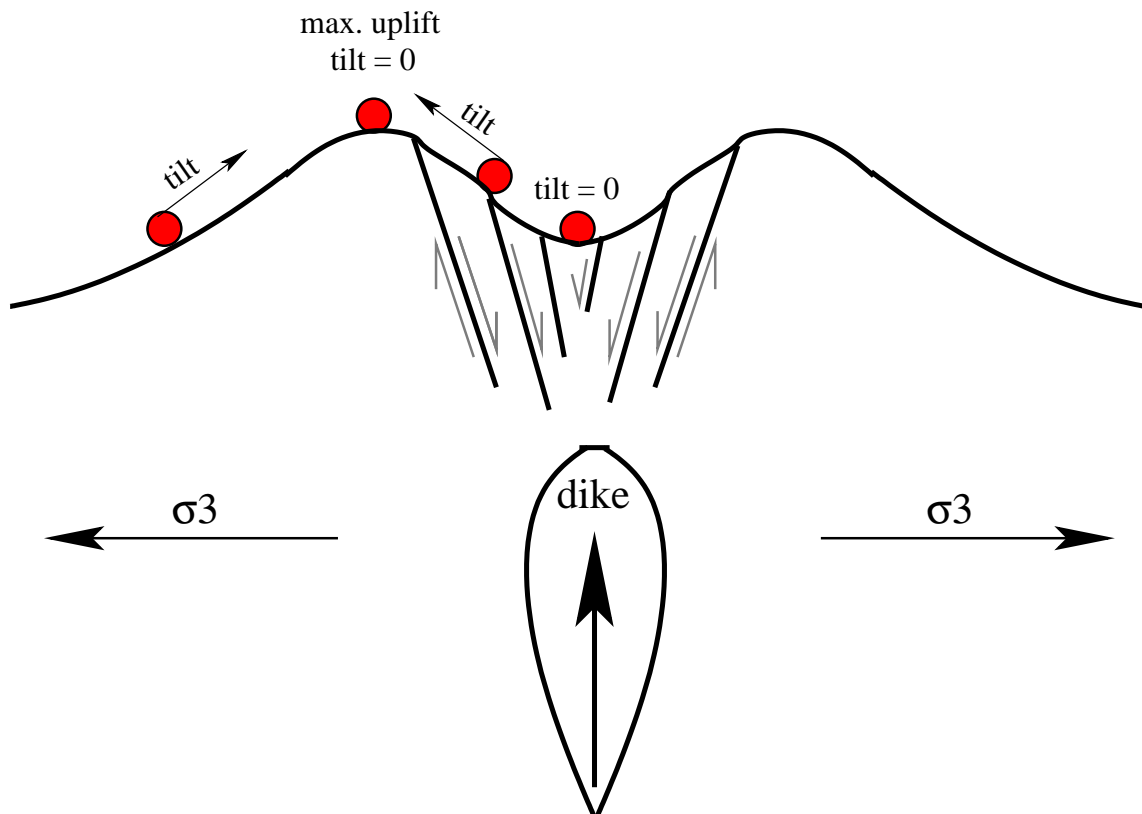


Figure 4.14: **Deformation due to magmatic diking:** Maximum uplift is observed beside the top of the source, negative tilt (or tilt away from the source) occurs between the source centroid and the point of maximum uplift. Tectonically, the approaching dike causes to a very local rift structure.

Fig. 4.14 demonstrates, how a shallow volumetric dike source causes normal faulting and thus relative subsidence on top of the source, which ends in negative tilt on close tiltmeters. The cause is simple: Normal faulting directly above the approaching dike leads to a local rift structure. For repeated dike intrusions, Kühn and Dahm (2008) have shown that cumulating

intrusions in the same source region cause an even more complicated deformation pattern, even uplift above the dike.

It is clear that we can not model for such sources with only three individual measurements. It is introduced to show the complex reality in opposite to the simple Mogi approach. To model for complex sources, methods such as InSAR or continuous GPS measurements are still indispensable, but technically limited to onshore volcanoes. Only a dense network of OBTs might enable more complex modeling in the future.

For our further work with the Columbo tiltmeter data, we will confine ourselves to the simple Mogi approach.

METHODS AND RESULTS 1

SEISMOLOGICAL ANALYSIS

This chapter summarizes methods and results of the seismological data analysis. Its first section describes event detection, picking and location, the second section deals with the estimation of fault plane solutions using moment tensor inversion.

5.1 Precise relative earthquake relocation

5.1.1 SEISAN: Picking and further parameterization

Picking and first single event locations, as well as determination of the P-wave polarization to derive preliminary fault plane solutions have been done with SEISAN (Havskov and Ottemöller, 2001), a set of earthquake analysis tools written mostly in FORTRAN and C. SEISAN furthermore allows the estimation of spectral parameters and magnitudes. All program-tools are tied to the same database and thus allows access of each tool on each event (organized by specific event-IDs).

We generated our SEISAN database based on over 14.000 coincidence-triggers found by an in-house developed STA/LTA (short term average / long term average) routine that was run over the hydrophone traces of all Hamburg OBSs/OBTs. This routine uses two data windows, one of 50 samples length, the short term average (STA), one of 500 samples length, the long term average (LTA). Both windows are moved over the complete time series, dividing STA through LTA for each step. Once a strong change of this ratio occurs while processing the timeseries, e.g. the onset of an earthquake, STA increases faster than LTA due to its short length, and the value of STA/LTA exceeds a threshold (in our case 2.5), which marks a trigger for this station at a given time.

Triggers on all stations are compared using an association routine. When at least 3 stations trigger within a time window of 10 s after the first trigger, this is declared a potential event and a data window around the trigger-time t_{trigg} of -30 s and $+60$ s is cut for each onshore

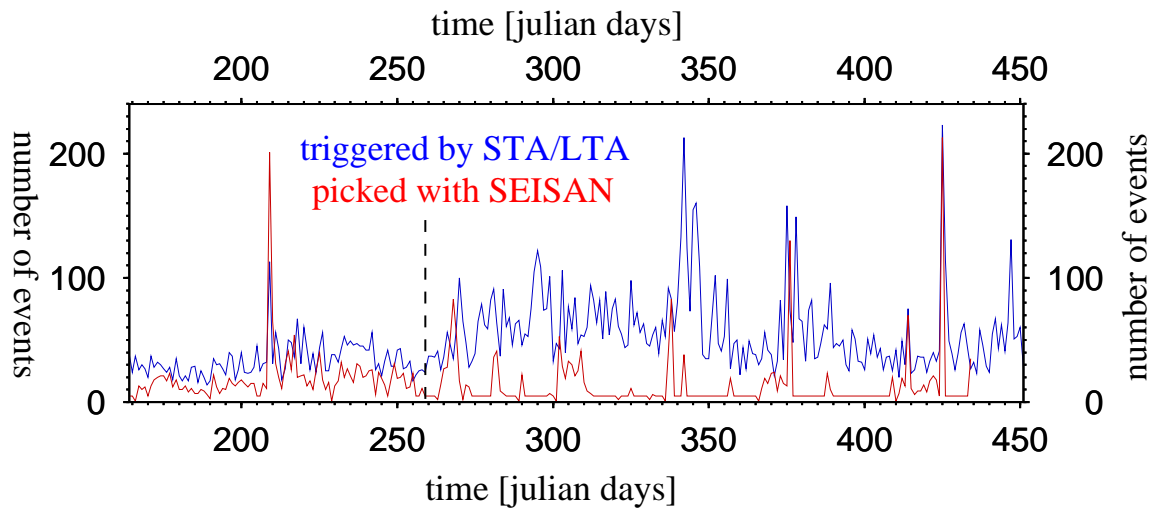


Figure 5.1: **Overview: STA/LTA triggered and picked events.** The blue curve shows all potential events that have been triggered (between 15 and 225 per days), the red curve marks the number of events that have been picked manually with SEISAN. The dashed line indicates the period of the first 3 months, for which the complete catalogue was compiled. For the rest of the experiment, only events during swarms or other interesting periods were picked.

and offshore station. Traces are tied together to one event and this event is then registered to the SEISAN data base to be picked.

Of 14.000 potential events, we manually picked around 4.000, which are all events of the first 3 months (July - September 2006) and most events occurring during earthquake swarms between November 2006 until the end of the experiment in March 2007. Fig. 5.1 gives an overview on the number of triggered events and finally picked events per day. The number of mistriggers (noise) was small, but events of too small magnitude have not been picked due to limited human resources, which sometimes leads to pick-rates of only 50% or less for days of normal activity (compare red and blue line in Fig. 5.1).

The typical Columbo event is a high frequency volcanotectonic earthquake (Fig. 5.2) of a magnitude between $M_L = 0.5$ and $M_L = 4.5$ and mainly located in the direct vicinity of the Columbo caldera. P-S traveltimes differences are in a range of 1 – 3 s for the closest stations and dominant frequencies are between 2 – 20 Hz (Fig. A.2).

This type of events occurs daily at Columbo, with event rates between 15 per day during periods of low activity and up to 225 during earthquake swarms. Partly, they could not be analyzed because waveforms of different events were overlying each other or weak events disappeared in the coda of the previous event. Fig. 5.3 shows the activity on OBS 50 during the earthquake swarm from 28th of July 2006: Within 7.5 min, over 10 local events occurred, some of them were so weak that they disappeared in ambient noise.

Additionally to P- and S-picks, a polarity reading was given with the P-pick to characterize if the first onset was positive or negative, and peak-to-peak amplitudes of S-waves

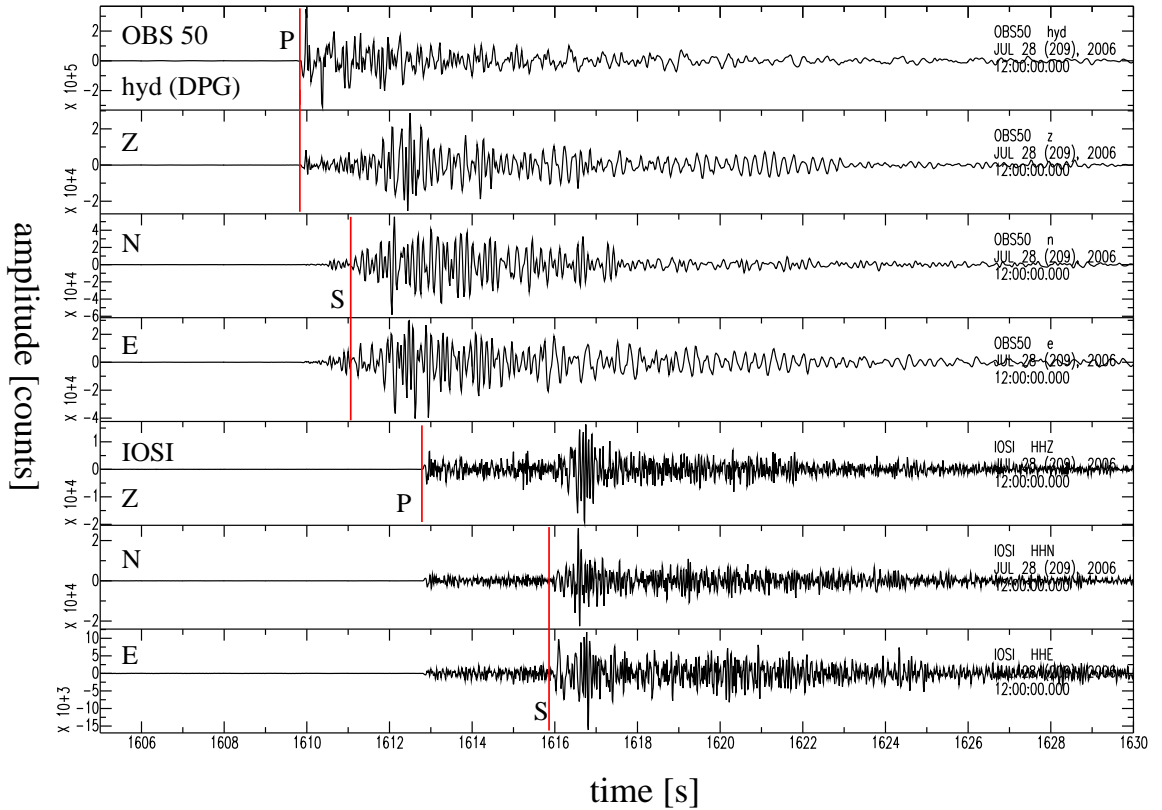


Figure 5.2: **Typical event at Columbo seamount (OBS 50 and IOSI)**. Local events like the shown one on 28th of July 2006 during an earthquake swarm are typical for Columbo. For OBS/OBT stations directly at the volcano, P-S traveltimes differences are 1 – 3 s.

were determined. Polarity readings were needed together with the hypocenter locations in order to estimate preliminary focal solutions (program FOCMEC, Snoke et al., 1984) and to resolve the polarity-ambiguity of moment tensor solutions from amplitude spectra inversion. Amplitudes of S-waves have been used for local magnitude (M_L) estimation together with the hypocenter location by using the program HYPO71 (Lee and Lahr, 1975, embedded in the SEISAN software). The local magnitude is based on the empirical relation (assuming a narrow band dominant period T , see Lay and Wallace, 1995):

$$M_L = \log A + 2.76 \log \Delta - 2.48 \quad (5.1)$$

where Δ is the epicentral distance and A is the peak to peak amplitude. We compared our magnitudes for strongest events with those of the permanent NOA network (see <http://www.gein.noa.gr/>) and found relatively good correlations: Most of our magnitude estimations are slightly higher than those of NOA. Due to the down time of 10 s of the STA/LTA trigger after each event detection and varying noise over the complete experiment, a clear magnitude threshold can not be given. Weakest events that we were able to pick on OBSs/OBTs were of magnitude $M_L \geq 0.5$.

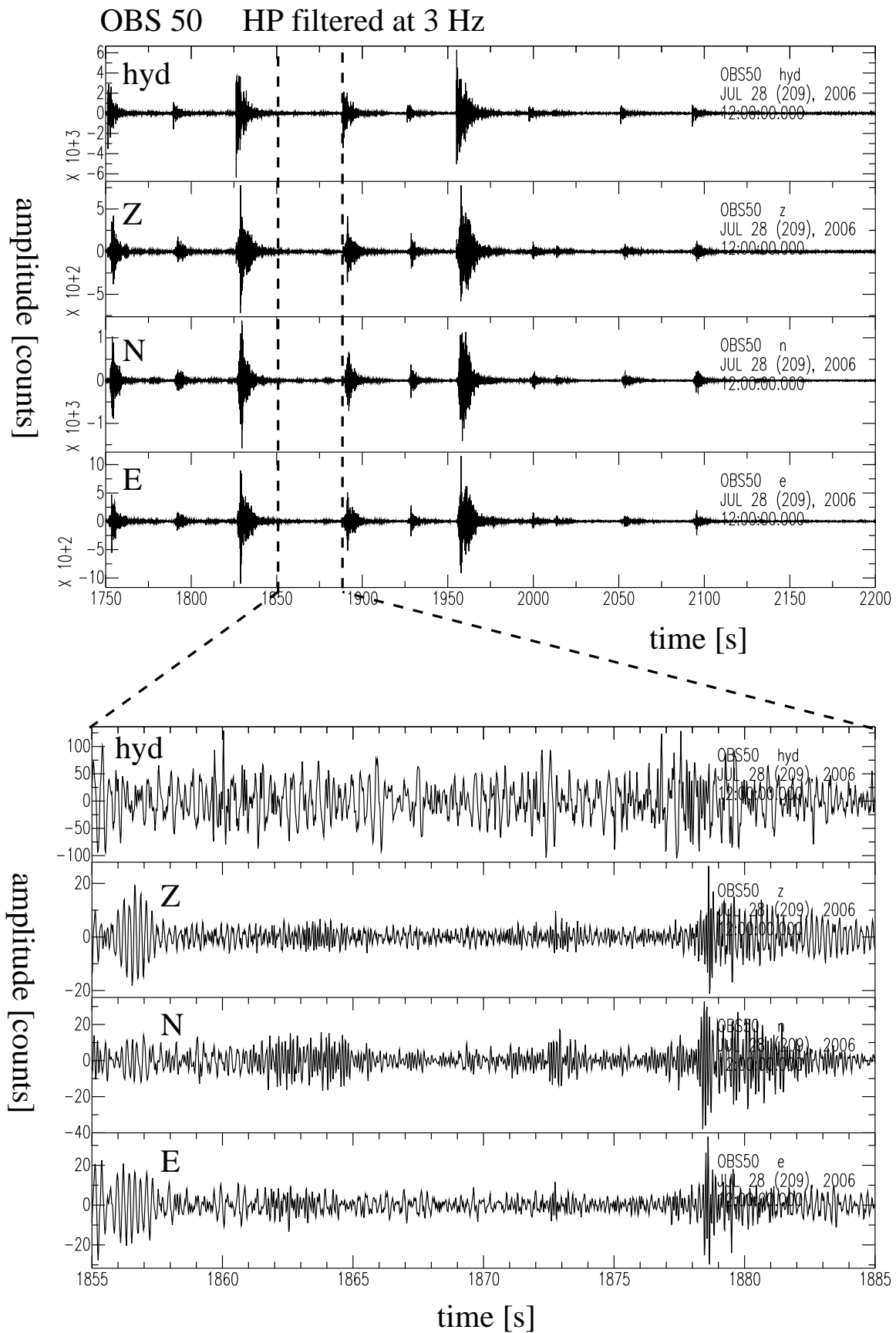


Figure 5.3: **Earthquake swarm at Columbo:** 7.5 min long snapshot of continuous data on OBS 50. In the upper plot, at least 10 events of the typical local type can be clearly seen, and even in the cutout of an obviously quiet period of 40 s length (lower plot), 1-3 further events can be estimated.

5.1.2 Velocity model

The velocity model has been taken from Dimitriadis et al. (2009). It is based on an onshore experiment of the Aristotle University of Thessaloniki (AUTH). The model predicts two low velocity layers. As SEISAN does not allow any velocity decrease with depth, it was slightly modified. Theoretical and finally applied models are given in Fig. 5.4 and Tab. 5.1.2.

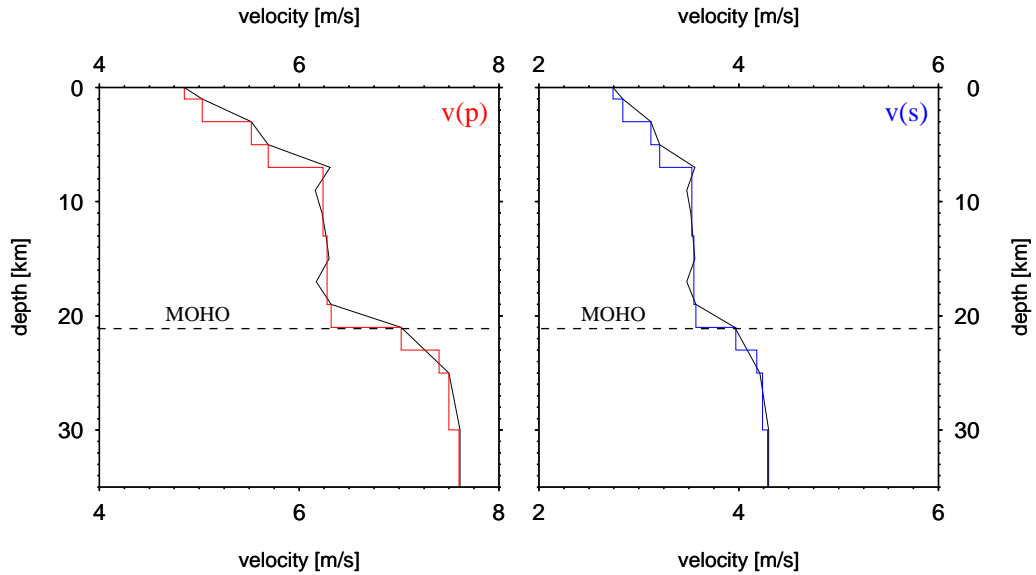


Figure 5.4: **Velocity model for v_P and v_S** , based on Dimitriadis et al. (2009) (black curves) and how it was applied in SEISAN and further processing (red curve for v_P and blue curve for v_S). Models differ, since SEISAN does not allow for low velocity layers.

A Wadati diagram was calculated with our picked events, which predicts a slightly smaller v_p/v_s ratio than compared to what our Greek colleagues derived from their island based tomography experiment (1.78, see Dimitriadis et al., 2009, and Fig. 5.5). But with a ratio of 1.77, it is still higher than what would be expected for ideal elastic media (1.73). This has already been discussed by Dimitriadis et al. (2009) being due to the influence of a magma reservoir (decreased shear modulus μ) underneath Columbo.

The slope trend of the wadati-diagram is (Lay and Wallace (1995))

$$m = \frac{v_P}{v_S} - 1 \quad (5.2)$$

thus it follows for the ratio of P- and S-wave velocity

$$\frac{v_P}{v_S} = m + 1 \quad (5.3)$$

and with $m=0.77$ we get $\frac{v_P}{v_S} = \mathbf{1.77}$.

Depth [km]	$v_P[\frac{km}{s}]$ AUTH	$v_P[\frac{km}{s}]$ SEISAN	$v_S[\frac{km}{s}]$ AUTH	$v_S[\frac{km}{s}]$ SEISAN
0	4.85	4.85	2.74	2.74
1	5.03	5.03	2.84	2.84
3	5.52	5.52	3.12	3.12
5	5.69	5.69	3.21	3.22
7	6.31	6.24	3.56	3.53
9	6.16	6.24	3.48	3.53
11	6.23	6.24	3.52	3.53
13	6.27	6.28	3.54	3.55
15	6.30	6.28	3.56	3.55
17	6.17	6.28	3.48	3.55
19	6.32	6.32	3.57	3.57
21 (MOHO)	7.02	7.02	3.96	3.97
23	7.26	7.40	4.09	4.18
25	7.50	7.50	4.21	4.24
30	7.60	7.60	4.30	4.29

Table 5.1: Velocity models as they were estimated by the Aristotle University of Thessaloniki (AUTH) and as they were applied in SEISAN. Note: The model of the Greek colleagues of the AUTH is a gradient model, while we applied a step-model in SEISAN.

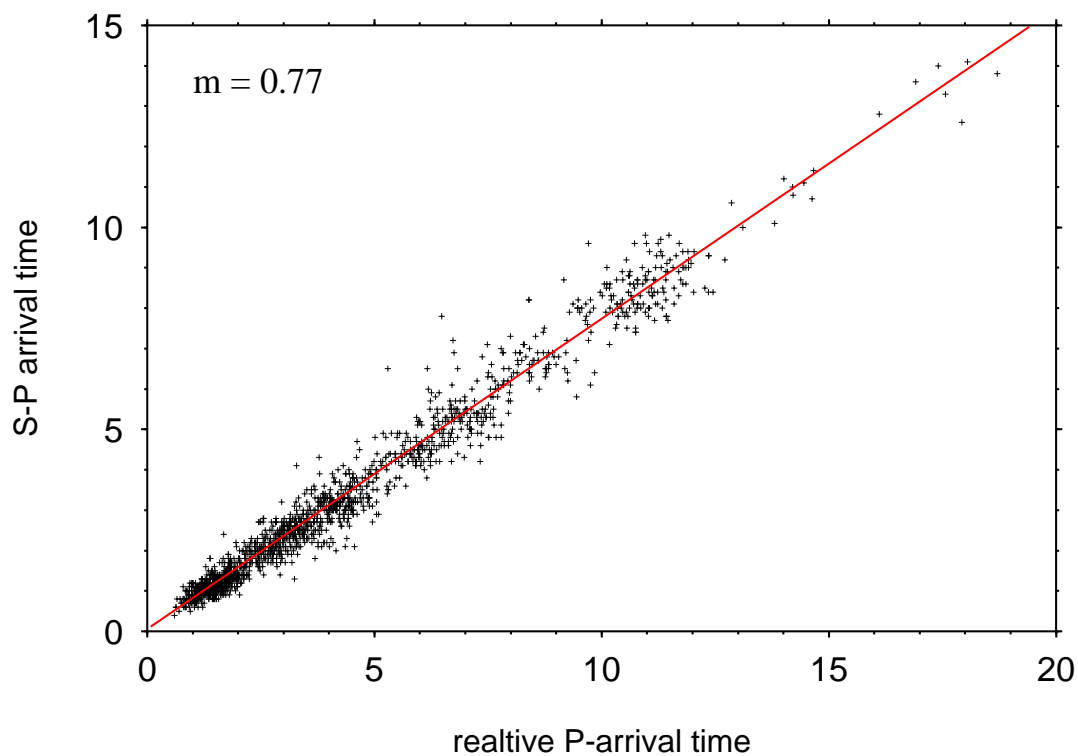


Figure 5.5: A Wadati diagram based on SEISAN picks suggests a v_P/v_S ratio of 1.77.

5.1.3 3 component cross correlation

To precisely relocate earthquakes within a cluster, waveform similarities (correlation coefficients) have been calculated: The cross-correlation function $\Phi_{ijk}(t)$ at station k (5.4) represents the correlation of function $x_{ik}(t)$ with function $y_{jk}(t)$ at the time t . The functions $x_{ik}(t)$ and $y_{jk}(t)$ are waveform time series of the events i and j at station k . $\Phi_{ijk}(t)$ is given with:

$$\Phi_{ijk}(t) = \int_{-\infty}^{+\infty} x_{ik}(\tau)y_{jk}(\tau+t)d\tau \quad (5.4)$$

The correlation coefficient $cc_{ijk}^{p,s}$, which is the maximum of the normalized function Φ_{ijk} , indicates the similarity of two different seismograms recorded at the same station (Maurer and Deichmann, 1995). For each station k and each phase P and S , the correlation coefficient is calculated by

$$cc_{ijk}^{p,s} = \frac{\Phi_{ijk}^{p,s}(\tau_{ijk,max}^{p,s})}{\sqrt{\Phi_{iik}(0)\Phi_{jjk}(0)}} \quad , \quad (5.5)$$

with

$\Phi_{ijk}^{p,s}(t)$: coefficient of cross-correlation of P - and S -Phase of events i and j at station k

$\Phi_{iik}^{p,s}(t)$: coefficient of auto-correlation of event i at station k

$\tau_{ijk,max}^{p,s}$: time of maximum of cross-correlation function

A three-component seismometer delivers three time series for each event. Calculating the correlation coefficient over all three components compensates effects due to different azimuth or incidence angle and avoids high correlation due to random similarity on one component. Thus, we calculate the correlation coefficient of all three components by

$$cc_{ijk}^{p,s}(all) = \frac{\Phi_{ijk}^{p,s}(\tau_{ijk,max}^{p,s})^N + \Phi_{ijk}^{p,s}(\tau_{ijk,max}^{p,s})^E + \Phi_{ijk}^{p,s}(\tau_{ijk,max}^{p,s})^Z}{\sqrt{(\Phi_{iik}^{N(p,s)} + \Phi_{iik}^{E(p,s)} + \Phi_{iik}^{Z(p,s)}) \cdot (\Phi_{jjk}^{N(p,s)} + \Phi_{jjk}^{E(p,s)} + \Phi_{jjk}^{Z(p,s)})}} \quad . \quad (5.6)$$

The respective value of the time of maximum cross-correlation τ_{max} of each event pair is stored in a time shift matrix and used for relative time correction of the manually set picks.

If the incoming waves have very similar waveforms on all three components, $cc_{ijk}^{p,s}(All)$ is nearly 1. Differing time-series have smaller magnitudes of $cc_{ijk}^{p,s}(All)$.

Fig. 5.6 shows time windows that were cut off the continuous data: ± 0.5 s for P- and ± 1 s for S-phases. Before running the correlation process, a bandpass filter and a cosine taper were applied to the data (see Tab. A.6, App. A.3 for parameters), in order to eliminate noise outside the signal frequency band due to long period ocean waves (e.g. Dahm et al., 2005) and high frequency noise caused by breaking sea waves (e.g. Deane and Stokes, 2002).

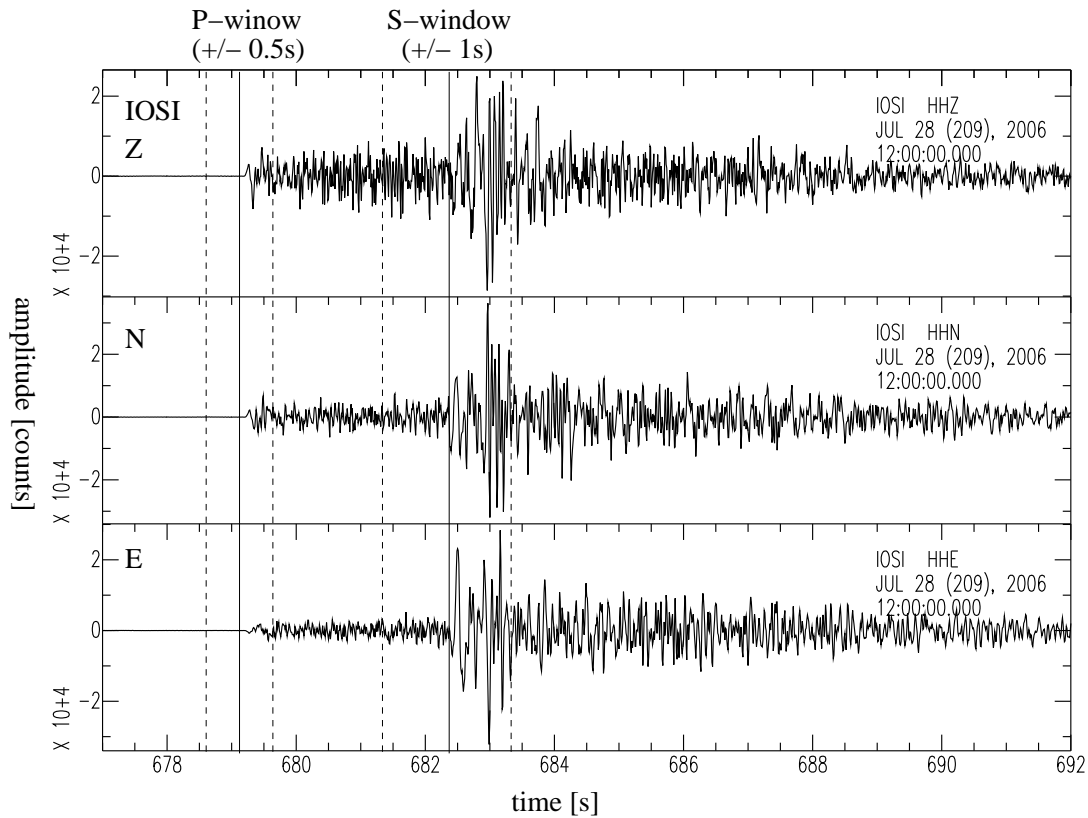


Figure 5.6: Example for time windows cut off continuous data

Above average high correlation coefficients require high similarity of the waveforms of the compared events. This requires that adjacent events are in a maximum distance of the first Fresnel Zone, i.e. less or equal to $\frac{\lambda}{4}$ (Maurer and Deichmann, 1995), where λ is the dominant wavelength of the phase. For high dominant frequencies of about 10 Hz the maximal event separation is around 500 m at the utmost.

From our experience, it is impossible to get a correlation coefficient of 0, which would mean no similarities for the complete timetrace, even if pure noise was analyzed. A correlation of 1 for two similar events not occurring exactly at the same location has never been observed. Random correlation leads to correlation coefficients of ± 0.5 on average. A histogram giving the number of event pairs versus the correlation coefficient (cc-distribution) shows two normal distributions (positive and negative) with their maxima around ± 0.5 (see Hensch, 2005).

While a cluster of highly correlating events should form a second maximum for high positive correlation coefficients, these data should separate from the rest of the cc-distribution. This separation is improved if all three components of each record are correlated as given in Eq. 5.6. The three component cross-correlation has been introduced by Hensch (2005) and has the following three advantages:

- It reduces effects of random correlation on one component.
- It is independent of the azimuth and incidence angle and of the polarization of the wave.
- It improves the resolution of an earthquake cluster against random noise.

Once a peak of the cluster separated from the distribution of the random noise has been identified in the cc-distribution, a threshold is introduced individually for each station and each phase, for which all matrix-values of cross-correlation are set to 0 if they were below the threshold T_s :

$$cc_{ijk}^{p,s} = \begin{cases} cc_{ijk}^{p,s} & cc_{ijk}^{p,s} \geq T_s \\ 0 & otherwise \end{cases} \quad (5.7)$$

Most literature suggests the usage of a global threshold for all stations and phases (usually chosen between 0.7-0.9 Maurer and Deichmann, 1995). The introduction of individual thresholds for each station and phase allows the manual choice of data depending on its quality. cc-distributions can extremely differ between several stations. An individual threshold increases data quality by suppressing data of noisy stations and can raise data quantity of stations with better signal-noise ratios. An exhaustive description of 3 component cross-correlation, data preparation and choice of thresholds is given in Hensch (2005). Plots and specific threshold values for each station and phase are given in App. B.

5.1.4 HYPOSAT single event location

The Columbo submarine volcano and the adjacent region around it show strongly varying velocity structures (Dimitriadis et al., 2009), but the used location and relocation routines only allow for 1D models (see section 5.1.2). This leads to station corrections that are even in short distances in a range of some tens of a second. For instance, the S-wave at IOSI on average arrives 0.41 s earlier than predicted by the model, although this station is only about 25 km away from Columbo. Fig. 5.7 shows station corrections for all stations and phases that were used. Strongest correction values were found for S-waves observed outside the volcanic belt between Santorini and Anidros, i.e. IOSI, ANAF and ASTY. The reason therefor is simple: The used 1D velocity model was derived from data collected on Santorini and Anidros and thus does not consider faster S-wave velocities outside the volcanically active belt. For a detailed list of station corrections for all station and phases see Tab. A.1 in App. A.1.

A preliminary single-event location was done using HYPOSAT (Schweitzer, 2001), a program which uses arrival times and traveltime differences and solves the equation system in

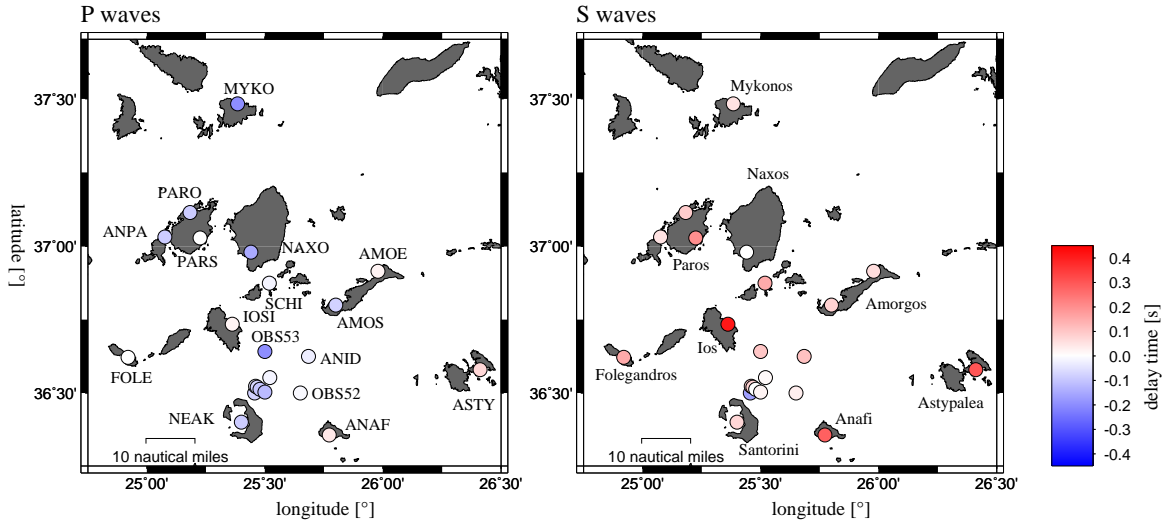


Figure 5.7: **Station corrections for P- and S-phases:** Colours show average time difference between picked and theoretical arrival times of P- and S-waves for all used stations. Positive (red) stands for actual arrivals before the theoretical onset time, negative (blue) stands for actual arrivals later than the predicted onset time.

Eq. 5.8 with the Generalized-Matrix Inversion approach (Menke, 1978):

$$\begin{pmatrix} 1 & \frac{\partial t_i}{\partial lat} & \frac{\partial t_i}{\partial lon} & \frac{\partial t_i}{\partial z_0} \\ 0 & \frac{\partial dt_j}{\partial lat} & \frac{\partial dt_j}{\partial lon} & \frac{\partial dt_j}{\partial z_0} \end{pmatrix} \cdot \begin{pmatrix} \delta t_0 \\ \delta lat \\ \delta lon \\ \delta z_0 \end{pmatrix} = \begin{pmatrix} \Delta t_i \\ \Delta dt_j \end{pmatrix} \quad (5.8)$$

With t_i as arrival times and dt_i arrivaltime differences of two phases observed at one station. We used the direct SEISAN output, i.e. station corrections and hypocenter coordinates (lat , lon , z_0 and t_0), and calculated changes of model parameters δt_0 , δlat , δlon and δz_0 .

HYPOSAT offers the possibility to include a local and a different global velocity model. We considered a very local velocity model (radius $r = 0.1^\circ$ around the volcano) around Columbo and the IASPEI91 model for the adjacent region. This did not lead to significant changes, but to slightly oscillating locations (see also Schweitzer, 2001).

Aim of the usage of HYPOSAT was to find good locations of earthquake clusters by including station corrections. Fig. 5.8 shows the effect of the HYPOSAT single event location using station corrections and travelttime differences in opposite to HYPO71 (single event location algorithm implemented in SEISAN) locations. The complete cluster is shifted in ESE direction and single clusters get more separated and structured. A significant vertical shift has not been found. The found values for the average cluster centroid are:

- Uncorrected: $lat = 25.4936^\circ$, $lon = 36.5301^\circ$
- Corrected: $lat = 25.4751^\circ$, $lon = 36.5348^\circ$

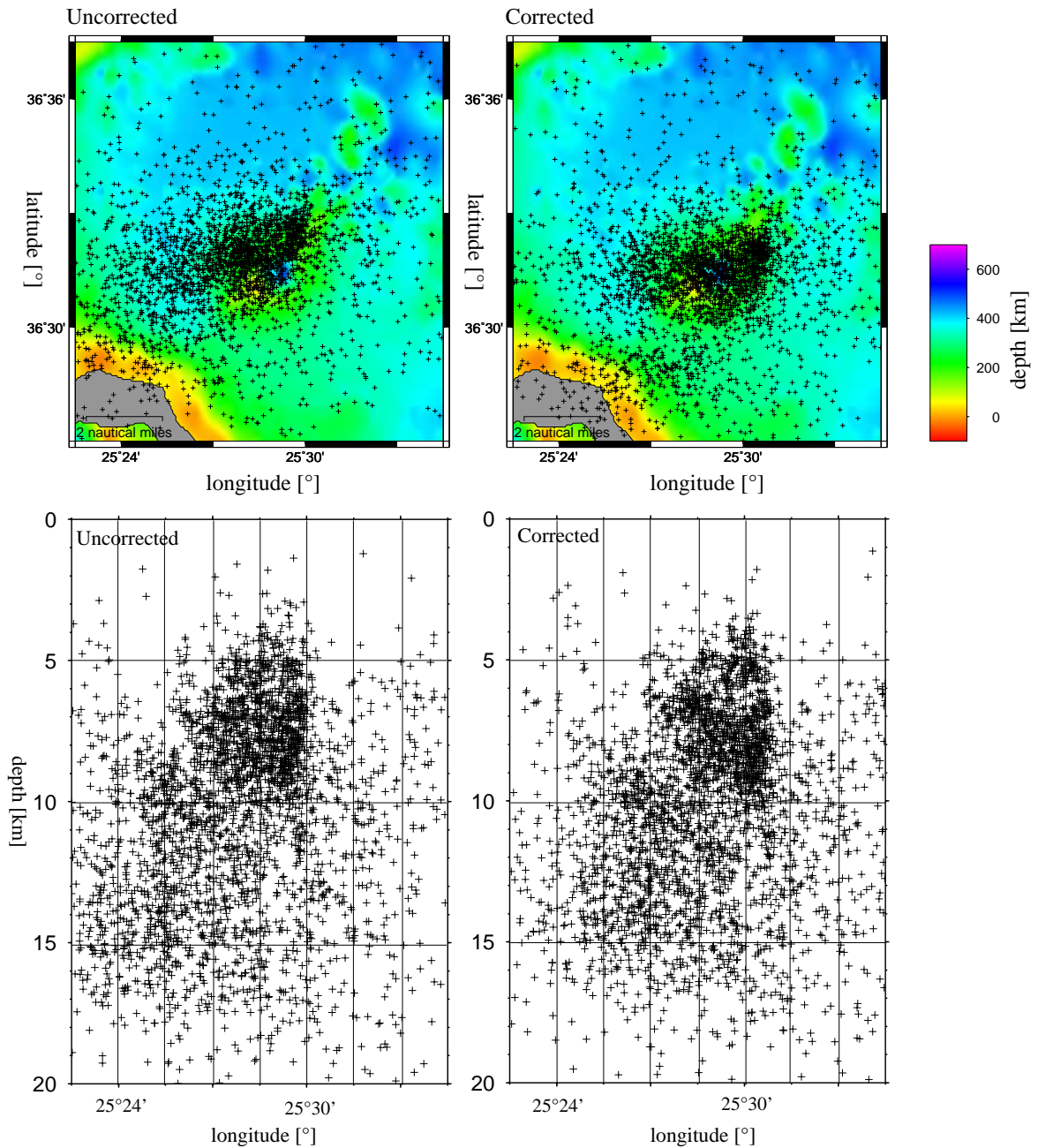


Figure 5.8: Comparison of original HYPO71 and improved HYPOSAT locations, which considered station corrections and traveltimes differences. Black crosses mark events located using SEISAN single event locations (left hand side) and once these results are corrected for station residuals and again located with HYPOSAT (right hand side). A shift of the cluster towards the Columbo volcano is visible.

- Shift: $\Delta lat = 0.0185^\circ$ eastwards, $\Delta lon = 0.0047^\circ$ northwards, $dist \simeq 2 \text{ km}$

5.1.5 HYPODD relative earthquake relocation

To receive high-resolution hypocenter locations, relative location methods (master event methods), which precisely determine the spatial offsets between the hypocenters, are required. If

the distance between two earthquakes is small compared to the paths between the events and the seismometer, ray paths between the source region and the station are nearly similar along almost the entire path. Master event methods take advantage of this, because they include the arrival time difference from two or more events at the same station in the location approach. The 2nd event is precisely located against the 1st event and finally, all events are accurately located relative to the cluster centroid. A modern routine of this approach was written by Waldhauser and Ellsworth (2000). Time differences determined by cross correlation have a precision of a few *ms*. This allows a relocation within some tens of meters of uncertainties for the ideal case.

The double difference method can be characterized as a combination of a Geiger method and master event relocalization in one code. The program *hypoDD* (Waldhauser, 2001) is able to handle both, ordinary absolute travel times as well as differential travel times of cross-correlated data.

With \mathbf{G} defined as a $M \times 4N$ matrix (M = number of double-difference observations (either picked or cross correlated data) and N = number of events), the data vector \vec{d} containing M double-differences, vector \vec{m} (length $4N$ ($\Delta x, \Delta y, \Delta z, \Delta \tau$)) containing the hypocentral parameter changes and the diagonal weighting matrix \mathbf{W} (see Tab. 5.2, dimension $M \times M$), all results are summarized by

$$\mathbf{W}\mathbf{G}\vec{m} = \mathbf{W}\vec{d} \quad . \quad (5.9)$$

The weighting matrix \mathbf{W} can be changed separately for cross correlation and catalogue data after a predefined number of iterations, which are chosen within the initial control parameters of hypoDD (see tab. 5.2).

<i>IT</i>	<i>WPCT</i>	<i>WSCT</i>	<i>RTCT</i>	<i>MDCT</i>	<i>WPCC</i>	<i>WSCC</i>	<i>RTCC</i>	<i>MDCC</i>	<i>DAMP</i>
1-5	1.0	0.8	10	10	0.5	0.1	none	∞	60
6-10	1.0	0.8	7	10	0.5	0.5	none	∞	50
11-15	0.8	0.8	3	10	1.0	1.0	none	∞	45

Table 5.2: Initial control parameters of hypoDD (description below).

With:

IT = number of iterations

WPCT, WSCT = weighting of catalog data P and S

WPCC, WSCC = weighting of cross-correlation data P and S

RT(CT,CC) = residual threshold in [s] for catalog and cross-correlation data

MD(CT,CC) = maximum distance [km] between linked pairs

DAMP = damping (LSQR)

Control parameters were initially chosen on the basis of former experiments (e.g. Iceland, see Hensch, 2005) and subsequently refined by trial and error. HypoDD offers the methods of Singular Value Decomposition (SVD) to find the Generalized Inverse of the coefficient matrix, with the advantage, that both, model and data resolution matrices, are calculated to derive reliable errors. Due to enormous computing time, the SVD mode is only practicable for small clusters, i.e. < 100 events.

The LSQR mode of HypoDD allows the relocation of much larger clusters, but it does not ensure to find the best minimum and only gives estimated errors. We have run HypoDD in the LSQR mode to derive relocations of huge swarm clusters and checked them with smaller datasets in the SVD mode for spatial and temporal errors with the following average results (depending on size and position of the cluster relative to the network):

- horizontal error: $\pm 50 - 300$ m
- depth error: $\pm 70 - 500$ m
- source time error: $\pm 20-100$ ms

5.2 Moment Tensor Inversion

Moment tensor solutions of earthquakes are retrieved by the inversion of waveforms and/or amplitude spectra. Synthetic waveform data, i.e. Green's functions G , are generated using a step function as the source time function. The moment tensor representation is written in matrix form as:

$$d_n(t) = \sum_{k=1}^6 G_{nk}(t)M_k \quad (5.10)$$

where $d_n(t)$ is the measured ground displacement at receiver n (e.g. vertical component) and G_{nk} the seismogram at station n that is caused by the moment tensor component M_k (Stein and Wysession, 2003). The complete moment tensor consists of 6 independent components (i.e. m_{11} , m_{12} , m_{13} , m_{23} , m_{22} , m_{33}) which compose the vector 6×1 matrix \mathbf{M} . Structural effects of the earth along the travel path between source and receiver are included in $G_{nk}(t)$. Thus, the seismogram at receiver n is for each time sample the sum of Green's functions weighted by moment tensor components:

$$\mathbf{d} = \mathbf{GM} \quad (5.11)$$

Or explicitly:

$$\begin{pmatrix} d_1 \\ d_2 \\ \cdot \\ \cdot \\ \cdot \\ d_i \end{pmatrix} = \begin{pmatrix} G_{11} & G_{12} & G_{13} & G_{14} & G_{15} & G_{16} \\ G_{21} & G_{22} & G_{23} & G_{24} & G_{25} & G_{26} \\ \cdot & \cdot & \cdot & \cdot & \cdot & \cdot \\ \cdot & \cdot & \cdot & \cdot & \cdot & \cdot \\ \cdot & \cdot & \cdot & \cdot & \cdot & \cdot \\ G_{i1} & G_{i2} & G_{i3} & G_{i4} & G_{i5} & G_{i6} \end{pmatrix} \cdot \begin{pmatrix} M_1 \\ M_2 \\ \cdot \\ \cdot \\ \cdot \\ M_6 \end{pmatrix} \quad (5.12)$$

with \mathbf{d} as an $(i \times n) \times 1$ matrix (n = number of samples) of concatenated seismograms of i stations and \mathbf{G} as the $(i \times n) \times 6$ matrix of Green's functions. A similar matrix equation can be derived in frequency domain. The linear system of equations (eq. 5.12) is overdetermined ($i \times n$) equations and 6 unknown parameters. It is solved as follows:

$$\vec{M} = (\mathbf{G}^T \mathbf{G})^{-1} \mathbf{G}^T \vec{d} = \mathbf{H} \vec{d} \quad (5.13)$$

with \mathbf{H} as the generalized inverse of \mathbf{G} . Matrix \mathbf{M} is transferred to tensor notation by

$$\begin{pmatrix} M_1 \\ M_2 \\ M_3 \\ M_4 \\ M_5 \\ M_6 \end{pmatrix} = \begin{pmatrix} m_{11} \\ m_{22} \\ m_{33} \\ m_{12} (= m_{21}) \\ m_{13} (= m_{31}) \\ m_{23} (= m_{32}) \end{pmatrix} \implies \begin{bmatrix} m_{11} & m_{12} & m_{13} \\ m_{21} & m_{22} & m_{23} \\ m_{31} & m_{32} & m_{33} \end{bmatrix} \quad (5.14)$$

Fig. 5.9 shows the procedure of the complete moment tensor inversion in form of a struotogram. The routine is taken of the Diploma thesis of Barbara Hofmann (Hofmann, 2008). We cross checked solution of events of magnitude $M_L > 3.5$ with FOCMEC (Snoke et al., 1984), only using P-wave polarity constraints. Main purpose of this cross check was to determine the polarity of the moment tensor solution, since most often only amplitude spectra have been inverted. For events of magnitude $2 - 2.5 < M_L < 3.5$ (depending on data quality), we have only moment tensor solutions, because not enough polarities could be retrieved to apply FOCMEC.

Hydrophones of all OBSs/OBTs were also included in the inversion - with varying success. The conversion of relative pressure P to vertical ground motion $d_{seafloor}$ was performed according to Tilmann et al. (2008). After the removal of the hydrophone response, traces were multiplied with

$$\begin{aligned} d_{seafloor} &= \rho v_p \cdot P \cdot \sin\Phi \implies \rho v_p P \quad (\text{for } \phi = 90^\circ) \\ &= 1000 \frac{\text{kg}}{\text{m}^3} \cdot 1500 \frac{\text{m}}{\text{s}} \cdot P \end{aligned} \quad (5.15)$$

Where v_p is the P-wave velocity, ρ the water density and Φ the incidence angle of the plane wave arriving at the seafloor. In our case, we assumed $\Phi \simeq 90^\circ$. The resulting trace is identical to the ground displacement of a plane P-wave with vertical incidence and an impedance contrast of zero. Both of these assumptions are not fulfilled exactly, but for nearly zero offset stations a nearly vertical incidence can be assumed and also the impedance contrast from a mud to a water layer is close to zero.

Also the weighting of different phases was depending on data quality and for some events found by trial and error based on the residuals of the solutions. We mostly started with a weighting of -1.0 for P phases on Z components and 0.25 for the transversal component of the S phase as well as the P phases on hydrophones. For cases of too large residuals, hydrophone

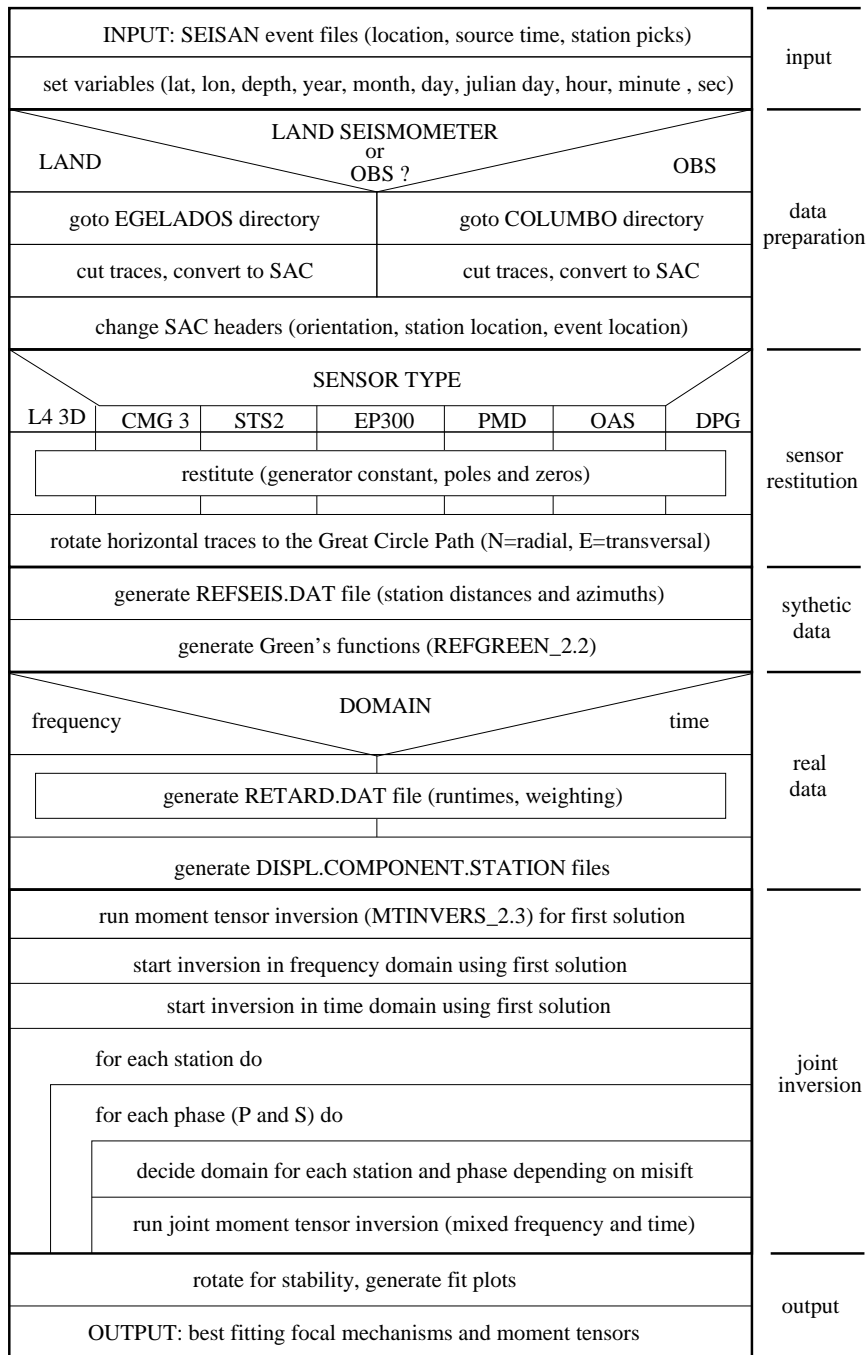


Figure 5.9: Structogram of data processing and moment tensor inversion (modified from Hofmann, 2008).

and transversal component were step by step downweighted or completely taken out of the inversion.

The inversion routine is a modified version of *mtinvers* (Dahm and Krüger, 1999; Cesca, 2005). A complete description on the generation of Green's functions and the inversion of amplitude spectra is given in Hofmann (2008), details on the generation of Green's functions are to be found in Dahm et al. (2004).

5.2.1 Moment Tensor solutions

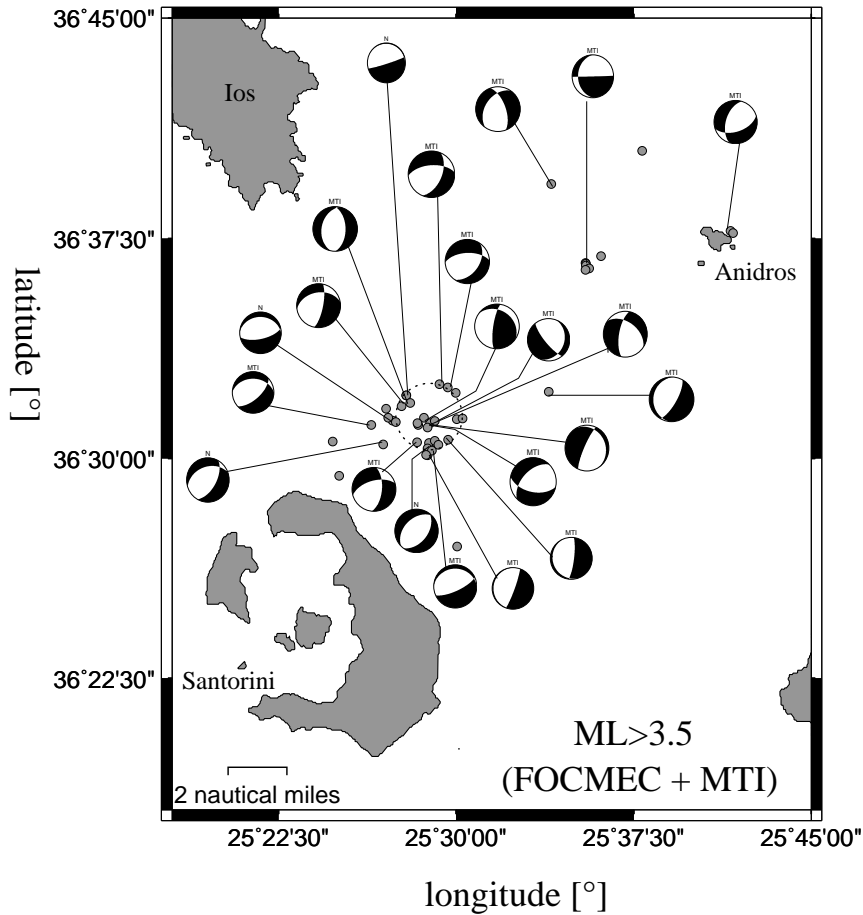


Figure 5.10: **Focal mechanisms of all events $M_L \geq 3.5$** (lower hemisphere, white indicates dilatational quadrants). MTInvers solutions were cross-checked with FOCMEC, only double couple components are plotted.

We separate two quality types of moment tensor solutions: Events of magnitude $M_L \geq 3.5$ (black-white beachballs in the following, see Fig. 5.10) that have been cross-checked with polarities (FOCMEC), and non checked solutions for events of magnitude $M_L < 3.5$ (grey-white beachballs, see Fig. 5.11).

Fig. 5.12 is an overview on an earthquake that was inverted with MTInvers and cross checked with FOCMEC. Both methods led to comparable solutions. A second sketch of this summary plot shows the residuals around the P-, T- and B- axes. Found solutions were rotated around all three axes to investigate their stability. For most solutions, a clear minimum for all three axes is found, but also cases of instability of one axis were observed. Finally, the lower diagrams give an overview on the fits of amplitude spectra or, in case of a good signal-noise

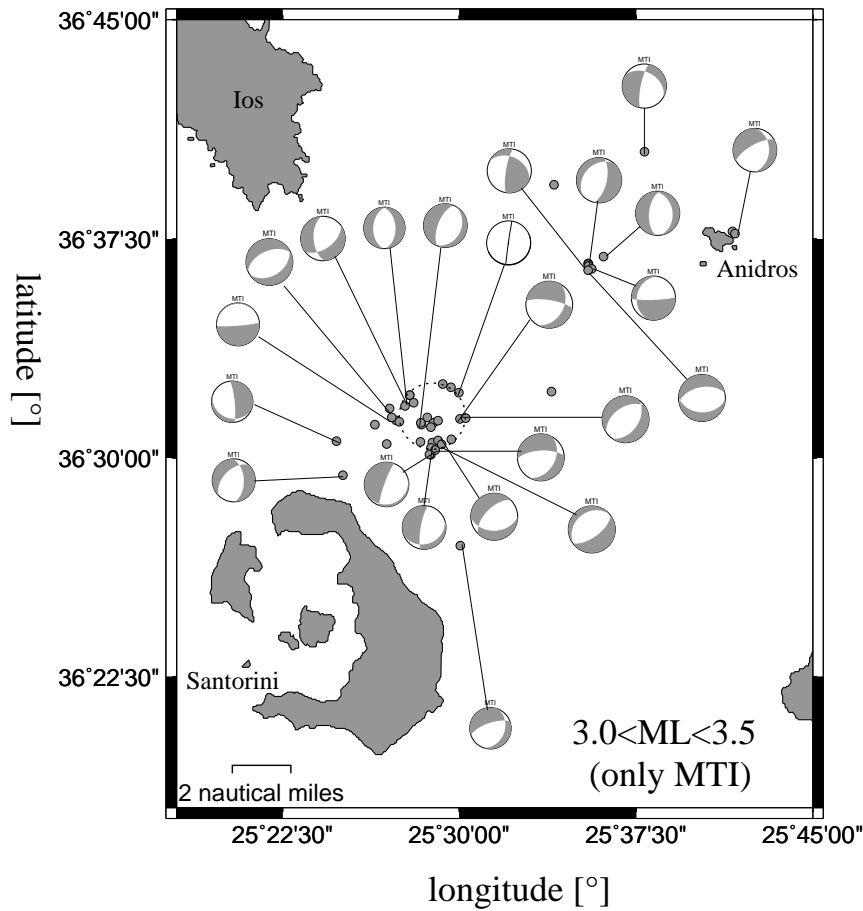
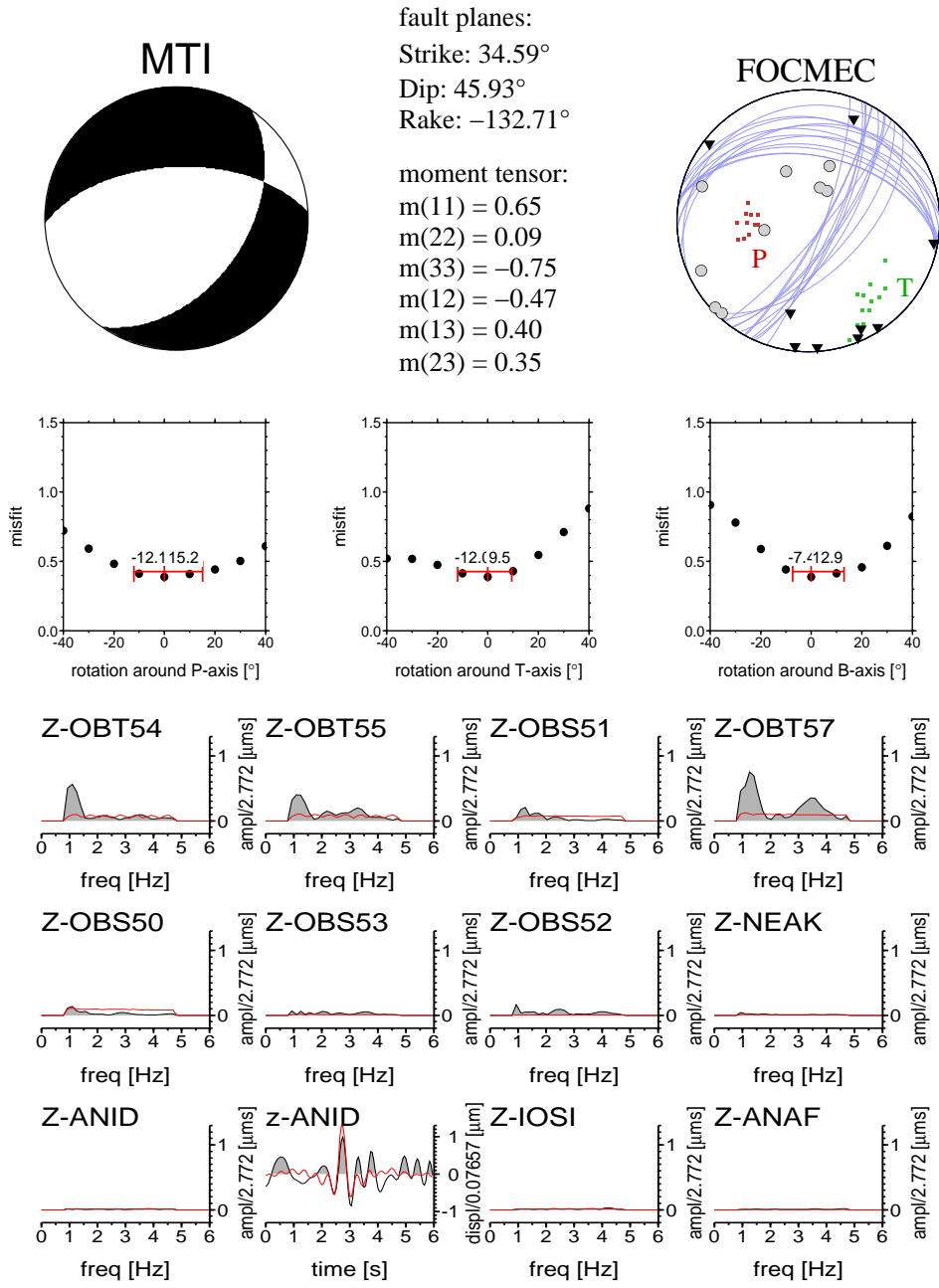


Figure 5.11: **Focal mechanisms of all events $3.5 > M_L \geq 3.0$.** For unchecked focal mechanisms (inverted onlys), the polarity of the solution was determined based on findings of checked solutions (normal faulting). If not possible, only planes and no polarity is given. See Fig. 5.10 for further description.

ratio and correlating waveforms, also waveform fits (here the z-component of AMOS). Due to uncertainties in the applied 1D velocity model and strong inhomogeneities in the real velocity structure (compare station corrections in Fig. 5.7), both, waveforms and amplitude spectra are much more complicated than predicted by our model. Differences are mainly found in the complexity of the real data in opposite to the model, but also sometimes in large amplitude discrepancies.

Nearly all found solutions are north-easterly striking normal faulting focal mechanisms. Their double-couple (DC) component is on average around 70–80 %. For some solutions, the DC component is significantly lower, although these were strong and well constrained events. We have not inverted for the isotropic component. On average, the DC component decreases with the magnitude and thus the quality of the solution, but high DC values are also found

Event: 2006/10/22 20:48:52.2 lat.: 36.540401° lon.: 25.494159° depth: 8.7km
 Gap: 68° ML = 3.8 M(0) = 0.51E+15Nm Mw = 3.7 misfit = 0.388E+00 DC = 95%



Weighting: Land: P = 1.00 S = 0.25 OBS/OBT: P = 0.25

Figure 5.12: **Example for a cross checked moment tensor solution.** Upper plots: MTInvers solution on the left hand side, FOCMEC solution on the right hand side (white symbols mark negative, black positive P-wave polarity, blue lines mark possible fault-/auxiliary-planes). Middle plot: Stability of the solution (rotation around P-, T- and B-axes). Lower plot: Fits of model and data in mostly frequency domain. The red curve marks the Green's function (or its amplitude spectrum), the black and grey shaded curve reflects the real data.

for weak events just like small DC components were found for stronger ones.

All faultplane solutions found are listed in Tab. 5.3 and a detailed result plot for each event can be found in appendix E. In the table, only one fault plane solution is listed, which does not mean that there is any hint that this is the correct fault plane or the auxiliary plane. Fig. 5.13 compares the average source mechanisms of our experiment and an independent study in the year 2003 by our Greek colleagues of the Aristotle University of Thessaloniki (AUTH). The solution on the left hand side is the average solution of all inverted events of the Columbo experiment (UHH, University of Hamburg) derived from averaging the moment tensors ($M_{av} = \frac{1}{N} \sum_{i=1}^N M_i$), the right hand side shows the average solution as derived from an onshore experiment on the surrounding islands (AUTH, see Dimitriadis et al., 2009).

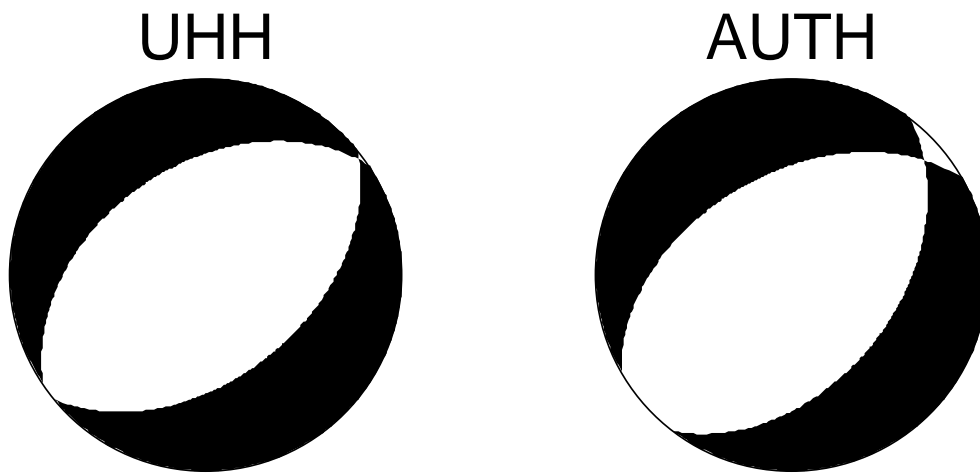


Figure 5.13: **Comparison of average focal mechanisms.** Left hand side: Double couple of the average moment tensor of the Columbo data (University of Hamburg, UHH). All moment tensors were cross checked with P-wave polarity analysis. Right hand side: Average solution of the onshore network of the Aristotle University of Thessaloniki (AUTH), estimated using P-wave polarities and amplitude ratio of P and S coda. Both solutions only differ by a few degrees for each fault plane angle.

The average solutions are:

- UHH: strike = $43^\circ \pm 40^\circ$, dip = $49^\circ \pm 17^\circ$, rake = $-91^\circ \pm 33^\circ$
(auxiliary plane: strike = $236^\circ \pm 40^\circ$, dip = $44^\circ \pm 17^\circ$, rake = $-85^\circ \pm 33^\circ$)
- AUTH: strike = 37° , dip = 45° , rake = -107°
(auxiliary plane: strike = 240° , dip = 47° , rake = -74°)
(Dimitriadis et al. (2009), residuals unknown)

Average solutions are relatively similar, although calculated using different techniques (AUTH: P-wave polarity readings and P-/S-coda amplitude ratio) and different data sets.

<i>lat.</i> [°]	<i>lon.</i> [°]	<i>z</i> [km]	<i>date</i>	<i>time</i>	<i>strike</i> [°]	<i>dip</i> [°]	<i>rake</i> [°]	M_w	<i>DC</i> [%]
36.5215	25.4551	9.2	2006.07.28	12:11:14.5	272.01	25.08	-76.77	3.8	77
36.5190	25.4403	11.1	2006.07.28	12:24:29.4	270.57	34.65	-52.94	3.9	73
36.5080	25.4484	11.1	2006.07.28	12:26:48.0	254.74	41.63	-47.28	3.9	91
36.6292	25.6933	9.4	2006.08.24	09:28:25.4	196.83	52.79	-130.92	3.4	73
36.5018	25.4797	13.2	2006.09.03	15:34:29.3	210.90	43.46	-85.10	3.6	40
36.5358	25.4648	10.7	2006.09.27	01:23:24.4	293.71	5.37	-49.30	3.6	49
36.5378	25.5650	6.9	2006.10.11	20:33:21.0	185.86	19.35	-112.31	3.9	67
36.5404	25.4941	8.7	2006.10.22	20:48:52.2	267.59	58.14	-54.98	3.7	95
36.5423	25.4880	9.0	2006.10.22	20:50:04.2	275.28	62.47	-49.44	3.6	52
36.5092	25.4724	8.6	2006.11.11	11:26:45.6	254.33	57.65	-35.74	3.8	92
36.5082	25.4818	6.4	2006.11.13	08:04:24.2	184.34	6.90	-105.49	3.8	65
36.5088	25.4808	7.1	2006.11.13	08:49:50.7	270.15	19.20	-66.44	4.1	88
36.5201	25.4817	7.9	2006.11.14	12:42:33.9	306.60	26.86	-28.82	3.9	81
36.5213	25.4848	7.8	2006.11.14	12:45:29.7	197.25	33.03	-146.52	3.7	73
36.5358	25.4648	8.5	2006.12.06	10:24:37.9	179.31	51.72	-97.57	3.2	34
36.6559	25.5669	8.8	2007.01.10	17:22:16.4	214.96	42.51	-43.37	3.6	74
36.5315	25.4676	7.9	2007.02.18	17:23:34.1	260.45	39.72	-26.23	3.8	30
36.6109	25.5910	8.4	2007.02.26	13:24:51.1	179.87	29.02	-178.52	3.4	82
36.5176	25.4798	8.3	2007.03.01	11:48:25.4	305.04	45.86	-146.70	3.7	63
36.5190	25.4731	8.4	2007.03.01	11:48:42.7	328.86	17.42	-144.12	4.1	35
36.5230	25.4772	7.9	2007.03.01	11:53:41.2	225.27	52.37	-132.73	3.6	60
36.5107	25.4943	7.7	2007.03.01	12:46:15.6	160.12	11.82	-116.32	3.2	82
36.4900	25.4176	13.9	2006.07.12	11:50:01.5	224.64	49.51	-54.90	3.1	62
36.5097	25.4130	13.8	2006.07.22	11:22:31.5	353.93	80.57	-72.13	3.1	74
36.5296	25.4615	8.5	2006.07.28	15:48:22.3	182.75	44.75	-105.94	3.2	18
36.6280	25.6949	9.6	2006.08.07	18:47:30.7	240.61	69.91	-59.82	2.9	19
36.6747	25.6310	10.6	2006.08.08	03:38:34.5	299.47	37.89	-157.87	2.8	47
36.4499	25.5007	10.2	2006.09.26	06:19:49.9	251.07	69.13	-66.06	2.9	58
36.5057	25.4799	11.1	2006.09.27	22:48:30.0	189.96	76.97	-111.01	3.0	85
36.5373	25.4996	7.9	2006.10.11	09:57:53.9	188.13	88.70	-102.12	2.8	97
36.5100	25.4848	8.4	2006.10.16	17:19:05.9	224.93	59.07	-116.29	2.7	38
36.5231	25.4522	9.8	2006.11.01	07:33:41.1	248.09	5.56	-87.36	3.2	55
36.5045	25.4828	9.0	2006.11.01	22:20:58.0	266.83	66.45	-57.61	3.3	51
36.5077	25.4874	8.9	2006.11.01	23:10:48.9	231.16	26.88	-92.04	3.2	33
36.5200	25.4726	8.2	2006.11.09	09:13:37.4	202.13	62.53	-91.55	3.4	51
36.5019	25.4789	8.8	2006.11.20	02:20:50.5	199.79	81.76	-98.44	3.1	58
36.5283	25.4505	7.3	2006.12.06	10:34:06.0	175.88	55.09	-132.41	3.0	79
36.5223	25.5004	10.4	2006.12.09	20:23:21.2	279.07	74.28	-54.27	3.2	57
36.6149	25.6019	6.6	2007.01.11	16:13:30.9	352.14	33.09	-101.17	2.9	74
36.5228	25.5045	8.9	2007.02.18	04:38:30.4	235.43	47.77	-75.98	3.0	40
36.6107	25.5914	7.7	2007.02.26	15:45:01.0	223.29	31.31	-62.94	2.9	55
36.6096	25.5912	7.3	2007.02.26	15:58:01.8	192.65	25.72	-163.90	2.7	96
36.6080	25.5936	7.7	2007.02.26	23:29:43.1	258.77	52.18	-98.23	3.1	82
36.6070	25.5910	7.7	2007.02.26	23:34:05.9	296.35	36.84	20.95	3.3	95
36.5207	25.4575	9.3	2007.03.01	11:47:03.9	246.56	50.53	-84.42	2.8	33

Table 5.3: **List of Moment Tensor solutions** Events in the upper part of the table have been inverted with MTI and cross-checked with FOCMEC, events in the lower part of the table are only inverted with MTI, their polarization is estimated based on crosschecked solutions. Detailed fit-, misfit- and focal-mechanism-plots for each event are listed in App. E.

5.2.2 Stress inversion

The stress tensor was inverted from slip vector data of our focal mechanisms with the approach of Dahm and Plenefisch (2001), for a detailed description see Reinhardt (2007). For given stress vectors $[\Phi_k, \delta_k, \lambda_k]$ with $k = 1, \dots, K$ with $K =$ number of focal mechanisms, the average homogeneous stress tensor in form of its three principal stress axes σ_1 , σ_2 and σ_3 and its shape ratio $R = \frac{\sigma_1 - \sigma_2}{\sigma_1 - \sigma_3} = 0.43 \pm 0.16$ is estimated.

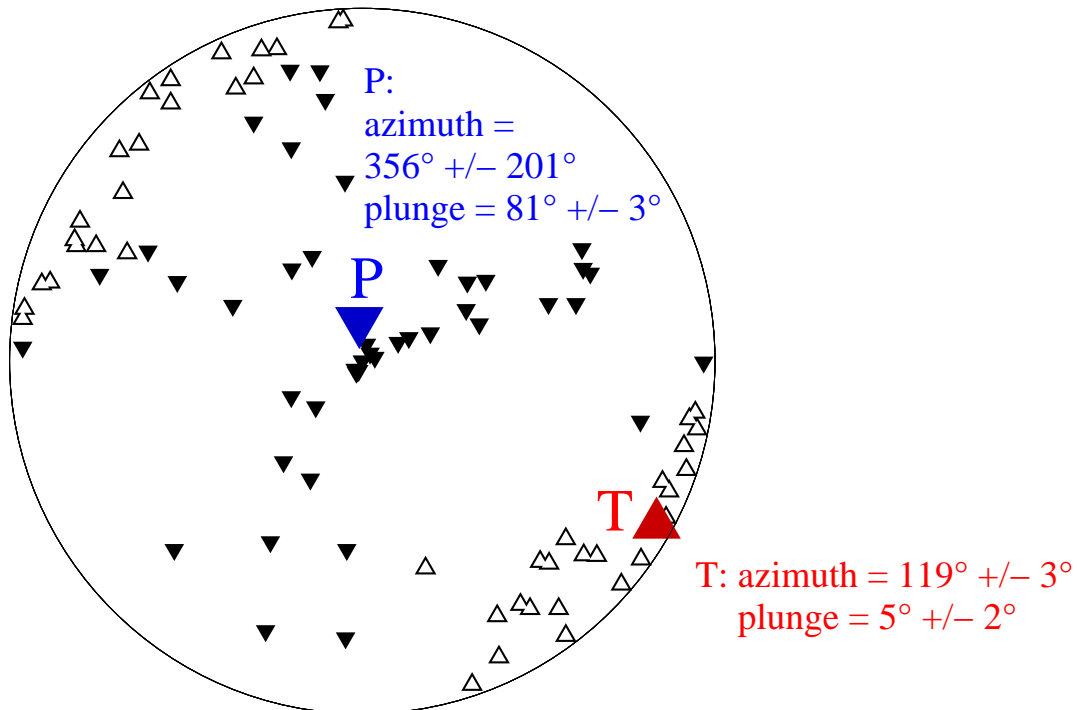


Figure 5.14: **Result plot of stress inversion** The stress inversion was started using 10 events with $M_L > 3.5$ to derive a starting model and then including all other events for which a focal mechanism has been estimated. Inverse triangles mark P-axes (pressure), black for each single event, large and blue for the average P-axis derived by the stress inversion, inverse triangles mark T-Axes (tension), white for each single event, large end red for the average T-axis. P-axes scatter more than T-axes, which reflects the larger stability of the σ_3 axis (see stabilities of single moment tensor solutions in App. E)

Azimuth and plunge angles for all inverted focal mechanisms and the according average angles are given in Fig. 5.14. It is obvious, that the T-axes (tension) are more stable than the scattering P-axes (pressure). This is the effect of the regional extensional stress field, where σ_3 is regionally very stable, but σ_1 is unstable due to local stress perturbations caused by volcanotectonic processes, possible reactivation of existing faults and the generally inhomogeneous structure at Columbo.

The estimated stress tensor fits well with the entry of the World Stress Map (WSM) for

this region. Based on focal mechanisms of the 1956 earthquakes at the Santorini-Amorgos-Fault (Kiritzi and Louvari, 2003), the WSM expects a T-axis of azimuth 335° and plunge 5° (Heidbach et al., 2008). This corresponds to a horizontal tension axis of $155^\circ / 335^\circ$ according to WSM and $119^\circ / 299^\circ$ according to our stress inversion. The difference between the azimuth angles of 36° can be explained by the eastward bending of the Santorini-Amorgos Fault north of Columbo.

METHODS AND RESULTS 2 CLUSTER AND DEFORMATION ANALYSIS

In this chapter I summarize my investigation of cluster migration during earthquake swarms and the analysis of deformation data, i.e. tilt and absolute pressure data. In the first section the determination of different migration velocities is explained and all found velocities of all swarms during our experiment are listed. The second section describes the analysis of deformation data in detail. It includes the re-orientation of the freefall instruments, the removal of leveling gaps and a final summary of all found tilt and absolute pressure signals.

6.1 Analysis of earthquake swarms

6.1.1 Estimation of cluster migration velocities

Earthquake swarms beneath Columbo often stretch over an extended depth interval, aligned on a vertical plane. When plotting the source times of the relocated events versus depth (depth-time- or z -time-distribution), possible depth migrations of single events, clusters of events (centroids) or of a ceasing front of events (backfront) can be identified. We analyzed event densities with a spatial grid interval of 20 m and a temporal grid interval of $\frac{1}{500}$ of the swarm length. The grid was smoothed out by overlapping depth-time windows over the three previous and three following intervals.

Fig. 6.1 shows the depth-time distribution (A) and its gridded event density (B) of the earthquake swarm on 28th of July 2006 which occurred at the south-western flank of Columbo seamount. Migration velocities can be estimated from linear approximations of seismic fronts (see Hensch et al., 2008):

- **The initial fast front v_{IF}** : Visual estimation of the forefront of seismicity. Error limits are the maximum and minimum velocity (see dotted lines in Fig. 6.1)

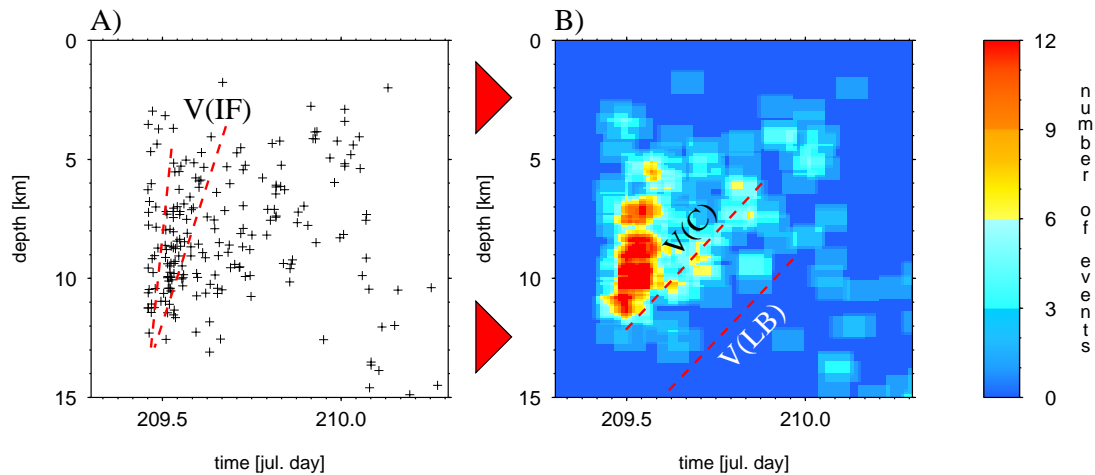


Figure 6.1: A) Depth-time distribution of an earthquake swarm on 28th of July 2006 at the south-western flank of Columbo.

B) Event densities in a zt-plot. Slopes of possible linear fronts and backfronts are marked: $v(\text{IF})$ is declared as the initial fast front, $v(\text{C})$ as the main cluster velocity and $v(\text{LB})$ as the velocity of the backfront (lower boundary of the earthquake swarm).

- **The velocity of the main cluster (centroid) v_c** : Fitting of time-dependent depth of the clusters to Gaussian curves is used to estimate the centroid migration and its width (standard deviation)
- **The backfront velocity (lower boundary of the earthquake swarm) v_{LB}** : Crude estimation of the lower boundary of the seismic active region in a, event-density- or zt-distribution

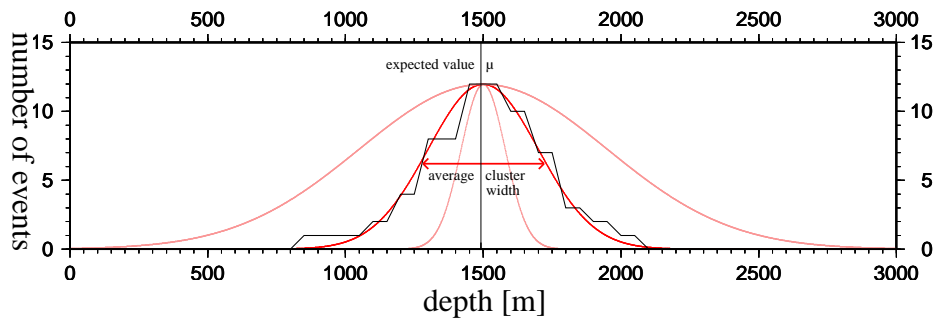


Figure 6.2: Example of centroid depth estimation. The earthquake depth histogram (black line) of a chosen time window is approximated by Gaussian curves (sampled with grid search approach, red line: best fit, pink lines: other cluster widths). In the example, the depth of the cluster is estimated at 1.5 km depth, the average cluster width is found at 240 m (from Hensch, 2005).

To estimate the centroid (depth) of a cluster, histograms (number of event within a fixed time-window over the depth) were calculated, which due to the smoothing often have a crude shape of a normal distribution with a single peak (expected value μ) and can be fitted to a Gaussian curve

$$f(x) = \frac{a}{\Delta t} \cdot \frac{1}{\sigma\sqrt{2\pi}} e^{-\frac{1}{2}\left(\frac{x-\mu}{\sigma}\right)^2}, \quad (6.1)$$

where μ is the depth of the cluster centroid, σ the cluster width and $a/\Delta t$ defines the strength (number of events) normalized by the time window. Thus, by minimizing its residuals, this curve can be fitted to the event histogram and cluster widths can be estimated (see Fig. 6.2). If one assumes that all events of a cluster occurred only at a single depth and any scatter was caused by depth errors from location, the width of the cluster would give a crude estimation of the standard deviation of the cluster.

Handling of this method is partly tricky, especially when clusters are located temporally or spatially close to each other: Parameters like μ or the depth interval of the cluster had to be precisely chosen to find a unique minimum. Standard deviation indeed represents residuals of the relocated clusters, but is not calculated orthogonal to the migration path and thus is biased to larger values, especially for fast ascending clusters. Anyway, estimated cluster widths are in a plausible and expected range. More examples and details are given in Hensch (2005).

The three migration fronts were found for several swarms, especially for swarms of short duration ($< 2 \text{ days}$). An average velocity was estimated by picking the starting and final depth and duration of each cluster.

6.1.2 Results for cluster migration velocities at Columbo

Earthquake swarms run through different phases of activity. As already discussed in Hensch et al. (2008) for earthquake swarms in Iceland, we observed two kinds of earthquake swarms: Swarms of short duration ($< 24 \text{ h}$) and swarms of longer duration ($> 48 \text{ h}$ and up to a week).

At Columbo, 6 earthquake swarms were observed during our experiment (for locations see Fig. 6.11), one additional swarm in the region south-west of Anidros island was also detected, but was lying too far outside our OBS/OBT network and therefor not investigated in terms of deformation. Of the 6 swarms at Columbo, 4 were classified as of short duration and 2 of longer duration. From here on we adapt the following nomenclature for the observed swarms (*C* for Columbo, *A* for Anidros, *S* for short and *L* for longer duration):

Swarms of short duration:

- CS-1: 28th - 29th of July 2006
south-western flank of Columbo, 19 hours
- CS-2: 10th - 11th of January 2007
north-eastern flank of Columbo, 22.5 hours
- CS-3: 18th of February 2007
eastern flank of Columbo, main swarm 2.5 hours plus 20 hours unrest
- CS-4: 1st of March 2007
inside the Columbo caldera, 28 hours

Swarms of longer duration:

- CL-1: 23rd of September - 1st of October 2006
Columbo caldera, south-eastern, southern and western flanks, 175 hours
- CL-2: 10th of January 2007
from Columbo caldera along the volcanic belt in direction of Anidros (north-west of Columbo), 48.5 hours

Other swarms:

- AS-1: 26th of February 2007
south-west of Anidros island (12 km north east of Columbo), 11.5 hours

Most short swarms can be subdivided in typical phases of activity and associated migration velocities:

- Most events occur within a first phase of strongest activity. This phase includes the fastest migration velocities v_{IF} ("initial fast seismicity front") and is typically only a few hours long. At the end of this phase, a second front characterized by the "main cluster velocity" v_C - in case it can be detected - is observed to begin ascending in the deeper part of the cluster. $v_c \ll v_{IF}$ and in the range of cm/s .
- Activity decreases rapidly and is less energetic during the second phase of the swarm. Most activity is then concentrated in the center of the main cluster. During this phase, the backfront of seismicity, characterized by the "lower boundary velocity" v_{LB} , becomes observable for most swarms. This velocity is often similar to or slightly faster than v_C .

<i>swarm</i>	<i>type</i>	$\Delta z[m] \pm 500m$	$\Delta t[s] \pm 1.800s$	$v[\frac{cm}{s}]$	$\sigma_v[\frac{cm}{s}]$
Jul. 28th, 2006 CS-1	$v_{IF}(1)$	9.000	12.600	70	± 30
	$v_{IF}(2)$	10.000	3.600	280	± 140
	$v_{MC}(1)$	4.000	14.400	28	± 5
	$v_{MC}(2)$	6.000	37.800	16	± 1.5
	v_{LB}	5.500	28.800	19	± 2
Sep. 21st - 30th, 2006 CL-1	$v_{intF}(1)$	-16.500	52.200	-32	± 2
	$v_{intF}(2)$	12.300	25.200	50	± 4
	$v_{MC}(1)$	1.900	396.900	0.5	± 0.2
	$v_{MC}(2)$	2.000	155.500	1.3	± 0.3
	v_{LB}	not observed	not observed	$(v_{LB} = v_{MC}?)$	-
Dec. 6 - 8th, 2006 CL-2	v_{IF}	not observed	not observed	-	-
	$v_{MC}(1)$	-3.200	41.400	-7.8	± 1.5
	$v_{MC}(2)$	2.800	66.600	4	± 0.8
	$v_{MC}(3)$	6.000	79.200	8	± 2
	v_{LB}	not observed	not observed	-	-
Jan. 9th, 2007 CS-2	v_{IF}	4.000	5.400	74	± 3
	$v_{MC}(1)$	2.750	38.900	7.1	± 1.3
	$v_{MC}(2)$	1.200	30.200	4.0	± 1.7
	v_{LB}	1.500	14.400	10.4	
Feb. 18th, 2007 CS-3	$v_{IF}(?)$	5.000	7.200	70	± 15
	$v_{MC}(1)$	1.300	7.200	21	± 8
	$v_{MC}(2)$	600	3.600	20	± 15
	v_{LB}	not observed	not observed	-	-
Mar. 1st, 2007 CS-4	v_{IF}	6.000	9.000	67	± 14
	$v_{MC}(1)$	1.800	9.000	20	± 7
	$v_{MC}(2)$	-1.000	41.400	-2.5	± 1.3
	$v_{LB}(1)$	3.200	21.600	15	± 3
	$v_{LB}(2)$	4.500	27.000	17	± 2

Table 6.1: **List of all migration velocities** v_{IF} = initial fast velocity, (v_{intF} = intern fast velocity for the CL-1 swarms), v_{MC} = velocity of main cluster, v_{LB} = velocity of the z -distribution's lower boundary, Δt = duration of migration, Δz = relative depth range of migration, $v = \frac{\Delta z}{\Delta t}$. Residuals of parameters are estimated as $\pm 500 m$ for depth and $\pm 1.800 s$ for time. A negative migration velocity means a descent of the cluster.

- For some swarms, a third phase of scattered seismicity can be observed. Occurrence rates decrease further and no migration is observed (see e.g. CS-1 swarm at 210.0 Jul. days and later, Fig. 6.3).

For longer lasting swarms and the AS-1 swarm near Anidros island, these phases were not found. Longer lasting swarms do not show specific patterns of which migration velocities can directly be concluded. Although the CL-1 swarm includes two faster migration paths in the 2nd half of its duration, there does not seem to be a systematic and repeated pattern. Table 6.1 is an overview of all migration velocities that were observed during the Columbo experiment. Most of the slopes of fronts and backfronts are positive, which means that clusters

are ascending. Horizontal or downward migrations are rare and of much smaller scale (see latitude and longitude over time plots in App. D), they were not systematically investigated.

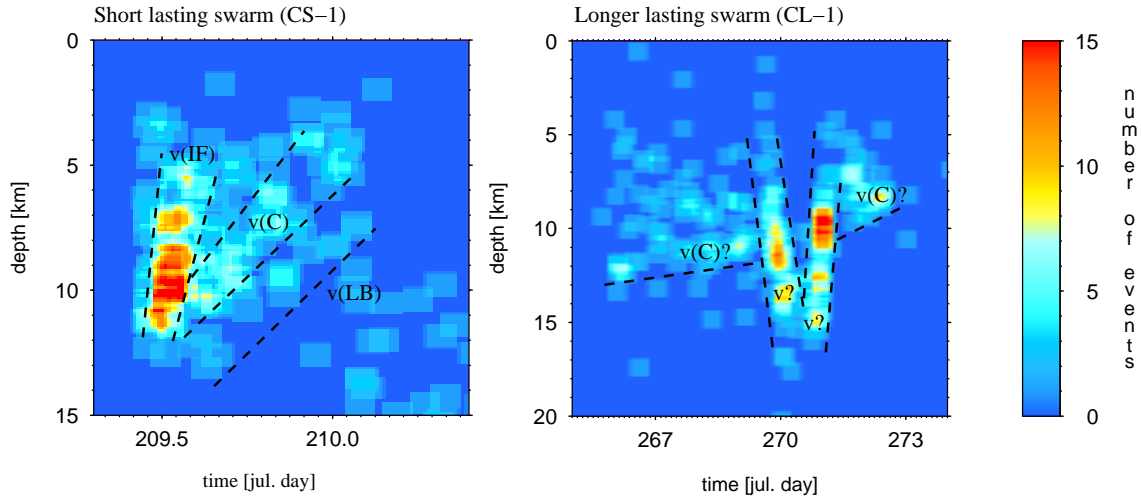


Figure 6.3: **Example of migration velocities for both swarm types:** Depth-time (zt) distributions of a short lasting swarm (CS-1) with its typical three types of migration velocities and in comparison a longer lasting swarm (CL-1), that shows 2 fast migration paths, but not as usual during its initial phase, and a possible main cluster. All observable velocities, independent whether they were explainable or not, are listed in Tab. 6.1.

Two examples, depth-time (zt) distributions for each type of earthquake swarm, are given in Fig. 6.3. The short lasting swarm in this example (CS-1) shows the typical three types of seismicity fronts as described above: A fast front during its initial phase and a slower front and backfront for the period of about 12 hours.

Systematic plots, spatial and temporal distributions of all earthquake swarms are given in Appendix D.

6.2 Additional findings

6.2.1 Further swarm parameters

Tab. 6.2 gives an overview on further swarm parameters, such as orientation of the best fitting plane through the hypocenter distribution and the swarm duration. All investigated earthquake swarms have best fitting planes striking in NE direction, i.e. crudely perpendicular to the smallest principle stress axis σ_3 .

<i>swarm</i>	<i>duration [h]</i>	<i>strike and dip of the best fitting plane [°]</i>
CS-1	19	N62E / 85
CS-2	22.5	N41E / 76
CS-3	2.5 + 20	N33E / 79
CS-4	28	N48E / 51
AS-1	11.5	N28E / -74
CL-1	175	N60.5E / 59
CL-2	48.5	N37E / -79

Table 6.2: **List of further swarm parameters:** Duration of the seismic crisis and best fitting planes. The separation in two types of swarm, short and long lasting, is obvious. The best fitting plane was calculated with a least squares method searching the minimum of the distances to a plane laid through the scattered hypocenter distribution.

6.2.2 Magnitude distribution

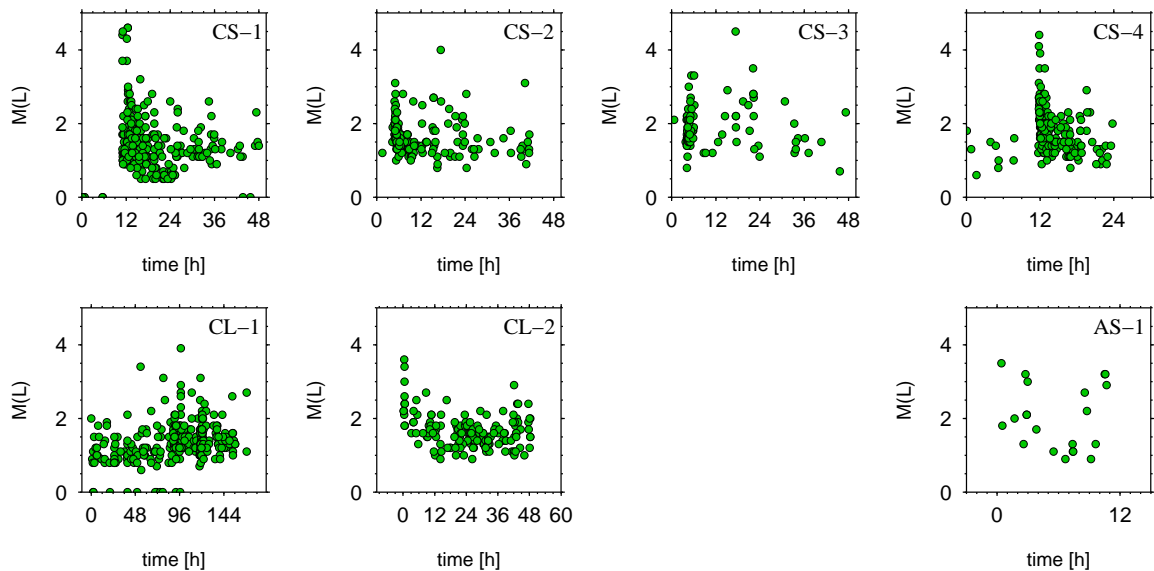


Figure 6.4: **Magnitude-time distribution for all earthquake swarms.** For most swarms, the intensity of its events increases rapidly up to highest magnitudes which are mostly observed during the first 25% of the swarm duration. Afterwards, intensity and number of events slowly decrease. The start of the time scale does not represent the actual beginning of the swarm.

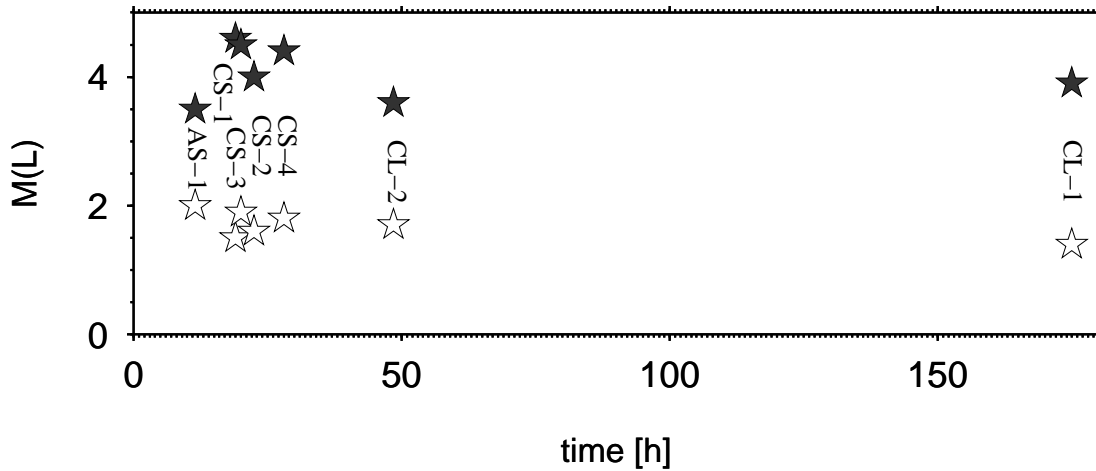


Figure 6.5: Time dependence of average (white stars) and maximum (grey stars) magnitudes: There is no obvious relation between intensity and swarm length found.

The magnitude distribution over time (Fig. 6.4) for most swarms show their maxima within the first quarter of the swarm duration. After the maximum, the number of aftershocks decreases slightly, but not as typically predicted by Omori's law ($\sim \frac{1}{t}$ Lay and Wallace, 1995) for a mainshock-aftershock sequence, mostly more linear. There also seems to be no correlation between the maximum magnitude and the swarm duration (Fig. 6.5), what would also be predicted for a tectonic sequence following Omori's law.

6.2.3 Activation of adjacent faults

The possible activation of adjacent faults was observed for two swarms: The CL-2 swarm of longer duration and the short CS-4 swarm (Fig. 6.6). While for the CL-2 swarm many events on a fault west of the cluster and possibly even a ringfault south-east of the cluster were found, the activation of the fault west of the CS-4 cluster (dotted ring in Fig. 6.6) started suddenly during this swarm. The activity more or less jumped from the main- to this sub-cluster.

If the swarms were dike-induced, theoretical models of Rubin and Gillard (1998a) predict stress increase in σ_3 direction. If the former σ_3 axes became the strongest principal stress axis, then the former σ_1 would be reduced to σ_2 , former σ_2 to σ_3 . This would result in a flip of the fault plane solution on the activated fault from expected normal faulting to strike slip faulting is expected (Roman et al., 2006).

When comparing faults found here with focal mechanisms given in the swarm synopsis (App. D), these events were too weak to invert more than a few for a reliable moment tensor. And these few are rather normal faulting events than strike-slip faulting.

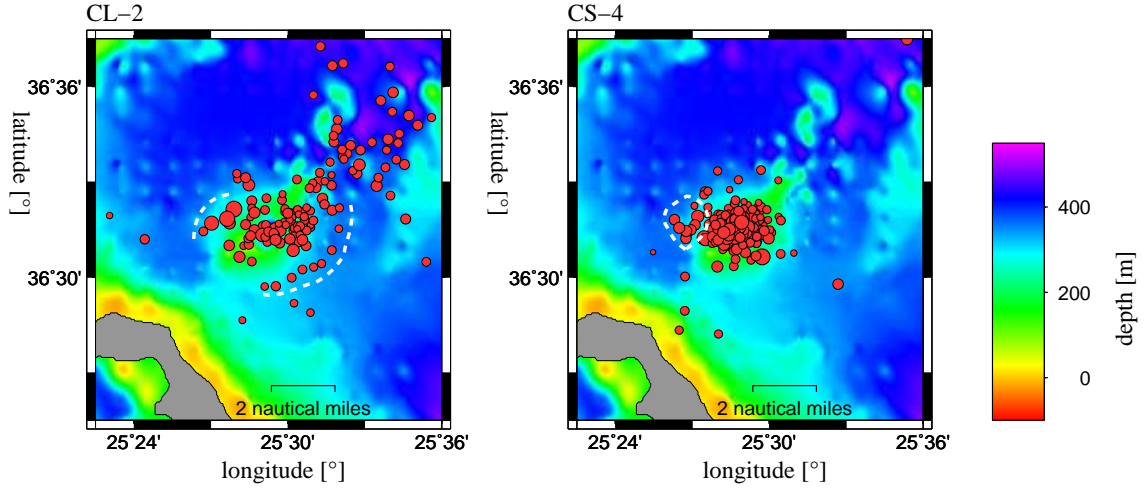


Figure 6.6: **Activation of adjacent faults.** Sudden activity on adjacent faults (dotted lines, dotted ring) was observed for a short and a long lasting swarm. For the case of the long lasting CL-2 swarm, even the activation of a ringfault may be assumed.

6.3 Analysis of deformation data

One focus of this work was to collect tilt and absolute pressure data at the seafloor. As the tilt device was developed in-house and deployed for the first time to observe longterm tilt, the processing of the data is explained in detail in this section.

6.3.1 Re-orientation of freefall tiltmeters

The Hamburg OBT system is a freefall instrument and thus the two components of the tiltmeter have to be rotated such that they are aligned NS and EW. Unfortunately, electronic and mechanic compasses failed because of a large disturbance due to the anchor weight and other metallic parts of the OBS/OBT frame.

After different trials to extract the sensor orientations from earthquake data and noise, we finally used a method similar to the seismic data correlation, described in section 5.1.3. Longperiod surface waves of strong teleseismic earthquakes were taken to correlate the 2D horizontal particle motion (N and E components) of the same surface wave train f at two different stations p and q , an OBS/OBT and a near land seismometer with known orientation. Equation 6.2 was used. While now the traces of the offshore station are kept stable, the onshore traces are rotated in 1° steps and correlated with the OBS/OBT for each step.

$$cc_{pq}^f(N, E) = \frac{\Phi_{pq}^f(\tau_{pq,max}^f)^N + \Phi_{pq}^f(\tau_{pq,max}^f)^E}{\sqrt{(\Phi_{pp}^{N(f)} + \Phi_{pp}^{E(f)}) \cdot (\Phi_{qq}^{N(f)} + \Phi_{qq}^{E(f)})}} \quad (6.2)$$

The correlation coefficient is supposed to derive its maximum, when the rotated data traces are orientated parallel and in phase with those of the reference sensor. An example for the

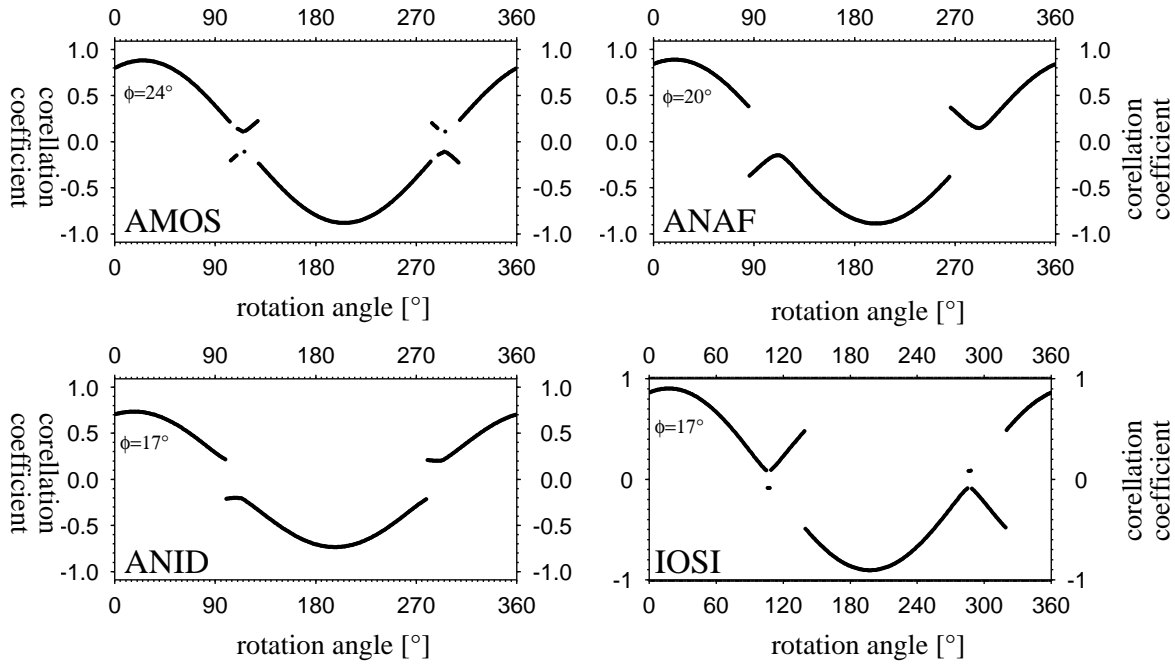


Figure 6.7: Correlation coefficients between OBT 54 and near land stations AMOS, ANAF, ANID and IOSI (see Fig. 2.1). Re-orientation of OBSs/OBTs using surface wave correlation. Correct orientation is assumed at the curve's maximum. The curve becomes unstable for small positive and negative correlation coefficients, since a random correlation can be found for every time series and thus a correlation of 0 is nearly impossible.

distribution of the correlation coefficients over the orientation ($0^\circ - 360^\circ$) is given in Fig. 6.7. Time delays $\Delta\tau$ between the signals were in the range of a few seconds, corresponding to the relative differential epicentral distance Δx and typical surface wave velocities $v_{surface}$.

For each Ocean-Bottom-Station, this procedure was performed for the five closest onshore seismometers (AMOS, ANAF, ANID, IOSI and NEAK) and the two strongest teleseismic events that occurred during the experiment [*source: www.gfz-potsdam.de/geofon/*]:

- 15th of November 2006, 11:14:21 UTC, $M = 8.3$, $46.51^\circ N$, $153.47^\circ E$, 76 km depth, Kuril Islands (SW of Kamtschatka, Russia)
- 21st of January 2007, 11:27:49 UTC, $M = 7.6$, $1.16^\circ N$, $126.36^\circ E$, 63 km depth, Northern Molucca Sea (NE of Sulawesi, Indonesia)

Within the 35 days where OBT56 was running, no teleseismic event generated surface waves of sufficient low frequencies to credibly investigate the instrument's orientation.

Tab. 6.3 summarizes azimuthal angles, by which the OBSs/OBTs have to be clockwise rotated for re-orientation. In some cases, we found a phase-reversal of 180° , but for 6 out of 7 cases, one direction is dominant (at least 70 % of all found values). For OBS52, results scatter extremely due to a malfunction of the instrument's E-component. Fig. 6.8 illustrates

<i>OB:</i>	<i>AMOS</i>	<i>ANAF</i>	<i>ANID</i>	<i>IOSI</i>	<i>NEAK</i>	<i>Average</i>
50	43°/41°	39°/(220°)	36°/33°	(216°)/(215°)	42°/41°	39° ± 4°
51	173°/171°	167°/174°	163°/162°	(342°)/(340°)	167°/173°	169° ± 4°
52	267°/291°	272°/(81°)	(71°)/(89°)	264°/298°	(42°)/336°	(288° ± 25°)
53	(138°)/339°	(133°)/(145°)	307°/334°	319°/333°	(129°)/333°	328° ± 11°
54	24°/7°	20°/17°	17°/(186°)	17°/2°	24°/19°	16° ± 6°
55	128°/117°	124°/121°	122°/(290°)	120°/113°	127°/131°	122° ± 5°
57	206°/195°	201°/198°	195°/(12°)	198°/189°	204°/207°	199° ± 6°

Table 6.3: Angles for which the azimuth angle of ocean bottom stations has to be corrected (clockwise rotation).

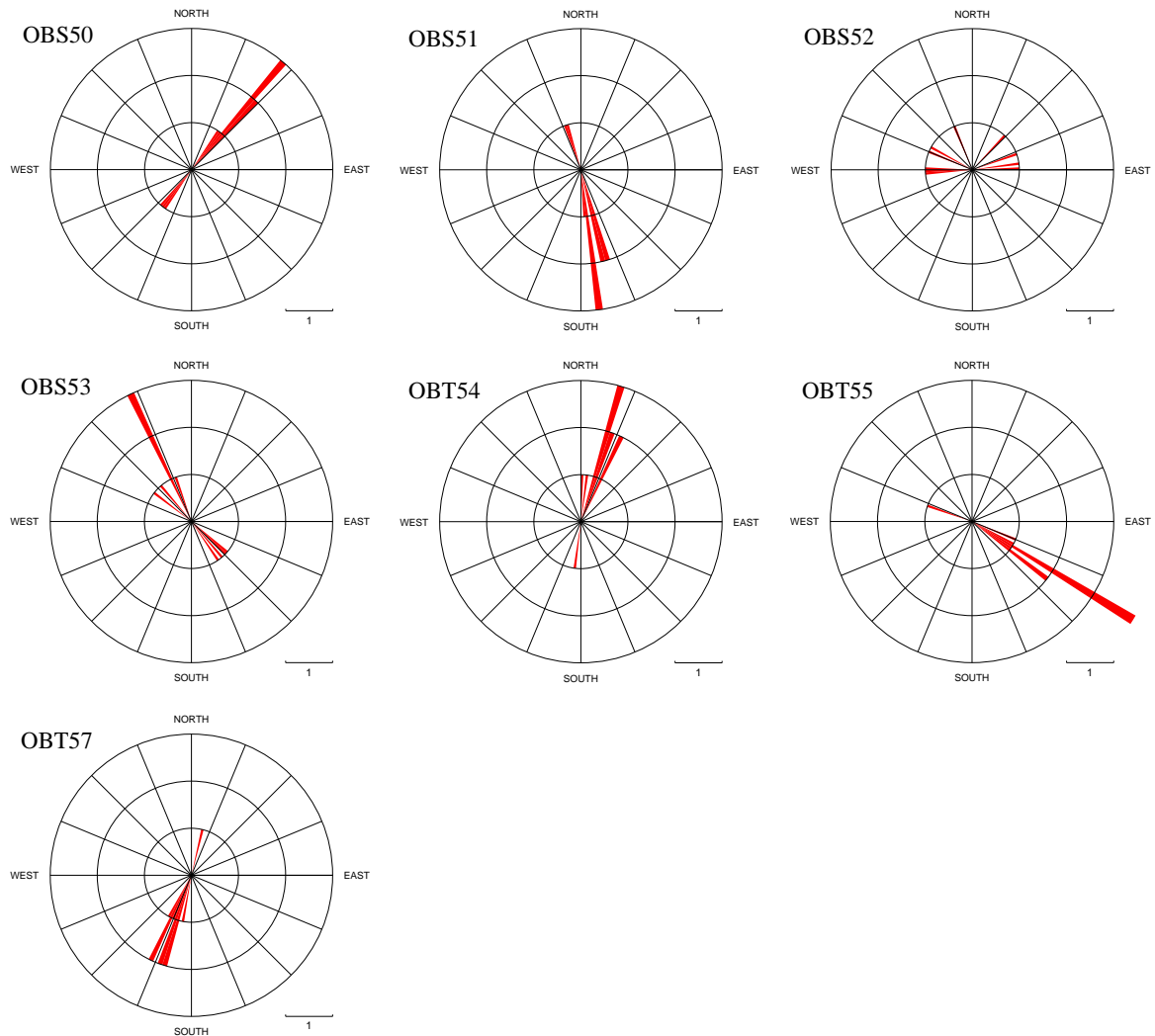


Figure 6.8: **Re-orientation of OBS/OBT stations.** Rosediagrams show maximum correlation results (see Tab. 6.3). Instabilities of the routine in terms of phase reversal are rare (maximum 30 %). Except for OBS52 (bug of E-component) and OBT56 (too short recording period), an orientation is found with an accuracy of mostly about $\pm 5^\circ$ for each offshore station.

the results of Tab. 6.3 in rose diagrams. We estimate the accuracy of the method in the range of $5 - 10^\circ$.

6.3.2 Removal of levelling- and high frequency jumps

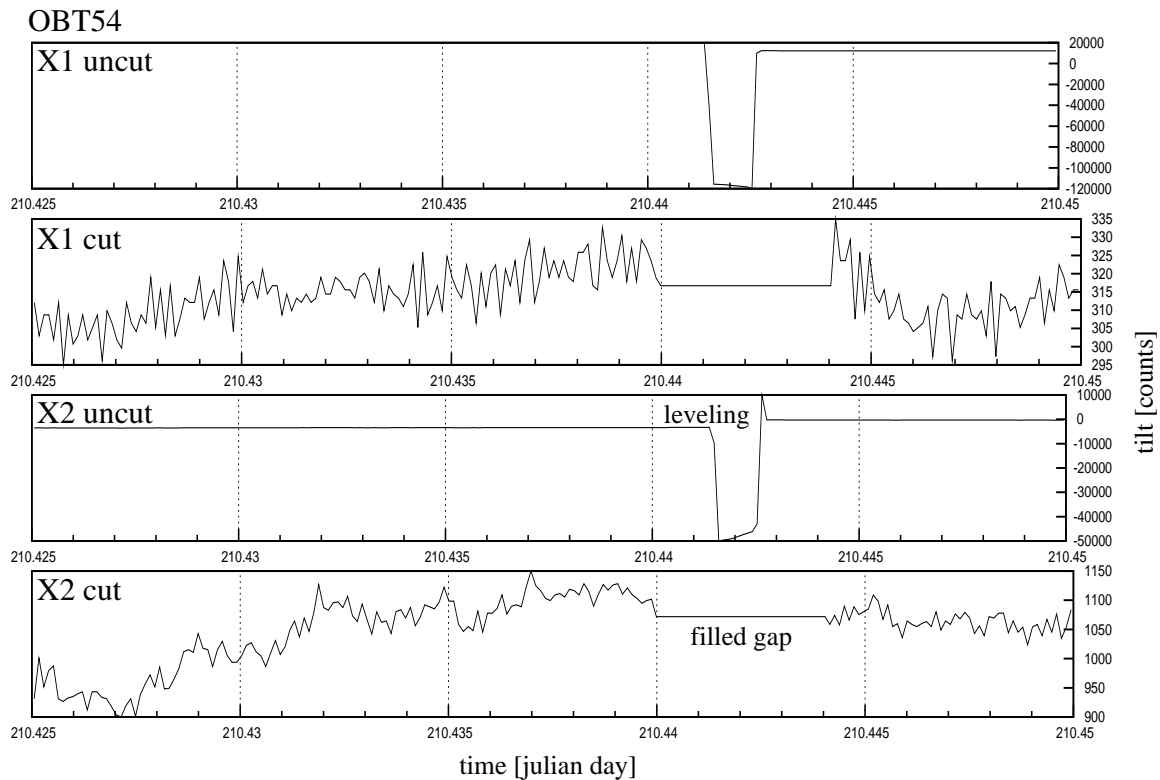


Figure 6.9: **Example for the removal of a levelling event on OBT 54**

The cut off sequence is filled with the average value of the prior 100 samples. When comparing amplitudes of the levelling events (>12.000 counts which is according to more than $170 \mu rad$) with the noise amplitude (around 100 counts or $1.5 \mu rad$), the necessity of this procedure becomes clear.

To analyze tilt trends and signals of longer period, steps in the time traces, such as due to levelling events or static tilt accompanying stronger earthquakes, have to be removed from the continuous data. For that, we developed a program to replace the removed data with average values and to compensate for the removed offset in the rest of the time series. Start and end time of the window to be corrected are patched, assuming a continuous average trend. 100 samples before the start time and 100 samples afterwards the end time (500 s each) are taken to calculate two average values. The difference between first and second average is then subtracted from the complete time series following the removed data in order to compensate the step. The gap which is usually very small (500 s for levelling) is then filled with the average of the previous 100 samples.

Although this constant interpolation interrupts a possible linear tilt trend, data gaps are in the range of some minutes and can be neglected when investigating longer trends of several hours or days. Fig. 6.9 shows the correction of a levelling event for both traces of a tiltmeter, Fig. 6.10 shows the removal of jumps due to a sequence of stronger ($M_L > 4$) earthquakes during an earthquake swarm.

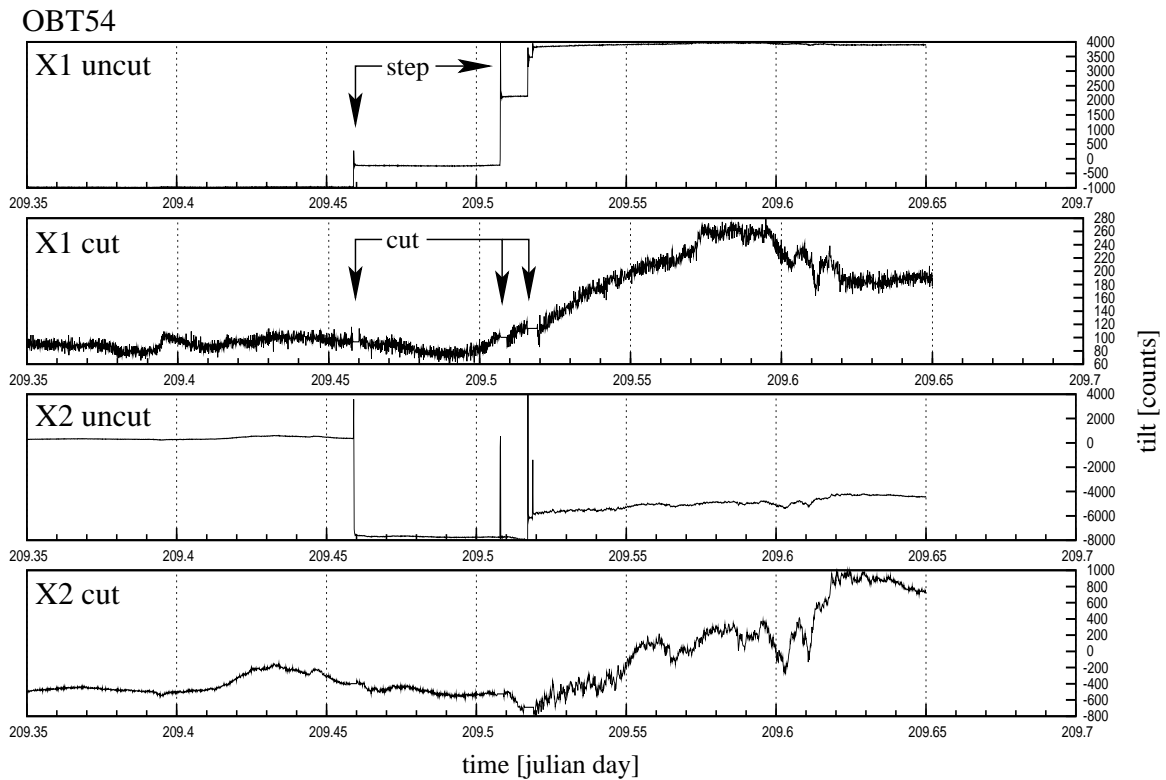


Figure 6.10: **Correction example for a jump due to an earthquake on OBT 54**

Relatively similar to the previous plot, this example shows, how the continuing trace after a cut off sequence is readjusted to the time series by subtracting the difference between the prior and the subsequent average from the following part of the trace.

To save processing time, time series were resampled to a sampling rate of 10 *s* or 0.1 *Hz*. All leveling events (every 48 hours at exactly the same time) and all jumps due to earthquakes or other influences, as far as they were clearly separated from noise and if they have been occurring within a few samples, were corrected. Steps occurring over more than about 5 samples have only been corrected if the period was of special interest. We assumed that longer tilt excursions are caused by creeping processes and are not related to elastic near-field terms or ground shaking from earthquakes.

6.3.3 Results of tilt measurements

Once the tilt traces are resampled at 0.1 *Hz* and re-orientated, the observed signals have to be regarded in three scales:

- short period signals (sudden steps)
- intermediate period tilt transients (hours to days)
- global trends (weeks to months)

Short period signals

Sudden steps or jumps in the tilt traces have been shown to be clearly related to strong and near earthquakes. These steps mostly occurred parallel to the S- or surface waves. In Chapter 4.2 (Source Theory), the simulation of rectangular shear faults, associated with the strongest observed magnitude at Columbo ($M_L = 4.6$), showed that elastic near-field steps could be measured either on our OBTs or on absolute pressure sensors. The amplitude measured for sudden steps is partly that large, that this signal can only be caused by an anelastic local tilting of the sensor or station, induced by ground shaking. We can not answer whether this local effect was a tilt of the complete OBS/OBT frame, or a displacement of the sensor platform within the glass sphere, which would also end in a static tilt signal. The fact that a tilt-typical signal has also been found on the seismic sensors of the ocean bottom stations suggests, that the complete frame is displaced and tilted during strong ground motions. Seismometers are mounted in a similar sphere, but passively leveled by being immersed in high-viscous oil. It is highly unlikely that the seismometer itself gets tilted that quick within this oil-bath.

Thus, sudden steps of high amplitudes are suggested to be caused by a constructional deficiency of our OBS carrier system, or by one-sided compaction of the mushy seafloor. High frequent steps will not further be discussed in this work, unless their origin has not been clarified.

Intermediate period tilt transients

Intermediate period signals, i.e. deformation signals of a period of hours to a few days, that occur during or slightly before or after an earthquake swarm are prime suspects to be linked to seismic activity or its cause. In case of fluid induced earthquake swarms, correlation with a possible volume source, e.g. a dike, is probable.

An overview on potential sources, i.e. all earthquake swarms and three other possible sources of deformation (caldera, reef and the elevated region between Columbo and Santorini)

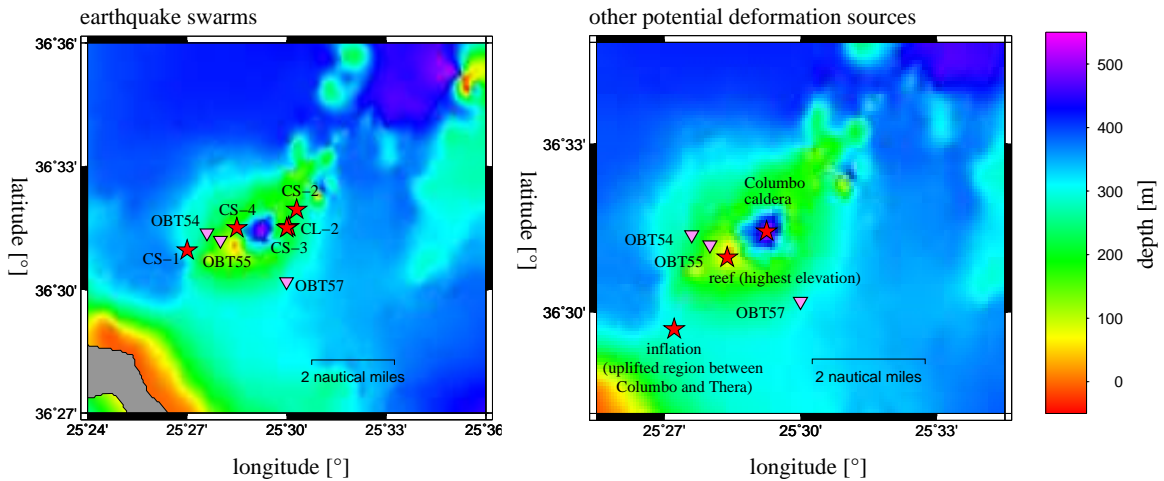


Figure 6.11: **Location of potential deformation sources.** Despite of earthquake swarms (centroids given as red stars in the left hand side plot), three other locations at and near Columbo have been determined as potential sources of deformation signals: The center of the caldera (as it is the center of the volcano and known to host hydrothermally active regions), the Columbo reef as the highest elevation of the seamount (17 m below the sea surface) and the inflated region between the Columbo reef and Cape Columbo on Thira island.

are marked in Fig. 6.11, their position relative to the deformation sensors is given in Tab. 6.4. The elevated region between Columbo and Santorini as well as the volcano itself (caldera and reef) are potentially related to longterm trends due to continuous deep routed activity.

To investigate signals of shorter periods, linear trends were removed by calculating a linear regression over each trace and subtracting the linear trend from the respective time series.

Once this correction is applied, the movement of the pendulum tip (tilt-walk, equivalent to horizontal particle motion plots of seismograms) was plotted to result in an overview of directions of possible long term trends and tilt excursions. Fig. 6.12 shows the horizontal tilt-walk of the tiltmeter pendulum over a period of 20 *h* during an earthquake swarm on 28th of July 2006. The back-azimuths for all signals on all OBTs and a map of the respective earthquake swarm south-west of Columbo are given in Fig. 6.12.

Fig. 6.13 shows the OBT traces of the same swarm, plotted together with the event density. Simultaneously to the onset of seismic activity, we observe an increasing tilt-walk on all three tiltmeters (position number 1 in Fig. 6.13). While it is only a slight increase of the tilt-rate on OBT 57, increased noise and tilting away from the source centroid is observed on OBTs 54 and 55, which both are located close to the swarm centroid. By the end of the swarm, a strong signal of intermediate period (approx. 3 – 4 *hours*) is observed on both near tiltmeters (position number 2 and 3 in the plot), with amplitudes of up to 40 μrad . The complete tilt episode and especially the strong signal at the end of the swarm are obviously caused by a local deformation source.

Intermediate signals and short term trends that were occurring during earthquake swarms

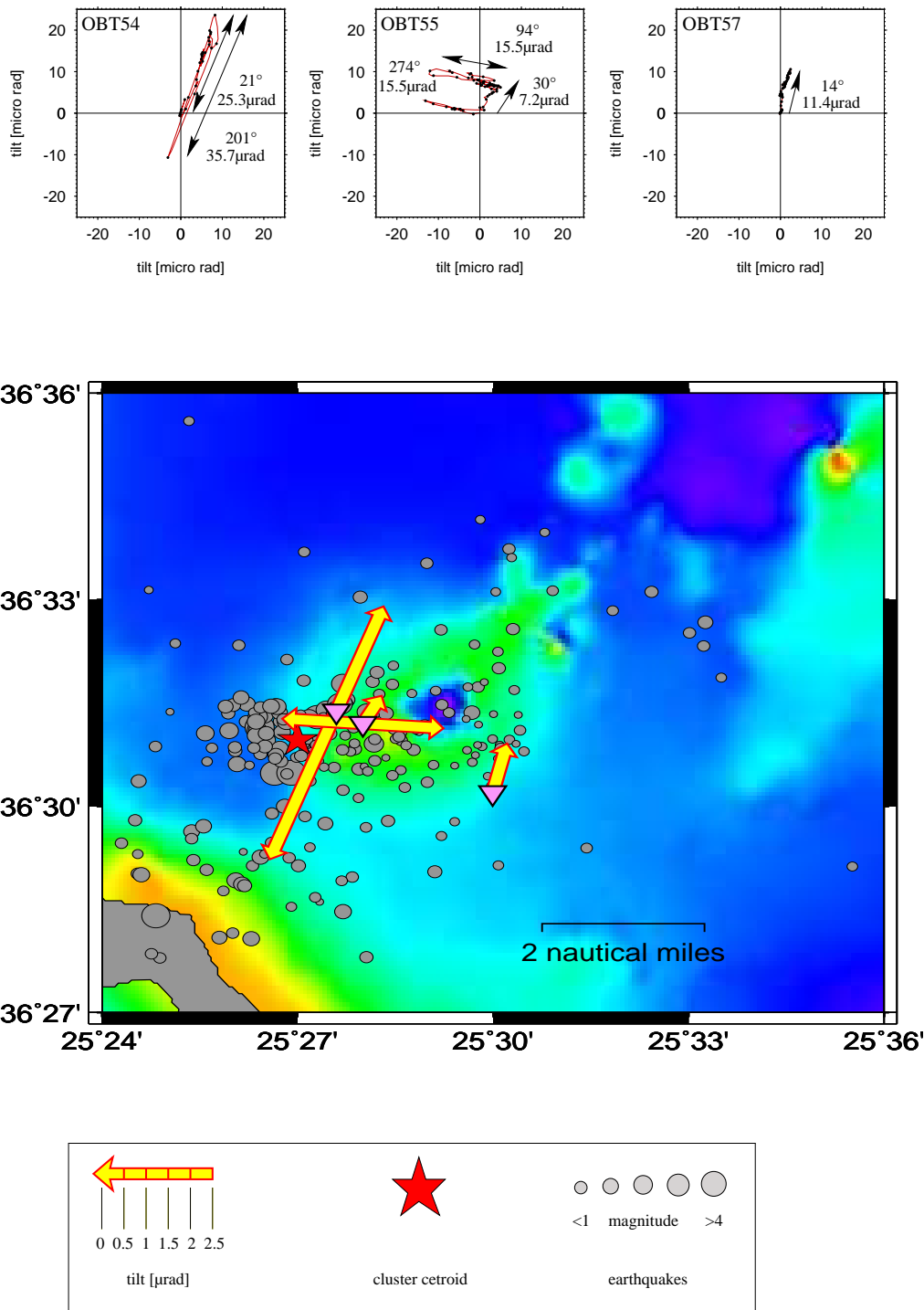


Figure 6.12: **Tilt-walk of the tiltmeter pendulum during an earthquake swarm**
 The upper plots show the pendulum's tilt-walk for each tiltmeter. While those of OBTs 54 and 55 are scattering crudely in direction of the cluster centroid, OBT 57 is too far away from the source and thus simply shows a trend in direction of the Columbo caldera. The lower plot shows arrows scaled to the tilt amplitude. The arrows give the back-azimuth directions of the signal.

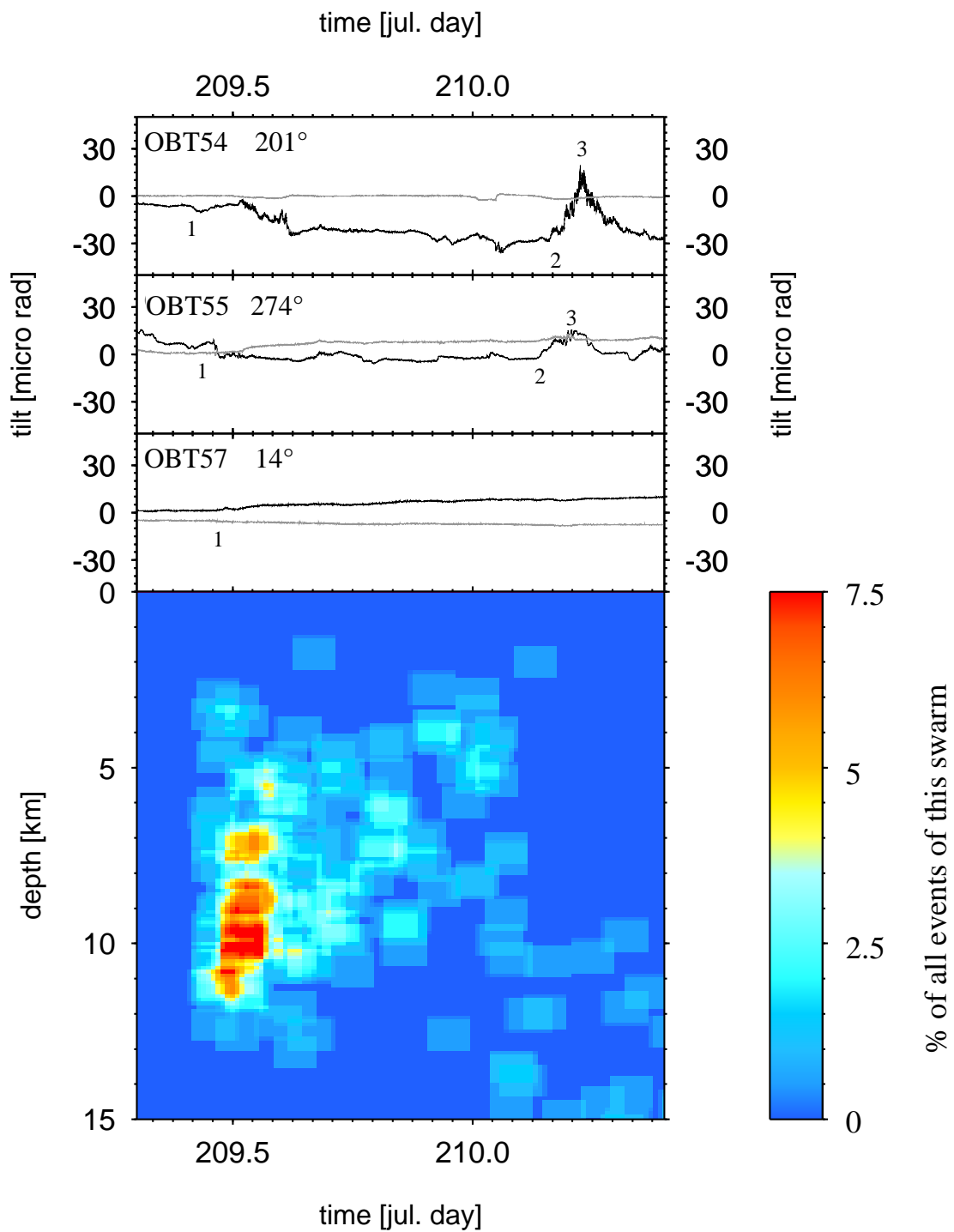


Figure 6.13: **Tiltmeter traces rotated in back-azimuth direction** (given angles are backazimuths) For the ideal case of a point source, the complete tilt signal should be observed on the radial trace. Despite of noise, the signal on the transversal component should be zero. It is indeed possible to rotate the traces such that the main part of the signal or the trends and peaks of interest are limited to the radial trace, but unrest on the transversal component often predicts a spacious or even more than one source.

<i>station</i>	OBT 54		OBT 55		OBT 57	
	Δx [km]	back azimuth [°]	Δx [km]	b. azi. [°]	Δx [km]	b. azi. [°]
CS-1 Jul. 28th 2006	1.3 ± 0.1	235 ± 5	1.9 ± 0.1	257 ± 5	4.7 ± 0.1	284 ± 5
CL-1 Sep. 23rd - Oct. 1st	-	-	-	-	-	-
CL-2 Dez. 6th-8th	3.7 ± 0.1	86 ± 5	3.1 ± 0.1	81 ± 5	2.5 ± 0.1	3 ± 5
CS-2 Jan. 10th 2007	4.2 ± 0.1	78 ± 5	3.7 ± 0.1	72 ± 5	3.3 ± 0.1	10 ± 5
CS-3 Feb. 18th	3.6 ± 0.1	87 ± 5	3.0 ± 0.1	81 ± 5	2.4 ± 0.1	0 ± 5
AS-1 Feb. 26th	15.2 ± 0.1	57 ± 5	15.0 ± 0.1	55 ± 5	14.4 ± 0.1	41 ± 5
CS-4 Mar. 1st	1.4 ± 0.1	82 ± 5	0.9 ± 0.1	58 ± 5	3.3 ± 0.1	311 ± 5
caldera	2.5 ± 0.1	88 ± 5	1.9 ± 0.1	79 ± 5	2.6 ± 0.1	329 ± 5
reef	1.4 ± 0.1	117 ± 5	0.7 ± 0.1	122 ± 5	2.8 ± 0.1	296 ± 5
swell	3.2 ± 0.1	193 ± 5	3.0 ± 0.1	208 ± 5	4.2 ± 0.1	258 ± 5

Table 6.4: List of cluster centroids and other possible deformation sources. The epicenter distribution of the CL-1 swarm is scattered over a too large region to a average for a centroid. Swarms closest to the deformation sensors are the CS-1, CS-3 and CS-4 swarm.

are listed in Tab. 6.5. The table gives an overview on absolute tilt and tilt rate, as well as the orientation of the station to the source and in comparison the strike angle of the incoming signal to analyze its possible linkage to the earthquake cluster. Especially for swarms of short duration (CS-x swarms), stronger tilt signals are observed parallel to the seismic activity, e.g. Fig. 3.11 in the OBT chapter (Ch. 3) and XY- and trace-plots in App. D. The most frequent observations are raised amplitudes of the tilt walk, crudely orientated radial to the earthquake cluster centroid, and an increased general noise on the tiltmeters which is not inevitably orientated in direction of the source. The comparison of the predominant noise orientation of each tiltmeter suggests a preferred noise axis for each sensor that seems to be chosen randomly, i.e. not in the specific direction of a potential source. These axes are: A strike angle of about 20° to the north for OBT 54, about 100° for OBT 55 and not really estimable for OBT 57. It has not been further investigated whether this predominant noise axes were caused by shallow local activity such as e.g. fumaroles, or if it was a constructional deficiency of the OBT.

For a few clusters located very close to the sensors, signals clearly orientated towards the

cluster are observed, e.g. on OBT 54 and 55 for the final phase of the CS-1 swarm or on OBT 57 for the CS-3 swarm. In all of these cases, the signal suddenly increases significantly in direction of the source centroid, which marks uplift of the area above the centroid, and decreases again with about the same tilt rates once it has reached its maximum. Modeling of these effects is deferred to the discussion.

<i>swarm</i>	<i>OBT</i>	<i>day</i>	<i>dur. [h]</i>	<i>b. azi. [°]</i>	<i>sign. strike [°]</i>	<i>T [μrad]</i>	<i>δT/δt [μrad/h]</i>
CS-1 07/28 2006	54 1	209.5	16	235 ± 5	21 ± 5	25 ± 1	1.6 ± 0.1
	54 2	210.2	1.5	235 ± 5	201 ± 5	35 ± 1	23.3 ± 0.1
	54 3	210.25	3.5	235 ± 5	21 ± 5	30 ± 1	8.6 ± 0.1
	55 1	209.45	3	257 ± 5	30 ± 5	7 ± 1	2.3 ± 0.1
	55 2	210.15	3	257 ± 5	274 ± 5	16 ± 1	5.3 ± 0.1
	55 3	210.25	3	257 ± 5	94 ± 5	15 ± 1	5 ± 0.1
	57 1	209.5	end	284 ± 5	14 ± 5	11 ± 1	0.5 ± 0.1
CL-1 09/23 - 10/01 2006	54 1	268	end	-	25 ± 5	29 ± 1	0.13 ± 0.1
	54 2	269	end	-	205 ± 5	10 ± 1	0.8 ± 0.1
	55 1	-	-	-	-	-	-
	57 1	268	end	-	332 ± 5	35 ± 1	0.16 ± 0.1
CL-2 12/06 - 12/08 2006	54 1	341.7	6	86 ± 5	20 ± 5	24 ± 1	4 ± 0.1
	54 2	342.0	2	86 ± 5	205 ± 5	16 ± 1	8 ± 0.1
	55 1	340.5	noise	81 ± 5	105 ± 5	10 ± 1	-
	55 2	340.5	noise	81 ± 5	285 ± 5	10 ± 1	-
	55 3	341.6	1	81 ± 5	65 ± 5	2.5 ± 1	2.5 ± 0.1
	57 1	340.5	36	3 ± 5	0 ± 5	8 ± 1	0.2 ± 0.1
	57 2	340.5	end	3 ± 5	270 ± 5	24 ± 1	0.4 ± 0.1
CS-2 01/10 - 01/11 2007	54 1	375.2	2	78 ± 5	± 5	7 ± 1	3.5 ± 0.1
	55 1	375.1	8	71 ± 5	± 5	5 ± 1	0.7 ± 0.1
	57 1	375.2	1	9 ± 5	23 ± 5	7 ± 1	7 ± 0.1
	57 2	375.6	2	9 ± 5	23 ± 5	7 ± 1	3.5 ± 0.1
	57 3	376.2	2	9 ± 5	23 ± 5	7 ± 1	3.5 ± 0.1
CS-3 02/18 2007	54 1	414.1	1	87 ± 5	208 ± 5	7 ± 1	7 ± 0.1
	54 2	414.4	3	87 ± 5	28 ± 5	15 ± 1	3 ± 0.1
	54 3	414.5	22	87 ± 5	29 ± 5	19 ± 1	0.9 ± 0.1
	54 4	414.9	1.5	87 ± 5	29 ± 5	10 ± 1	6.7 ± 0.1
	55 1	414.4	20	81 ± 5	343 ± 5	11 ± 1	0.6 ± 0.1
	57 1	414.4	20	0 ± 5	300 ± 5	11 ± 1	0.6 ± 0.1
	57 2	414.9	2	0 ± 5	30 ± 5	17 ± 1	8.5 ± 0.1
CS-4 03/01 2007	54 1	425.45	1	82 ± 5	29 ± 5	8 ± 1	8 ± 0.1
	54 2	425.8	1.5	82 ± 5	29 ± 5	15 ± 1	10 ± 0.1
	55 1	425.55	2	57 ± 5	295 ± 5	10 ± 1	5 ± 0.1
	57 1	trend	-	312 ± 5	220 ± 5	6 ± 1	0.3 ± 0.1

Table 6.5: List of deformation signals of longer period for all earthquake swarms. Strongest tilt rates are observed parallel to shortlasting earthquake swarms. But also for longer lasting swarms, an increase of activity can be found.

In contrast to periods of increased seismic activity, Fig. 6.14 shows the typical signals

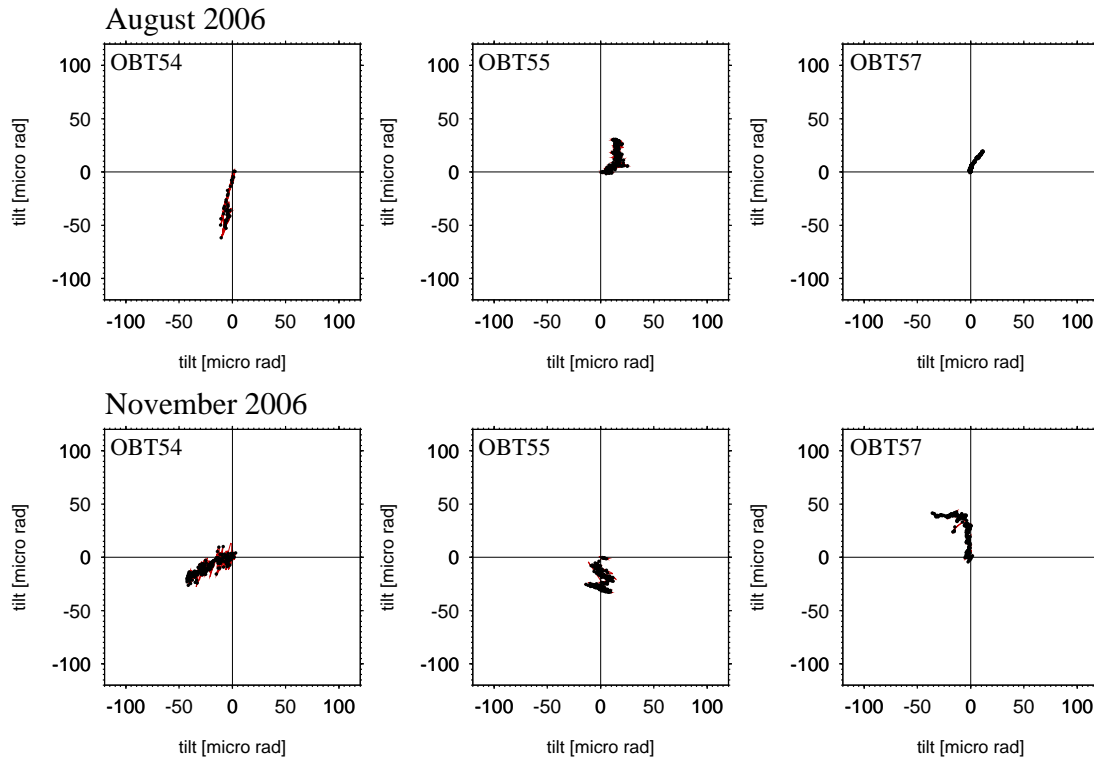


Figure 6.14: **Tilt traces for two months of sparse activity:**

For two months without increased activity and earthquake swarms (August and November 2006), tilt rates are significantly decreased compared to those during swarms. This figure is to illustrate the differences even in terms of noise between seismically more and less active periods.

on the tiltmeters for two months of very sparse activity (August and November 2006). The absolute tilt is between 20 and 80 μrad , which is equivalent to tilt rates of not more than 0.7 – 2.7 $\mu rad/day$ or 0.03 – 0.1 $\mu rad/hour$ contrary to rates of 0.3 – 30 $\mu rad/hour$ for short lasting swarms. Another comparison of tilt amplitudes and the state of activity is given at the end of appendix D: 1000 s highpass filtered tilt traces plotted over the event rate (earthquakes per day) show peaks of the noise amplitudes for days and periods of increased activity. However, this effect could not be observed for all swarms or sometimes not on all sensors at the same time.

Long term trends

Fig. 6.15 shows the tilt walk of all 4 OBTs for the complete time of the experiment (OBT 56 shut down after 35 days and is not discussed further). The graph marks the tip of the pendulum above the ground over the entire duration of the experiment. A similar plot has been developed to study the longterm development of tilt signals for a fluid injection at the KTB in Germany (Jahr et al., 2008). Both OBTs closest to the bathymetrically elevated region between the Columbo Reef and Cape Columbo on Santorini (OBT 54 and 55) show tilt rates of

some tens of μrad per month, crudely in direction of this elevated ridge for the first months of the experiment, OBT 54 until middle of November 2006. Then, a slight backshift for another 1.5 months is observed for OBT 55 until February 2007, before both stations show a strong tilt transient of up to $200 \mu rad$. It is unclear if the source of this strong tiltsignal observed on both OBTs has the same origin, because both strong trends are orientated completely different and their occurrence is temporally separated by weeks (complete January until end February for OBT 54 and middle of February until end of March). OBT 57 that is furthest away from the elevated ridge and shows at the same time a more or less permanent tilt walk in direction of the caldera of Columbo. Possibly, it measures slow uplift of the seamount. However, OBT 57 might alternatively be drifting away from Columbo due to sinking of the anchor in downhill direction.

For the remaining time periods, the tilt walks on OBT 54 and 55 correlate and might be caused by a potential inflation along the submarine rift between Santorini and Columbo (see red stars in Fig. 6.11 (right panel) for potential centers of inflation). Periods of tilt trends towards the rift structure between Columbo and Santorini (Tab. 6.6) are definitely worth a discussion and a comparison with findings of absolute pressure measurements (OBS 50 on top of this elevated ridge was equipped with an absolute pressure sensor, see Ch. 6.3.4).

<i>station</i>	<i>start</i>	<i>end</i>	Δt [d]	T [μrad]	<i>rate</i> [$\mu rad/d$]	<i>strike</i> [$^\circ$]
OBT 54	2006.07.01	2006.11.10	133 ± 1	270 ± 10	2.0 ± 0.2	175 ± 5
OBT 54	2006.11.10	2006.12.25	45 ± 1	160 ± 10	3.6 ± 0.2	22 ± 5
OBT 55	2006.07.01	2007.02.20	235 ± 1	520 ± 10	2.2 ± 0.2	137 ± 5
OBT 57	2006.07.01	2007.03.27	270 ± 1	850 ± 10	3.2 ± 0.2	320 ± 5

Table 6.6: Overview on long period trends

6.3.4 Absolute pressure data

Of all deployed absolute pressure sensors (mounted on all OBTs and OBS 50 between Columbo and Santorini), only one (OBT 50) was running until the end of the experiment, two (OBT 54 and OBT 55) stopped recording shortly before their recovery and absolute pressure sensors of OBT 56 and OBT 57 shut down during an early stage of the experiment. Thus, absolute pressure data could only be used of OBS 50, OBT 54 and OBT 55.

Fig. 6.16 gives an overview on the used absolute pressure gauges, their position and the differential pressure between different stations. We subtracted data of one station from another to get the pressure difference and thus the relative uplift or subsidence between both. The resolution of the pressure sensors is about $0.1 mbar$, which corresponds to a vertical displacement of $1 mm$. Because the average noise is around $\pm 1 mbar$ or $\pm 1 cm$ and some

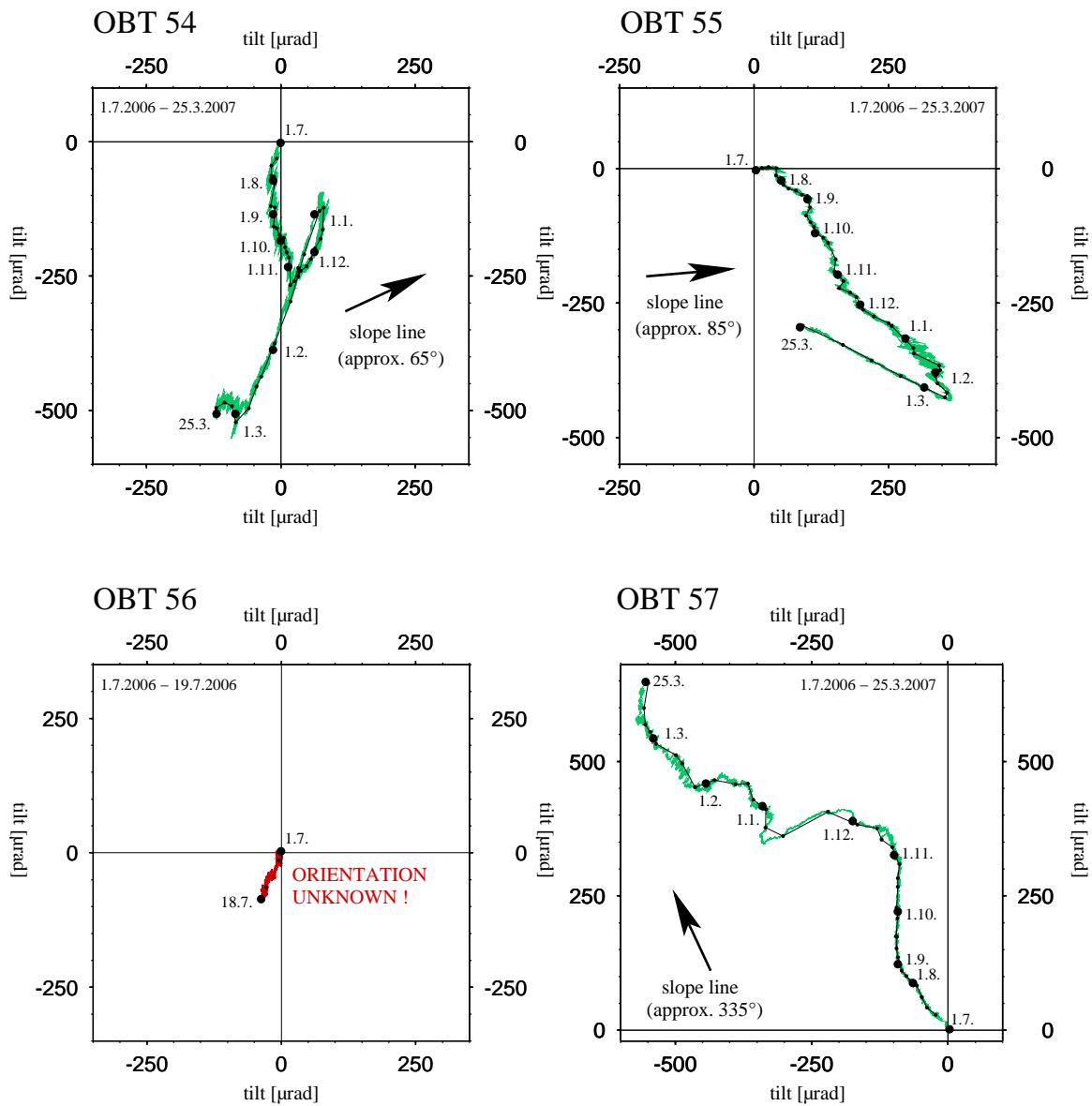


Figure 6.15: Trends of OBTs over the complete experiment. Trend for each OBT (starting at point (0;0)) in 10 min (green graph) and weekly steps (black dots and line). For orientation, start, end and 1st of each month is marked. Arrows show in upwards direction of the volcano's slope line. Except for OBT 56, whose orientation is unknown, traces were rotated according to Tab 6.3. OBTs 54, 55 and 57 show phases of clear trends and differing tilt rates (e.g. high tilt rates for January and March on OBTs 54 and 55, relatively low at the beginning for all OBTs).

even larger noise bursts are observed, we only took the average trend of each pressure sensor relative to both others.

It is found, that OBS 50 ascends about 5.5 cm compared to OBT 54 and about 4.5 cm to OBT 55. These values are relative and may alternatively indicate a subsidence of the OBTs with respect to the OBS. Hence, OBT 54 slightly descends by about 1 cm over the experiment compared to OBT 55 (or ascent of OBT 55 relative to OBT 54).

On average, these results suggest an inflation of the region between Columbo Seamount

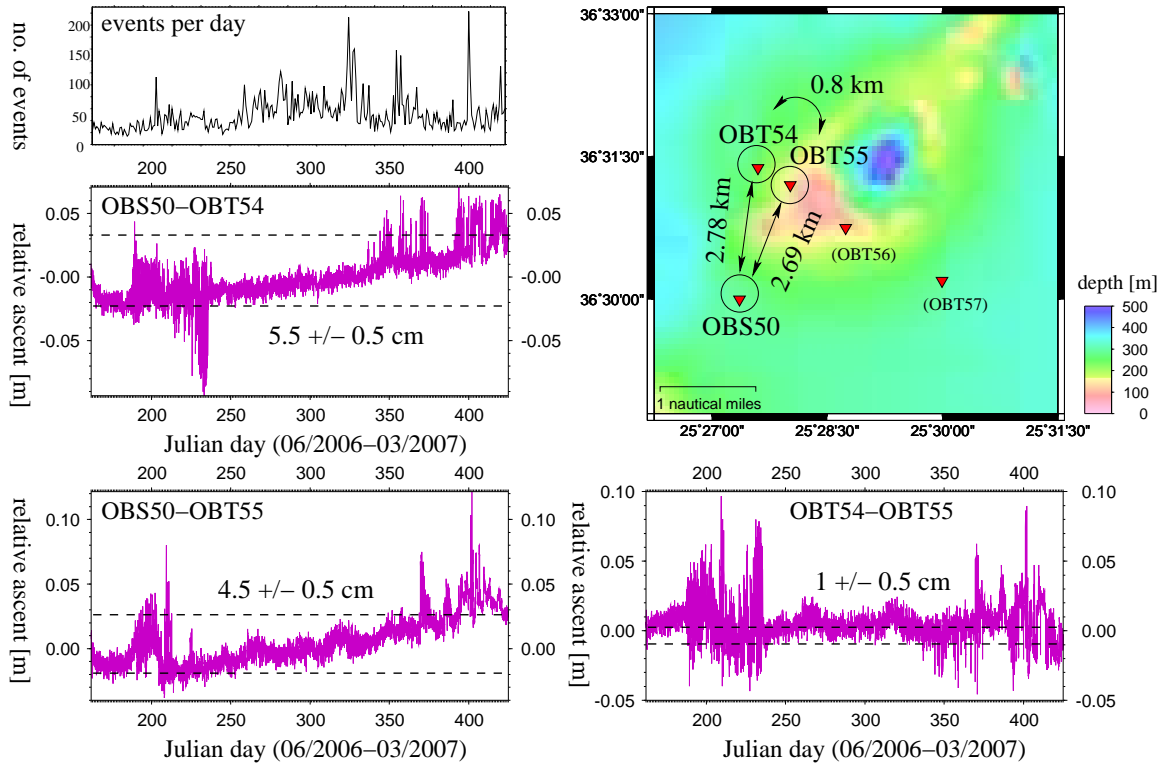


Figure 6.16: **Pressure difference traces of OBS 50 in opposite to OBTs 54 and 55** (violet traces) in comparison to the event rate (black graph). While a direct linkage to the event rate could not be observed, OBS 50 is obviously ascending relative to the OBTs (or the OBTs are descending relative to the OBS). Comparison of both OBTs suggests a small ascent of OBT 55. The map shows positions and distances of the systems with operating absolute pressure sensors.

<i>stat. 1</i>	<i>stat. 2</i>	Δx [m]	ΔP [mbar]	Δz [m]	<i>av. tilt</i> [μrad]	<i>rate</i> [$\mu\text{rad}/\text{day}$]
OBS 50	OBT 54	2.780	4.5 ± 0.5	0.045 ± 0.005	16.2 ± 2	0.054 ± 0.005
OBS 50	OBT 55	2.690	5.5 ± 0.5	0.055 ± 0.005	20.4 ± 2	0.068 ± 0.005
OBT 55	OBT 54	710	1 ± 0.5	0.01 ± 0.005	14.1 ± 2	0.047 ± 0.005

Table 6.7: List of absolute pressure measurements between the three permanently running absolute pressure gauges (OBS 50 on the inflated region between the Columbo Reef and Cape Columbo on Thira island, as well as OBTs 54 and 55). OBS 50 seems to ascent relative to the OBTs by round about 5 cm over the complete time of the experiment.

and Cape Columbo on Thira. But absolute pressure data in comparison with tilt data have to be treated with due care: The tiltmeter measures local tilt variations on a point, while the absolute pressure sensors measure uplift and subsidence over a long baseline, i.e. regional tilt. The regional tilt can not resolve small wavelengths, i.e. local deformation. However, liability of signals of larger wave lengths is increased for regional tilt. As Fig. 6.17 illustrates, tiltmeter measurements on a point lead to the derivative of uplift over distance, $\partial u_z / \partial u_h$, at exactly this point. For the extreme cases, this can be a maximum tilt for a tiltmeter in the inflexion point of the vertical deformation (OBT 1 in the example Fig.6.17) or a tilt of zero, when the tiltmeter is placed on top of the elevated region (OBT 2 in the example). For a signal

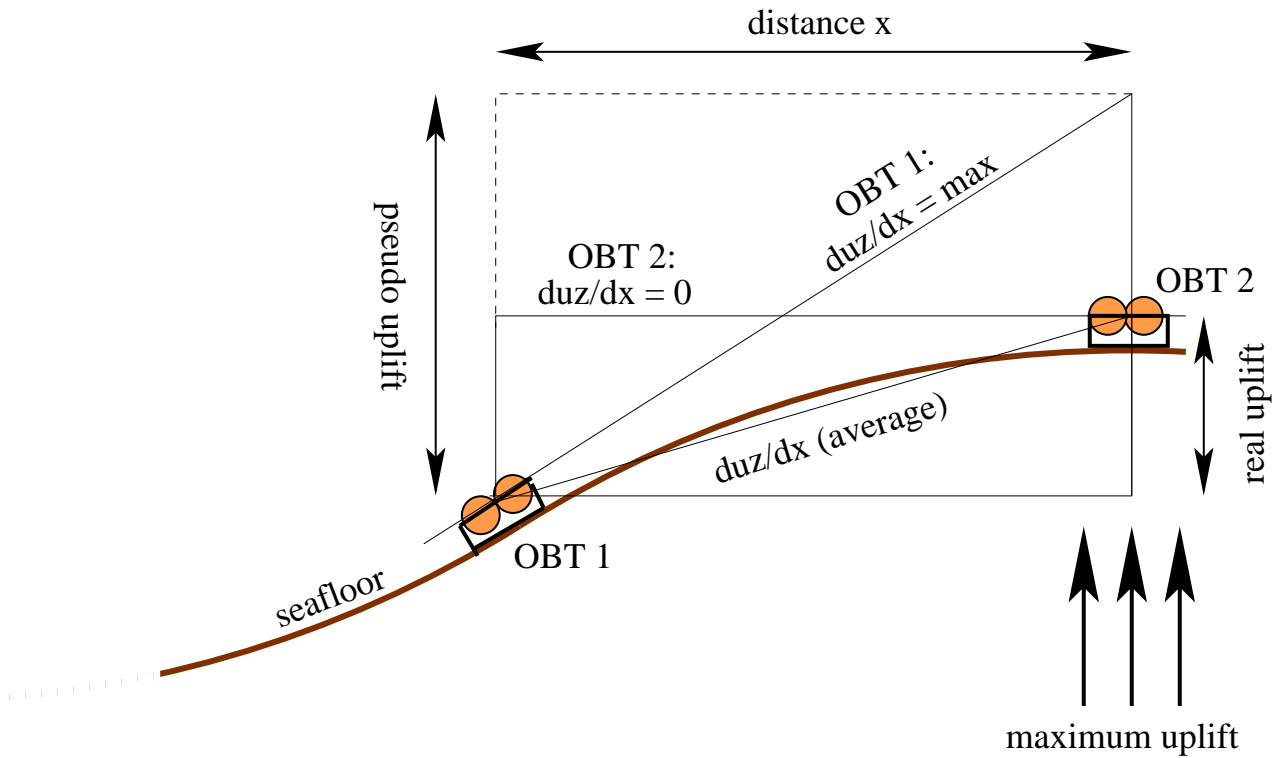


Figure 6.17: **Comparison: Tilt measurement on a point and over distance.** Example for critical position on the "tilt curve", i.e. the spatial derivative of the uplift signal: OBS 1 is standing in the inflexion point of $\partial u_z / \partial x$. This makes the tilt signal to become maximal, the uplift at this position is 1/2 of the maximum uplift which is measured at OBS 2. But for this point, tilt becomes zero, because it is the maximum of the uplift curve. An average tilt can be estimated by calculating the average between both tilt signals of OBS 1 and 2, or by measuring distance and pressure difference between both stations.

of larger wavelength, tilt measurements at single points can extremely falsify the results to smaller (OBS 2) and larger (OBS 1) values. This has to be kept in mind when interpreting both deformation measurements.

Compared with global tilt trends, both methods evidence the inflation of this region in the range of a few *cm/year* independent from each other. But short baseline tilt trends suggest a much higher uplift than it is evidenced by absolute pressure observations.

CHAPTER 7

DISCUSSION

With the temporary installation of additional land seismometers on the adjacent islands around Columbo and the deployment of OBSs and OBTs, azimuthal gaps of the permanent network were successfully closed. Seismic sensors in the zero-offset region of the earthquake cluster beneath Columbo and their relative relocation using catalogue and correlated waveform data significantly improved event locations. Simultaneously, the increased number of stations decreased the magnitude threshold for localized earthquakes down to $M_W = 0.5$. Summarizing, these network improvements led to relocation results with acceptable small rms-residuals, on average below 100 *ms*. Reliable moment tensor solutions of relocated events with $M_W > 3$ were estimated using a huge amount of data, even hydrophone data of the OBSs/OBTs. Independently, solutions were verified by analyzing P-wave polarization.

Both was important to successfully study the nature of seismicity in the Columbo region, especially the 6 earthquake swarms that occurred directly at the volcano and another small swarm located close to the seamounts SW of Anidros. Another important result concerned the verification of the technical functionality of our deformation sensors, that was proved in various period ranges.

7.1 Classification of earthquake swarms

Three types of earthquake swarms have to be taken into account to classify sequences of seismicity above background:

- Tectonic mainshock-aftershock sequences
- Swarms induced by dike or fluid ascent
- Seismic unrest due to increased hydrothermal activity

To discriminate tectonic earthquake clusters from volcanic swarms, their event rate is investigated for a possible hyperbolic decay, as it is predicted by Omori's law for a purely

tectonic sequence (Lay and Wallace, 1995). Additionally, tectonic clusters are expected to occur along faults and show fault-typical focal mechanisms (e.g. Hauksson et al., 2001, for a tectonic swarm at the San Andreas Fault). The separation based on fault-plane solutions fails at Columbo, since tectonic earthquakes due to the extensional stress regime at the Santorini-Amorgos Faultzone show the same mechanism (normal faulting) as events at Columbo that are interpreted to have a volcanic origin (Dimitriadis et al., 2005). Regarding event rates over time, clear mainshock-aftershock sequences can not be observed. Although strongest event rates were mostly observed during the initial phase of the swarms, they mostly did not decrease hyperbolically. We thus exclude solely tectonic causes for the observed swarms, which does not mean that fluid-induced regional stress perturbations may not cause tectonic subsequences accompanying volcanic swarms.

As a volcanic origin is expected, both, hydrothermal activity (e.g. Sigurdsson et al., 2006) and magma ascent have to be considered as possible swarm triggers at Columbo. Magma ascent is evident from the 1650 eruption (Dominey-Howes et al., 2000) and indicated by recent studies of Dimitriadis et al. (2009).

The investigation of hypocenter pattern, migration paths of seismic fronts and duration of swarms has shown to be promising to classify volcanic earthquake swarms and to deduce insights in their causes (Hensch et al., 2008). We have classified these swarms and will discuss their parameters compared to similar swarm events of known origins.

A prime suspect is an ascending magma dike. Such a dike might be fed from a shallow crustal reservoir beneath Columbo. Earthquakes beneath the volcano cluster in a depth range of 3 – 12 *km*, and Dimitriadis et al. (2005) suggests a seismic low velocity layer below 15 *km* depth to reflect the main magma reservoir of Columbo. Seismic activity above this depth is expected to be linked to magmatic intrusions and dike emplacement. This assumption is supported by magnetic observations (Landschulze, 2009, and Fig. 2.7). Strong magnetic anomalies of small wavelengths beneath Columbo are interpreted as the expression of solidified intrusions at an average depth of about 5 *km*. Earthquake swarms caused by dike-growth and propagation are frequently observed prior to volcanic eruptions (e.g. Battaglia et al. (1999) at Piton de la Fournaise, Patané et al. (2002) at Mt. Etna). Two important observations for dike-induced earthquake swarms have been recently published: (1) The duration of the swarm is limited to some hours up to a few days. (2) more than 80 % of the activity occur within the initial phase of the swarm (Aoki et al., 1999; Patané et al., 2002, for a swarm offshore Izu island (Japan) and at Mt. Etna) and additionally show a typical depth-time distribution (Hensch et al., 2008).

Parallel thereto, the occurrence of longer lasting earthquake swarms with a duration of several days up to weeks ($> 5 d$, Hensch, 2005) and an unstructured hypocenter pattern (Del Pezzo et al., 1984) can be excluded to be caused by dike intrusion only, since a dike rapidly

gets arrested due to buoyancy loss caused by solidifying magma once it approaches cooler regions in the crust. A dike needs a critical length to start buoyancy-driven propagation (Dahm, 2000). Thus, the propagation time under continuous volume loss is limited.

Long lasting swarms are discussed to be linked to increased hydrothermal activity (e.g. Fischer, 2003; Bianco et al., 2004; Hensch et al., 2008). Their hypocenter distribution does not show typical migration paths and fronts of seismicity, as it has been found for short lasting swarms. In the following, I discuss four short lasting swarms (CS-1 - CS-4) and their possible correlation with deformation data in more detail. The two long lasting swarms CL-1 and CL-2 are not further discussed.

7.2 Correlation of deformation signals and short lasting swarms

After shortly introducing our model for earthquake swarms triggered by dike ascent, the discussion mainly concentrates on possible correlations of seismic observations and deformation signals measured simultaneously.

7.2.1 Model for dike-induced earthquake swarms

Fig. 7.1 shows the lateral and vertical extension of the CS-1 earthquake swarm of July 2006. Earthquakes locally concentrate in a lenticular shaped cluster (2.6 km lateral and 9 km vertical). Fault plane solutions show normal faulting crudely in the same strike direction as the best fitting plane through the hypocenter distribution (NE-SW) as well as parallel to the orientation of the extensional Santorini-Amorgos Fault.

Short lasting and supposedly dike-induced earthquake swarms show most of their activity and fastest upwards migration of hypocenters during their initial phase. Often, the following phase is characterized by a secondary cluster with much slower migration velocities (ascent) and a more or less sharp backfront of seismicity at the lower end to a region of lacking earthquakes. This backfront is also migrating upwards and thus, the typical triangular shape of the z -distribution of the hypocenters is visible (see Fig. 7.2, intensively discussed in Hensch, 2005). Similar patterns have been described for known dike ascents in Japan (Aoki et al., 1999), at Piton de la Fournaise (Battaglia et al., 1999), or Mt. Etna (Patané et al., 2002).

Based on the findings of our previous investigations offshore North Iceland (Hensch et al., 2008), we derived the following hypothesis for various hypocenter migration velocities that were recurrently found in the hypocenter pattern of short lasting swarms (see Fig. 7.2):

The beginning of the dike ascent is characterized by the seismically most active phase. Overcritical stress accumulates at the upper tip of the dike and causes a rapidly increasing damage zone characterized by interacting micro-cracks (Rubin and Gillard, 1998a). This

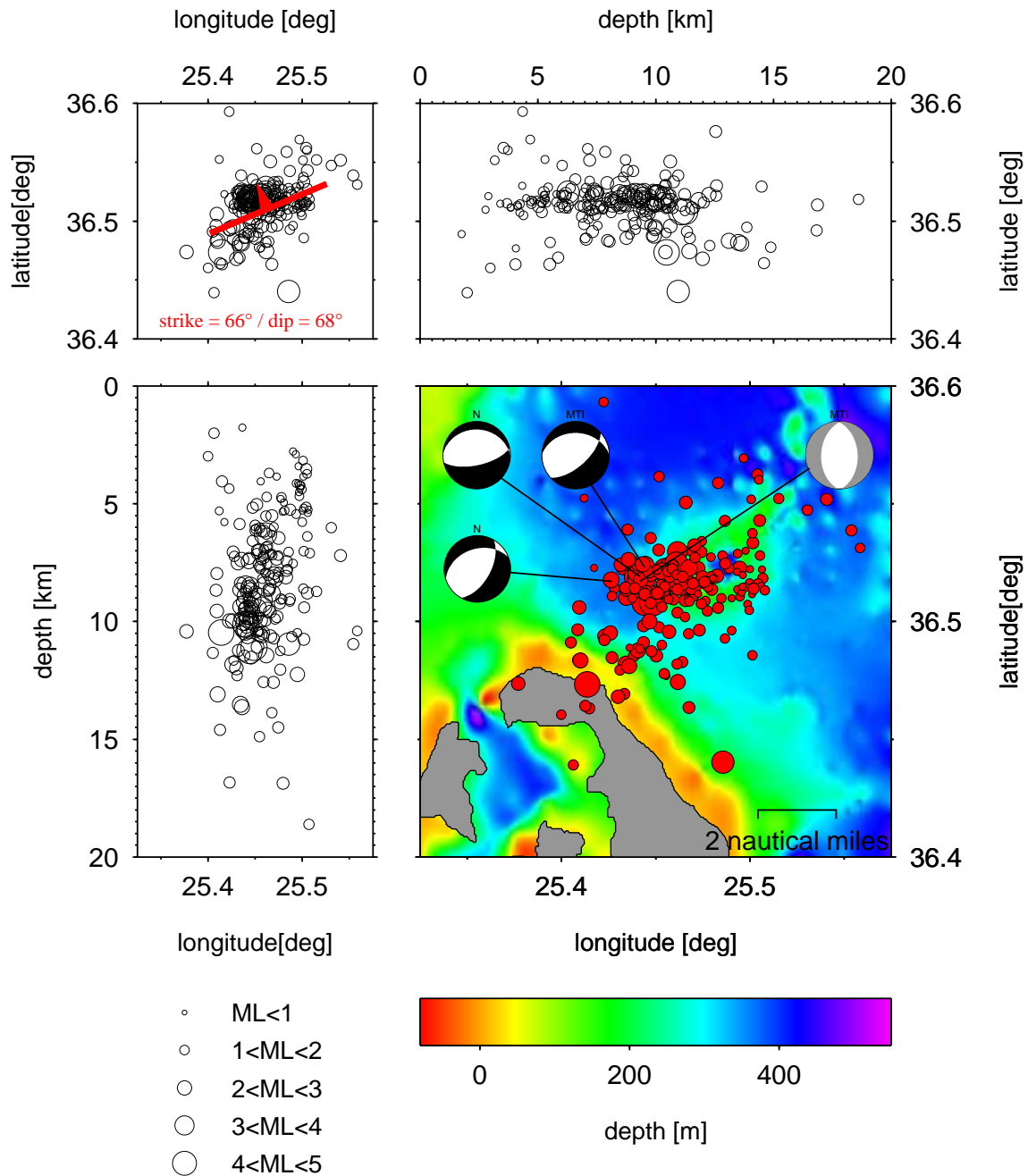


Figure 7.1: **Result-Plot for swarm CS-1 close to OBTs 54 and 55.** Events cluster in a vertical column of about 9 km length, the lateral extensions of the cluster are about 2 km NW-SE and 6 km NE-SW. A best fitting plane through the hypocenter distribution is found at a strike of 66° and a dip of 68° . Moment tensor solutions calculated for the strongest events show normal faulting with comparable strike angles. The cluster centroid is located below the outer SW slope of Columbo, close to OBTs 54 and 55 (see also Fig. 6.12). Equivalent overview plots for each swarm are given in App. D.

system of cracks may grow with up to a few tens of centimeters per second. For Columbo, these **initial fast velocities** v_{IF} of the seismic forefront were found in the range of $60 - 280 \frac{cm}{s}$, on average about $70 \frac{cm}{s}$.

The actual ascent of the fluid or magmatic volume is assumed to be much slower and represented by a second hypocenter front, migrating with a smaller velocity than the damage zone. Modeling predicts an accumulation of stress in the complete head region of a dike, mostly concentrated at its tips (Rubin and Gillard, 1998a,b; Thorwart, 2002), which explains micro-earthquake clustering above the dike and sparsely around its head. These **main cluster or main front velocities** v_{MC} were found in a range of $4 - 28 \frac{cm}{s}$ for short lasting swarms at Columbo, $15 \frac{cm}{s}$ on average.

As mentioned above, further stress accumulation in the complete head region of the dike is the result of its characteristic lenticular shape (see Dahm, 2000; Rivalta and Dahm, 2004). Further, Toda et al. (2002) found, that dike-induced stress is proportional to the earthquake rate. This was confirmed by a recent study of thermally induced micro-cracks in a salt mine (Becker et al., 2009). This could explain a reduced seismicity rate behind the seismic front and below the thickest part of the dike (Dahm et al., 2009). Once its point of maximum lateral extension has passed, stress decreases and seismicity stops at this depth. This **velocity of the lower boundary** v_{LB} or **backfront velocity** gives the z -distribution its typical triangular shape. Clear values for v_{LB} were only found for the CS-1, CS-2 and CS-4 swarm at Columbo, all in a range of $10 - 19 \frac{cm}{s}$ and thus for all three swarms slightly higher than v_{MC} , respectively.

The model assumes that the dike loses volume due to magma solidification at the edge of the dike and disposition of viscous fluid in its tail. Furthermore, changes of its shape due to further opening of the dike (Rivalta and Dahm, 2004, predicted by theory and proven by experiments) lead to an upwards shift of the point of maximum lateral dike extent. This causes a slightly higher velocity v_{LB} compared to v_{MC} (Fig. 7.2, right plot). Permanent volume decrease leads to a loss of buoyancy and finally arrests the dike.

The hypothesis has originally been derived from observations at the Mid-Atlantic Ridge (Hensch et al., 2008) and seems well confirmed for the short lasting swarms at the arc volcano Columbo. We thus assume that short lasting earthquake swarms at Columbo are mostly induced by ascending magma (or another fluid).

Here found migration velocities are slightly higher as they were observed for a dike ascent at Piton de la Fournaise in 1998 (Battaglia et al., 1999), at Mt. Etna in 2001 (Patané et al., 2002) or the lateral dike propagation at Krafla (Iceland) in 1978 (Einarsson and Brandsdóttir, 1980). While the shape of the z -distribution in terms of various seismically active fronts is comparable in different volcanic regions, variations of migration velocities might be related to different types of magma and the surrounding rock (density contrast).

For the remaining swarms of short duration at Columbo, CS-3 and AS-1, our observations differ from the model. The CS-3 swarm shows a high seismicity rate at the beginning, including fast upwards migration. But the sequence does not continue with a seismic main- and a backfront. Their absence may indicate a directly arrested dike. The AS-1 swarm SW of

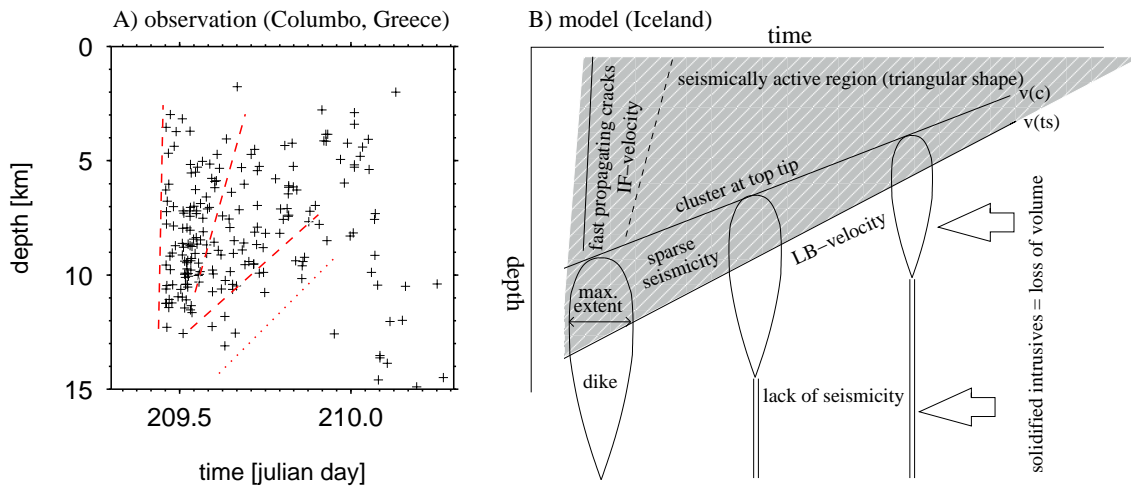


Figure 7.2: **Hypothetical model for short lasting earthquake swarms.** A) zt -distribution of the CS-1 swarm at Columbo. Highest seismicity rate is observed within the initial phase's fast upwards migration paths (seismic forefront), followed slower ascending cluster (main front), both marked with red dashed lines. The lower boundary (backfront) of the triangular zt -distribution is marked by a red dotted line. B) Simplified model for short lasting swarms (seismically active region is shaded grey) of upwards propagation of a dike with continuous volume decrease due to material loss caused by solidification of magma (Hensch et al., 2008, derived from supposedly dike-induced earthquake swarms offshore North Iceland).

Anidros is a scattered cluster of events, without any structure or obvious migrations pattern. As this swarm was lying outside our OBS/OBT network and locations have larger errors, it could not be resolved whether this was any other kind of seismic sequence or not.

7.2.2 Accompanying deformation

Near-field terms can only be measured in the direct vicinity of their origin. Of the 4 short lasting swarms at Columbo, only one was located close enough to OBTs 54 and 55 to observe clear signals of intermediate period deformation. Both tiltmeters were located only 1315 m (OBT 54) and 1896 m (OBT 55) away from the cluster centroid of the CS-1 swarm. Clear signals of deformation transients for the CS-3 swarm were observed with OBT 57 only, so that the CS-3 swarm can not be used for hypothesis testing, unfortunately. However, it is interesting that tiltmeters situated even further away from the earthquake swarm centroids frequently showed intermediate tilt noise on the radial component rather than on the transversal. This indicates a spatially limited deformation source (point source) located at or close to the seismic cluster. A correlation between seismic activity and the accompanying deformation is thus obvious.

Fig. 7.3 compares seismicity and tilt for the CS-1 swarm and shows unrest on the tiltmeter component radial to the cluster centroid, starting shortly after the beginning of an earthquake swarm and ending with a strong tilt pulse during the final phase of seismic activity. The strong pulse-like signal completely relaxes once seismicity has completely come to an end. A longer

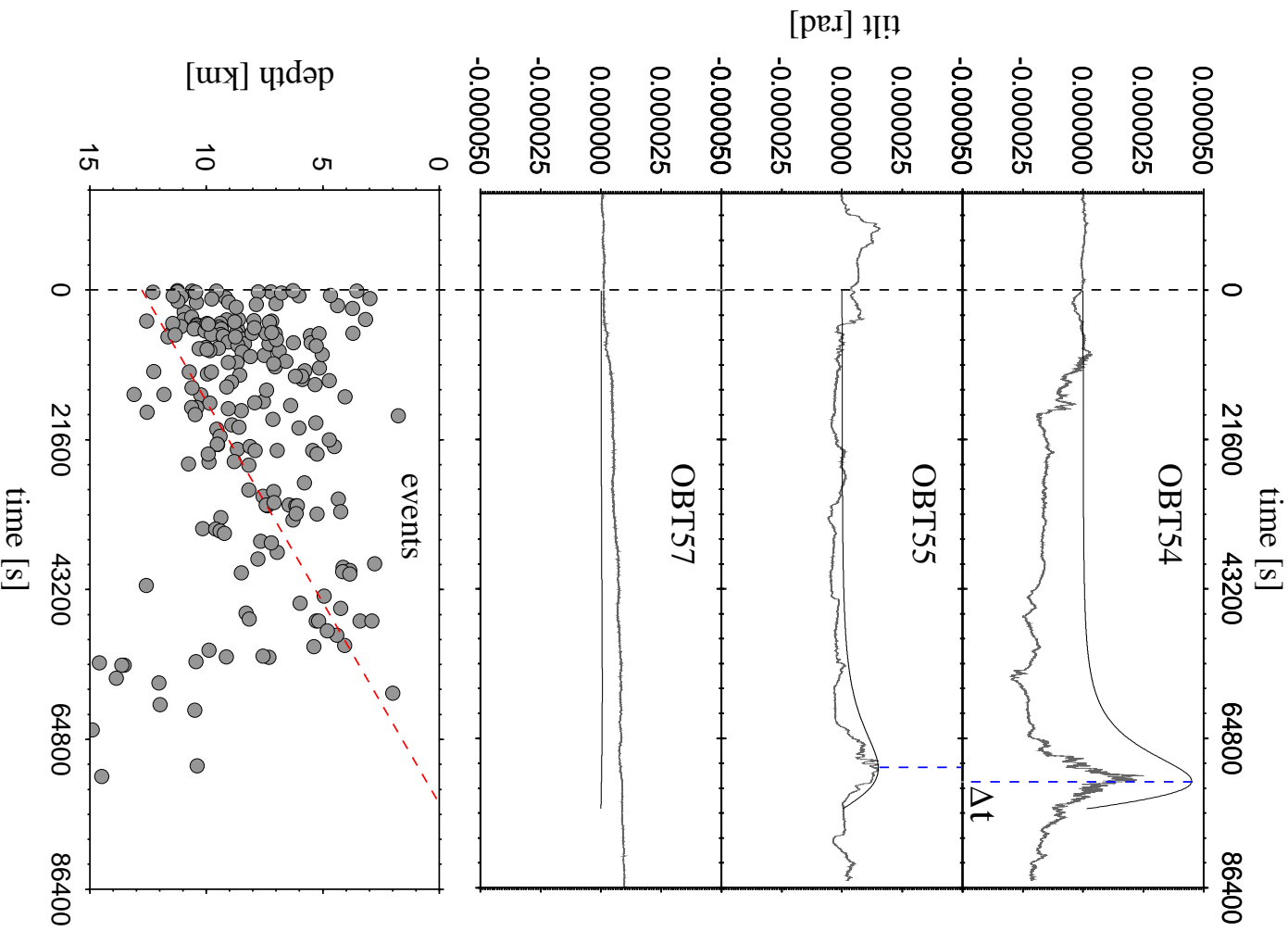


Figure 7.3: Unrest and inflation-deflation signal on OBTs during the CS-1 swarm: Modeling (black curves) for a vertically ascending Mogi source of 50 m radius, ascent velocity is the velocity of the main cluster $v_{MOC} = 0.16 \frac{m}{s}$ (red dashed line). Once the earthquake swarm (lower plot) has started (black dashed line), the traces (grey curves) clearly show increased noise. By the end of the swarm, strong signals of about $45 \pm 5 \mu rad$ on OBT 54 and $15 \pm 5 \mu rad$ on OBT 55 show the possible pass of the ascending source. The time shift of $\Delta t = 1700 \pm 100s$ between the tilt maxima on OBTs 54 and 55 is marked by blue dashed lines (the model predicts $\Delta t = 1.735 s$).

period of unrest signals of smaller amplitude is continuing and decaying over hours and days. Both signals, general unrest and the strong intermediate period tilt pulse, will be discussed separately. Finally, a joint model including seismological observations will be presented

General unrest

Unrest of the complete seamount, i.e. increased noise on tiltmeters standing further away from the earthquake cluster centroid, is a systematic observation also for all other earthquake swarms. It is also found for longer lasting hydrothermally induced swarms. Tab. 6.5, as well as tilt traces and tilt orientation plots in App. D show, that tilt rates of up to $20 \frac{\mu rad}{h}$ were observed for strongest tilt signals during earthquake swarms. An average tilt rate during periods of unrest is about $3 - 10 \frac{\mu rad}{h}$, compared to periods of low seismic activity, where tilt rates are less than $0.1 \frac{\mu rad}{h}$ ($\simeq 1 - 2 \frac{\mu rad}{day}$). Thus, tilt rates during periods of unrest increase by a factor of 30 and more, even at distances outside the direct near-field of a possible volumetric source.

Ongoing propagation of a deformation source initiated by a deep hot reservoir has been discussed and successfully modelled for the Campi Flegrei uplift crisis 1984 (Bonafede, 1991; De Natale and Pungue, 1993; Battaglia et al., 2006). Triggered by a deep magma intrusion, thermoelastic expansion caused deformation due to fluid overpressure. Same was found for another uplift sequence at Campi Flegrei in 2000. Bianco et al. (2004) found that variations of the fluid pressure initiated by a deeper intrusion plays the major role for the observed deformation. Both, heat flux due to a hydraulic gradient and fast fluid transport along shallow aquifers organized a rapid diffusion of thermal energy and thus deformation (Martini et al., 1984; Bonafede, 1991). Furthermore, Bonafede and Mazzanti (1999) discussed the release of volatiles due to differentiation of deeper arrested magma as a source of inflation above. Both seem to be reliable approaches to explain the further ascent of a volume source although the initiating dike has already been arrested in a larger depth.

The forced advection of hot fluids from a deep high-pressure reservoir to a shallow low pressure and temperature reservoir is a very efficient source for ground deformation (Bonafede, 1991). The migration velocity of hot fluids and thus the complete effect of thermoelastic expansion along aquifers can be expected to be faster than heat transport that is only caused by the propagation of pore fluids due to a hydraulic gradient. This is especially the case if the region has been altered by repeated volcanic events and/or diffuse volcanic degassing. Thus, the increase of hydrothermal activity and the rapid convection could cause unrest of the complete volcanic system once dike propagation and earthquake swarms have started. This is observed in the data. Despite of the strong tilt signals on OBTs 54 and 55 by the end of the swarm, a general unrest is observed on all tiltmeters, even on OBT 57. This unrest is starting already during the initial phase of seismic activity. While OBTs close to the swarm

centroid show sudden noise increase, the simultaneous intensification of the existing trend, or an overlying second trend, is observed on OBT 57 (see Figs. 6.12 and 7.3).

The efficiency of heat convection by aquifers has been shown by Martini et al. (1984). Fluids detected at fumaroles and boiling pools at Campi Flegrei were produced by boiling of shallow aquifers receiving a convective gaseous inflow from the underlying magma chamber. And the intensity of hydrothermal activity is depending on the state of activity of this deeper reservoir, i.e. increased for periods following a deep magma intrusion and thus simultaneous to uplift sequences. It is thus indeed possible, that a local magma intrusion causes fast extending and widespread thermoelastic deformation and hydrothermal unrest. This explains the nearly instantaneous occurrence of deformation signals on tiltmeters located outside the detectable near-field of the actual intrusion.

Strong near-field signals

For various volcanoes, harmonic inflation-deflation signals were observed instantaneously prior an eruption, e.g. at the Souffrière Hills volcano on Montserrat (Sparks, 2003; Neuberg et al., 2006) or during the Anatahan (Mariana Islands, Pacific) eruption sequence (Pozgay et al., 2005). Additionally, Green and Neuberg (2006) found, that the maximum inflation, i.e. tilt increase over time $\frac{dT}{dt}$, occurs simultaneous to or slightly after the maximum event rate. This coincides with our findings: Strongest tilt is observed once the earthquake activity has already passed its maximum. But tilt signals on OBTs 54 and 55 reach their maximum with a time shift of about $1.700 \pm 100s$ ($28 : 20 \pm 01 : 40 \text{ min}$). Such a large time shift over a relative distance of 581 m can not be explained by an inflating-deflating source at a constant depth. The apparent velocity of the tilt pulse at our stations is about $0.3 \frac{m}{s}$ and thus far below the typical velocities of free wave propagation (Lay and Wallace, 1995). Therefore, we exclude wave propagation effects as explanation for intermediate tilt pulses.

The polarization of the tilt signals and the amplitude decay clearly indicate a point like deformation source. We used a slowly ascending point source as a first order model to explain the signals. A horizontally migrating point source could explain time shifts between two maxima at different stations, but can be excluded for two reasons: (1) We have not found any tendencies for horizontal migration of the earthquake cluster, and (2) a horizontally shifted volume source would cause one uplift peak and thus two tilt peaks, one negative, one positive, while passing the tiltmeter. This has not been observed. In case of a sill intrusion once the dike has reached a level of neutral buoyancy, tilt signals indeed might look similar, but all of the found fault plane solutions show normal faulting and thus evidence vertical migration only.

The remaining question is, whether a vertically migrating point source can explain the time shift of about half an hour, although both stations are located only 581 m apart. As a

very simple approach, we modeled a Mogi source starting at the initial point of the swarm, i.e. the intersection of both seismicity fronts. For the CS-1 swarm, this is at 12.5 km depth. As starting time, the source time of the first event of the swarm was used. We let the source ascend with the estimated velocity of the main seismic cluster, $0.16 \frac{m}{s}$ (see Fig. 7.3). The source is assumed to continue ascending, even after the seismic activity ceases, until it reaches the surface. The resulting curves do predict time shifted maxima for OBTs 54 and 55. Additionally, the theoretical curves nicely predict the observed amplitudes at all three stations. A large amplitude at OBT 54, a smaller one at OBT 55 and a hardly visible signal at OBT 57. It is interesting that the curves reach their maxima and tilt decreases to zero before the source approaches the surface.

It was shown in Chapter 4.2.2 that the wavelength of the vertical deformation is depending on the depth of the source. It follows, that also the maximum of the tilt signal, located at the inflexion points of the uplift curve, is shifting towards the source as it approaches the surface. Fig. 7.4 illustrates the depth dependency of the tilt amplitude. While amplitudes are increasing exponential for decreasing source depths, the maximum of the tilt amplitude continuously shifts towards the epicenter with a constant apparent velocity c_x . We define this maximum as the *spatial tilt maximum* and c_x as the *apparent velocity of the spatial tilt maximum*.

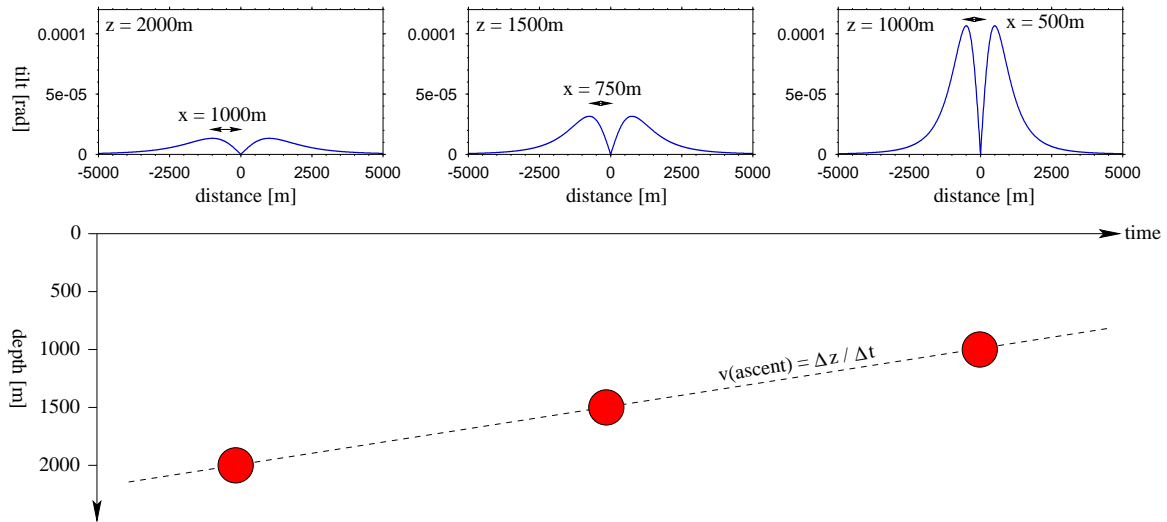


Figure 7.4: **Depth dependency of the tilt amplitude:** Upper curves show tilt for given depths as an overview of amplitude changes and the sourceward shift of the tilt maximum. Curves correspond to source depths shown in the lower graphic (for a source volume of $520.000 m^3$). The dashed line marks the vertical propagation velocity of the source, i.e. ascent over time.

We define the position of the ascending point source in **cylindrical coordinates** at $(0; z(\tau))$ with $\tau = t - t_0$ and the station at position $(x, t; 0)$. The source is ascending with the constant velocity v_z , so that $z(\tau) = z_0 - v_z \cdot \tau$. We omit the depth coordinate of the station

and define the tilt signal by $T(x, t; z(\tau))$ (x, t are the sensor coordinates, $z(\tau)$ is the source coordinate). The position of the spatial maximum can then be found by setting the derivative of $T(x, t; z(\tau))$ (Eq. 4.28) with respect to x to zero:

$$\begin{aligned} T(x, t; z(\tau)) &= \frac{3u_z}{x_s} \left(\frac{u_x}{u_r} \right)^2 \\ &= \frac{9V}{4\pi(x^2 + z^2(\tau))x} \cdot \frac{z(\tau)}{\sqrt{(x^2 + z^2(\tau))}} \cdot \left(\frac{x}{\sqrt{(x^2 + z^2(\tau))}} \right)^2 \end{aligned} \quad (7.1)$$

$$\frac{\partial T(x, t; z(\tau))}{\partial x} = -\frac{45Vx^2z(\tau)}{4\pi\sqrt{(x^2 + z^2(\tau))}^4} + \frac{9Vz(\tau)}{4\pi\sqrt{(x^2 + z^2(\tau))}^5} \quad (7.2)$$

$$\frac{\partial T(x, t; z(\tau))}{\partial x} = 0 \quad \text{for } z = \pm 2x \quad (7.3)$$

This means, that the depth of the point source (spherical source) is two times larger than the epicentral distance of the spatial tilt maximum. For a source ascending with the constant velocity v_z it follows, that the position of the spatial tilt maximum is moving with time towards the epicenter with a velocity of $c_x = \frac{1}{2}v_z$.

It is important to notice that the tilt amplitudes increase exponentially as the source approaches shallower depths. Thus, the maximum of $T(x, t; z(\tau))$ along the x -coordinate is not the same as the maximum along the $z(\tau)$ coordinate. Fig. 7.5 shows amplitudes and the shift of the amplitude maximum for three given epicentral distances and an ascending source (varying source depth or time). Amplitudes again increase exponentially for shallower depths and rapidly decrease as soon as the distance x is larger than the epicentral distance of the maximum tilt signal.

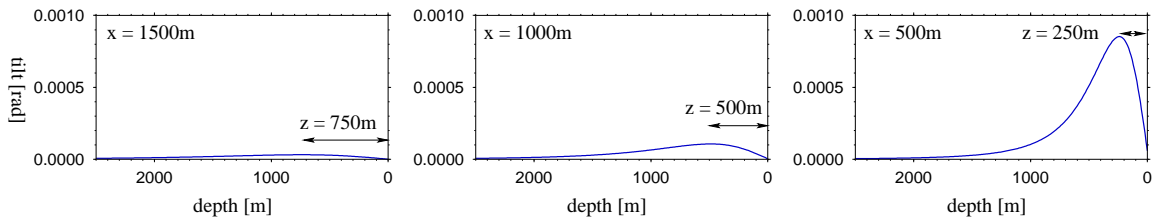


Figure 7.5: **Distance dependency of the tilt amplitude:** Curves show tilt for given distances of an ascending source to illustrate the significant amplitude increase when the source is approaching the surface. The source volume in this example is 520.000 m^3 .

Thus, the apparent maximum tilt amplitude at the epicentral distance x is the envelope of all curves $T(x, t; z(\tau))$ (see Fig. 7.6), derived by differentiating $T(x, t; z(\tau))$ with respect to

the source depth z :

$$\frac{\partial T(x, t; z(\tau))}{\partial z} = -\frac{45Vxz^2(\tau)}{4\pi\sqrt{(x^2 + z^2(\tau))^7}} + \frac{9Vx}{4\pi\sqrt{(x^2 + z^2(\tau))^5}} \quad (7.4)$$

$$\frac{\partial T(x, t; z(\tau))}{\partial z} = 0 \quad \text{for} \quad z = \pm \frac{x}{2} \quad (7.5)$$

When the ascent velocity v_z is known from seismic observations, the derivative of the tilt with respect of time is:

$$\begin{aligned} \frac{\partial T(x, t; \tau)}{\partial \tau} &= \frac{45Vv_zx(z_0 - v_z\tau)}{4\pi\sqrt{(x^2 + (z_0 - v_z\tau)^2)^7}} - \frac{9Vxv_z}{4\pi\sqrt{(x^2 + (z_0 - v_z\tau)^2)^5}} \\ &= \frac{9V}{4\pi} \left(\frac{5v_zx(z_0 - v_z\tau)^2}{\sqrt{(x^2 + (z_0 - v_z\tau)^2)^7}} - \frac{xv_z}{\sqrt{(x^2 + (z_0 - v_z\tau)^2)^5}} \right) \end{aligned} \quad (7.6)$$

$$\frac{\partial T(x, t; \tau)}{\partial \tau} = 0 \quad \text{for} \quad \tau = \frac{x}{2v_z} \quad \text{and} \quad \Delta t = \frac{\Delta x}{2v_z} \quad (7.7)$$

We define this maximum as the *temporal tilt maximum* and the apparent velocity c_t of its sourceward migration the *apparent velocity of the temporal maximum*. As the temporal maximum is found at a distance $x = 2z$, we find $c_t = 2v_z$.

Results are summarized in Fig. 7.6: The position of the spatial tilt maximum (green curve) intersects the family of tilt functions $T(x, t; z(\tau))$ (blue curves) at their respective maxima ($\partial T(x, t; z(\tau))/\partial x = 0$, left hand side plot). The temporal tilt maximum observed on a tiltmeter at a fixed distance x takes into account that amplitudes are increasing exponentially and is given by the envelope (red curve) of the family of tilt functions and is found by setting $\partial T(x, t; z(\tau))/\partial z = 0$. The right hand side plot shows the derivative of $T(x, t; z(\tau))$ with respect of z . Here, the temporal maximum is the intersection of the maxima (red curve) and the spatial maximum (green curve) the envelope of the family of functions, based on the symmetry of $T(x, t; z(\tau))$ (see Eq. 4.28). Using both plots, amplitude estimations can be done for each station and transferred to source depth and time shifts between the stations (dashed lines).

Both derived apparent velocities are useful for different types of measurements: The apparent velocity of the spatial maximum c_x reflects the actual position of the inflexion points of the vertical displacement u_z . Depth and ascent velocity v_z of the source can be estimated from deformation data such as continuous GPS or InSAR. In our case, tiltmeter observations at constant distances to the epicenter, the apparent velocity of the temporal maximum c_t , i.e. the envelope of $T(x, t; z(\tau))$ for varying z , can be used to derive v_z . Fig. 7.7 shows tilt

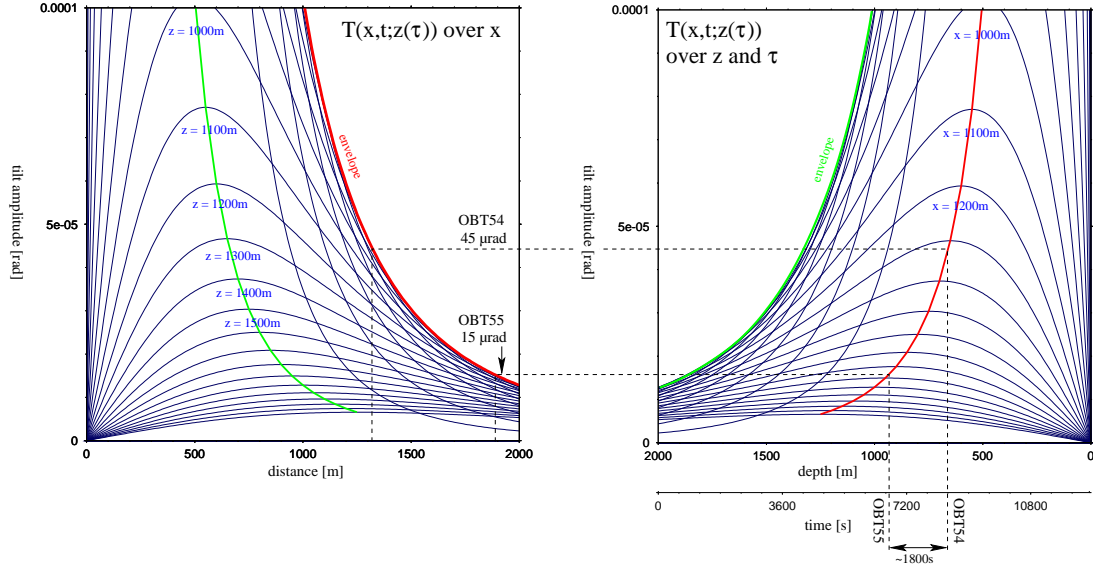


Figure 7.6: **Tilt amplitude over epicentral distance, depth and time:** The left hand side plot shows the family of tilt functions $T(x, t; z(\tau))$ over distance x for varying depth z (blue curves). The maxima intersection (green curve) gives the amplitude and position of the spatial tilt maximum, the envelope (red curve) reflects amplitude and position of the temporal tilt maximum. Symmetry of the tilt function $T(x, t; z(\tau))$ leads to the right hand side plot, where tilt amplitudes over depth and time are given, respectively. Here, the intersecting function gives the temporal and the envelope the spatial tilt maximum. Dashed lines illustrate how epicentral distances of tiltmeters are transferred to amplitudes and further to source depths and resulting time shifts.

amplitudes depending on depth over amplitudes depending on distance. The depth scale can be transferred to a time scale when the ascent velocity v_z is known. c_t (red line) intersects the temporal maxima of $T(x, t; z(\tau))$ and c_x (green line) the spatial maxima.

Summarizing, we find the following velocity ratios:

$$\frac{1}{2}c_t = v_z = 2c_x \quad \text{and} \quad c_t = 4c_x \quad (7.8)$$

This simple approach is confirmed by theoretical simulation. Using a numerical calculation, we find a time shift Δt of 1.735 s (28:55 min). This is only 35 s more as found in the data. The analytical solution using the shift of the temporal tilt maximum with the velocity c_t leads to a theoretical time shift of 1815 s (30:15 min), which is 115 s (1:55 min) longer as data suggests. Best fitting amplitudes were found for a source radius of 50 m, that corresponds to a source volume of about 520.000 m^3 . The measured amplitude ratio between OBT 54 ($45 \pm 5 \mu rad$) and OBT 55 ($15 \pm 5 \mu rad$) fits with the modelled ratio (see Fig. 7.8).

It is clear that a Mogi source as well as a constant velocity are only crude approximations. E.g. Rivalta et al. (2005) have found different ascent velocities of a fluid-batch for varying layer densities, using gelatine experiments. However, the model shows that vertical migration of any volume source can explain the unusual long time shifts Δt of the temporal maximum tilt peaks on the stations, their amplitudes and the general 'waveform' of the tilt transients.

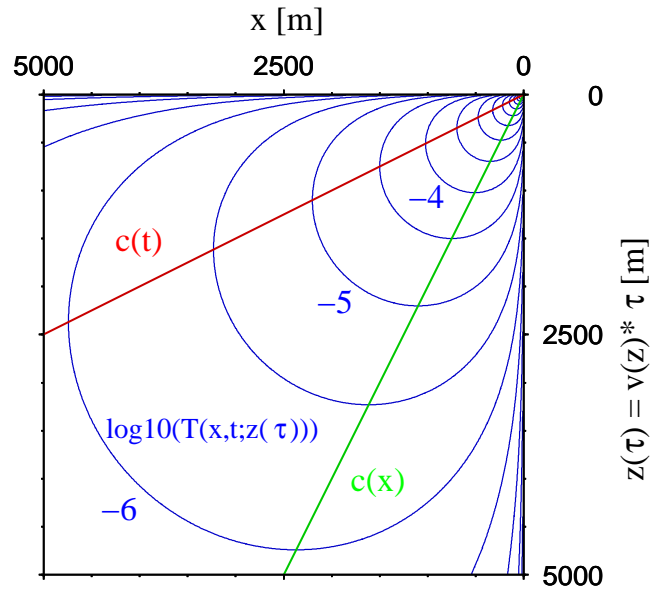


Figure 7.7: **Spatial and temporal tilt maxima:** Plotting the spatial over the temporal tilt amplitude leads to the velocities of temporal c_t (red) and spatial c_x (green) tilt maxima. Blue contour lines reflect the logarithmic tilt amplitude $\log_{10}(T(x,t;z(\tau)))$. As the source volume is known (again 520.000 m^3 in this example), amplitudes for given x and z can be estimated from the contour plot.

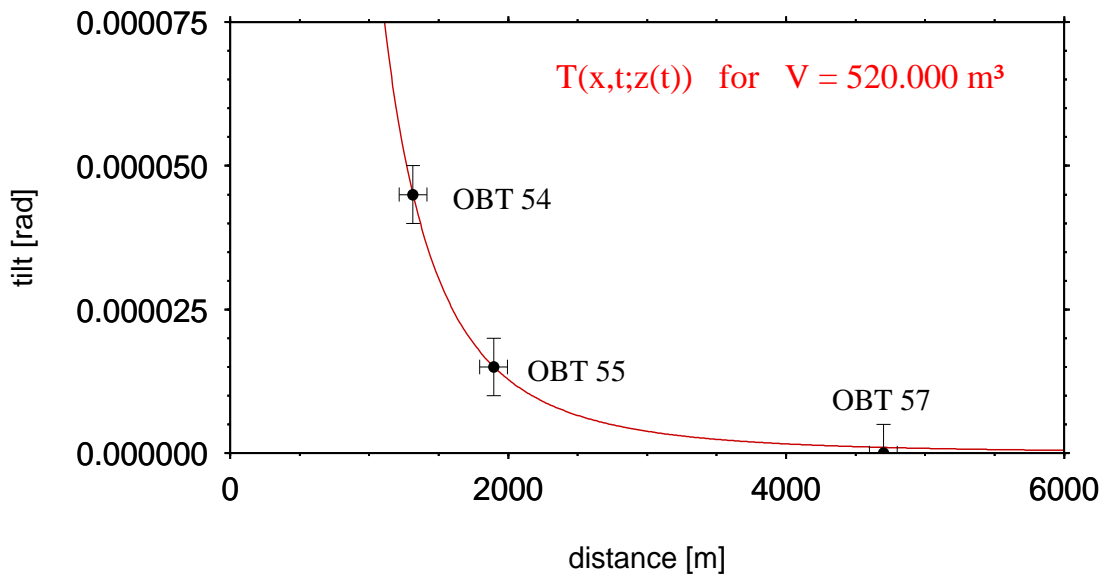


Figure 7.8: **Tilt amplitude versus epicentral distance**, modeled for a $V = 520000 \text{ m}^3$ source. Dots mark actually measured amplitudes on the three OBTs, including the respective location and amplitude errors.

The final question is the interpretation of the ascending source. Comparable signals have been observed prior the Fuego eruption in Guatemala 1977. A tiltmeter 6 km SE of the crater showed a sequence interpreted as inflation-deflation with an amplitude of $14 \pm 3 \mu\text{rad}$. The signals occurred after the initial phase of an earthquake swarm, the eruption started while

tilt was already decreasing. Both, seismicity and tilt were interpreted as an expression of subsurface magma movement (Yuan, 1984). Shape and amplitude of the signals show crude similarities with ours. If in our case a magma-dike was growing upwards to the shallow subsurface, the absence of earthquake activity within the uppermost 3 km might reflect a structural change. For instance, loose sediments and volcanic deposits are evident for at least the first 2 km, based on own active seismic profiling (Ruhnau, 2009). But as there is nothing known about a submarine eruption or outflow of magma at Columbo during the earthquake swarm, a second model could be discussed: The seismic activity itself stopped at about 3 km depth. This could indicate the possible arrest of the dike in this depth. Degassing of an arrested dike is temporary limited due to the drop of gas pressure down to the lithostatic pressure (Acocella and Neri, 2009). Furthermore, degassing leads to a significant volume loss of the magma batch, while its mass decrease is negligible. The resulting density increase leads to a buoyancy loss and possibly forces the dike to arrest. The temporal limitation of degassing could explain the fast relaxation of the tilt pulse.

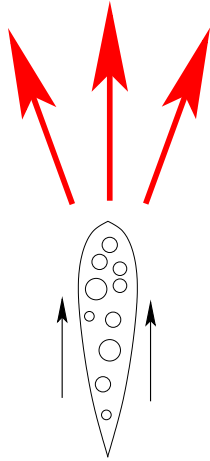
7.2.3 Joint hypothetical model for dike-induced earthquake swarms and accompanying deformation signals

Summarizing, we propose the following hypothesis (Fig. 7.9), which is based on our preexisting model for dike-induced earthquake swarms and the new findings. The seismic and volcanic unrest is initiated by the emplacement of a magma dike, fed from a shallow crustal reservoir. The dike can ascend freely once it has reached a critical length. The dike ascent is accompanied by a typically structured short lasting earthquake swarm, characterized by a fast upwards propagating seismic front and a much slower back front, which both form the characteristic triangular shape of the swarm's z -distribution (see Figs. 7.2 and 7.3). As the back front is supposed to represent the position of the largest lateral emplacement at the dike's head, we assume its depth by the end of the swarm as the position where the dike comes to rest. In case of Columbo, this is in a depth range of 3-5 km.

Effect 1 (Fig. 7.9): Simultaneous to the onset of the intrusion, hydrothermal activity and unrest are initiated by the approaching high temperature source. The relatively short time between the swarm onset and a general unrest, also observed on tiltmeters further away from the actual source suggest efficient and fast heat transport of hydrothermal fluids along aquifers and/or altered volcanic rocks with preexisting cracks, rather than convection of pore fluids with Darcy-velocities. Thus, a broad region around the intrusion possibly becomes thermoelastically deformed and acts as a large deformation source. The larger depth of this aquifer system causes small tilt amplitudes, but a long wavelength of the tilt signal. Local noise on individual tiltmeters might also be explained by the very local increase of fumarole activity and hydrothermal fluid outbursts. Unrest on the tiltmeters calms down within a few

Effect 1:
simultaneous to earthquake swarm

regional unrest and
thermoelastic deformation



Effect 2:
end of swarm / after dike arrest

local deformation
due to shallow volume sources

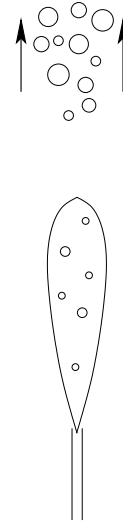


Figure 7.9: **Hypothetical model for deformation signals accompanying short swarms:** Effect 1 marks the sequence of dike ascent. Despite of the discussed seismic activity, widespread unrest and thermoelastic deformation are supposedly caused by fast conduction of hydrothermal fluids (red arrows), heated up by the intrusion. Effect 2 marks the sequence where the dike already came to rest. The temporary vertical release of volatiles is suggested to lead to a local deformation signal above the intrusion.

days after the earthquake swarm, as hydrothermal activity decreases again.

Effect 2 (Fig. 7.9): We explained the local but strong signal at the end of the swarm to be possibly caused by the release of volatiles from the cooling magma batch rather than strong vertical convection of hydrothermal fluids directly above the intrusion. Although strong convection directly above the dike might explain a short wavelength signal, the pulse form of the signal is difficult to understand by assuming convective processes. As discussed for the general unrest of the volcano during and after the intrusion, the cooling phase would be in the range of days up to weeks which can not explain the limited wavelength of the found pulse. Instead, the temporary release of gases (further migration of gases), until gas pressure has decreased again to the lithostatic pressure, is possibly sufficient to explain the temporal and spatial limits of the observed signal. Once the intrusion comes to rest, volatiles continue migrating upwards by spreading into the supposedly fractured rock above. The enrichment with gas and possibly also fluids causes volume increase and further thermoelastic expansion of the affected region. While the released volatiles continue ascending and the gas pressure of the dike decreases down to lithostatic pressure, strong degassing of the intrusion ends, despite of some slight release of gases due to magma crystallization. This might be an explanation

for a spatially limited source and thus could explain its short duration.

The degassing volatiles could be predominantly H_2O . 4 – 6 wt% water have been found for former eruptions of the Santorini volcano (Druitt et al., 1999), and the H_2O saturation of magma in 3 km depth (approx. $9 \cdot 10^7 Pa$) is at about 3.5 – 4 wt% (Dixon, 1997). This could explain the temporary release of a large amount of gas rather than the degassing of CO_2 or SO_2 .

Of course this gas migration can not directly be compared with a spherical Mogi source. And data of only three measuring points restrict to a very simple model. But it demonstrates two important facts:

- The epicentral distance of the maximum tilt signal is depth depend and thus time shifts Δt of maximum tilt between two tiltmeters can be explained by vertical migration of a volume source only.
- Once an intrusion comes to rest, it activates a spatially limited region above it - supposedly by the release of volatiles - which continues ascending. Although it is no pure spherical volume source, its deformation field is crudely equivalent to that of a Mogi source (here a spheric volume of about 50 m radius).

Very local tilt signals (phase 2) have only been observed on OBTs 54 and 55 for swarm CS-1 and on OBT 57 for CS-3. Regional unrest (phase one) has been found to occur parallel to all swarms, even long lasting swarms. However, the present state of this hypothetical model is clearly very speculative and requires further investigations.

7.3 Global trends and aseismic deformation signals

Recent studies suggest two different magmatic reservoirs beneath Santorini caldera and the Columbo submarine volcano. One associated with the volcanic center around the Kameni islands inside the Santorini caldera, and the other associated with the region between Columbo and Cape Columbo on Thira (Santorini) (Vougioukalakis, 1996; Francalanci et al., 2005). Recent and current seismic activity and volcanic unrest are concentrating on the Columbo region. Only sparse volcanic and nearly no seismic activity is presently observed around the Kameni islands (Sigurdsson et al., 2006; Dimitriadis et al., 2009, and own observations).

Fig. 7.10 shows an active seismic profile (SE to NW) perpendicular to the inflated region between the Columbo Reef and Cape Columbo. The dimensions of this inflation are approx. 4 km along σ_3 and 7-8 km between Thira and Columbo orthogonal to σ_3 . The region is clearly uplifted by some tens of meters at the maximum. OBS 50 was deployed exactly on top of

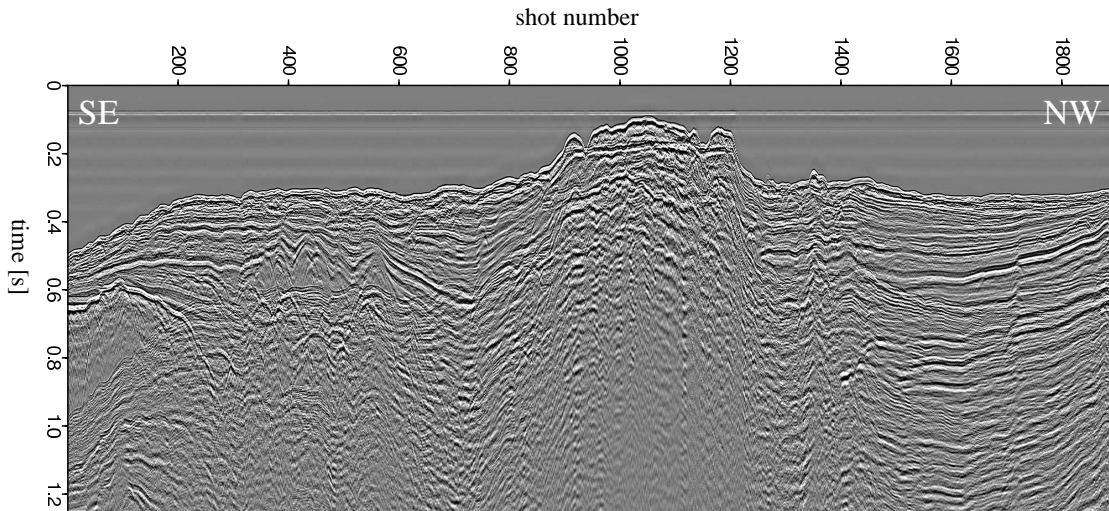


Figure 7.10: **Reflection seismic profile over the elevated region between Santorini and Columbo:** Raw data of high frequency reflection seismic profiling. The shot distance is 12.5 m. The uplifted area is lying between shot numbers 900 and 1200, its maximum and the position of OBS 50 are located at about shot number 1050.

this elevated area and equipped with an absolute pressure sensor to measure possible uplift or subsidence.

Compared to the pressure sensors of OBTs 54 and 55, OBS 50 shows an uplift of 5.5 ± 0.5 cm relative to OBT 54 and 4.5 ± 0.5 cm relative to OBT 55. These values correspond to an average long baseline tilt rate of $0.045 - 0.07 \frac{\mu\text{rad}}{\text{day}}$ along the 2.7 km baseline between the OBTs and OBS 50. As both OBTs show this trend relative to the OBS and there was nearly no trend found between both OBTs, this can be regarded as a real signal rather than instrumental drifts. Parallel thereto, global tilt trends on OBT 54 and 55 also indicate the slow but continuous uplift of this region. Both show trends in the range of $2.1 - 2.5 \frac{\mu\text{rad}}{\text{day}}$ for the first months of the experiment, which would correspond to a theoretical uplift of 1.8 m over a 2.7 km baseline. These huge differences between both measurements are probably the result of the different baseline lengths as it is illustrated in Fig. 6.17. The OBT measures tilt on a point and thus is able to observe signals of very short wavelengths, but also very sensitive for local effects. The estimation of tilt using pressure differences leads to an average tilt over the distance between both pressure sensors and thus only measures signals of long wavelengths. However, for signals of long wavelength, the measurement of the average tilt along a long baseline should be preferred to avoid local effects (Tolstoy et al., 1998).

Uplift rates observed by absolute pressure measurements also fit with onshore measured deformation rates using the Santorini GPS network (see Fig. 1.4). Both measurements indicate slight and continuous uplift of the already elevated area between both volcanic centers, Santorini and Columbo, in the range of some *cm/year*. Although sparse seismicity was ob-

served above this inflated region (see Fig. 5.8), earthquake swarms were absent. No indications for shallower intrusions, such as swarms, deformation signals of small wavelengths or magnetic anomalies, as they were all found at Columbo, have been observed in this area.

The long wavelength of the deformation signal and the sparse seismicity suggest a deep and large source. The observed uplift might be the expression of a deeper magma reservoir (5-10 km corresponding to Dimitriadis et al., 2009) along the Columbo line (as expected by Vougioukalakis, 1996). But as our experiment was optimized on the observation of seismicity and deformation caused by shallow intrusions, speculations about this large scale signal are beyond the scope of this study.

7.4 Possible technical improvements of the OBT

Coupling of the OBT to the seafloor remains an open question. The free-fall system couples with its anchor weight of 120 kg only. Including buoyancy of the flotation spheres, the weight of the complete system under water is 20 kg. Although these 20 kg seem sufficient to keep the system stable against moderate underwater currents, coupling effects due to unconsolidated volcanic deposits, on which the instruments are standing, are unknown, although a good long period response predicts consistent coupling of the OBTs relative to each other. Despite of possible subsidence in wet sand and instability of the sediments on the volcano's flank, sub-surface heterogeneities and topographic effects have been shown to influence the deformation field. Kirchdörfer (1999) used finite element computations and a conical model for volcanoes to investigate effects of topography. The most important result of his study was, that larger surface displacements can be expected for the conical model than for the half-space (Mogi model). Furthermore, ratios of horizontal and vertical displacement may vary from the Mogi model, which leads to slightly imprecise depth estimations of the source. Concerning heterogeneities of the ground, Wielandt and Forbriger (1999) found, that locally measured tilt might not represent the regional tilt at all. This means, that local variations of strain-tilt coupling affects the observed tilt. This is an important effect for our OBT, since it measures tilt on a point and not along a longer baseline.

The effect is not worth a more detailed discussion, because we do not know the exact conditions of the OBTs location on the seafloor. This is a large disadvantage of a freefall system. Although the position is precisely known to a few tens of meters, it is not known how the instrument was standing and coupling to the seafloor. Our simple modeling in section 7.2.2 suggests these effects to keep within a limit, since both amplitudes for the signals on OBTs 54 and 55 are crudely fitting to one source volume. But it can not be shown what the absolute effect of the Columbo topography and local heterogeneities on the modelled amplitudes is. Amplitudes of comparable observations (e.g. Yuan, 1984, at the Fuego volcano)

are crudely in the same range as ours. But the uncertainties mentioned above may lead to imprecise depth and volume estimations.

Another problematic point is the orientation of the tilt components. The usage of electronic as well as mechanic compasses failed due to the disturbance caused by anchor, frame and other metal elements of the complete OBT system. The application of a correlation method to re-orientate the sensor using data of a land seismometer with known orientation was more or less successful at Columbo, since a few onshore seismometers were standing close enough to derive and cross-check re-orientation angles for all OBTs. But this technique is not applicable for tilt measurements too far away from the coast, because global correlation maxima are only found for station distances of $< \frac{\lambda}{4}$ (Maurer and Deichmann, 1995), i.e. in case of the used low-frequency surface waves with a period of $T_{max} = 40$ s, the distance can be about 30-50 km at the maximum.

A last point is the exponential decreasing drift at the beginning of the experiment. As these signals were also found during our test measurements in the Black Forest Observatory, where the OBT frame was mounted on a concrete block coupled directly to the bedrock, this nonlinear trend is supposed not to reflect subsidence of the instrument due to unconsolidated seafloor sediments. One possibility might be the gradual relaxation of internal stresses of the OBT frame, caused by strongly fixed screws and one-sided weight of the battery tubes. But this is speculative. As far as it the origin of these trends remains unsure, the first 4-6 weeks of the data are unusable.

CHAPTER 8

CONCLUSIONS

The newly developed Hamburg Ocean Bottom Tiltmeter has successfully passed its pilot experiment. Its principle technical functionality has been proven contrary to most initial reservations and critics. Although first experiences in practical use threw up loads of questions about constructional deficiencies and problematic coupling, we were able to observe tilt signals of varying wavelengths. Basically, the system is able to measure high frequency tilt steps due to near-field terms of earthquakes, signals of longer period such as of an inflating magma reservoir, as well as trends over weeks and months. Furthermore, we were able to observe horizontal broadband seismic signals for the first time on the seafloor. Thus, the OBT was an essential completion of our amphibian seismic experiment at the Columbo Submarine Volcano.

Regarding seismological observations during the experiment, the improved event-station geometry and the implementation of our three component cross-correlation approach significantly decreased earthquake location residuals by a factor of 20-30. Parallel thereto, the magnitude threshold of the complete network was reduced to about $M_W > 0.5$. Improved location accuracy and a largely increased number of successfully relocated events enabled us to precisely study the clusters' hypocenter distributions on characteristic patterns and migration paths. Six major earthquake clusters have been observed during the experiment, of which four were classified as possibly dike-induced and two as a result of temporary increased hydrothermal activity. Reverse to the successful classification of earthquake swarms at Columbo, we found our preexisting model on swarm triggers well confirmed.

We found an obvious linkage between the seismic activity and simultaneous tilt observations. In general, noise on the tiltmeters increased and measured tilt rates rapidly raised by a factor of often 30 and more once an earthquake swarm had started. These signals calmed down slowly over hours and days after the swarm. As this general unrest was crudely polarized radial to the earthquake clusters, it has been interpreted as an activity increase of hydrothermal systems due to a high temperature intrusion. Recent studies evidenced the advection of hot fluids along hydrothermal aquifers to efficiently spread thermal energy from a deeper heat source to shallower low temperature reservoirs. Thus, we postulated a large deep

volumetric increase of a broader region above the intrusion to be thermoelastically expanded. This model is sufficient to explain the fast and wide extension of ground deformation.

Near-field terms of a vertically propagating deformation source have been observed for two earthquake swarms which occurred close enough to the tiltmeter profile. For one of these swarms, we were able to model for a migrating volumetric source, using an ascending Mogi source: The time shift between the tilt maxima on two tiltmeters in close epicentral distance to the swarm centroid was evidenced to represent the sourceward shift of the temporal tilt maximum. Although we could not finally clear whether this signals were caused by the ongoing ascent or by degassing of the dike, we redundantly found the migration velocity confirmed that was derived from seismological observations. We could numerically model for the exact time shift between both tiltmeters. The model has been proved analytically resulting in depth-dependent functions for spatial and temporal tilt maxima. Using these functions, depth and velocity of the ascending source can be estimated. A temporary maximum is observed for permanent measurements with tiltmeters at fixed epicentral distances. Onshore, a spatial maximum is predicted for continuous GPS measurements or repeated InSAR snapshots when differentiating uplift with respect to the epicentral distance. Source volume estimations derived from tilt amplitudes have to be regarded carefully, since the modeled Mogi source is a very basic approximation only.

Attendant investigations using different geophysical methods supported these findings: Magnetic anomalies of small wave lengths beneath Columbo have been suggested as solidified intrusions in about 5 *km* depth. This correlates with depths where earthquake swarms ended and dikes supposably came to rest. Results of moment tensor inversions for major earthquakes also confirm predominantly vertical propagation of fluids. Fault planes all showed normal faulting and thus evidenced the vertical orientation of the first principle stress axis σ_1 .

Summarizing, we postulate a model for the simultaneous occurrence of seismic swarms and local ground deformation: Characteristic hypocenter fronts and their migration velocities indicate a dike to have initiated migration towards the surface. The approaching heat source causes the immediate increase of hydrothermal activity. The fast spread of thermal energy forces expansion of a broader region around the intrusion. This deep and large source causes a deformation signal of a long wavelength, hydrothermal fluid propagation causes general noise increase. Strong, but very local near field terms around the epicentral region of the seismic cluster evidence the ascent of a volume up or close to the surface. As magnetic anomalies suggest intrusions to arrest in about 5 *km* depth, we suppose volatiles released by the magma batch to initiate the temporal limited expansion of the region above the intrusion.

This hypothesis remains speculative as far as it has not been proven by further field studies. The source of regional uplift between Santorini and Columbo remains completely unsure.

APPENDIX A

SENSOR PARAMETERS AND VELOCITY MODELS

A.1 Seismic stations

<i>Name</i>	<i>Location</i>	<i>Latitude</i>	<i>Longitude</i>	<i>Elevation [m]</i>	<i>Network</i>
AMOE	Amorgos East	36° 54.900'N	25° 58.728'E	210	EGELADOS
AMOS	Amorgos North	36° 47.736'N	25° 46.140'E	52	EGELADOS
ANAF	Anafi	36° 21.486'N	25° 46.698'E	35	EGELADOS
ANID	Anidros	36° 37.506'N	25° 41.082'E	179	EGELADOS
ANPA	Antiparos	37° 01.938'N	25° 04.578'E	41	EGELADOS
ASTY	Astypalaia	36° 34.770'N	26° 24.684'E	192	EGELADOS
FOLE	Folegandros	36° 37.296'N	24° 55.182'E	292	EGELADOS
IOSI	Ios	36° 44.082'N	25° 21.708'E	52	EGELADOS
MYKO	Mykonos	37° 28.932'N	25° 23.064'E	150	EGELADOS
NAXO	Naxos	36° 58.800'N	25° 26.400'E	157	EGELADOS
NEAK	Nea Kameni	36° 24.522'N	25° 24.084'E	57	EGELADOS
OBS50	SW of Columbo	36° 30.000'N	25° 27.350'E	-287	COLUMBO
OBS51	NE of Columbo	36° 33.180'N	25° 31.220'E	-203	COLUMBO
OBS52	betw. Anidros and Anafi	36° 30.000'N	25° 39.000'E	-367	COLUMBO
OBS53	betw. Ios and Anidros	36° 38.500'N	25° 30.000'E	-401	COLUMBO
OBT54	WNW slope of Columbo	36° 31.400'N	25° 27.600'E	-251	COLUMBO
OBT55	WNW summit of Columbo	36° 31.200'N	25° 28.000'E	-124	COLUMBO
OBT56	ESE summit of Columbo	36° 30.750'N	25° 28.730'E	-106	COLUMBO
OBT57	ESE slope of Columbo	36° 30.295'N	25° 29.995'E	-292	COLUMBO
PARO	Paros East	37° 06.900'N	25° 10.950'E	72	EGELADOS
PARS	Paros South	37° 01.710'N	25° 13.518'E	150	EGELADOS
SCHI	Schinoussa	36° 52.464'N	25° 31.080'E	100	EGELADOS

Table A.1: List of seismic stations of the EGELADOS and COLUMBO networks, of which data were used for processing.

All stations used for picking and further processing are listed in Tab. A.1. No stations of an epicentral distance of more the 80 km were used (farrest from Columbo is MYKO).

<i>Phase:</i>	<i>P [s]</i>	<i>S [s]</i>	<i>Phase:</i>	<i>P [s]</i>	<i>S [s]</i>
AMOE	+0.02	+0.06	PARO	-0.09	+0.09
AMOS	-0.08	+0.08	PARS	0.00	+0.20
ANAF	+0.04	+0.28	SCHI	-0.02	+0.15
ANID	-0.03	+0.11	OBS50	-0.08	+0.01
ANPA	-0.09	+0.05	OBS51	-0.02	+0.03
ASTY	+0.07	+0.30	OBS52	-0.01	+0.10
FOLE	0.00	+0.15	OBS53	-0.20	-0.17
IOSI	+0.02	+0.41	OBT54	-0.03	+0.09
MYKO	-0.20	+0.05	OBT55	-0.07	+0.08
NAXO	-0.15	0.00	OBT56	-0.10	0.00
NEAK	-0.09	+0.07	OBT57	-0.12	+0.02

Table A.2: Station corrections of SEISAN. Given values are average residuals of all P- or S-picks of a station. Positive values stand for theoretical onsets estimated after the given pick, negative values mark estimated onset before the given pick.

Station corrections given in Tab. A.2 are estimated of the average SEISAN pick-residuals for each P- and S-phase of all stations. With the found values, pick times were corrected and events were relocated in a single event location using HYPOSAT. In a second step, relative relocation using HYPODD was performed using the corrected HYPOSAT single locations.

A.2 Instrumentation

<i>station</i>	<i>seismometer</i>	<i>tiltmeter</i>	<i>hydrophone</i>	<i>absolute pressure</i>	<i>comments</i>
AMOE	L4-3D	-	-	-	ok
AMOS	CMG3	-	-	-	ok
ANAF	L4-3D	-	-	-	ok
ANID	L4-3D	-	-	-	noisy
ANPA	CMG3	-	-	-	ok
ASTY	STS2	-	-	-	noisy
FOLE	CMG3	-	-	-	ok
IOSI	STS2	-	-	-	ok
MYKO	STS2	-	-	-	ok
NAXO	L4-3D	-	-	-	ok
NEAK	L4-3D	-	-	-	extremely noisy
OBS50	EP300	-	DPG	RBR	ok
OBS51	EP300	-	DPG	-	Z weak
OBS52	PMD	-	OAS	-	E weak
OBS53	PMD	-	OAS	-	Z out of range
OBT54	-	Lippmann	OAS	RBR	RBR down March 2007
OBT55	-	Lippmann	OAS	RBR	RBR down January 2007
OBT56	-	Lippmann	OAS	RBR	shut down after 35 days
OBT57	-	Lippmann	OAS	RBR	RBR down September 2006
PARO	L4-3D	-	-	-	ok
PARS	L4-3D	-	-	-	ok
SCHI	L4-3D	-	-	-	noisy

Table A.3: List of instrumentation of each on- and offshore station.

- seismometers:
 - STS2: Streckeisen 120sec seismometer
 - CMG3: Guralp 30sec seismometer
 - L4-3D: Lennartz 4sec seismometer
 - PMD: Force Balanced Broadband Seismometer (manuf. PMD, model EP-105)
 - EP300: Force Balanced Broadband Seismometer (manuf. PMD, model EP-300)
- pressure sensors:
 - DPG: Differential Pressure Gauge (SCRIPPS), Period: 0.5-500 s
 - OAS: Relative pressure sensor
 - RBR: Absolute pressure sensor
- tilt sensor
 - Lippmann: 2 component tiltmeter

<i>network</i>	<i>data logger</i>	<i>sampling rate [Hz]</i>	<i>operating institution</i>
COLUMBO (OBSs/OBTs)	Send GEOLON MLS	50	University of Hamburg
EGELADOS (onshore stations)	Earth Data Logger	100	Ruhr University Bochum

Table A.4: List of all used data loggers and sampling rates

Ladstations of the EGELADOS project were run with Earth Data Loggers (EDL) of the German DEPAS Pool for amphibian seismology at a sampling rate of 100 Hz, the Hamburg OBSs/OBTs were run with GEOLON Marine Longterm Seismocorders (MLS) at 50 Hz (see Tab A.4).

<i>sensor</i>	<i>No. of zeros</i>	<i>zeros [re, im]</i>	<i>No. of poles</i>	<i>poles [re, im]</i>	<i>gain (incl. logger)</i>
STS2	2	0.0 0.0 0.0 0.0	2	-0.03674286 -0.03674286 -0.03674286 0.03674286	600 counts · s/μm
L4-3D	2	0.0 0.0 0.0 0.0	2	-4.65 4.69 -4.65 -4.69	190 counts · s/μm
CMG3	2	0.0 0.0 0.0 0.0	2	-0.147 0.147 -0.147 -0.147	787.2 counts · s/μm
OAS	1	0.0 0.0	1	-20. 0.0	524.25 counts/Pa
DPG	3 0.0 0.0	0.0 0.0 -6281.0 0.0	5	-3.29E-02 0.0 -316.4 0.0 -30.3 0.0 -0.21 0.0 -1377.4 0.0	463.2 counts/Pa

Table A.5: Poles and zeros of seismic sensors as they were used for magnitude estimation and moment tensor inversion.

Poles and zeros given in Tab. A.5 are standart values provided by manufacturers. As shown in App. C.1, poles & zeros provided for PMD are not reliable: Theoretically calculated sensor responses strongly differ from their real responses. Of OBSs/OBTs, only hydrophone data was taken for moment tensor inversion.

A.3 Bandpass filters

<i>Phase</i>	<i>fL1 [Hz]</i>	<i>fL2 [Hz]</i>	<i>fH1 [Hz]</i>	<i>fH2 [Hz]</i>	<i>cosine taper [%]</i>
P	3	6	15	20	15
S	3	6	20	24	10

Table A.6: Bandpass Filters applied to seismic data before cross correlation. Time windows cut off the continuous data were bandpass filtered before cross correlation with an acausal filter with the above given frequencies.

Bandpass filters given in Tab. A.6 are relatively similar to experiences of other experiments (e.g. North Iceland Experiment (Hensch, 2005)). They were found by analysing the frequency spectra of the earthquakes (see Figs. A.1 and A.2) and smoothly varied by trial and error to find the best correlation results. The filter is applied automatically by the COMA correlation routine (Reinhardt, 2002) on each time window for P- and S-phases.

Filter effects were eliminated by tapering beginning and end of the time windows. For P-phases, the length of the taper was chosen longer to also reduce effects due to reflected waves from the sea surface: These PwP waves flip their phase by 180° due to the negative contrast of impedance at the sea surface, while their energy keeps nearly stable because of a reflection coefficient of nearly 1 for the water-air boundary. This can cause above average high negative correlation coefficients, which is even found for shallow stations, where the PwP phase arrives shortly after the P phase (see Appendix B).

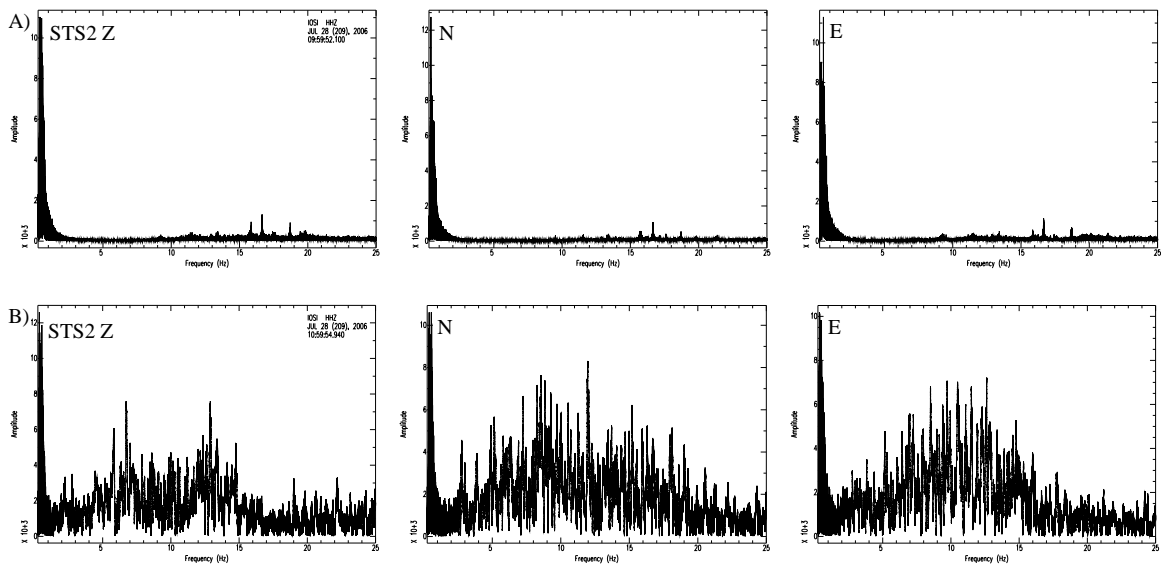


Figure A.1: Powerspectra of STS2 landstation IOSI, A) for an hour of quiescence and B) for an earthquake swarm with magnitudes between 1 and 4. While the sea microseismicity has a frequency of less than 1 Hz, the frequency domain of the earthquakes is between 2 and 20 Hz.

Figs. A.1 and A.2 show powerspectra for on- and offshore stations for the preceding and the initial hour of an earthquake swarm on 28th of July 2006. The peak below 1 Hz is caused by sea

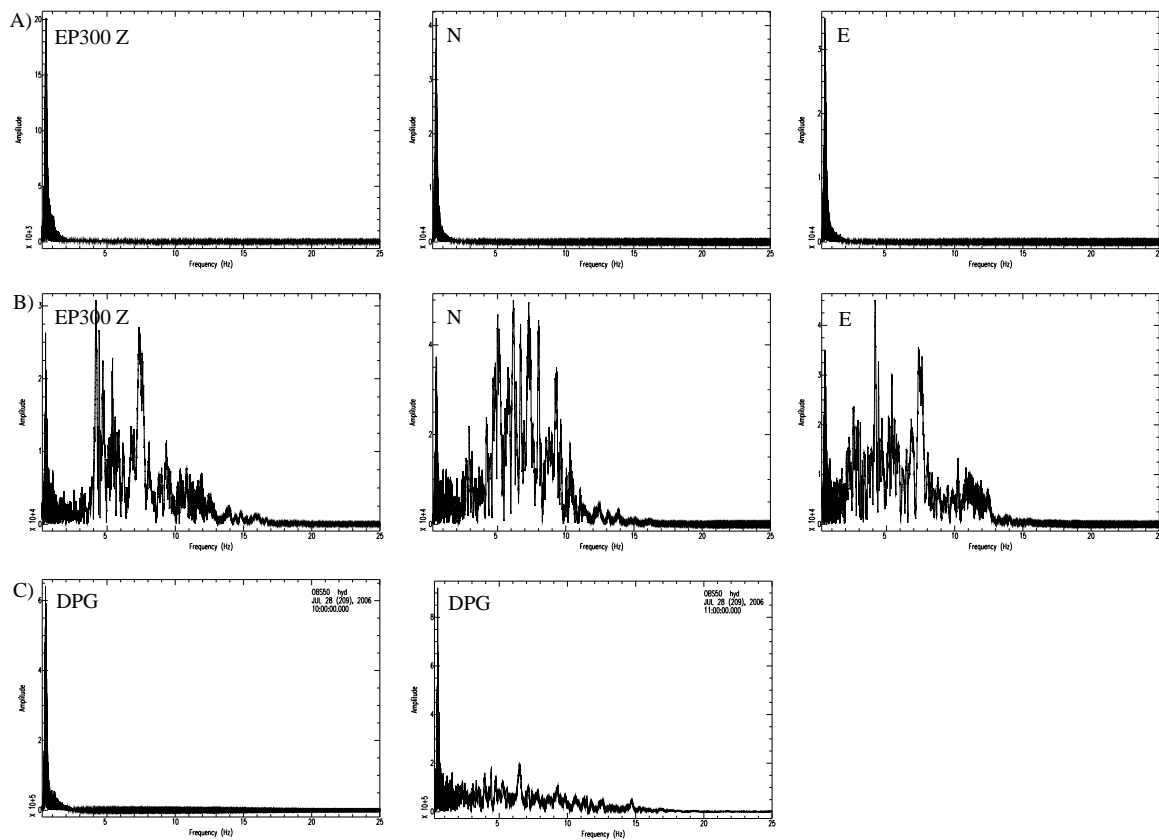


Figure A.2: Powerspectra of EP300/DPG offshore station OBS50, A) for an hour of quiescence, B) for an earthquake swarm with magnitudes between 1 and 4 and C) for the Differential Pressure Gauge (DPG), also quiescence and swarm.

microseismicity, the frequency domain of the events is between 2 and 20 Hz. Although there is event energy starting from 2 Hz, best filters were found as shown in Tab. A.6. Most events are of small magnitude, lower frequencies only occur for higher magnitudes, thus bandpasses start with 3-6 Hz. Due to strong effects of higher frequencies on the cross-correlation, these frequencies are also cut off.

Values given in this subsection only show filters used before cross-correlating the waveforms. Filters applied while picking were manually chosen case-dependent by the respective operator.

CORRELATION COEFFICIENTS

B.1 Correlation coefficients of the Columbo Experiment

The following histograms give an overview of the distributions of correlation coefficients. Thresholds (t_1 and t_2) are given for each station and each phase, from which on data was used for relocalisation. Green curves show positive, red curves negative correlation coefficients. Thresholds (t_1) were set on the position from which on the green curve is obviously dominating, usually at about $n(cc_{(red)}^-) < \frac{1}{2}n(cc_{(green)}^+)$. Another, mostly smaller value (t_2), marks the approximately end of a normal Gauss curve.

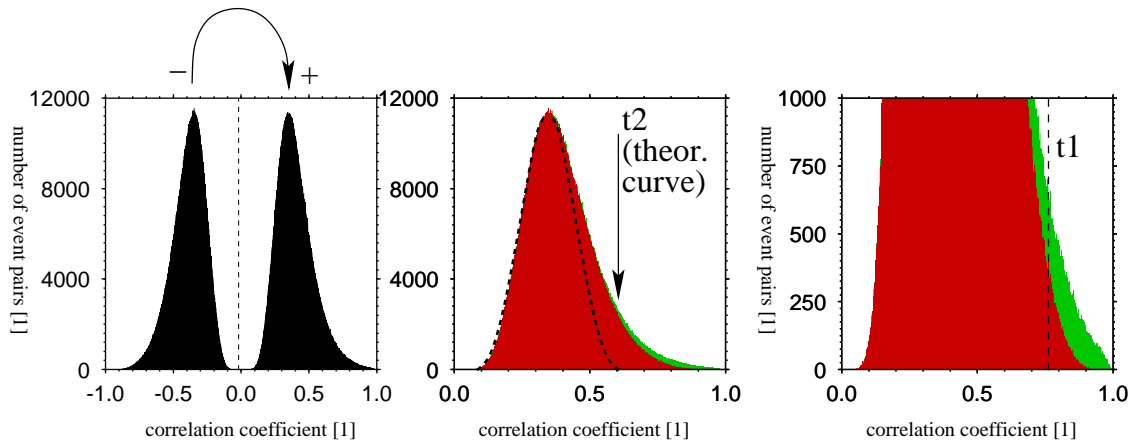


Figure B.1: Analysis of correlation curves: The negative (red) curve is mirrored at the y-axis and laid onto the positive (green) curve. The remaining tail of highly positive values is the data of interest.

Fig. B.1 shows how both estimated thresholds: The given curves are frequency distributions of correlation values, i.e. each point of the histogram stands for the correlation result of one event pair. Most events show some random correlation with mostly low cross correlation values. these events form the curve of average correlation, negative as positive. While a correlation of zero is nearly excluded due to a small similarity of all timetraces among each other, above average high correlation results of waveform similarities due to clustering in the same source region. These are the data of interest. Therefore, the curve of negative correlation

coefficients (here red) is mirrored at the y-axis and laid onto the curve of positive correlation coefficients (here green). Both threshold are then determined by hand, t_1 for values where the positive curve is dominant, t_2 for values larger than the estimated end of a symmetric curve.

Both matrices $M_{cc}(t_1)$ and $M_{cc}(t_2)$ of correlation values were tested in *hypodD* to relocate the clusters. Additionally, a third and fourth trial was done, where also above average high negative values were added to the matrices. While we found by trial and error, that a threshold orientated at the theoretical shape of the curve (t_2) includes too many randomly high correlating event pairs, the best solution was derived by taking threshold t_1 and including the negative values, whose absolute value is $> t_1$.

Above average high negative correlation can result of two factors:

- station close to nodal plane (180° flip of polarisation due to slight shifts of the faultplane orientation or location of the event)
- PwP phase for shallow OBSs/OBTs (phase reversal at water surface, see also App. A.3)

Figs. B.2-B.4 show cross correlation results as well as t_1 - and t_2 -values for each station and each phase that was used for relative relocation. Since all clusters, partly spatially separated by some kilometers, were correlated all together the green tail is often minimal in contrast to the rest of the curve, but still includes some tens to thousands of eventpairs.

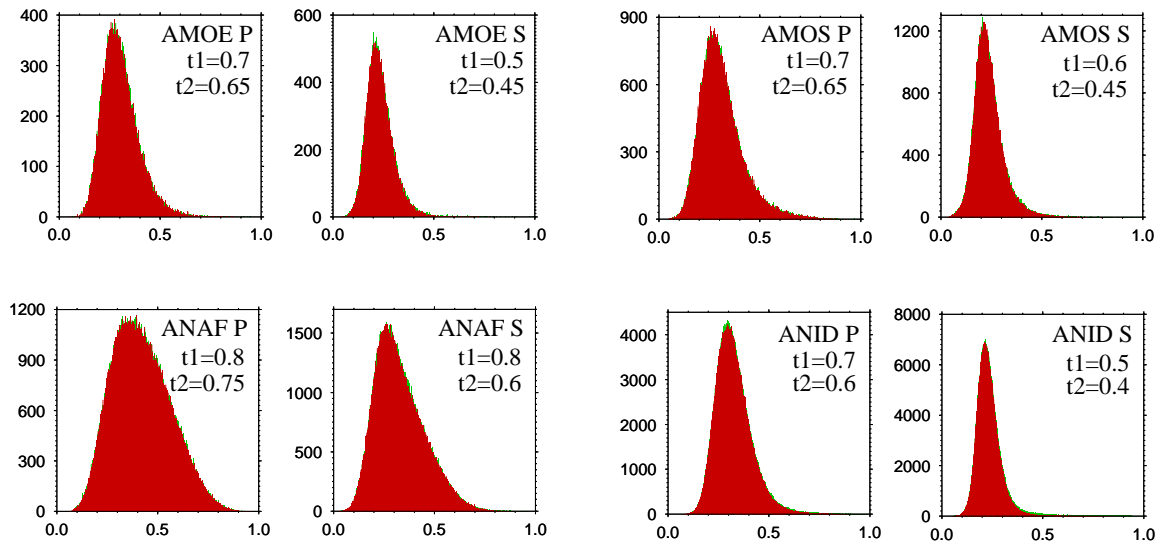


Figure B.2: Distributions of correlation coefficients

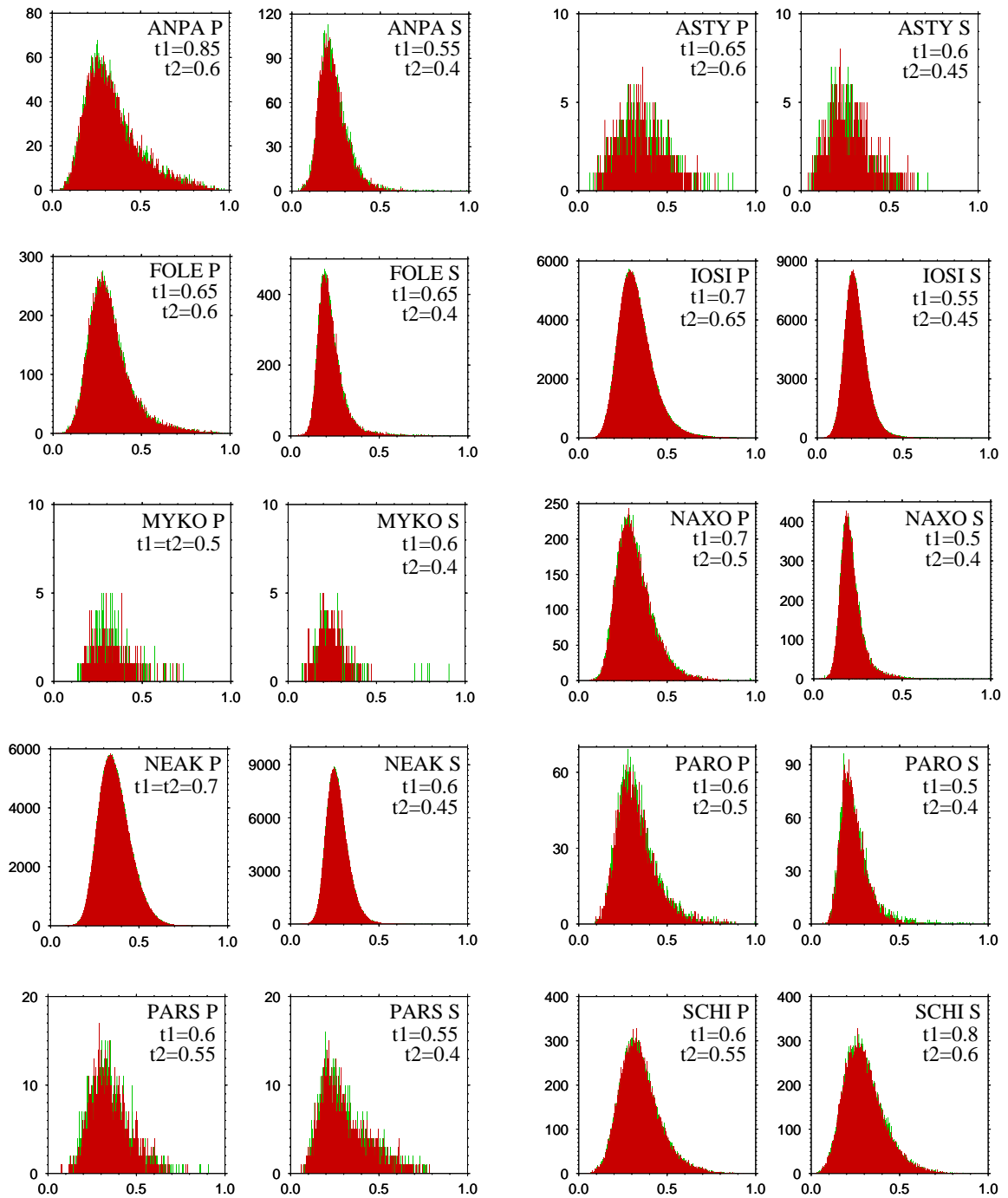


Figure B.3: Distributions of correlation coefficients

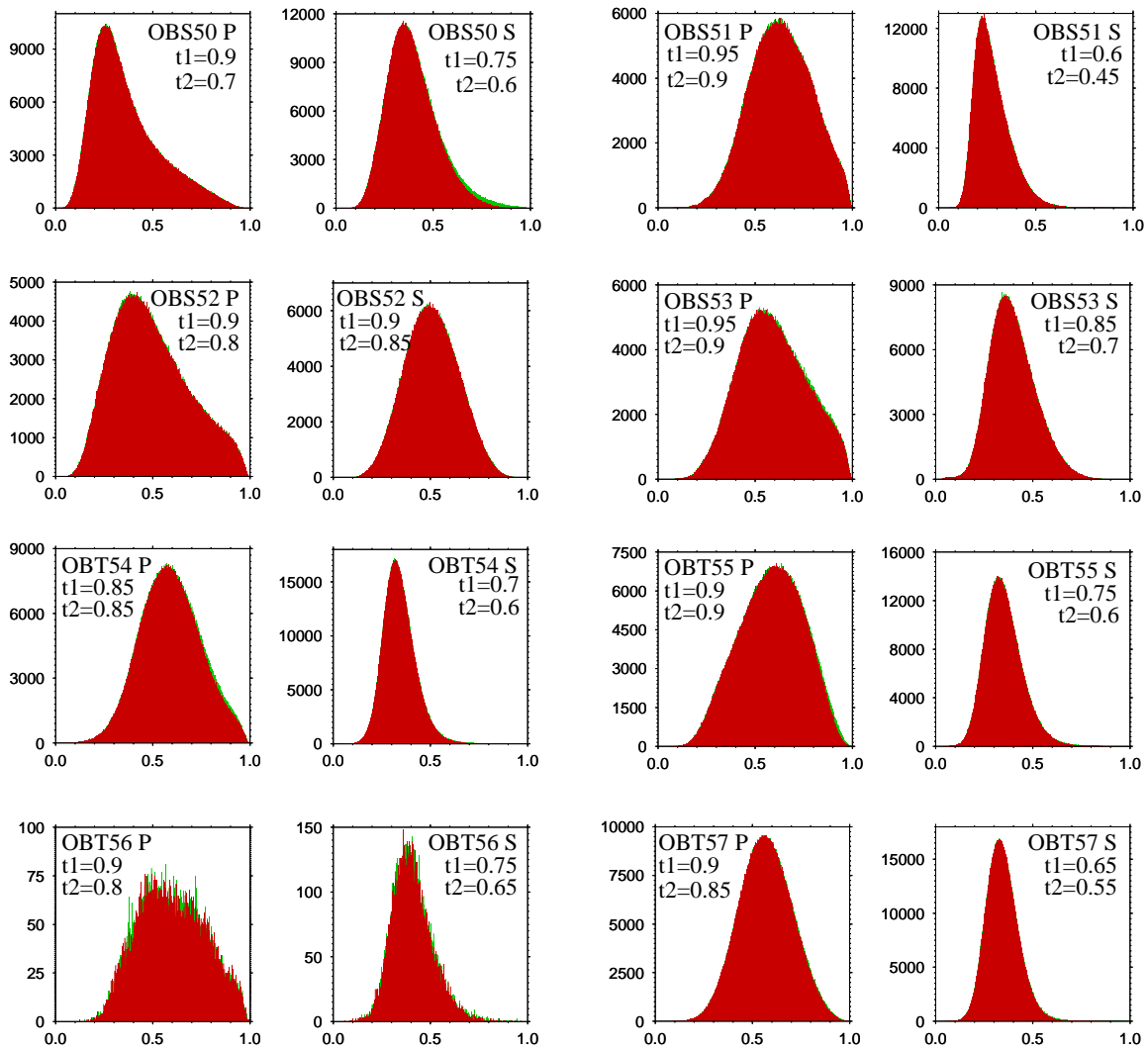


Figure B.4: Distributions of correlation coefficients

INSTRUMENT CALIBRATION

Knowledge about the transfer function of seismometers and tiltmeters is absolutely necessary for data-interpretation. The investigation of the sensor-response on seismic and tilt signals caused by known displacement, velocity or acceleration allows the later on interpretation of data caused by signals of unknown strength and source.

We used a tilt-table to cause small horizontal acceleration on the sensor by giving slight tilt-steps (see Fig.C.1). While a tiltmeter should show a linear response on increasing quasi-static deformation, a seismometer acts as a highpass filter and thus starts swinging with its lower corner frequency (the upper corner frequency is simply given by the Nyquist frequency, i.e. half of the recorders sampling rate, here $f_s = 50 \text{ Hz}$, i.e. $f_{Ny} = 25 \text{ Hz}$).

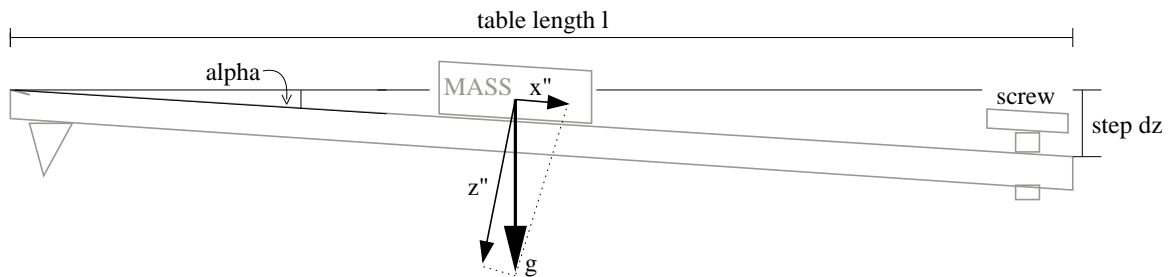


Figure C.1: Setup of tilt-table and sensor. The signal is given with a precise screw that lowers the table-height at one side. This causes low horizontal acceleration \ddot{x} on the mass.

The component of horizontal acceleration \ddot{x} is given with:

$$\ddot{x} = \sin \alpha \cdot g$$

$$\text{with } \alpha = 2 \cdot \arcsin \frac{\Delta z / 2}{l}$$

($l = 585 \text{ mm}$, i.e. length of the tilt-table).

C.1 Seismometer calibration

The expected output $U(\omega)$ for a known acceleration input $I_a(\omega)$ is given with:

$$U(\omega) = I_v(\omega)T_v(\omega) = i\omega I_d(\omega)T_v(\omega) = \frac{I_a(\omega)}{i\omega}T_v(\omega) \quad (\text{C.1})$$

where ω is the angular frequency, i the imaginary unit and the indices d , v and a stand for **d**isplacement, **v**elocity and **a**cceleration.

Equivalent velocity input to an acceleration step is an infinite ramp with a slope of given acceleration. The Laplace Transform of such a slope is proportional to $\frac{1}{(i\omega)^2}$ which shows that low frequencies are efficiently excited with a tilt table. While seismometers typically cannot measure very long period motions and quasi-static offsets, they act as highpass filters. Thus, the response due to a tilt step enables to investigate the transfer function at and slightly below the corner frequency of the sensor.

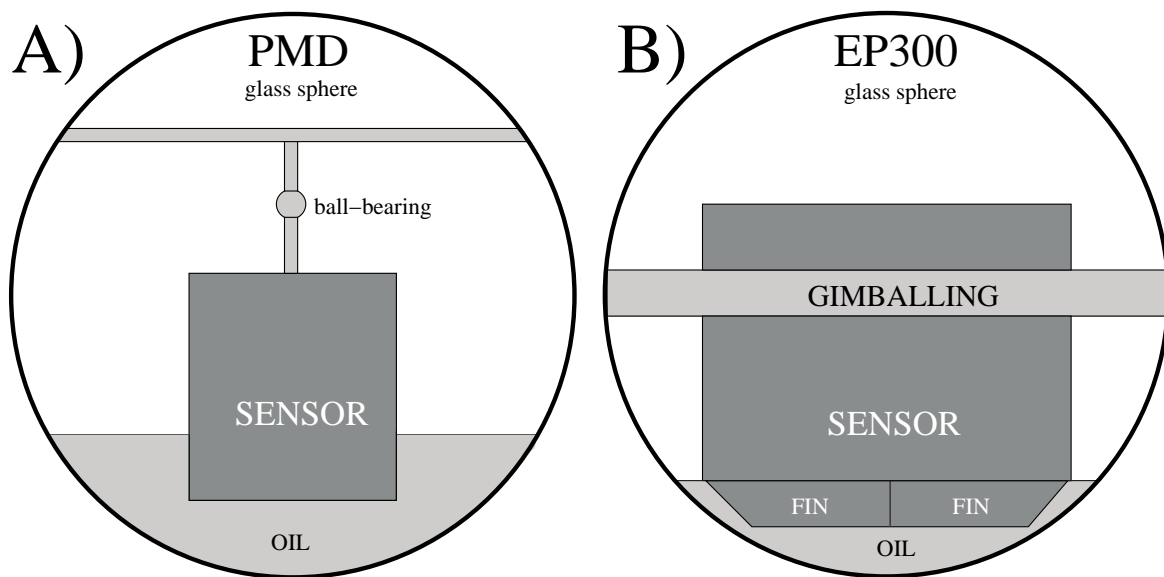


Figure C.2: Instrument spheres of PMD and EP300 seismometers. Whereas the PMD sensor is hanging at a ball-bearing directly in high viscous oil, the EP300 is mounted on a table that has contact to the oil by fins. The EP300 is gimballed by hanging in two rings with perpendicular axes.

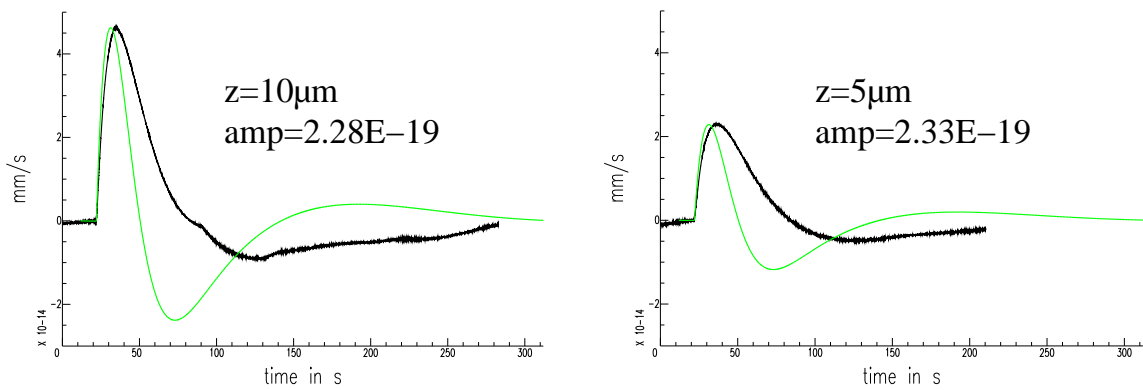
$\Delta z [\mu\text{m}]$	<i>residual</i> $\sigma_z [\mu\text{m}]$	$\Delta\alpha [\text{deg}]$	<i>residual</i> $\sigma_\alpha [\text{deg}]$	<i>horiz. acc.</i> $a [\frac{\text{m}}{\text{s}^2}]$	<i>residual</i> $\sigma_a [\frac{\text{m}}{\text{s}^2}]$
5	± 3	0.0005	± 0.0003	0.00009	± 0.00005
10	± 3	0.001	± 0.0003	0.00017	± 0.00005
20	± 3	0.0019	± 0.0003	0.00033	± 0.00005

Table C.1: Tilt-steps for seismometer calibration and resulting horizontal accelerations.

C.1.1 PMD sensor

Calibration curves for both used PMD sensors are given in Fig.C.3 and Fig.C.4:

NS component:



EW component:

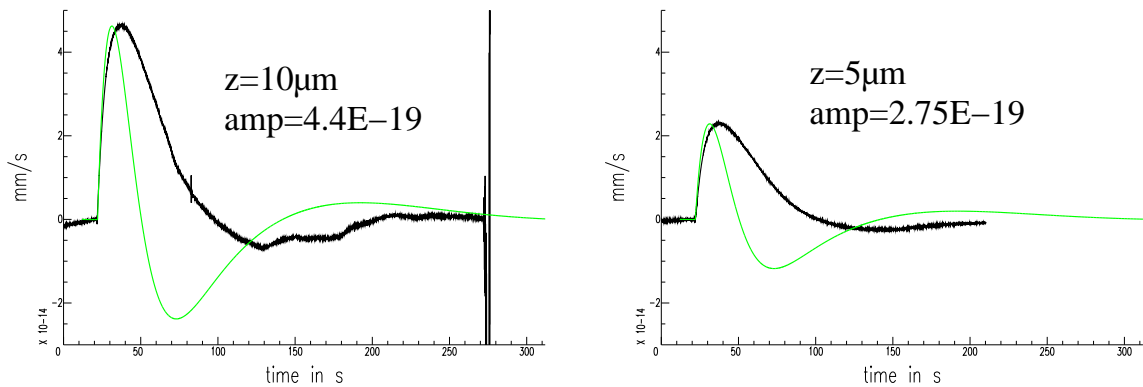
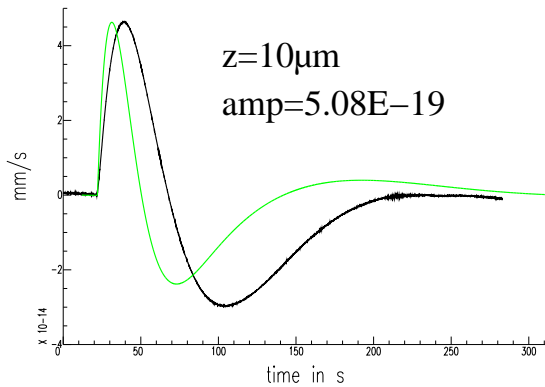


Figure C.3: Theoretic (green) and measured (black) velocity response curves for PMD sensor s/n 512.

Measured resonance frequencies are lower than theoretically predicted. Possible reasons therefor could be the interaction of both, characteristics of the seismometer and the high viscous oil. Also theoretical calculations assume an acceleration step in form of a static offset; the tilted oil-system slowly shifts back to a vertical position and thus decreases the horizontal acceleration. Non-linearity of the amplification factor as observed for PMD 512 may also be

NS component:



EW component:

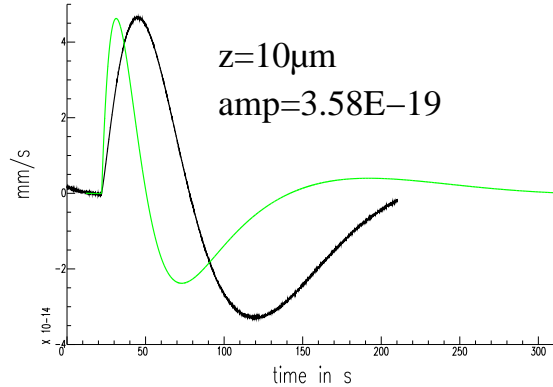
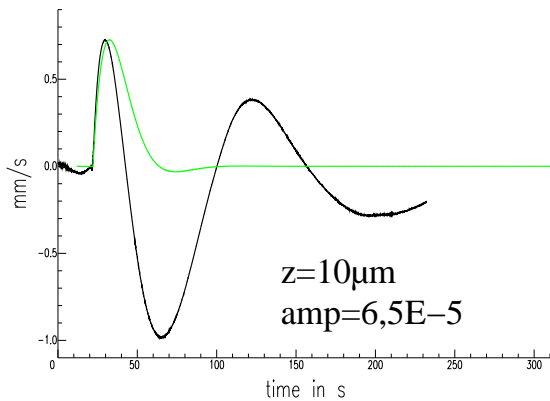


Figure C.4: Theoretic (green) and measured (black) velocity response curves for PMD sensor s/n 4. The same is observed here: The resonance frequency of the whole OBS system seems to be lower than the instrument's theoretic eigenfrequency.

result of systematic errors during the measurements, since a step of 5 μm is nearly in the range of the step residual.

C.1.2 EP300 sensor

NS component:



EW component:

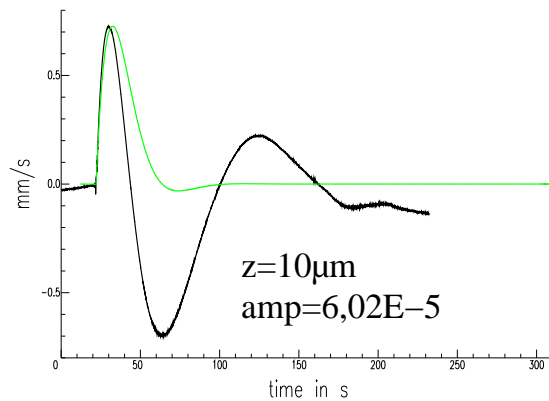


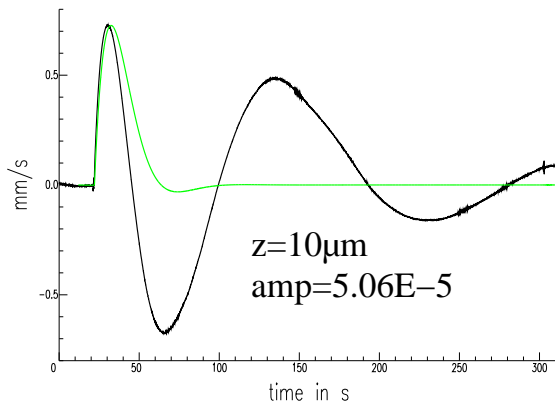
Figure C.5: Theoretic (green) and measured (black) velocity response curves for an EP300 seismometer (s/n 10535). The resonance frequency of the oil-system is slightly higher than the theoretic. Oscillation keeps on much longer than suggested by the theoretic curve.

Also the EP300 - oil system has an own characteristic, but here the resonance frequency of the whole system is slightly higher than for the seismometer itself.

C.1.3 Comparison

Quantitative description (see Fig.C.7):

NS component:



EW component:

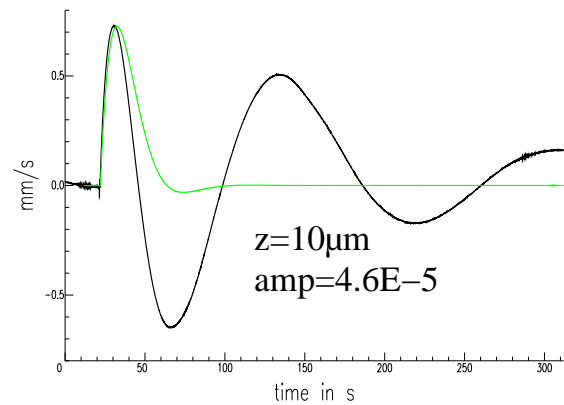


Figure C.6: Theoretic (green) and measured (black) velocity response curves for an EP300 seismometer (s/n 10536). Same here: Slightly higher resonance frequency of the seismometer in oil and subcritical attenuation.

- Theoretic curves show small similarity in terms of period.
- For measured curves (OBS - oil system) the resonance frequency increases in opposite to the theoretic curves for the EP300, for the PMD it decreases
- While for the PMD (instead of period) the measured curves crudely resemble the theoretic ones, at least in terms of shape, EP300 measurements totally differ from theory (period and attenuation).

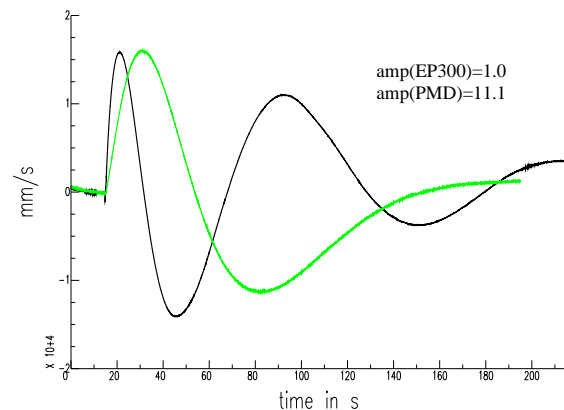
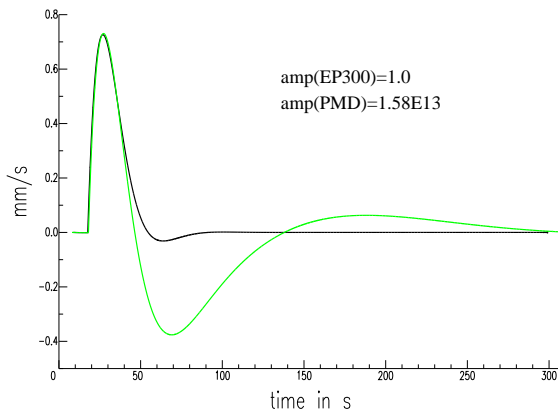


Figure C.7: Comparison of theoretic and measured curves of EP300 (black) and PMD (green) sensors. While there is a crude similarity of theoretic curves (left picture), measured curves differ (right picture): The EP300 delivers shorter periods as expected, the PMD longer periods. Additionally, the EP300 seems to be not well attenuated.

The subcritical attenuation of the EP300s is supposed to be a fault in construction of these seismometers. To verify that measured resonance frequencies resemble both, seismometer and oil characteristics, a crude modelling of the shifting velocity of the different sensors through the oil with respect to their immersion depths was done.

Fig.C.2 shows, that the PMD sensor is much deeper immersed in oil than the EP300 (5-8cm for the PMD in comparison to 3cm for the fins under the EP300). Also for non-spheric bodies, the Stokes equation (C.2) is a crude approximation for the velocity v_p of a particle, preconditioned that the Reynoldsnumber $R_e < 1$, which is the case for a body in high viscous oil (viscosity $\nu = 200.000 \frac{Ns}{m^2}$):

$$v_p = \frac{2r^2a(\rho_{eff} - \rho_{oil})}{9\nu} \quad (C.2)$$

ρ_{eff} is the effective density, i.e. the constant mass of the whole seismometer reduced on its immersed part:

$$\rho_{eff} = \frac{m_{seis}}{V_{eff}} = \frac{m_{seis}}{\frac{3}{4}\pi r_{eff}^3} \quad (C.3)$$

with

$$r_{eff} = \frac{r_{seis} + \frac{z_{immersed}}{2}}{2} \quad (C.4)$$

Thus, increasing the immersion depth has similar effects as increasing the particles volume while keeping the mass stable (density decrease). The result of this modelling is the curve in Fig.C.8: Especially for small immersion depths, the particle velocity decrease rapidly for increasing oil depth. Note, that this is a crude approximation with ideal values. But the effect discussed above can thus be verified.

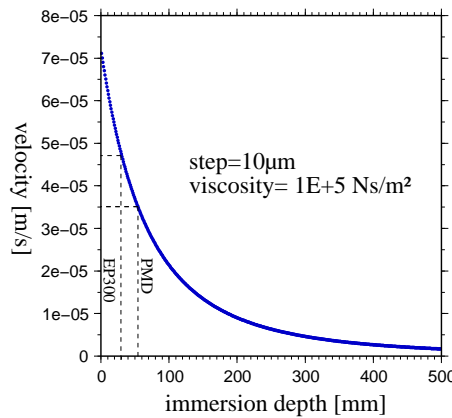


Figure C.8: Back-shift velocity according to immersion depth of the seismometer. The deeper the instrument is immersed in oil, the lower its velocity through it, i.e. the higher the system's period.

C.2 Tiltmeter calibration

All tiltmeters have been calibrated before deployment on the same tilt-table as it was used for the seismometers. The tiltmeter itself is a horizontal accelerometer and reacts as a causal lowpass filter on static (tilt) and dynamic (seismic waves) signals. For each component of each instrument, several tilt steps of varying size were performed, the individual calibration curve was estimated by linear regression.

$\Delta z[\text{mm}]$	<i>residual</i> $\sigma_z[\text{mm}]$	$\Delta\alpha[\text{deg}]$	<i>residual</i> $\sigma_\alpha[\text{deg}]$
0.5	± 0.01	0.0490	± 0.0001
1	± 0.01	0.0979	± 0.0001
1.5	± 0.01	0.1469	± 0.0001
2	± 0.01	0.1959	± 0.0001
3	± 0.01	0.2938	± 0.0001

Table C.2: Tilt-steps for tiltmeter calibration. Given misfit is the accuracy of the tilt steps.

Misfits in the following tables are calculated as an average of the measured values for a given time window before and after the tilt steps. For the calibration curve, they were calculated by linear regression error estimation.

The calibration curve is a line through the origin ($y = bx + a$ and $a = 0$), i.e. for linear regression the following simplified approach was used:

$$b = \frac{\sum_{i=1}^n x_i y_i}{\sum_{i=1}^n x_i^2} \quad (\text{C.5})$$

With a standart deviation of:

$$s_b = \sqrt{\frac{1}{n-1} \frac{\sum_{i=1}^n (y_i - bx_i)^2}{\sum_{i=1}^n x_i^2}} \quad (\text{C.6})$$

Tiltmeter OBT54 (sensor no. 1)

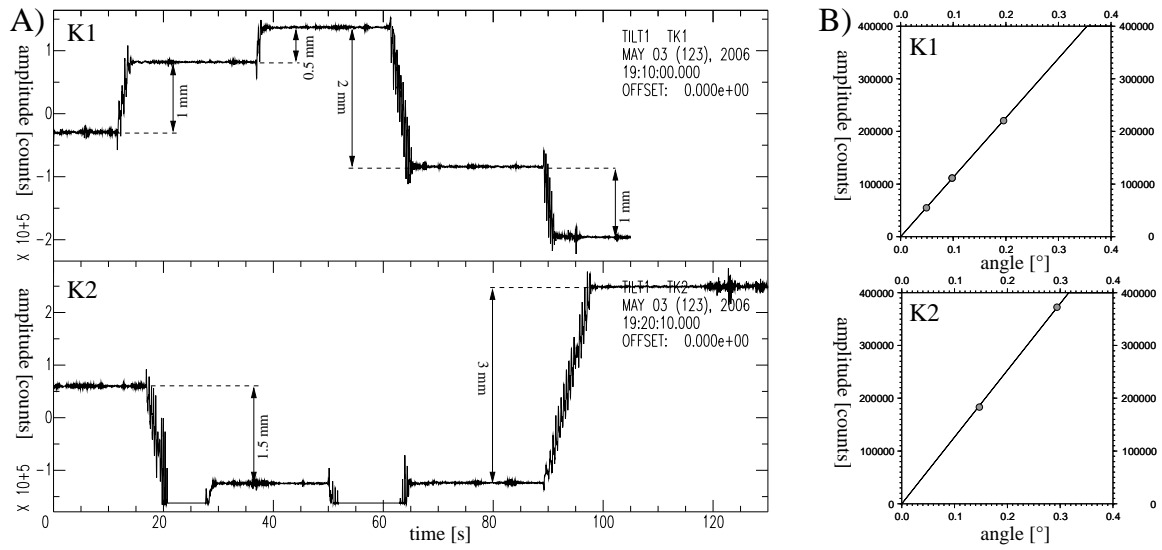


Figure C.9: Calibration measurements of tiltmeter 1: A) raw data with defined tilt-steps (see tables C.2 and C.3), B) linear regression of calibration data.

<i>comp</i>	$\Delta\alpha[deg]$	<i>start</i> [counts]	<i>end</i> [counts]	$ \Delta [counts]$
K1	0.0490 ± 0.0001	103000 ± 3000	158000 ± 3000	55000 ± 5000
K1	0.0979 ± 0.0001	-8000 ± 2000	103000 ± 3000	111000 ± 4000
K1	0.0979 ± 0.0001	-62000 ± 4000	-173000 ± 4000	111000 ± 6000
K1	0.1959 ± 0.0001	158000 ± 3000	-62000 ± 4000	220000 ± 5000
K2	0.1469 ± 0.0001	-6000 ± 2000	-189000 ± 6000	183000 ± 7000
K2	0.2938 ± 0.0001	-189000 ± 5000	183000 ± 3000	372000 ± 7000

Table C.3: Tilt-steps for tiltmeter 1 (OBT54) and resulting output signal.

- K1: $y = 1\,130\,000 \pm 5\,000 \frac{\text{counts}}{\text{deg}}$
- K2: $y = 1\,264\,000 \pm 7\,000 \frac{\text{counts}}{\text{deg}}$

Tiltmeter OBT55 (sensor no. 3)

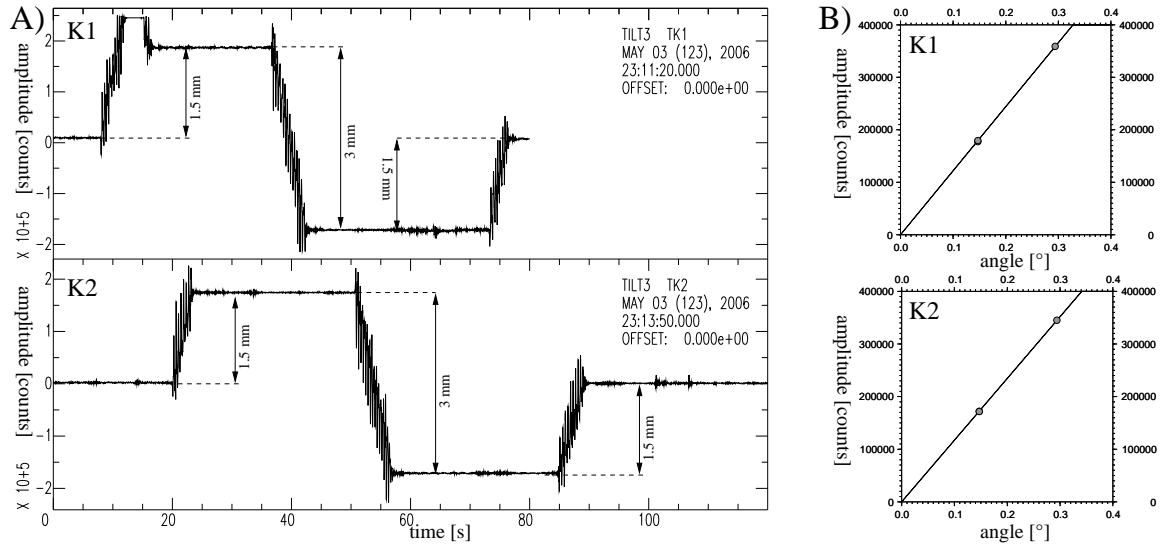


Figure C.10: Calibration measurements of tiltmeter 1: A) raw data with defined tilt-steps (see tables C.2 and C.4), B) linear regression of calibration data.

<i>comp</i>	$\Delta\alpha[\text{deg}]$	<i>start</i> [counts]	<i>end</i> [counts]	$ \Delta $ [counts]
K1	0.1469 ± 0.0001	-7000 ± 900	170000 ± 1000	177000 ± 1500
K1	0.1469 ± 0.0001	-188000 ± 2000	-9000 ± 700	179000 ± 2000
K1	0.2938 ± 0.0001	170000 ± 1000	-188000 ± 2000	358000 ± 2000
K2	0.1469 ± 0.0001	-3000 ± 1000	169000 ± 5000	172000 ± 5000
K2	0.1469 ± 0.0001	-176000 ± 4000	-4000 ± 1000	172000 ± 5000
K2	0.2938 ± 0.0001	169000 ± 4000	-176000 ± 4000	345000 ± 6000

Table C.4: Tilt-steps for tiltmeter 3 (OBT55) and resulting output signal.

- K1: $y = 1\,220\,000 \pm 3\,000 \frac{\text{counts}}{\text{deg}}$
- K2: $y = 1\,173\,000 \pm 5\,000 \frac{\text{counts}}{\text{deg}}$

Tiltmeter OBT56 (sensor no. 4)

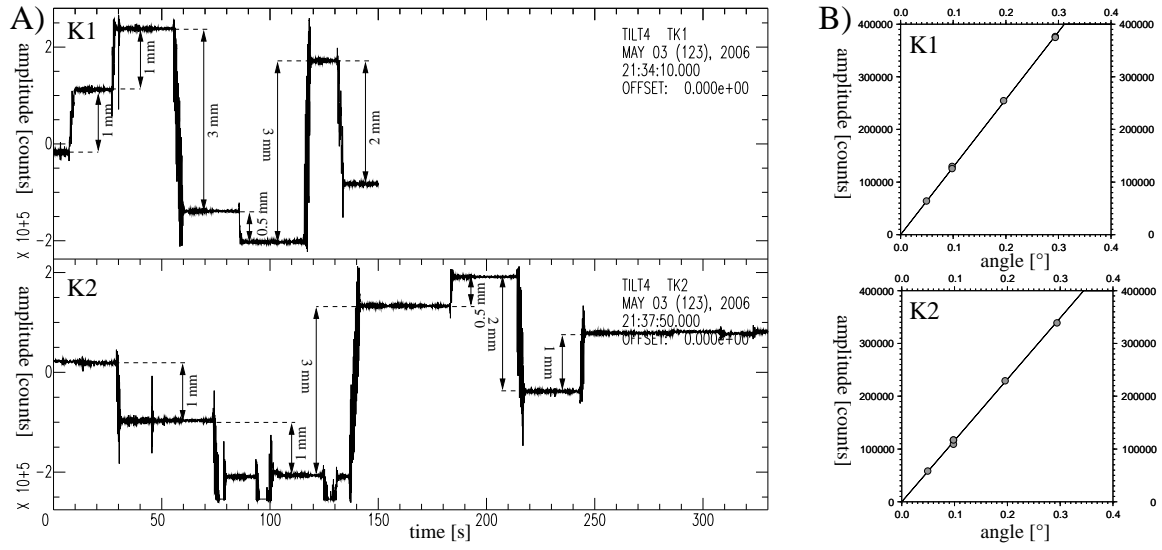


Figure C.11: Calibration measurements of tiltmeter 1: A) raw data with defined tilt-steps (see tables C.2 and C.5), B) linear regression of calibration data.

<i>comp</i>	$\Delta\alpha[\text{deg}]$	<i>start</i> [counts]	<i>end</i> [counts]	$ \Delta [\text{counts}]$
K1	0.0490 ± 0.0001	-163000 ± 1000	-227000 ± 2000	64000 ± 2000
K1	0.0979 ± 0.0001	-41000 ± 4000	88000 ± 2000	129000 ± 5000
K1	0.0979 ± 0.0001	88000 ± 2000	214000 ± 6000	126000 ± 7000
K1	0.1959 ± 0.0001	148000 ± 2000	-107000 ± 2000	255000 ± 3000
K1	0.2938 ± 0.0001	214000 ± 6000	-163000 ± 1000	377000 ± 6000
K1	0.2938 ± 0.0001	-227000 ± 2000	148000 ± 2000	375000 ± 3000
K2	0.0490 ± 0.0001	159000 ± 1000	217000 ± 1000	58000 ± 2000
K2	0.0979 ± 0.0001	45000 ± 2000	-71000 ± 4000	116000 ± 5000
K2	0.0979 ± 0.0001	-71000 ± 4000	-180000 ± 4000	109000 ± 6000
K2	0.0979 ± 0.0001	-13000 ± 1000	105000 ± 2000	118000 ± 3000
K2	0.1959 ± 0.0001	217000 ± 1000	-13000 ± 1000	230000 ± 2000
K2	0.2938 ± 0.0001	-180000 ± 4000	159000 ± 1000	339000 ± 5000

Table C.5: Tilt-steps for tiltmeter 4 (OBT56) and resulting output signal.

- K1: $y = 1\,285\,000 \pm 5\,000 \frac{\text{counts}}{\text{deg}}$
- K2: $y = 1\,161\,000 \pm 8\,000 \frac{\text{counts}}{\text{deg}}$

Tiltmeter OBT57 (sensor no. 5)

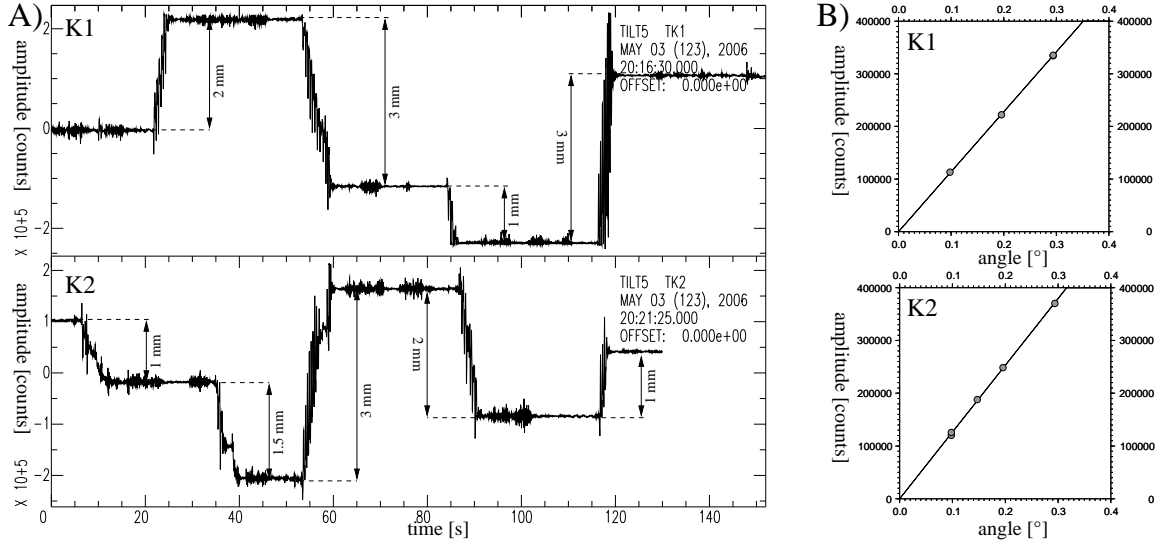


Figure C.12: Calibration measurements of tiltmeter 1: A) raw data with defined tilt-steps (see tables C.2 and C.6), B) linear regression of calibration data.

comp	$\Delta\alpha[\text{deg}]$	start[counts]	end[counts]	$ \Delta [\text{counts}]$
K1	0.0979 ± 0.0001	-114000 ± 3000	-227000 ± 3000	113000 ± 4000
K1	0.1959 ± 0.0001	-1000 ± 5000	221000 ± 4000	222000 ± 6000
K1	0.2938 ± 0.0001	220000 ± 4000	-114000 ± 3000	334000 ± 5000
K1	0.2938 ± 0.0001	-227000 ± 3000	109000 ± 2000	336000 ± 4000
K2	0.0979 ± 0.0001	121000 ± 4000	1000 ± 5000	122000 ± 6000
K2	0.0979 ± 0.0001	-65000 ± 5000	60000 ± 1000	125000 ± 5000
K2	0.1469 ± 0.0001	1000 ± 5000	-187000 ± 5000	188000 ± 7000
K2	0.1959 ± 0.0001	183000 ± 6000	-65000 ± 5000	248000 ± 7000
K2	0.2938 ± 0.0001	-187000 ± 5000	183000 ± 5000	370000 ± 7000

Table C.6: Tilt-steps for tiltmeter 5 (OBT57) and resulting output signal.

- K1: $y = 1\,139\,000 \pm 2\,000 \frac{\text{counts}}{\text{deg}}$
- K2: $y = 1\,264\,000 \pm 6\,000 \frac{\text{counts}}{\text{deg}}$

Final calibration value

The average sensitivity used for data processing is $1.200.000 \frac{\text{counts}}{\text{deg}}$ which corresponds to:

$$14.5 \frac{\text{mrad}}{\text{count}} \quad (\text{C.7})$$

SYNOPSIS OF EARTHQUAKE SWARMS

The following section summarizes all 7 earthquake swarms between June 2006 and March 2007. For each swarm, parameters such as cluster extension, migration velocities etc. are given in an extra text block, followed by 4 graphics:

- latitude-longitude-, longitude-depth- and latitude-depth-plots including best fitting plane through the earthquake cluster, as well as a lat-lon map plot to visualize the cluster's location and focal-mechanism as far as they are estimated for events during the swarm
- depth-time-, longitude-time and latitude-time-plots to investigate cluster migration. An additional event-density plot and a depth-time plot of migration pathes complete the analysis of all occuring migration velocities of the swarm
- tilt-traces rotated in radial (black curves) and transversal (grey curves) to the signal's back-azimuth, again plotted over the event-density to compare possible parallels between seismicity and deformation signals
- xy-plots of all tiltmeters for the time of each swarm to observe orientation and amplitude of the deformation signal. A map plot below informs about location of the seismic cluster, its centroid and the according deformation signals in form of amplitude-scaled arrows for each tiltmeter

D.1 Swarm on 28th of July 2006 (CS-1)

Main cluster:

- Initial event: July, 28th, 11:00:17.2
- Duration: 19 hours
- Number of events: 211
- Ext.: NW-SE approx. 2 km, NE-SW approx. 6 km, depth approx. 9km ($z=3-12\text{km}$)
- Best fitting plane: $strike = 66^\circ, dip = 68^\circ$
- Magnitudes: $M_L(max) = 4.6 / M_L(average) = 1.5$

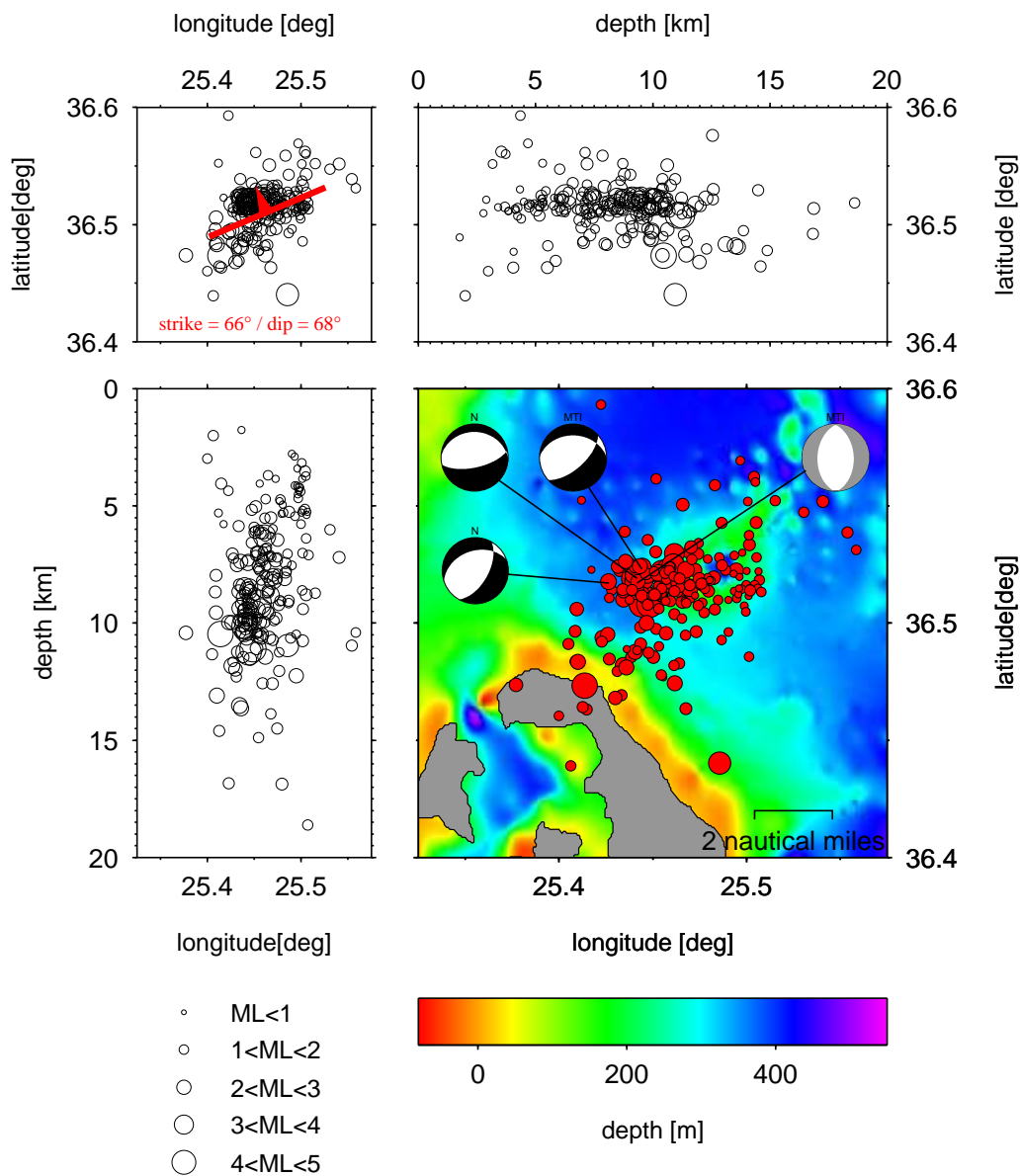


Figure D.1: Swarm CS-1: lat-lon, lat-z, lon-z, map

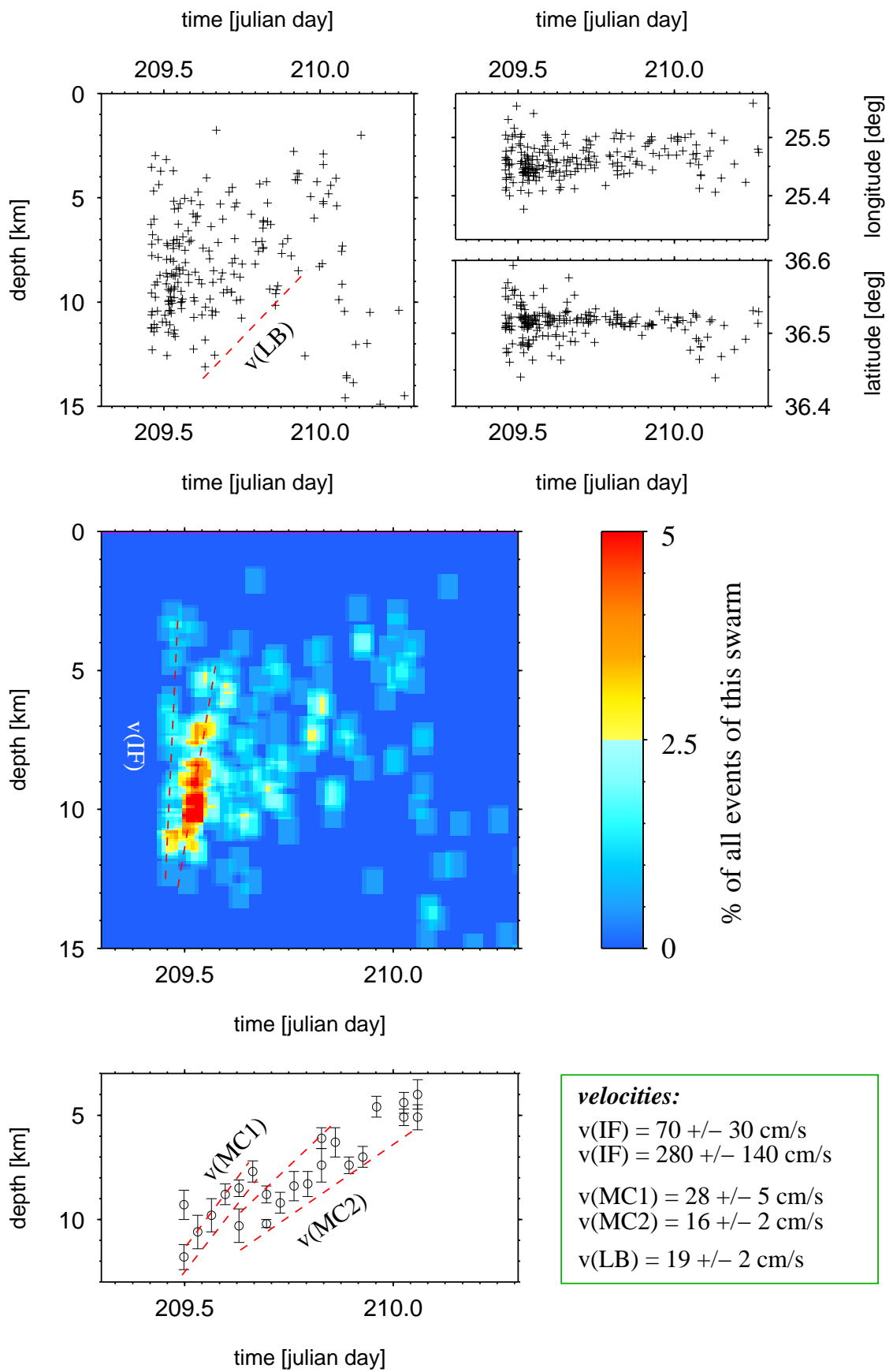


Figure D.2: Swarm CS-1: zt-distribution

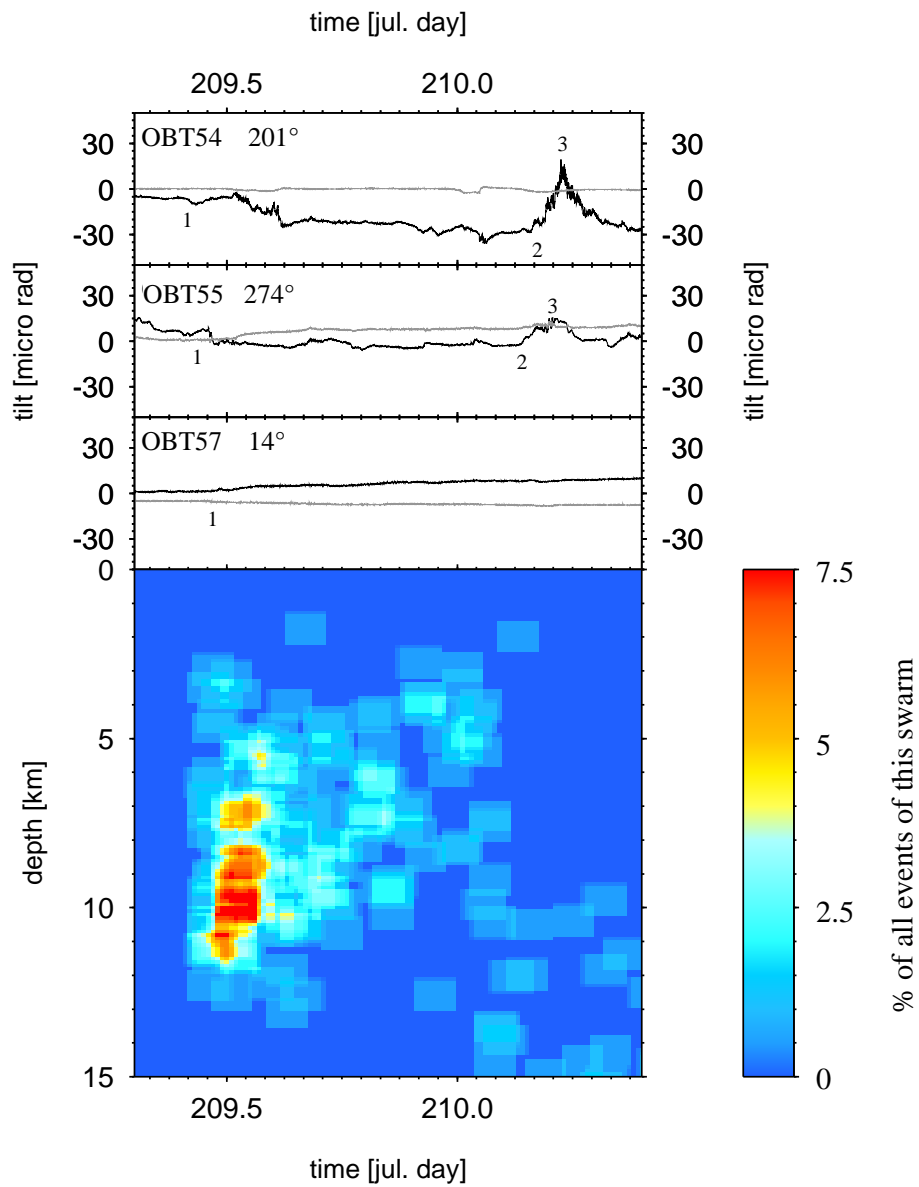


Figure D.3: Swarm CS-1: Tilt trace

<i>OBT</i>	<i>signal no.</i>	<i>day</i>	<i>dur. [h]</i>	<i>b. azi. [°]</i>	<i>sign. strike [°]</i>	T [μrad]	$\delta T/\delta t$ [$\mu\text{rad}/\text{h}$]
54	1	209.5	16	235 ± 5	21 ± 5	25 ± 1	1.6 ± 0.1
54	2	210.2	1.5	235 ± 5	201 ± 5	35 ± 1	23.3 ± 0.1
54	3	210.25	3.5	235 ± 5	21 ± 5	30 ± 1	8.6 ± 0.1
55	1	209.45	3	257 ± 5	30 ± 5	7 ± 1	2.3 ± 0.1
55	2	210.15	3	257 ± 5	274 ± 5	16 ± 1	5.3 ± 0.1
55	3	210.25	3	257 ± 5	94 ± 5	15 ± 1	5 ± 0.1
57	1	209.5	end	284 ± 5	14 ± 5	11 ± 1	0.5 ± 0.1

Table D.1: Deformation signals of the 28th of July 2006 swarm (CS-1).

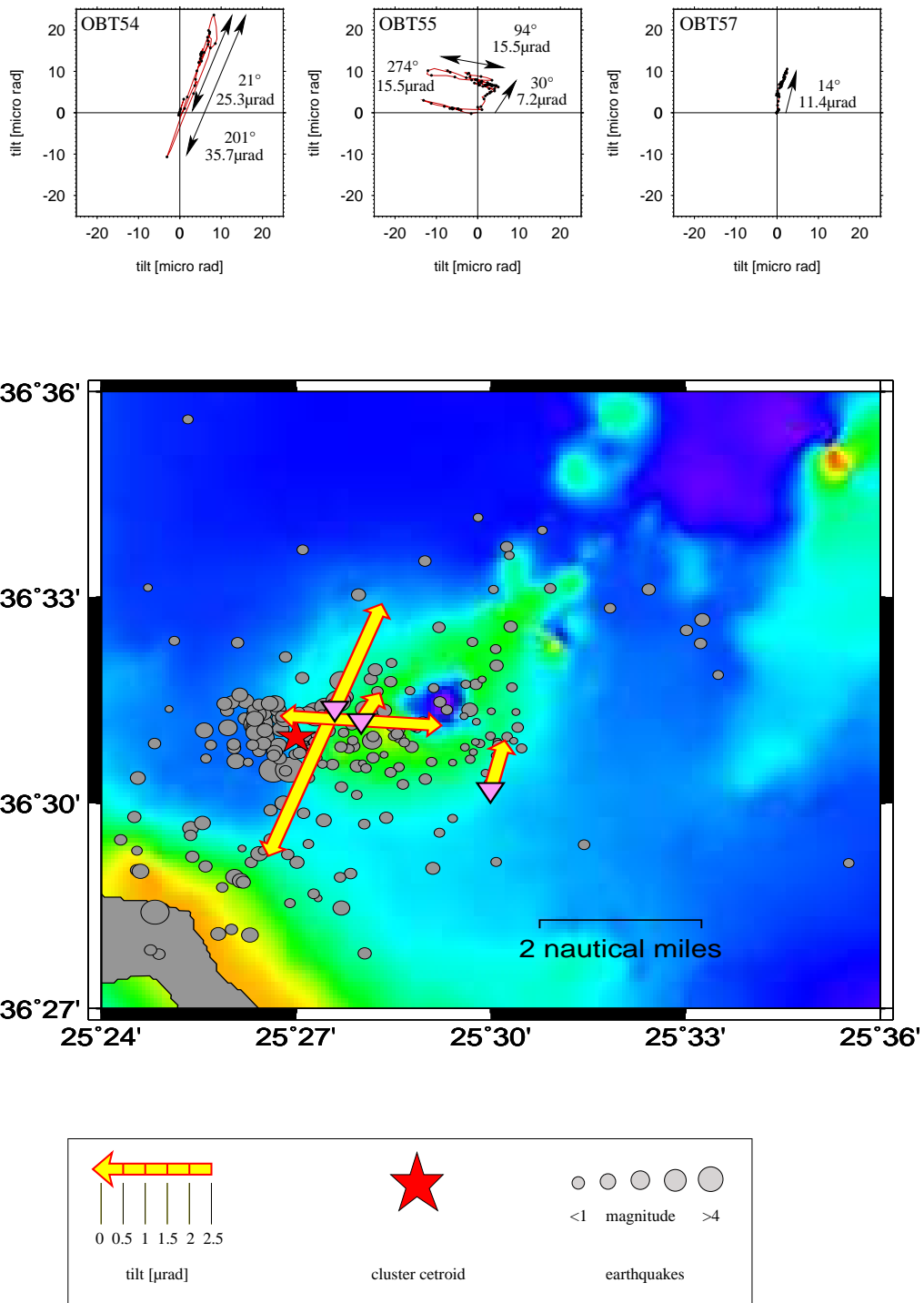


Figure D.4: Swarm CS-1: Tilt orientation

D.2 Swarm from 23rd Sept. until 1st of Oct. 2006 (CL-1)

Main cluster:

- Initial event: September 23rd, 00:10:24.9
- Duration: 175
- Number of events: 286
- Extension: NW-SE approx. 3.5 km, NE-SW approx. 8 km, depth approx. 10km (z=5-15km)
- Best fitting plane: $strike = 60.5^\circ, dip = 59^\circ$
- Magnitudes: $M_L(max) = 3.9 / M_L(average) = 1.4$

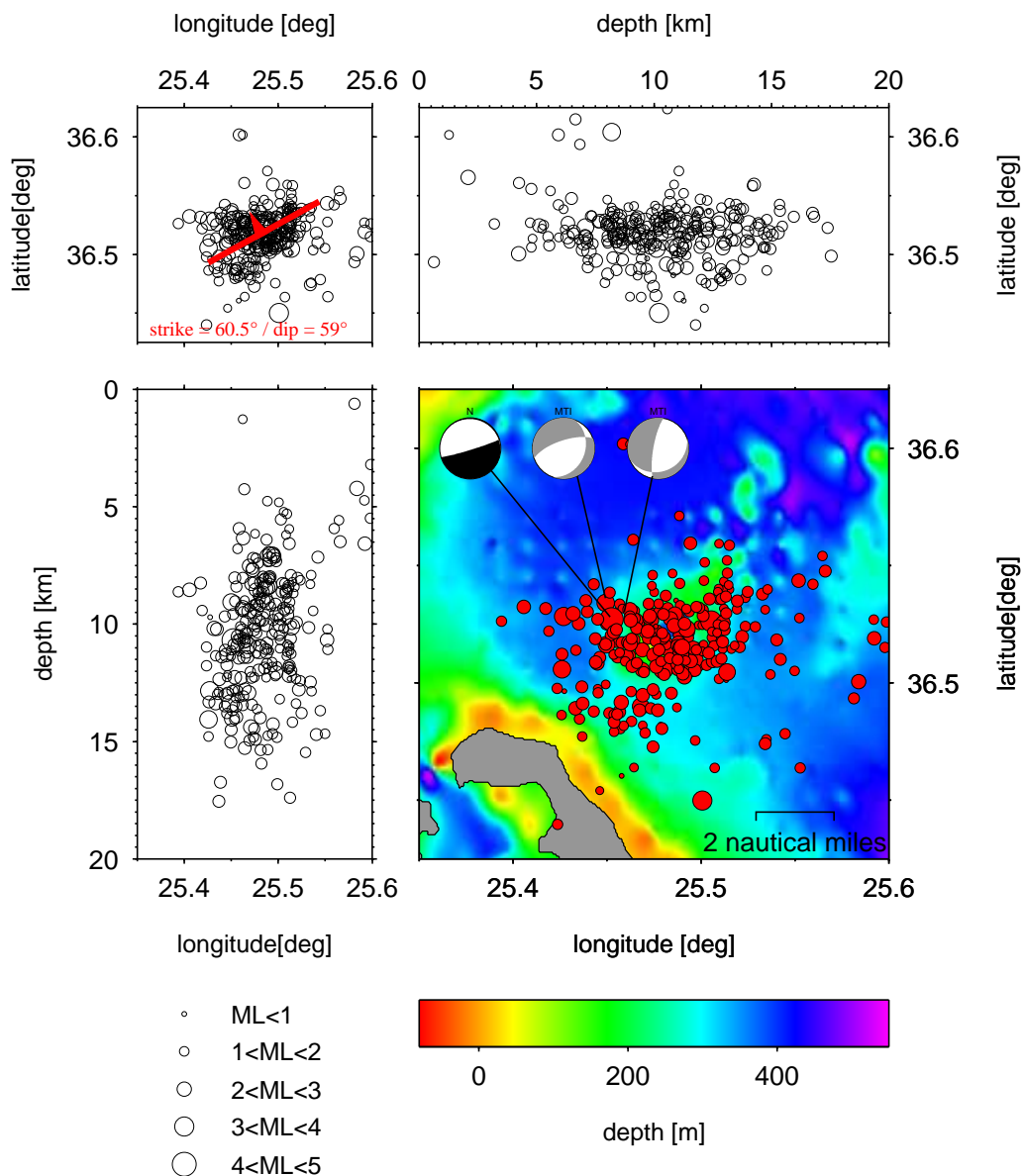


Figure D.5: Swarm CL-1: lat-lon, lat-z, lon-z, map

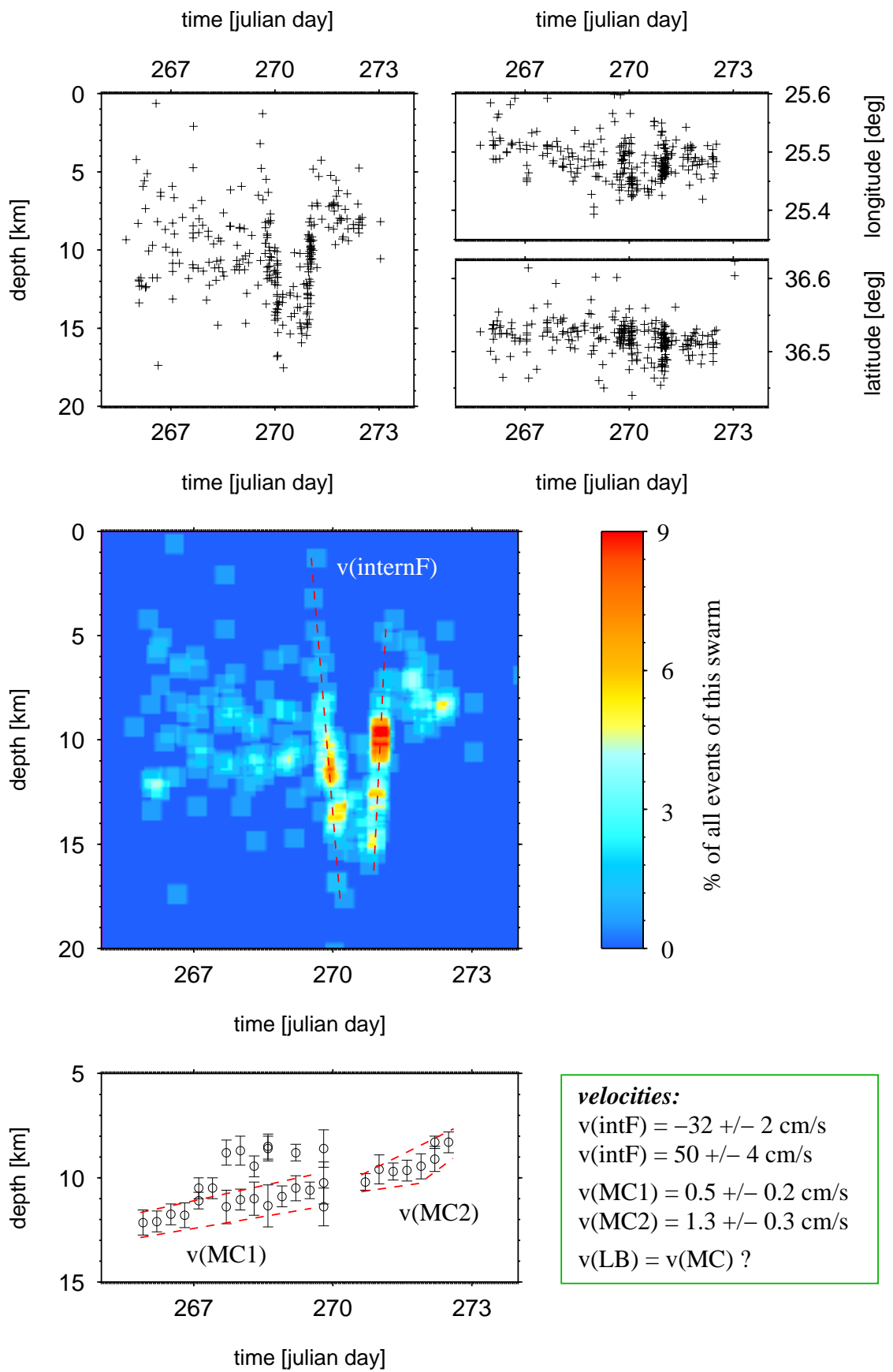


Figure D.6: Swarm CL-1: zt-distribution

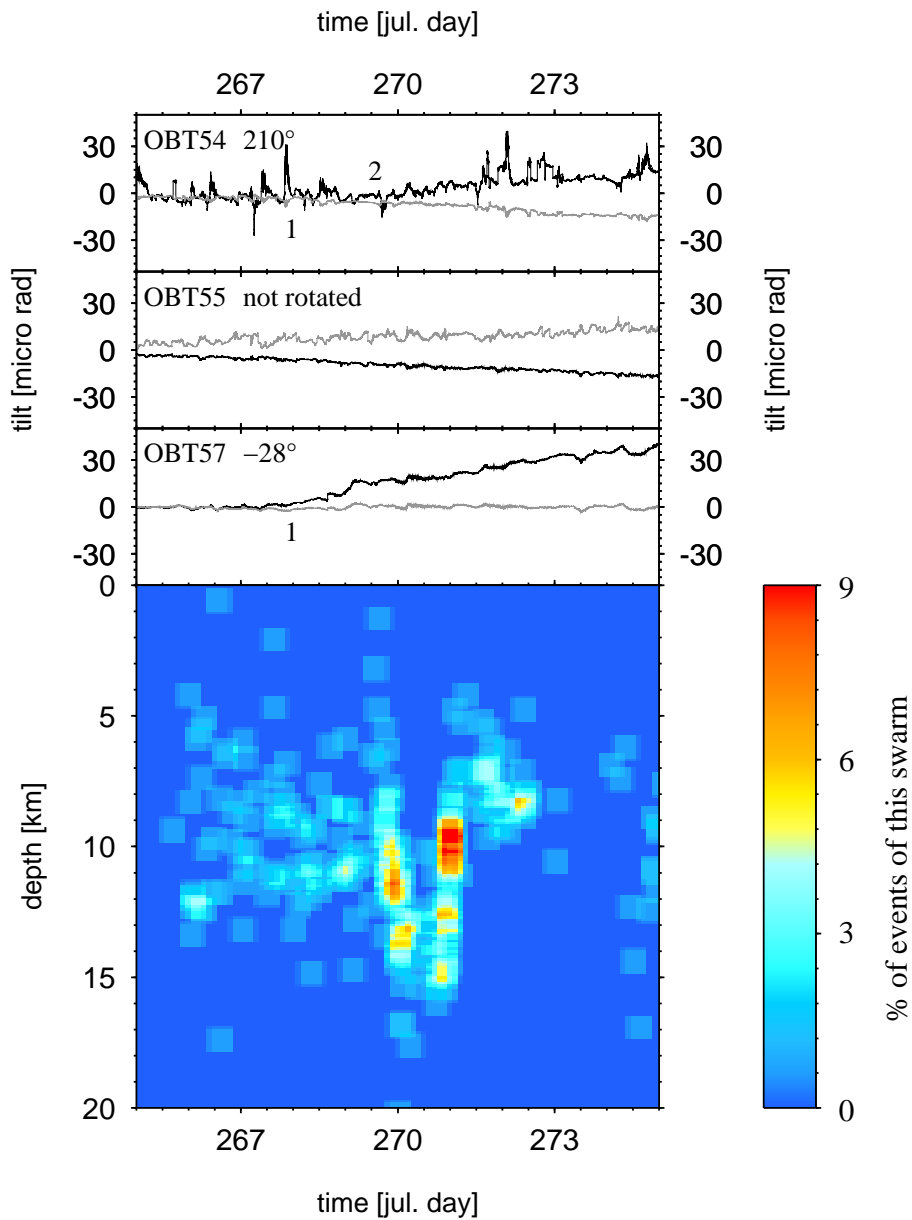


Figure D.7: Swarm CL-1: Tilt traces

<i>OBT</i>	<i>signal no.</i>	<i>day</i>	<i>dur. [h]</i>	<i>b. azi. [°]</i>	<i>sign. strike [°]</i>	<i>T [μrad]</i>	<i>δT/δt [μrad/h]</i>
54	1	268	end	-	25 ± 5	29 ± 1	0.13 ± 0.1
54	2	269	end	-	205 ± 5	10 ± 1	0.8 ± 0.1
55	1	-	-	-	-	-	-
57	1	268	end	-	332 ± 5	35 ± 1	0.16 ± 0.1

Table D.2: Deformation signals of the 23rd of Sept.-1st of Oct. 2006 swarm (CL-1)

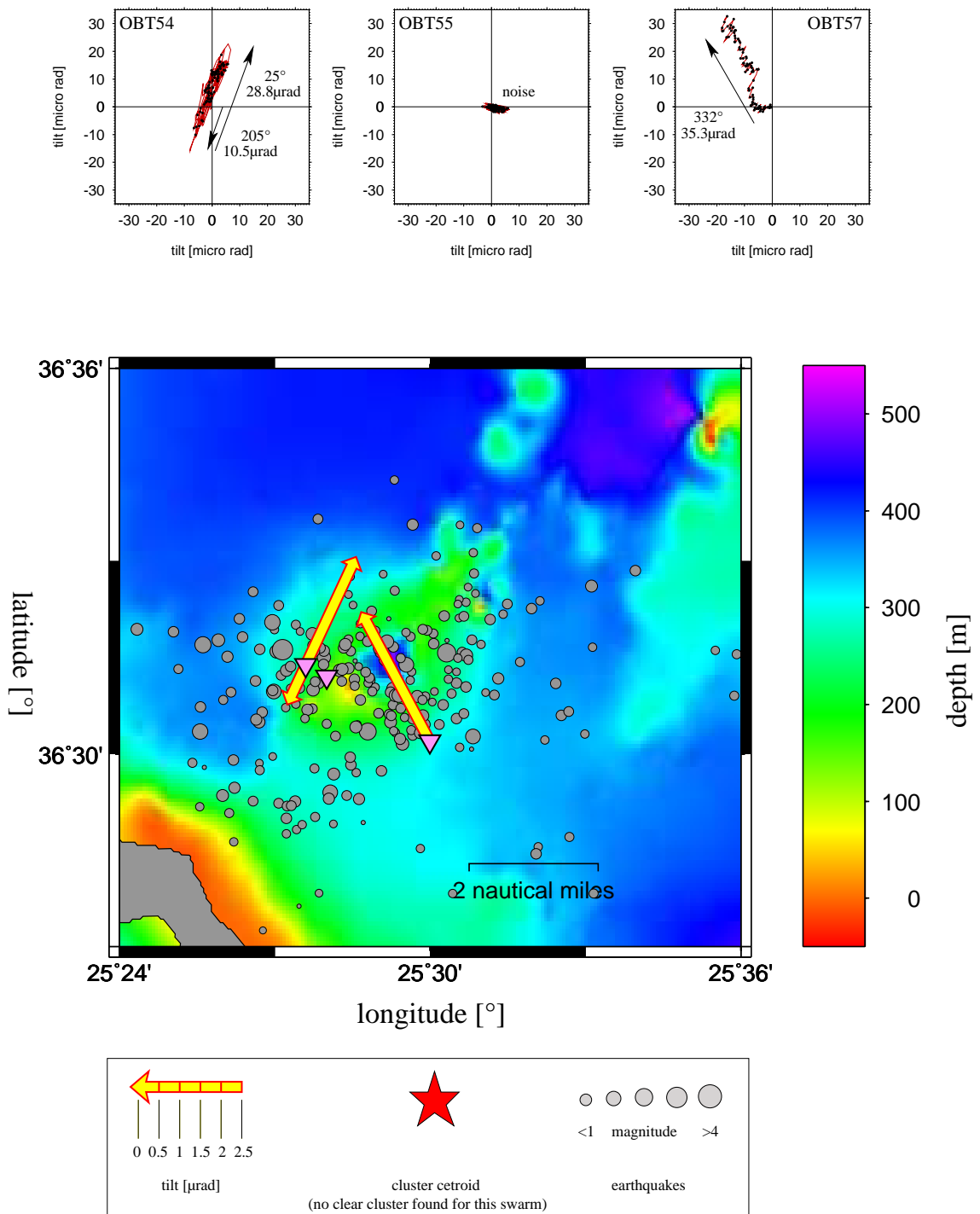


Figure D.8: Swarm CL-1: Tilt orientation

D.3 Swarm from 6th until 8th of December 2006 (CL-2)

Main cluster:

- Initial event: December, 6th, 10:14:46.5
- Duration: 48.5 hours
- Number of events: 154
- Extension: NW-SE approx. 3 km, NE-SW approx. 6 km, depth approx. 8km ($z=3-11\text{km}$)
- Best fitting plane: $strike = 37^\circ, dip = -79^\circ$
- Magnitudes: $M_L(max) = 3.9 / M_L(average) = 1.7$

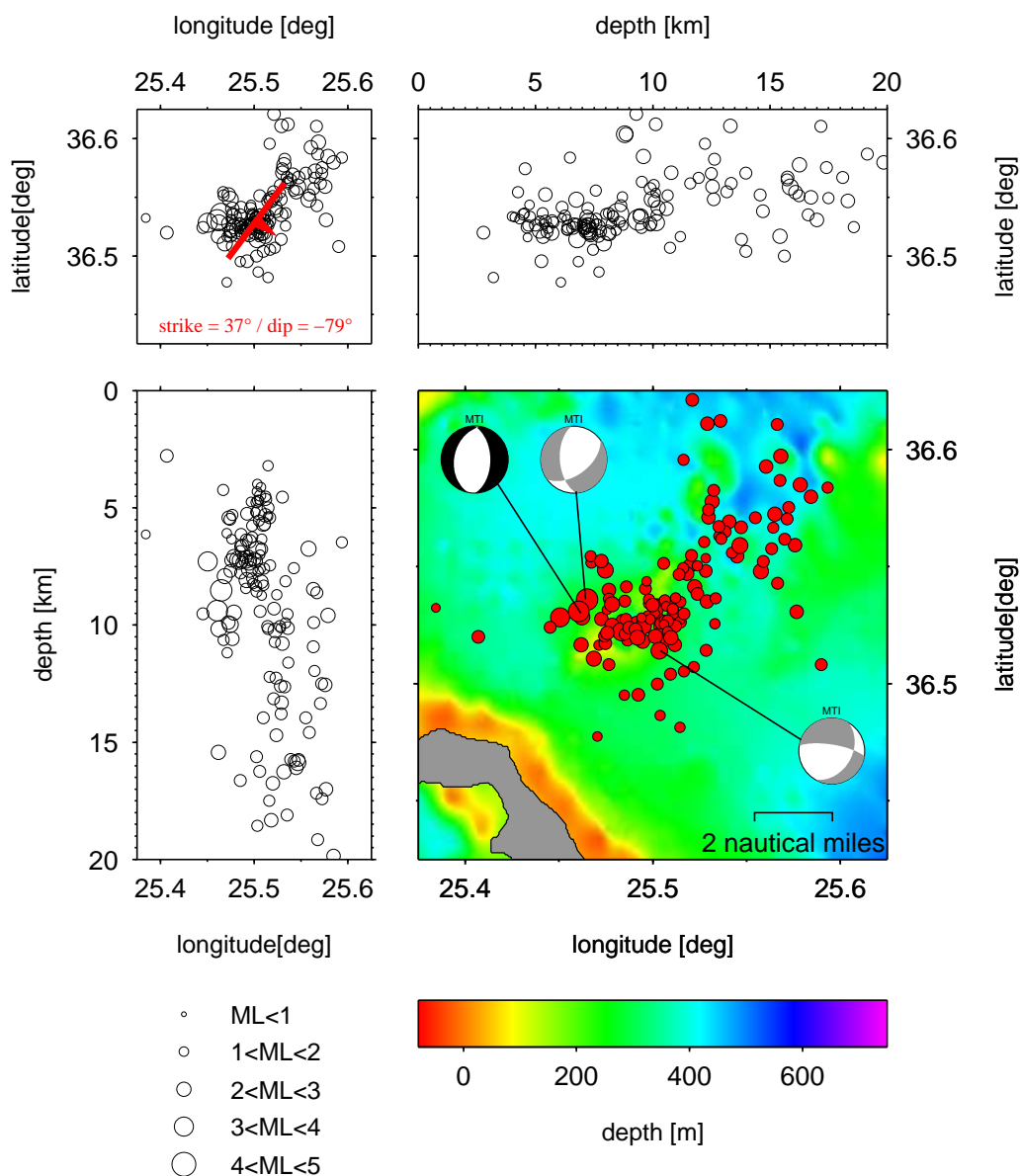


Figure D.9: Swarm CL-2: lat-lon, lat-z, lon-z, map

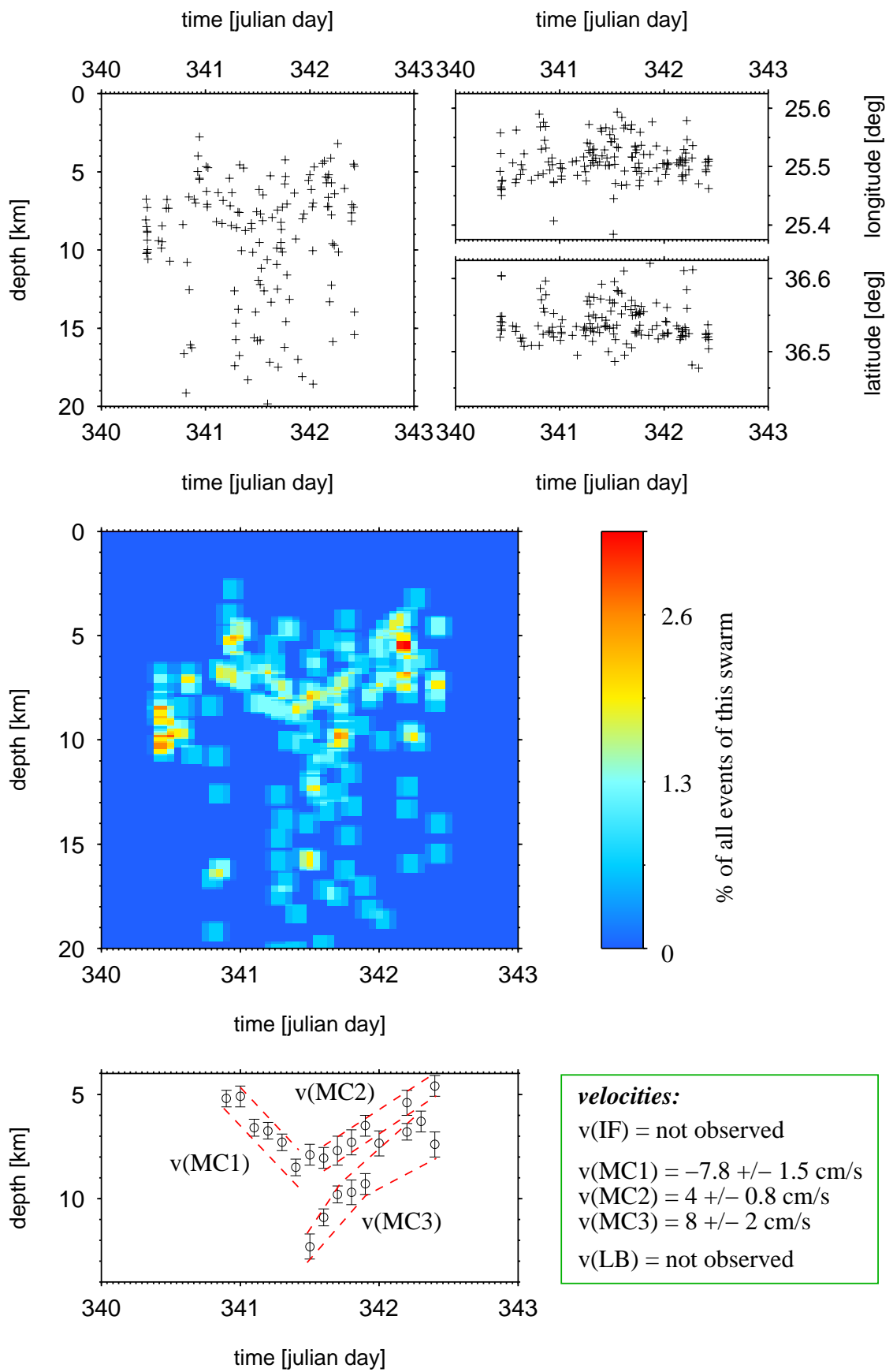


Figure D.10: Swarm CL-2: zt-distribution

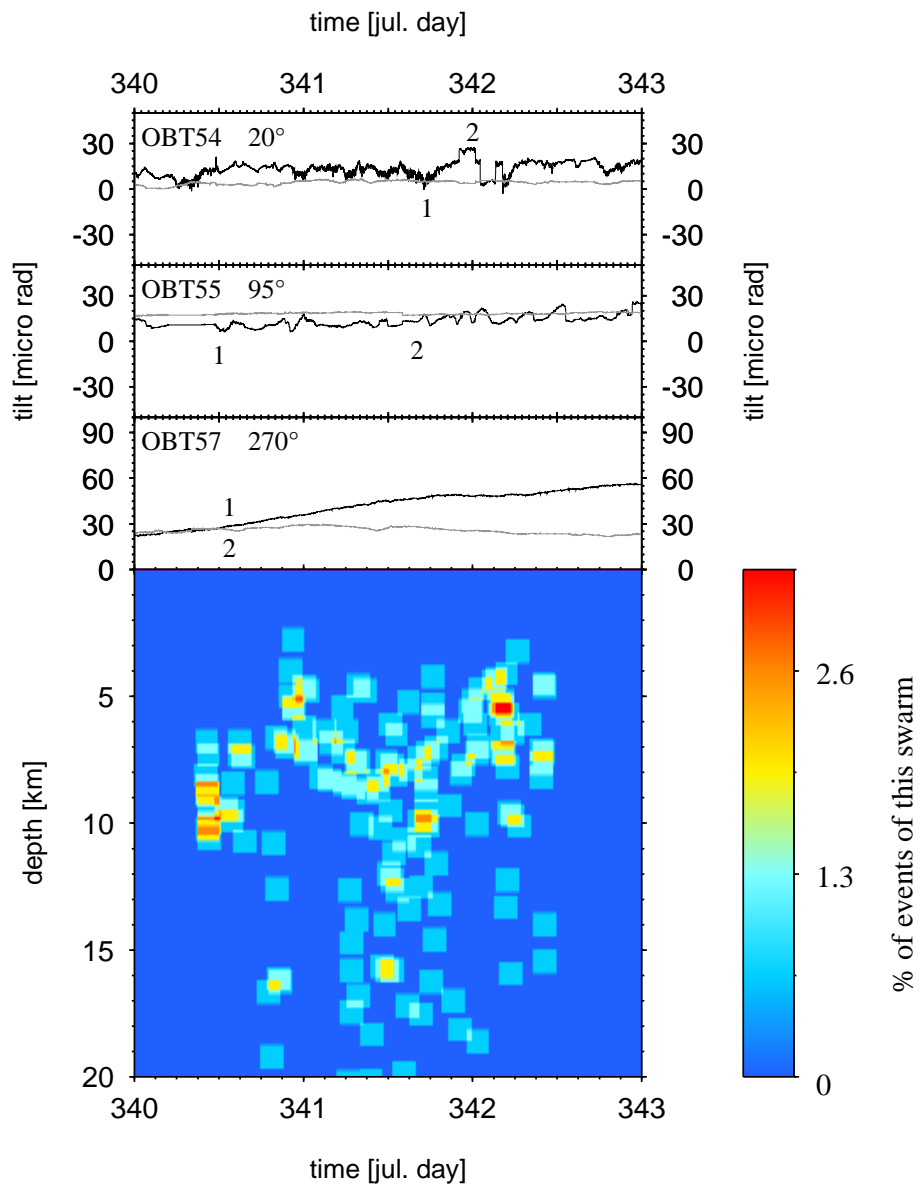


Figure D.11: Swarm CL-2: Tilt traces

<i>OBT</i>	<i>signal no.</i>	<i>day</i>	<i>dur. [h]</i>	<i>b. azi. [°]</i>	<i>sign. strike [°]</i>	<i>T [μrad]</i>	<i>δT/δt [μrad/h]</i>
54	1	341.7	6	86 ± 5	20 ± 5	24 ± 1	4 ± 0.1
54	2	342.0	2	86 ± 5	205 ± 5	16 ± 1	8 ± 0.1
55	1	340.5	noise	81 ± 5	105 ± 5	10 ± 1	-
55	2	340.5	noise	81 ± 5	285 ± 5	10 ± 1	-
55	3	341.6	1	81 ± 5	65 ± 5	2.5 ± 1	2.5 ± 0.1
57	1	340.5	36	3 ± 5	0 ± 5	8 ± 1	0.2 ± 0.1
57	2	340.5	end	3 ± 5	270 ± 5	24 ± 1	0.4 ± 0.1

Table D.3: Deformation signals of the 6th-8th of December 2006 swarm (CL-2).

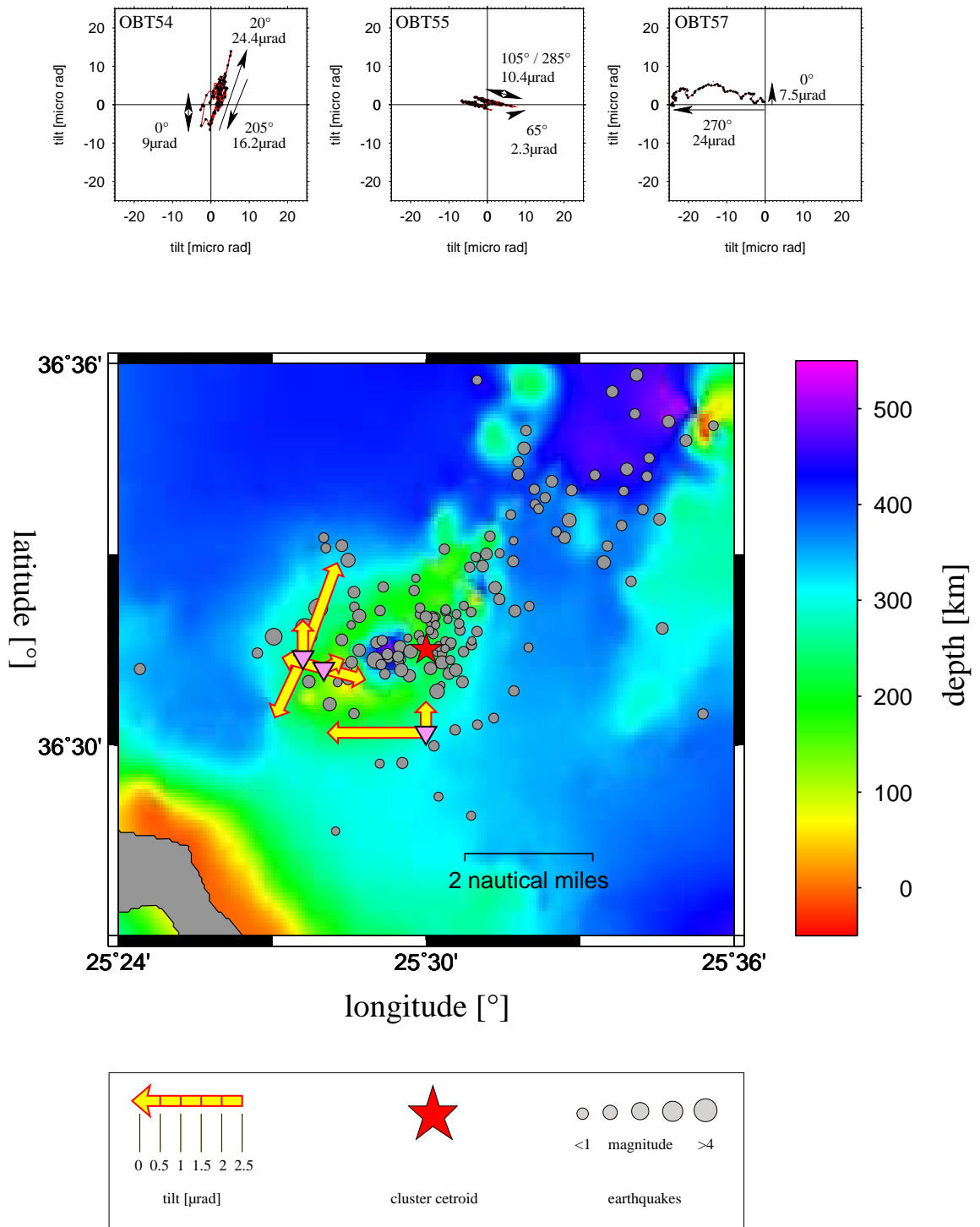


Figure D.12: Swarm CL-2: Tilt orientation

D.4 Swarm on 10th of January 2007 (CS-2)

Main cluster:

- Initial event: January, 10th, 04:15:10.3
- Duration: 22.5 hours
- Number of events: 128
- Ext.: NW-SE approx. 1.5 km, NE-SW approx. 3.5 km, depth approx. 7km ($z=3\text{-}10\text{km}$)
- Best fitting plane: $strike = 41^\circ, dip = 76^\circ$
- Magnitudes: $M_L(max) = 4.0 / M_L(average) = 1.7$

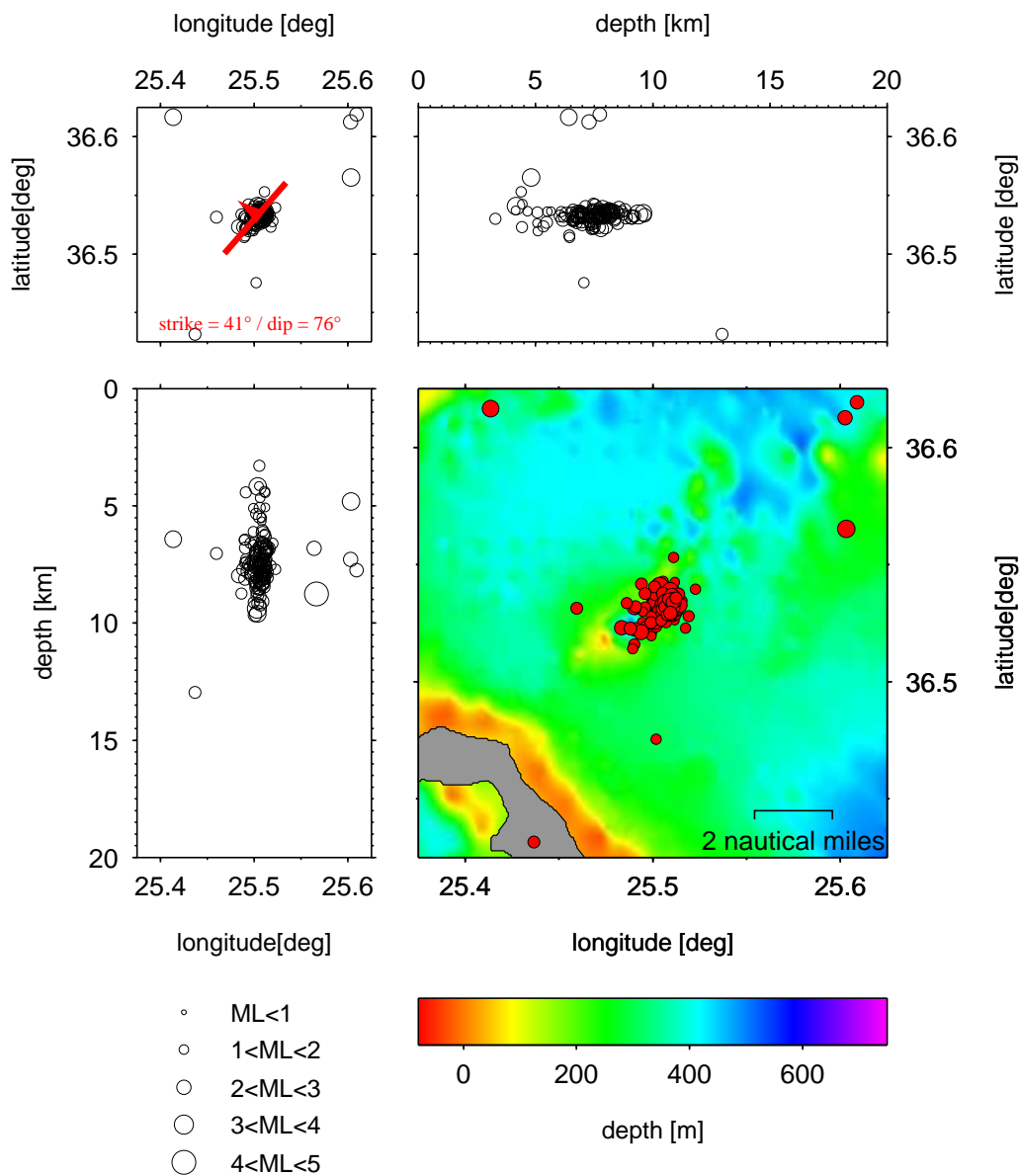


Figure D.13: Swarm CS-2: lat-lon, lat-z, lon-z, map

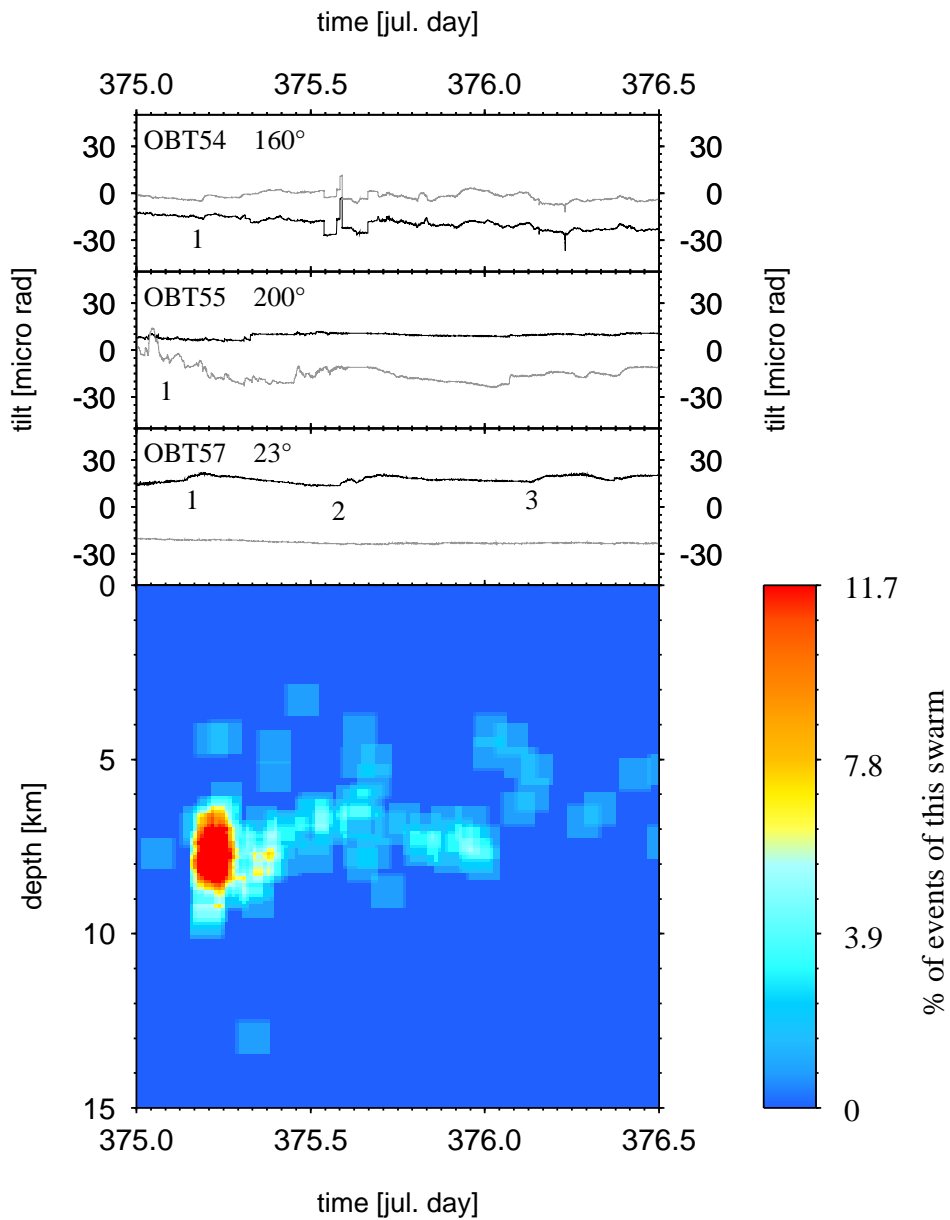


Figure D.15: Swarm CS-2: Tilt traces

<i>OBT</i>	<i>signal no.</i>	<i>day</i>	<i>dur. [h]</i>	<i>b. azi. [°]</i>	<i>sign. strike [°]</i>	<i>T [μrad]</i>	<i>δT/δt [μrad/h]</i>
54	1	375.2	2	78 ± 5	± 5	7 ± 1	3.5 ± 0.1
55	1	375.1	8	71 ± 5	± 5	5 ± 1	0.7 ± 0.1
57	1	375.2	1	9 ± 5	23 ± 5	7 ± 1	7 ± 0.1
57	2	375.6	2	9 ± 5	23 ± 5	7 ± 1	3.5 ± 0.1
57	3	376.2	2	9 ± 5	23 ± 5	7 ± 1	3.5 ± 0.1

Table D.4: Deformation signals of the 10th of January 2007 swarm (CS-2).

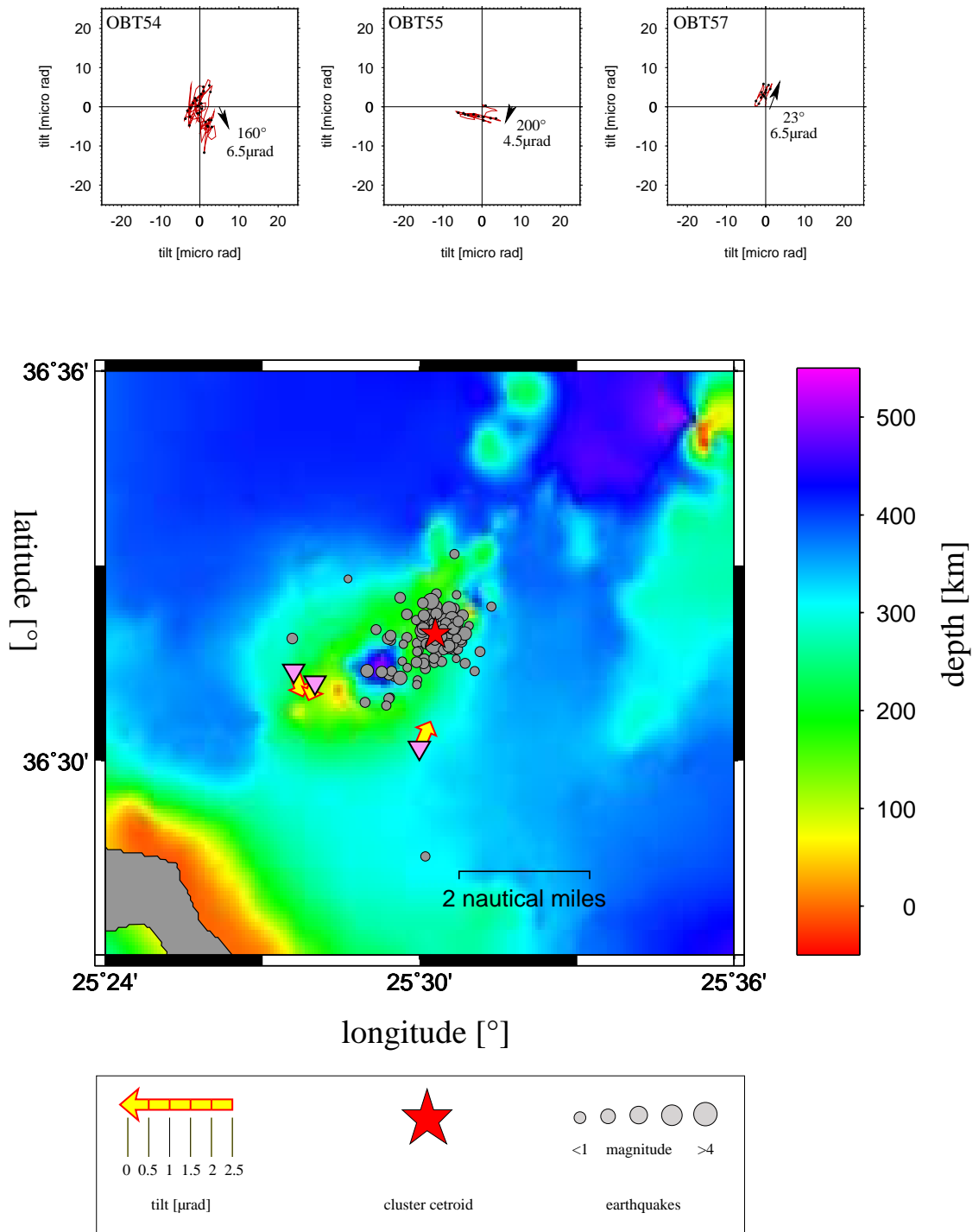


Figure D.16: Swarm CS-2: Tilt orientation

D.5 Swarm on 18th of February 2007 (CS-3)

Main cluster:

- Initial event: February, 18th, 03:49:22.2
- Duration: 2.5 hours
- Number of events: 46
- Extension: NW-SE approx. 1.5 km, NE-SW approx. 2 km, depth approx. 4km ($z=6-10\text{km}$)
- Best fitting plane: $strike = 33^\circ, dip = 79^\circ$
- Magnitudes: $M_L(max) = 3.3 / M_L(average) = 1.9$

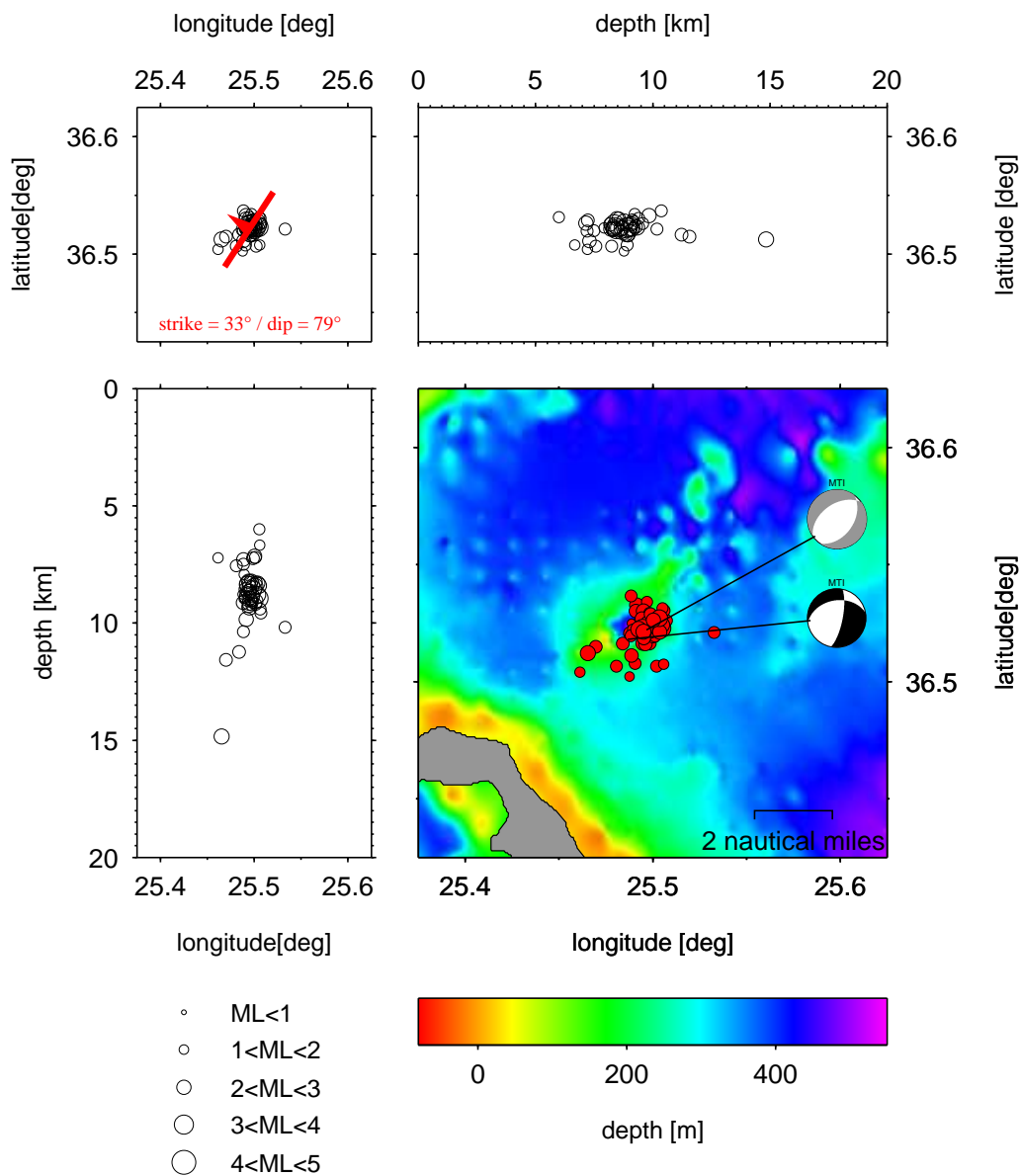


Figure D.17: Swarm CS-3: lat-lon, lat-z, lon-z, map

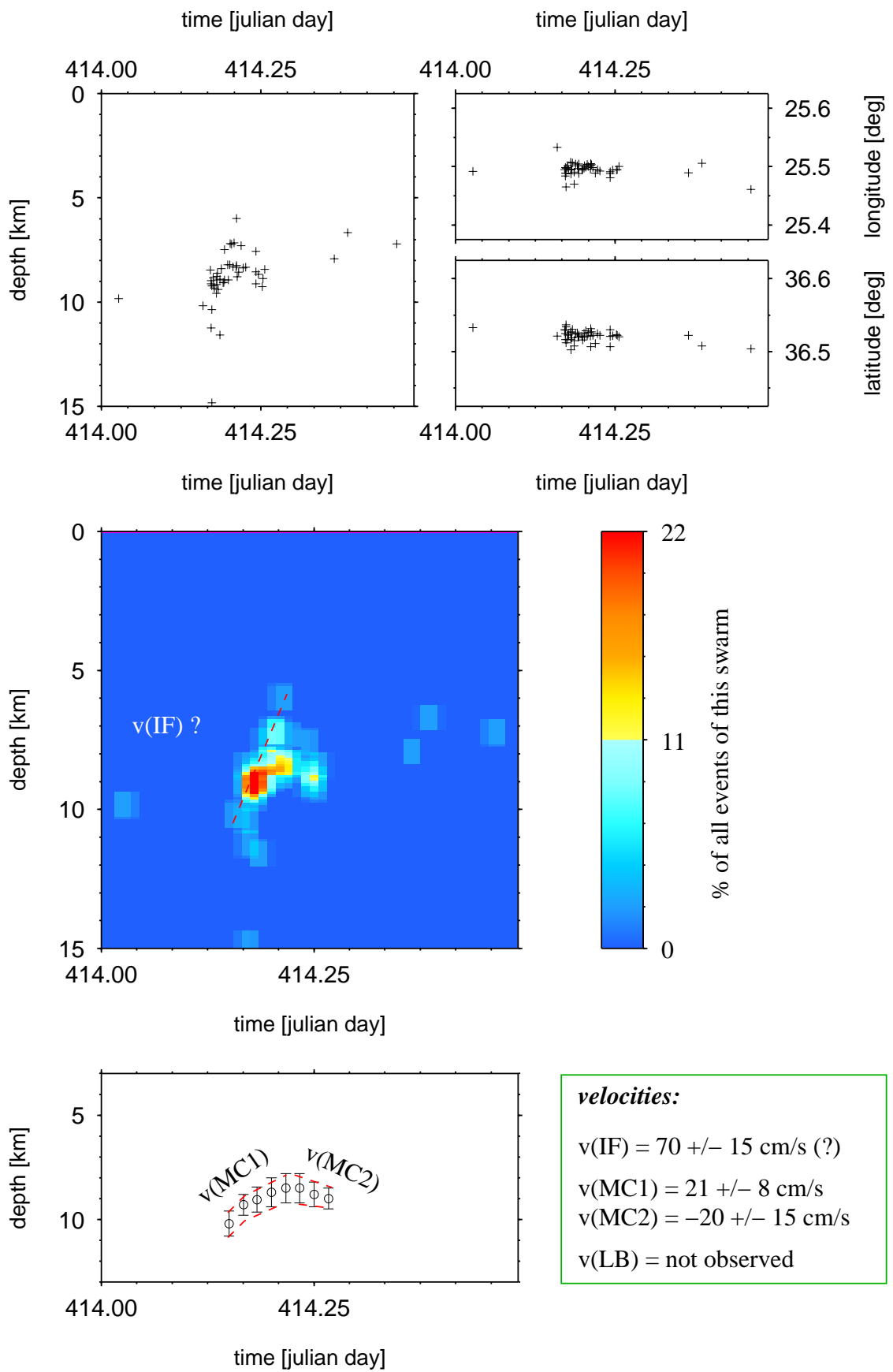


Figure D.18: Swarm CS-3: zt-distribution

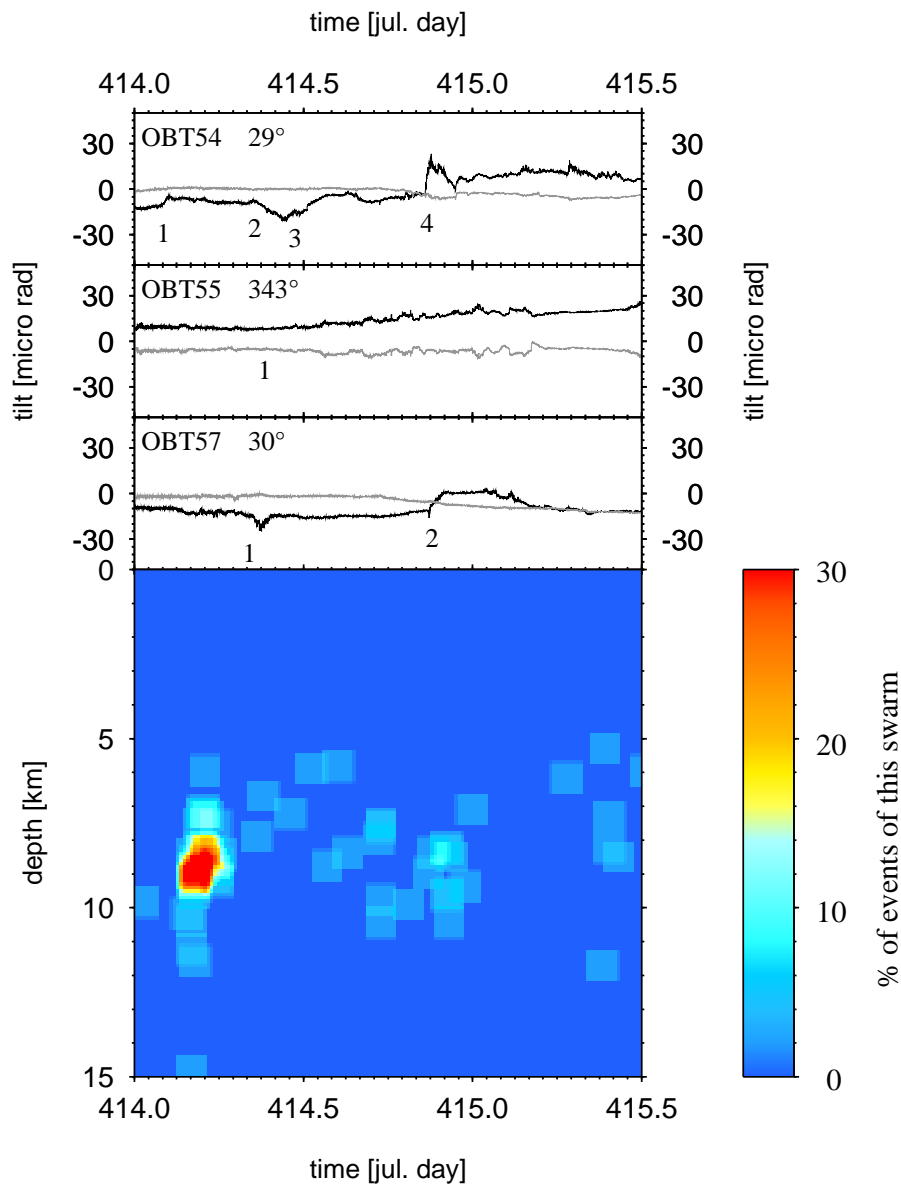


Figure D.19: Swarm CS-3: Tilt traces

<i>OBT</i>	<i>signal no.</i>	<i>day</i>	<i>dur. [h]</i>	<i>b. azi. [°]</i>	<i>sign. strike [°]</i>	<i>T [μrad]</i>	<i>δT/δt [μrad/h]</i>
54	1	414.1	1	87 ± 5	208 ± 5	7 ± 1	7 ± 0.1
54	2	414.4	3	87 ± 5	28 ± 5	15 ± 1	3 ± 0.1
54	3	414.5	22	87 ± 5	29 ± 5	19 ± 1	0.9 ± 0.1
54	4	414.9	1.5	87 ± 5	29 ± 5	10 ± 1	6.7 ± 0.1
55	1	414.4	20	81 ± 5	343 ± 5	11 ± 1	0.6 ± 0.1
57	1	414.4	20	0 ± 5	300 ± 5	11 ± 1	0.6 ± 0.1
57	2	414.9	2	0 ± 5	30 ± 5	17 ± 1	8.5 ± 0.1

Table D.5: Deformation signals of the 18th of February 2007 swarm (CS-3).

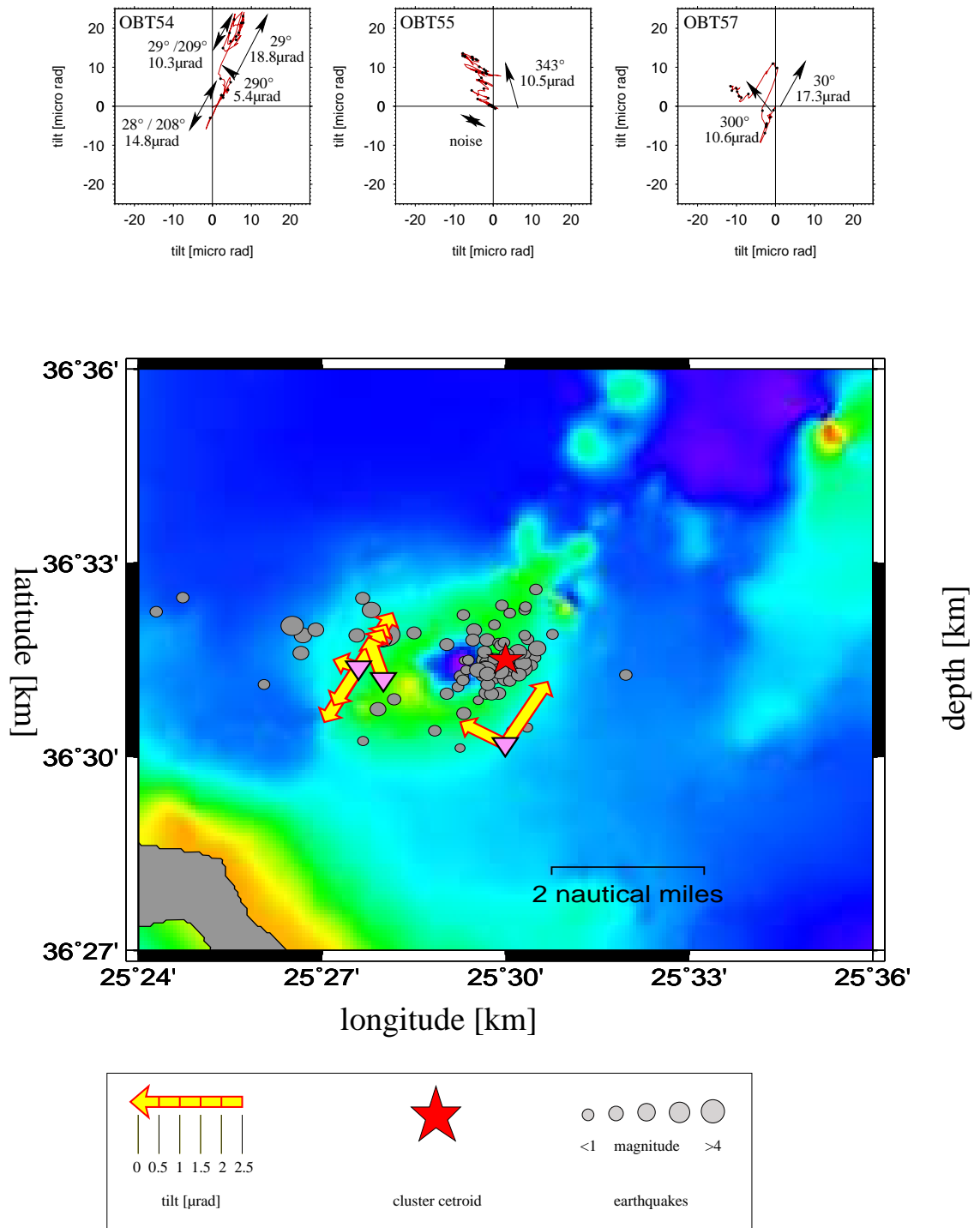


Figure D.20: Swarm CS-3: Tilt orientation

D.6 Swarm on 26th of February 2007 (AS-1)

Main cluster:

- Initial event: February, 26th, 03:49:22.2
- Duration: 11.5 hours
- Number of events: 13
- Extension: NW-SE approx. 1 km, NE-SW approx. 2.5 km, depth 3km ($z=6.5-9.5\text{km}$)
- Best fitting plane: $strike = 28^\circ, dip = -74^\circ$
- Magnitudes: $M_L(max) = 3.5 / M_L(average) = 2.7$

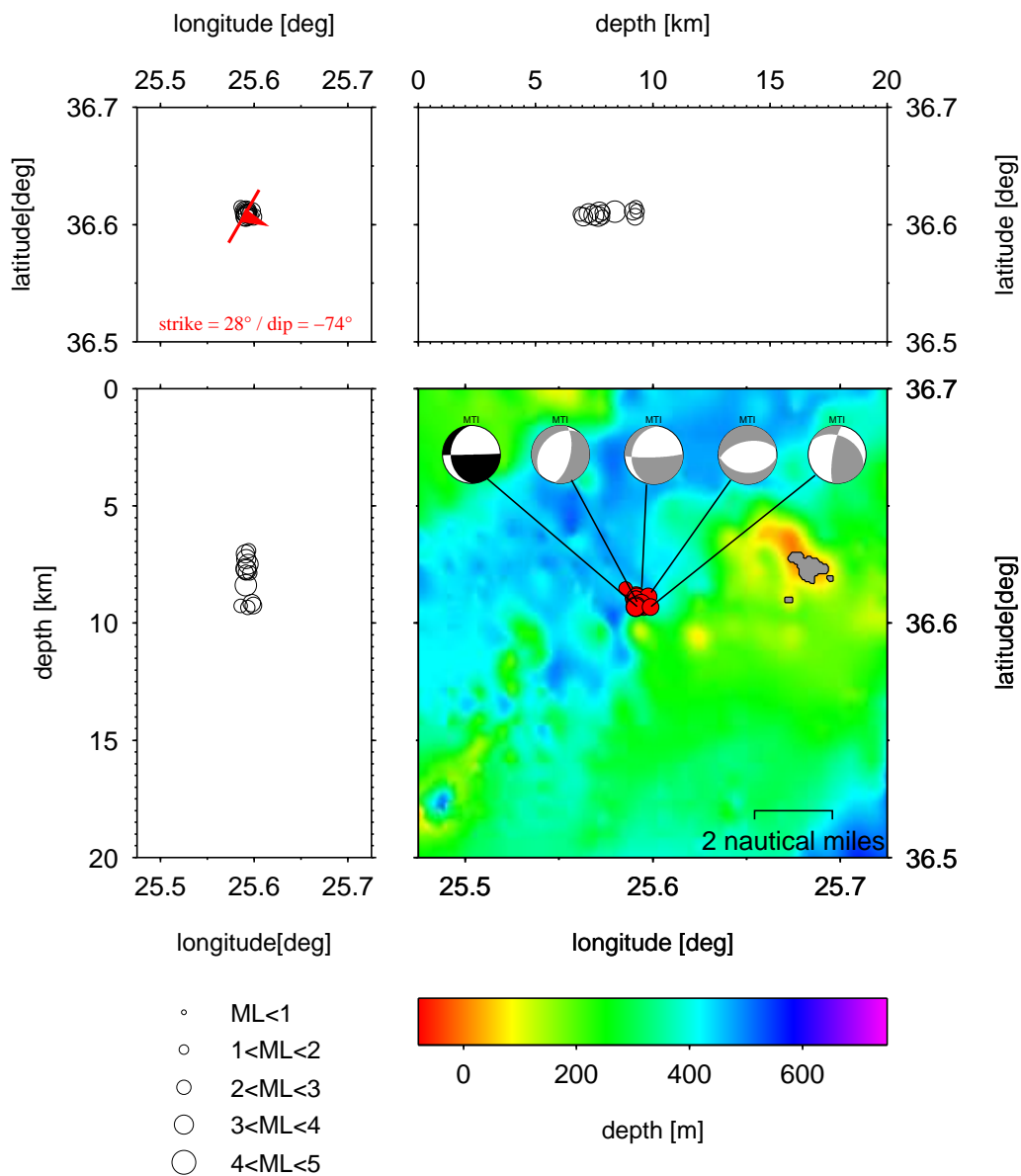


Figure D.21: Swarm AS-1: lat-lon, lat-z, lon-z, map

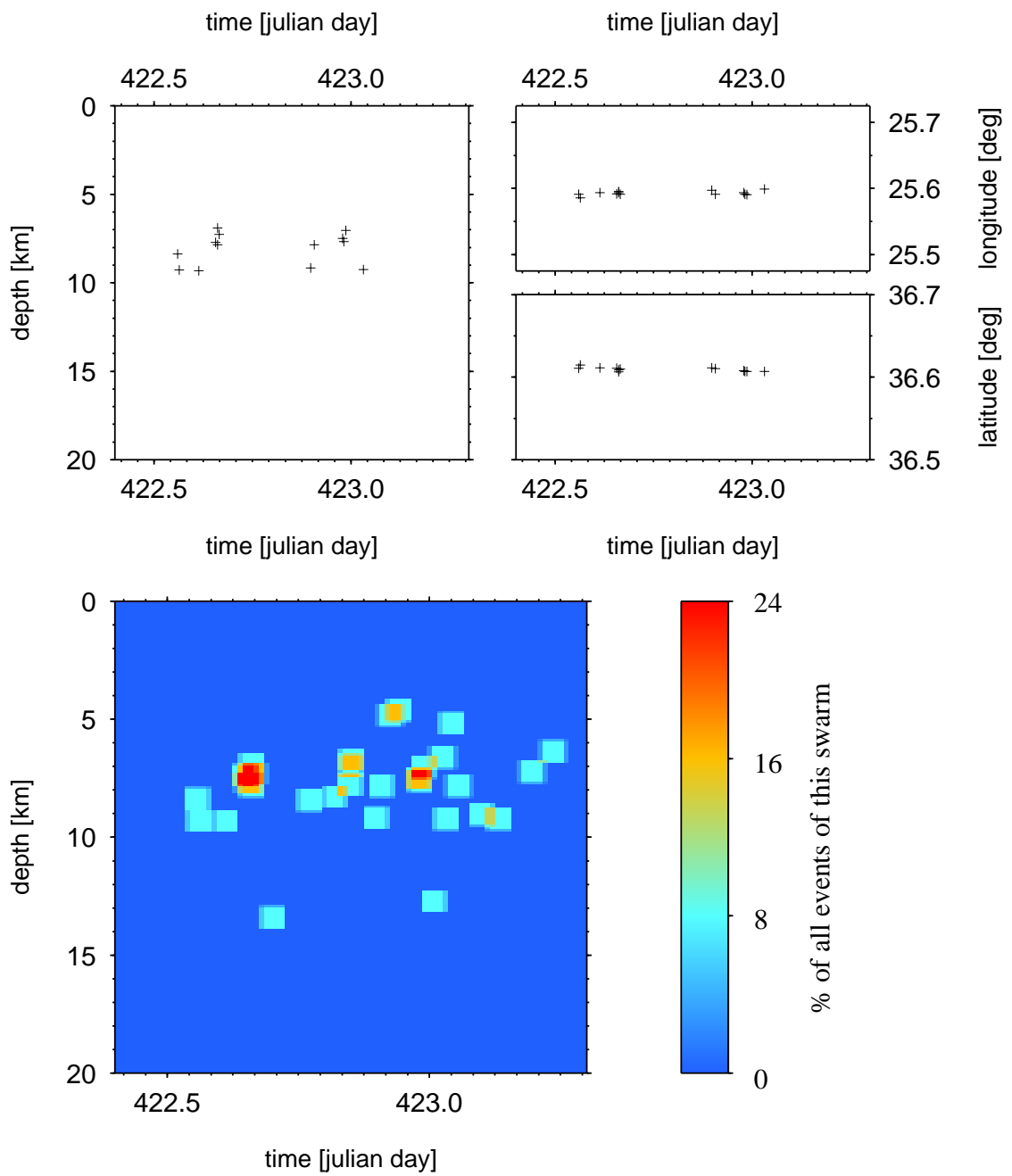


Figure D.22: Swarm AS-1: zt-distribution

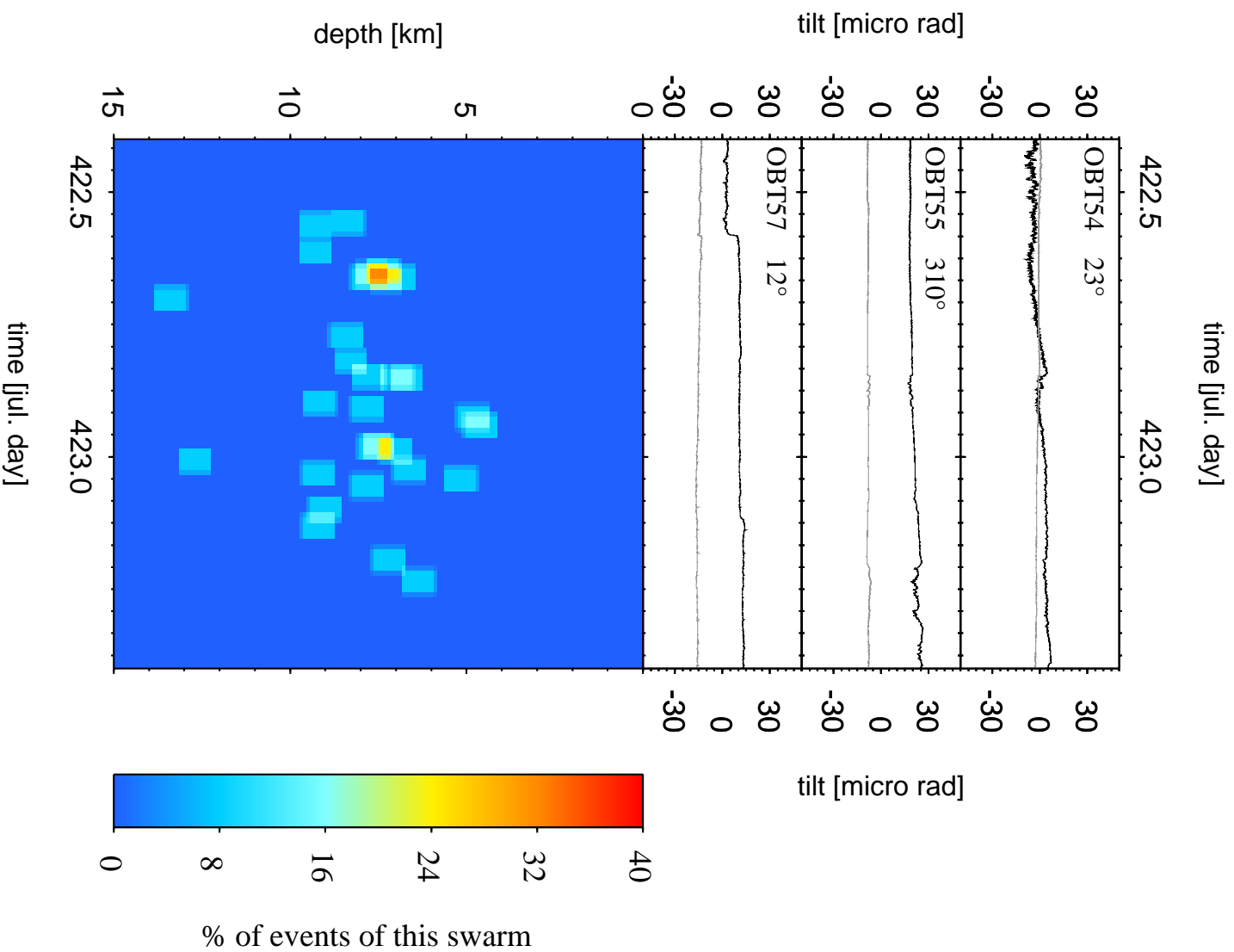


Figure D.23: Swarm AS-1: Tilt traces

The 26th of February swarm is too far away of the offshore deformation network to derive tilt or uplift/subsidence signals of it.

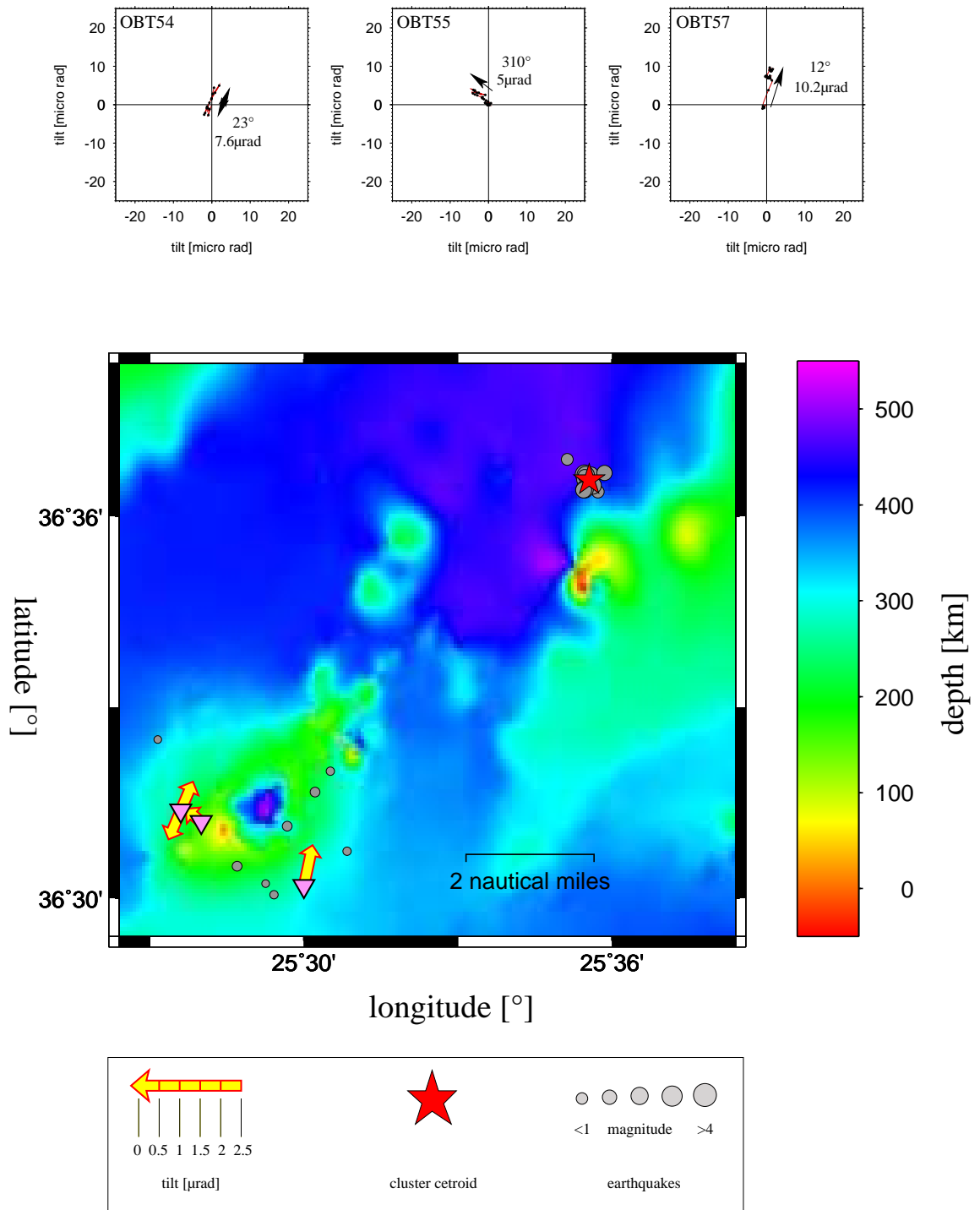


Figure D.24: Swarm AS-1: Tilt orientation

D.7 Swarm on 1st of March 2007 (CS-4)

Main cluster:

- Initial event: March, 1st, 11:42:31.8
- Duration: 28 hours
- Number of events: 252
- Extension: NW-SE approx. 2 km, NE-SW approx. 3 km, depth approx. 6km (z=4-10km)
- Best fitting plane: *strike* = 48°, *dip* = 51°
- Magnitudes: $M_L(max) = 4.4$ / $M_L(average) = 1.8$

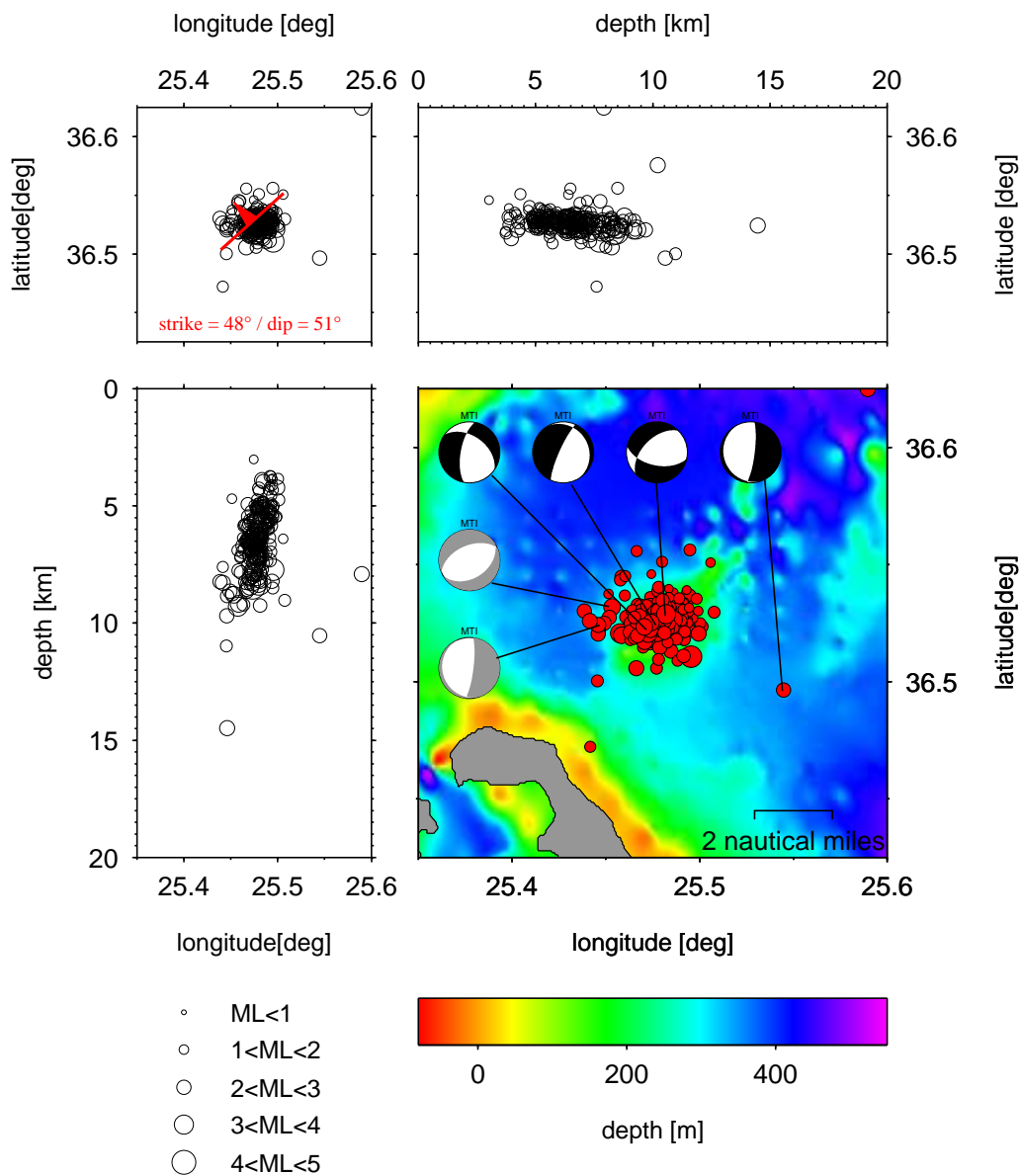


Figure D.25: Swarm CS-4: lat-lon, lat-z, lon-z, map

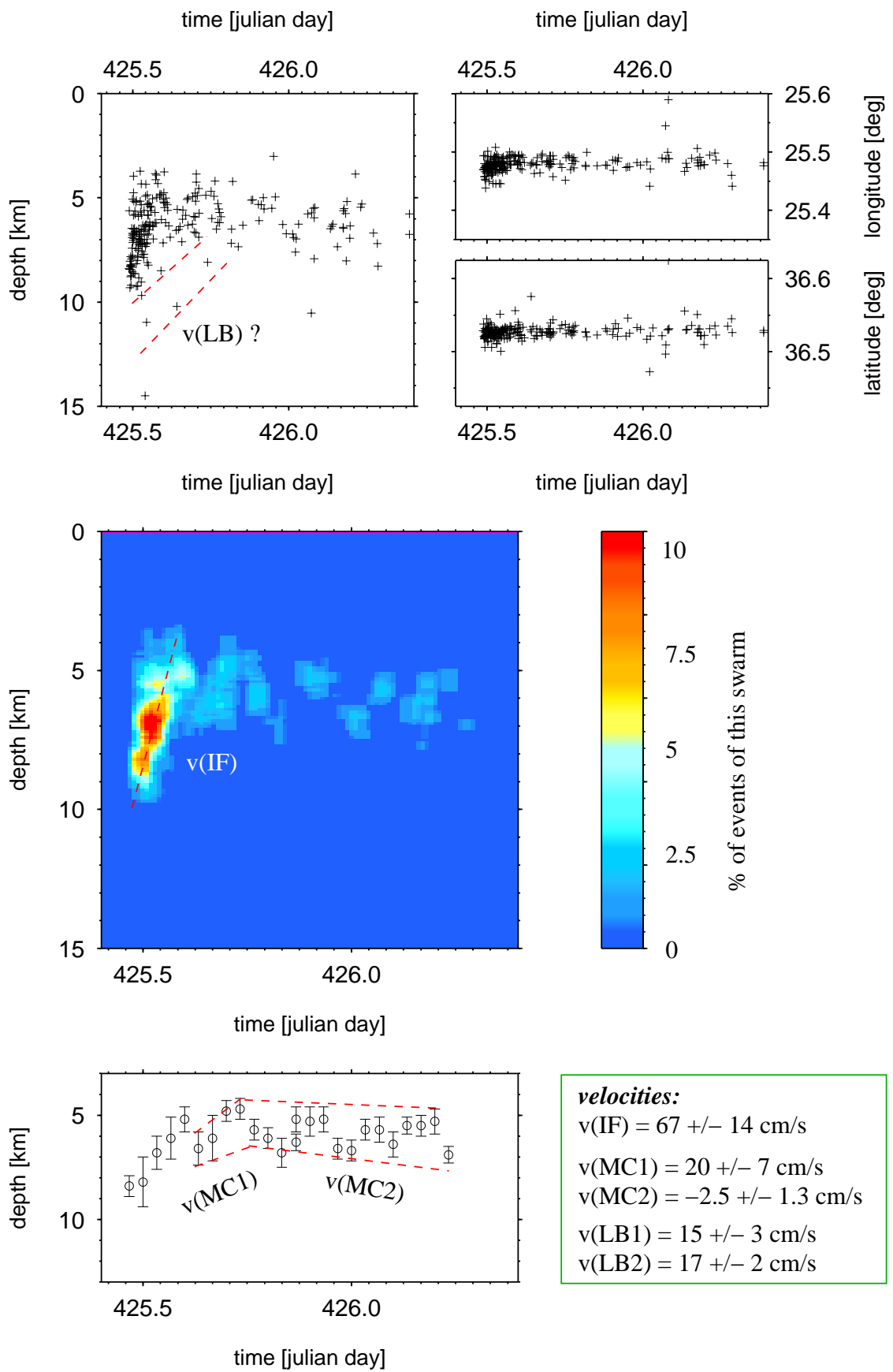


Figure D.26: Swarm CS-4: zt-distribution

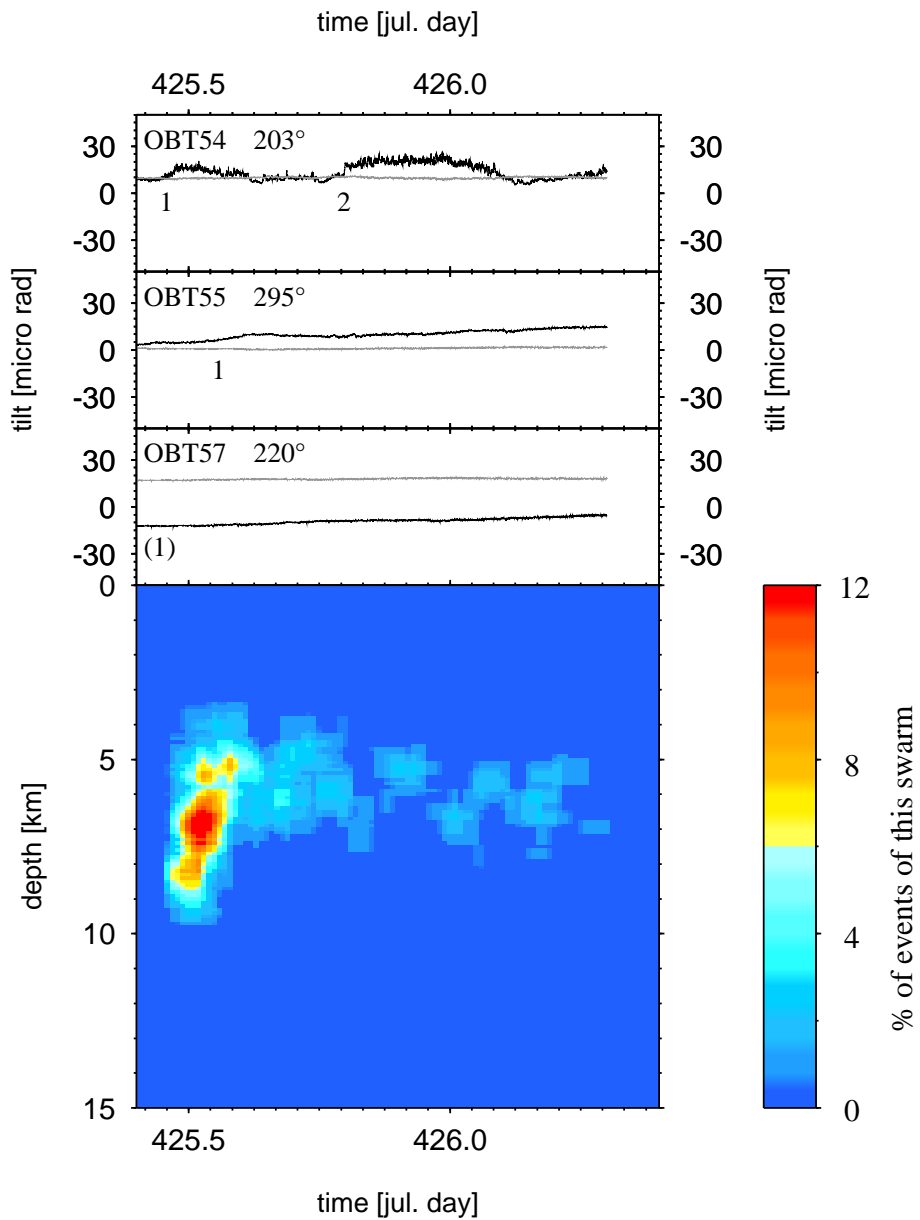


Figure D.27: Swarm CS-4: Tilt traces

<i>OBT</i>	<i>signal no.</i>	<i>day</i>	<i>dur. [h]</i>	<i>b. azi. [°]</i>	<i>sign. strike [°]</i>	<i>T [μrad]</i>	<i>δT/δt [μrad/h]</i>
54	1	425.45	1	82 ± 5	29 ± 5	8 ± 1	8 ± 0.1
54	2	425.8	1.5	82 ± 5	29 ± 5	15 ± 1	10 ± 0.1
55	1	425.55	2	57 ± 5	295 ± 5	10 ± 1	5 ± 0.1
57	1	trend	-	312 ± 5	220 ± 5	6 ± 1	0.3 ± 0.1

Table D.6: Deformation signals of the 1st of March 2007 swarm (CS-4).

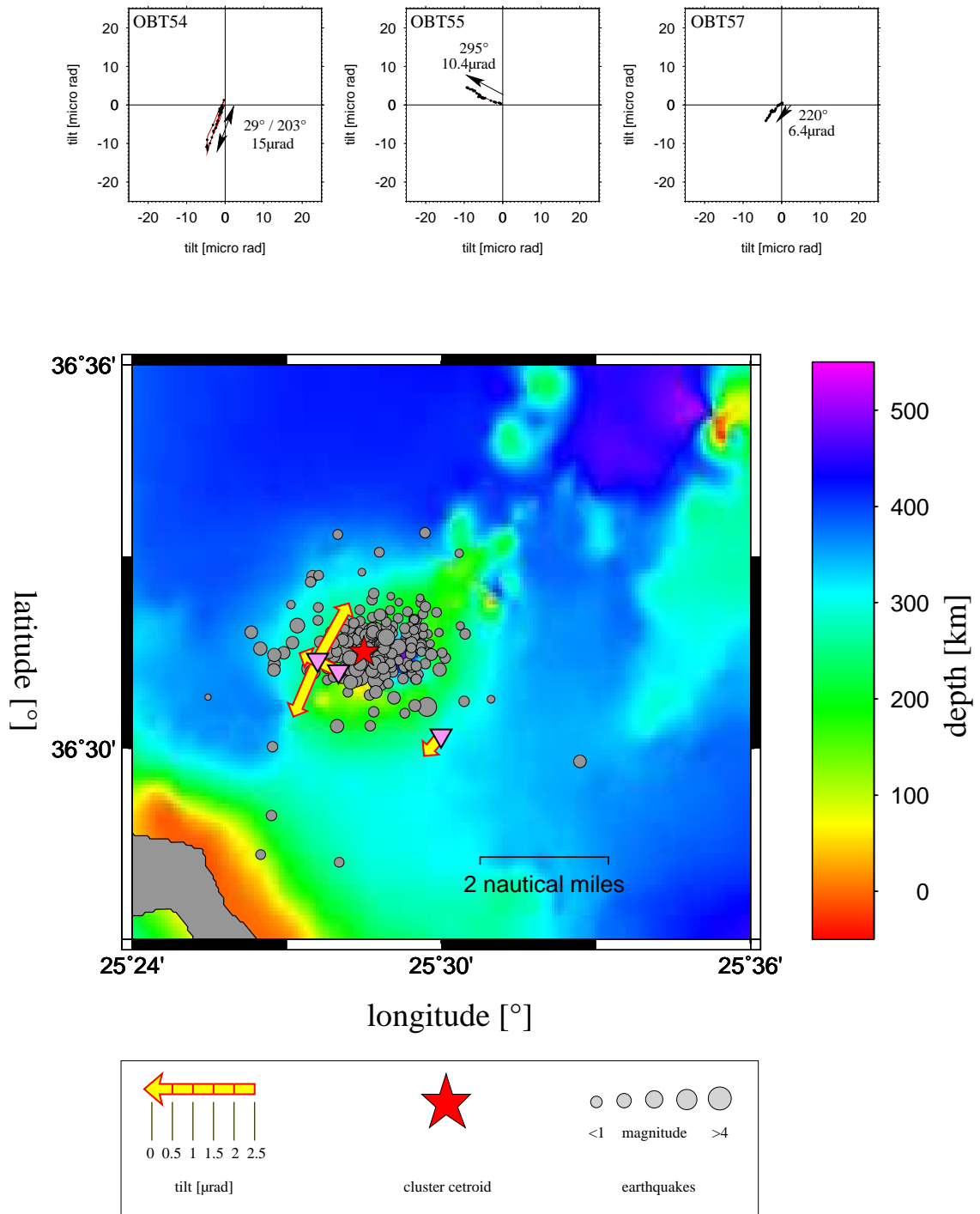


Figure D.28: Swarm CS-4: Tilt orientation

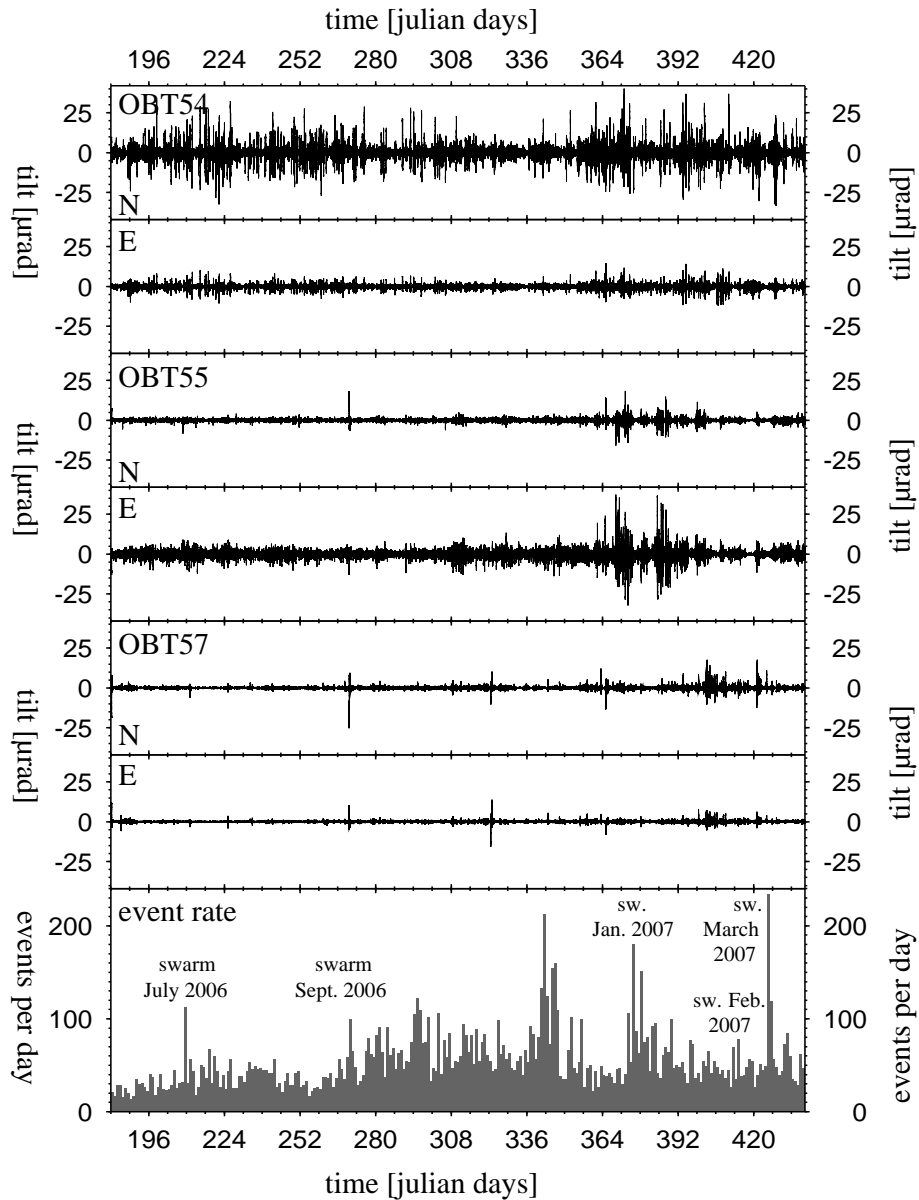


Figure D.29: Tilt traces over event rate: The plot shows the tilt amplitude in comparison to the events rate for each day. Tilt traces were highpass filtered at 1000 s. A significant correlation can not be observed, but for some swarms, peaks of increased amplitude on some or all OBTs are visible.

Finally, Fig. D.29 compares the tilt amplitude with the earthquake rate per day. Amplitude peaks are indeed observed for some of the seismically active periods. However, this effect can not be described as really systematic.

SYNOPSIS OF FOCAL MECHANISMS

The following section summarizes all events that were inverted for their moment tensor. Events $M_L \geq 3.5$ have been cross-checked with FOCMEC (P-wave polarity analysis, Snook et al., 1984), Events $M_L < 3.5$ have been calculated with both program with the following criteria:

- FOCMEC: At least 10 polarity readings
- MTI: At least 8 stations of which at least 6 are onshore

This led to the result that most events between M_L 3.0 – 3.4 were only inverted for their moment tensor, since both, the number of stations and the signal-noise ratio, which is important for the determination of P-wave polarity, get reduced the weaker the events are.

No solutions were found for events $M_L < 2.5$, events between M_L 2.5 – 3.0 that were invertable are rare.

Origin of given parameters:

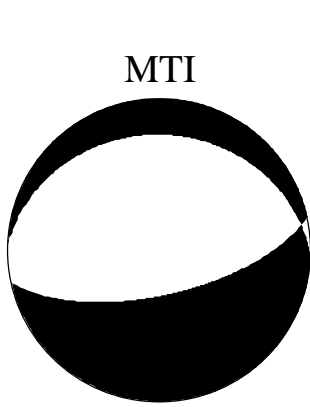
- SEISAN: Azimuthal gap and local earthquake magnitude M_L
- HYPODD: Location, depth and source time
- MTI: Fault planes, moment tensor, seismic moment M_0 , misfit, double couple component
- Chosen by operator: Weights

Residual (dimensionless):

$$rm = \frac{\sum_{i=1}^m \sum_{j=1}^n w_j (s_{ij} - r_{ij})^2}{\sum_{i=1}^m \sum_{j=1}^n w_j (r_{ij})^2} \quad (\text{E.1})$$

With m as the number of traces, n as the number of samples within the inversion window, w_j as the weight applied to trace j, s_{ij} as the synthetic and r_{ij} as the real data.

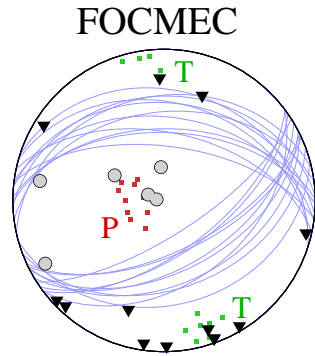
Event: 2006/07/28 12:11:14.5 lat.: 36.521545° lon.: 25.455115° depth: 9.2km
 Gap: 83° ML = 4.3 M(0) = 0.45E+15Nm Mw = 3.8 misfit = 0.540E+00 DC = 77%



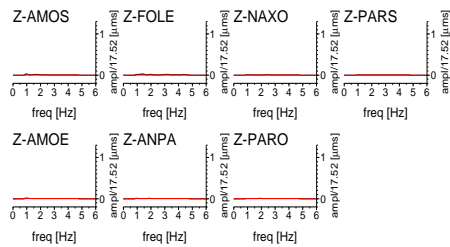
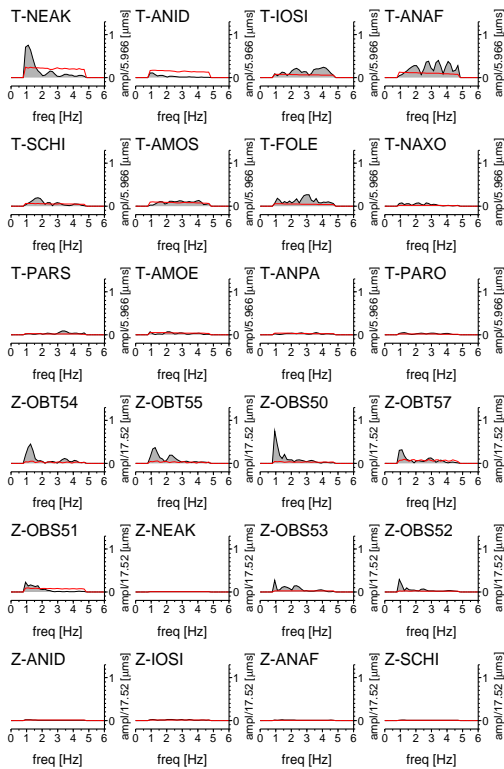
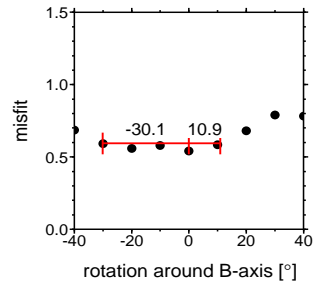
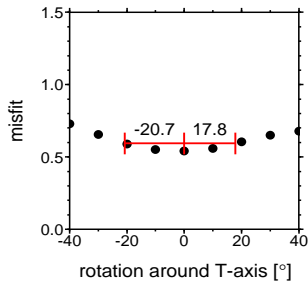
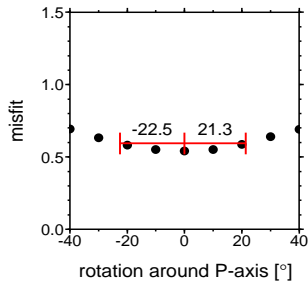
MTI

fault planes:
 Strike: 272.01°
 Dip: 25.08°
 Rake: -76.77°

moment tensor:
 $m(11) = -0.86$
 $m(22) = 0.27$
 $m(33) = 0.59$
 $m(12) = 0.14$
 $m(13) = 0.62$
 $m(23) = -0.14$



FOCMEC



Event 2006.07.28 12:11:14.5 lat:36.522 lon:25.454 depth:9.25

Weighting:

Land: P = 1.00 S = 0.25

OBS/OBT: P = 0.40

Figure E.1: Focal mechanism of MTInvers and FOCMEC of event 2006.07.28 12:11:14.5

Event: 2006/07/28 12:24:29.4 lat.: 36.519055° lon.: 25.440316° depth: 11.1km
 Gap: 86° ML = 4.6 M(0) = 0.90E+15Nm Mw = 3.9 misfit = 0.630E+00 DC = 73%

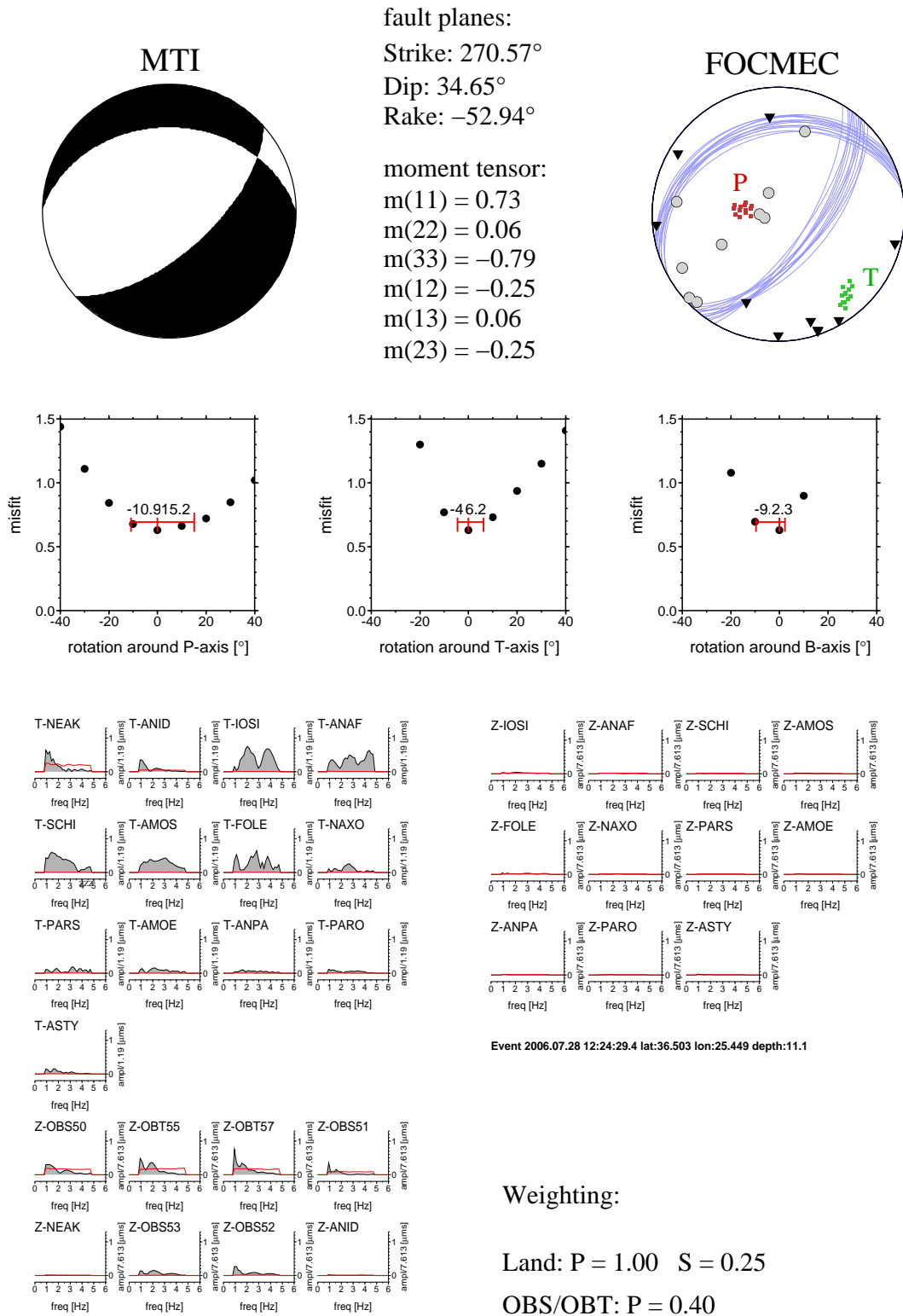


Figure E.2: Focal mechanism of MTInvers and FOCMEC of event 2006.07.28 12:24:29.4

Event: 2006/07/28 12:26:48.0 lat.: 36.508077° lon.: 25.448482° depth: 11.1km
 Gap: 82° ML = 4.5 M(0) = 0.82E+15Nm Mw=3.9 misfit = 0.537E+00 DC = 91%

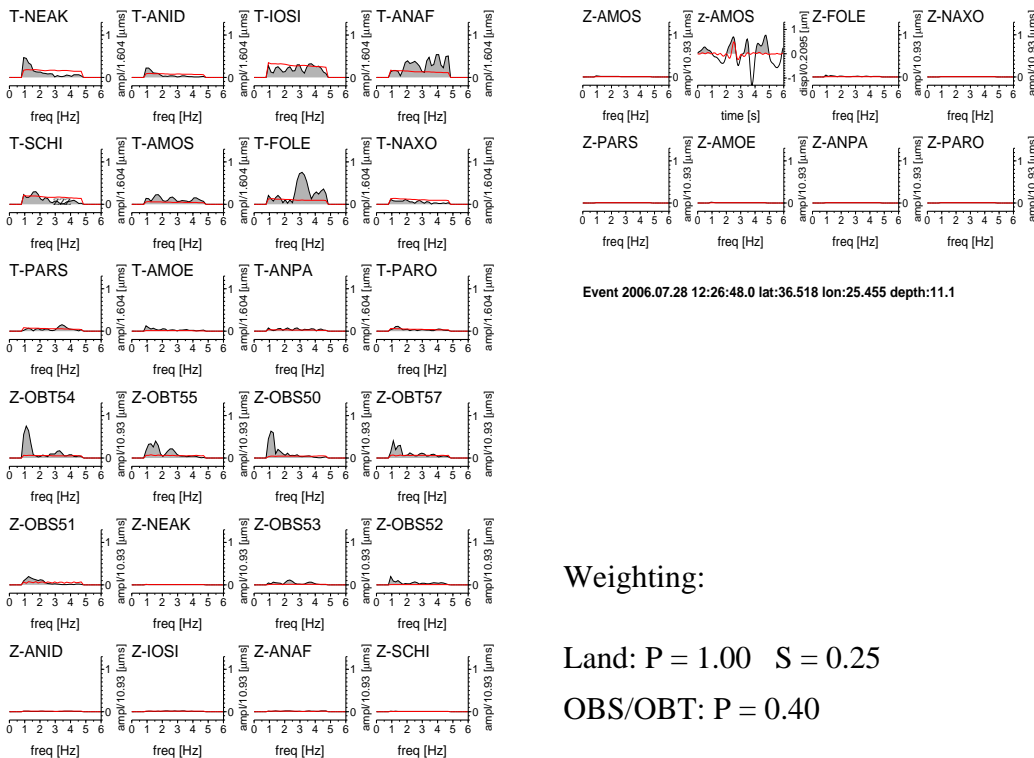
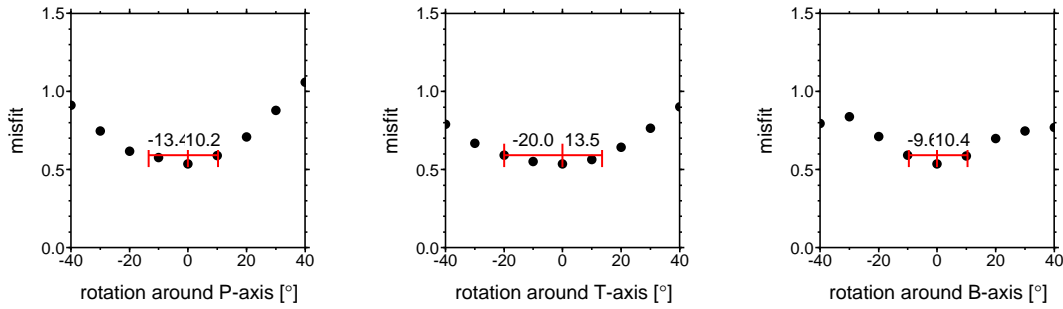
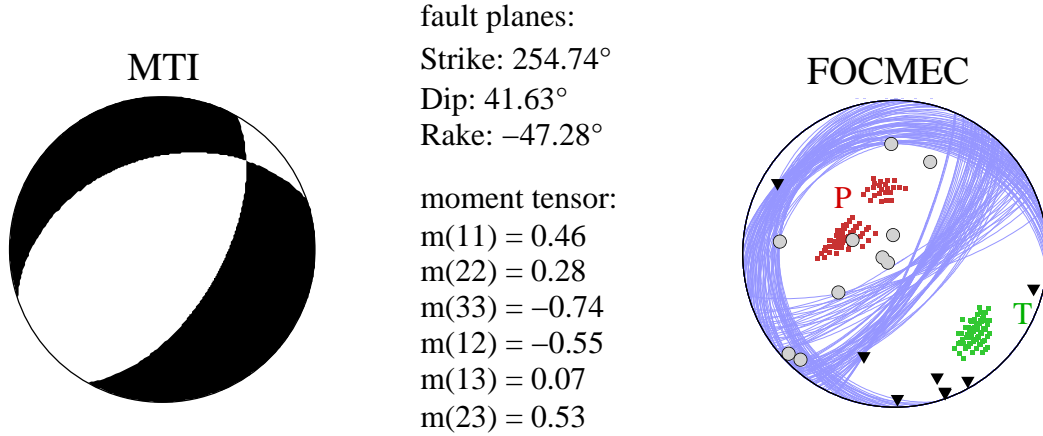
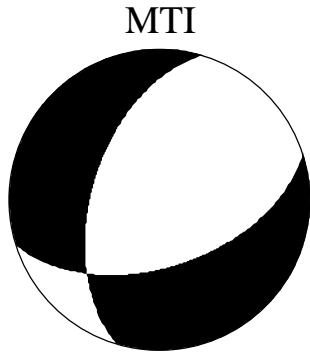


Figure E.3: Focal mechanism of MTInvers and FOCMEC of event 2006.07.28 12:26:48.0

Event: 2006/08/24 09:28:25.4 lat.: 36.629220° lon.: 25.693309° depth: 9.4km
 Gap: 71° ML = 3.7 M(0) = 0.15E+15Nm Mw = 3.4 misfit = 0.256E+00 DC = 73%



fault planes:
 Strike: 196.83°
 Dip: 52.79°
 Rake: -130.92°

moment tensor:
 $m(11) = 0.34$
 $m(22) = 0.37$
 $m(33) = -0.71$
 $m(12) = -0.71$
 $m(13) = -0.25$
 $m(23) = -0.24$

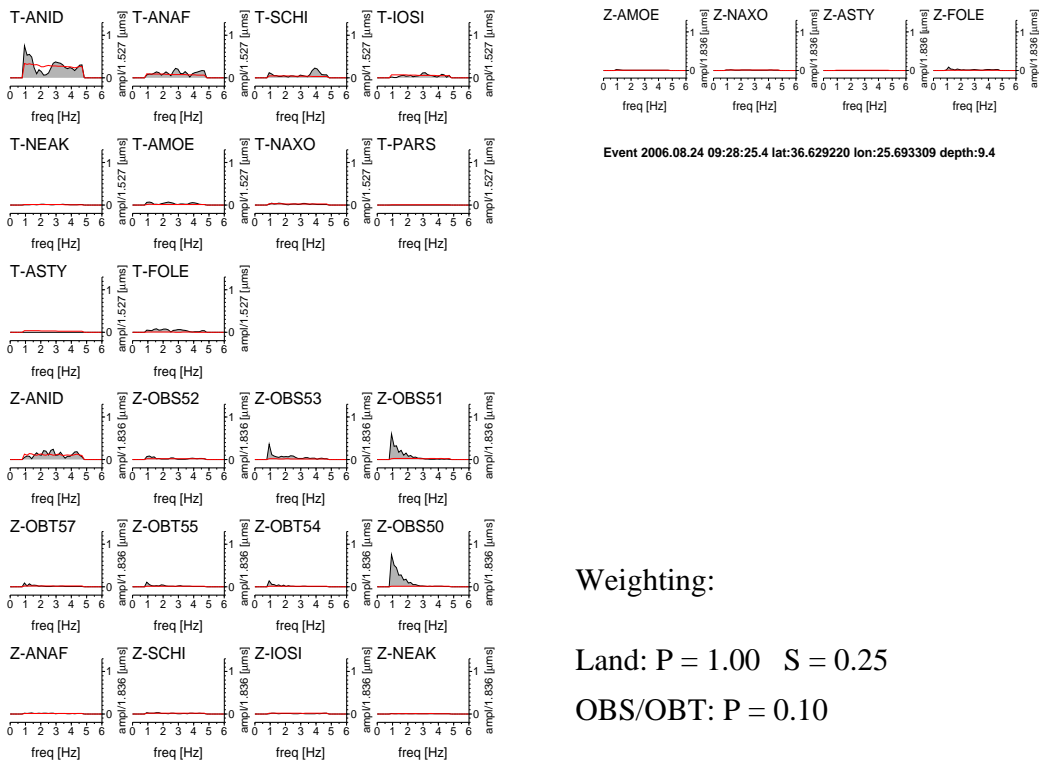
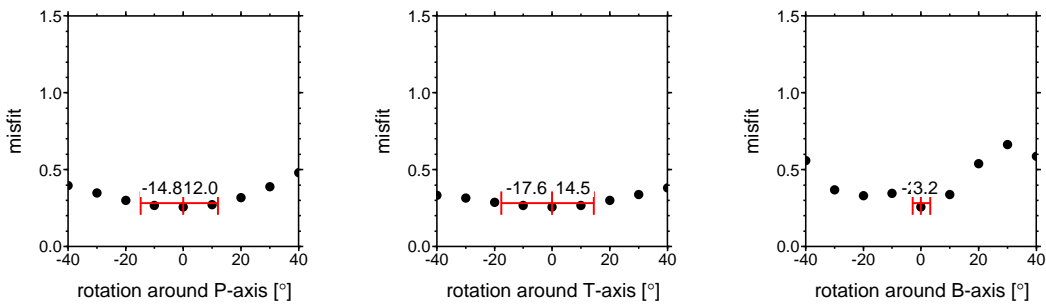
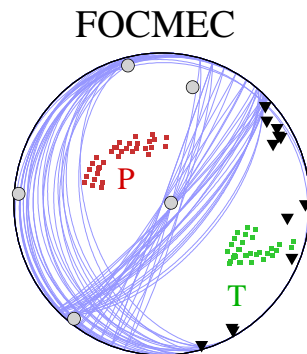


Figure E.4: Focal mechanism of MTInvers and FOCMEC of event 2006.08.24 09:28:25.4

Event: 2006/09/03 15:34:29.3 lat.: 36.501831° lon.: 25.479785° depth: 13.2km
 Gap: 79° ML = 3.6 M(0) = 0.33E+15Nm MW=3.6 misfit = 0.870E+00 DC = 40%

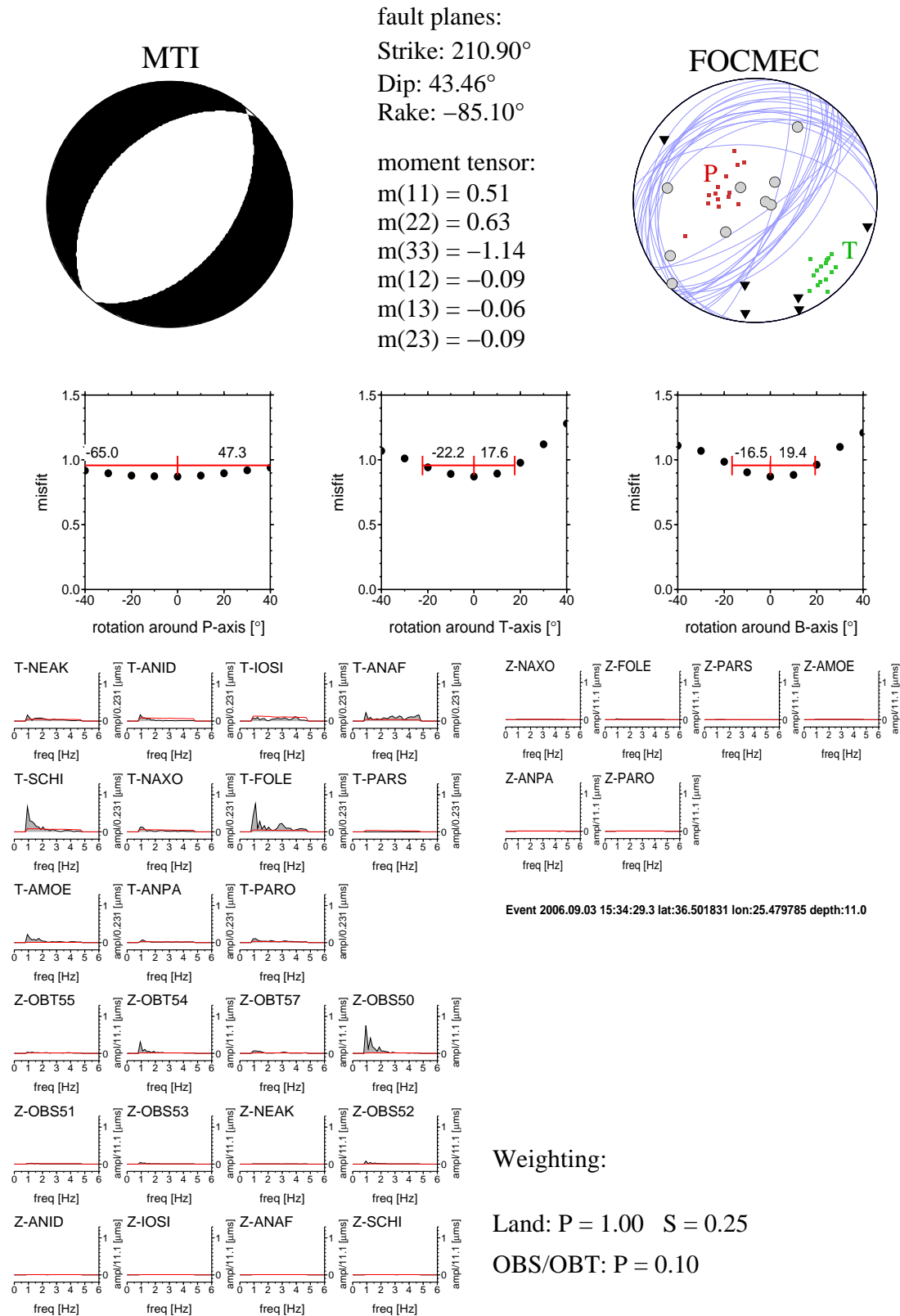


Figure E.5: Focal mechanism of MTInvers and FOCMEC of event 2006.09.03 15:34:29.3

Event: 2006/09/27 01:23:24.4 lat.: 36.535832° lon.: 25.464870° depth: 10.7km
 Gap: 80° ML = 3.6M(0) = 0.27E+15Nm MW=3.6 misfit = 0.843E+00 DC = 49%

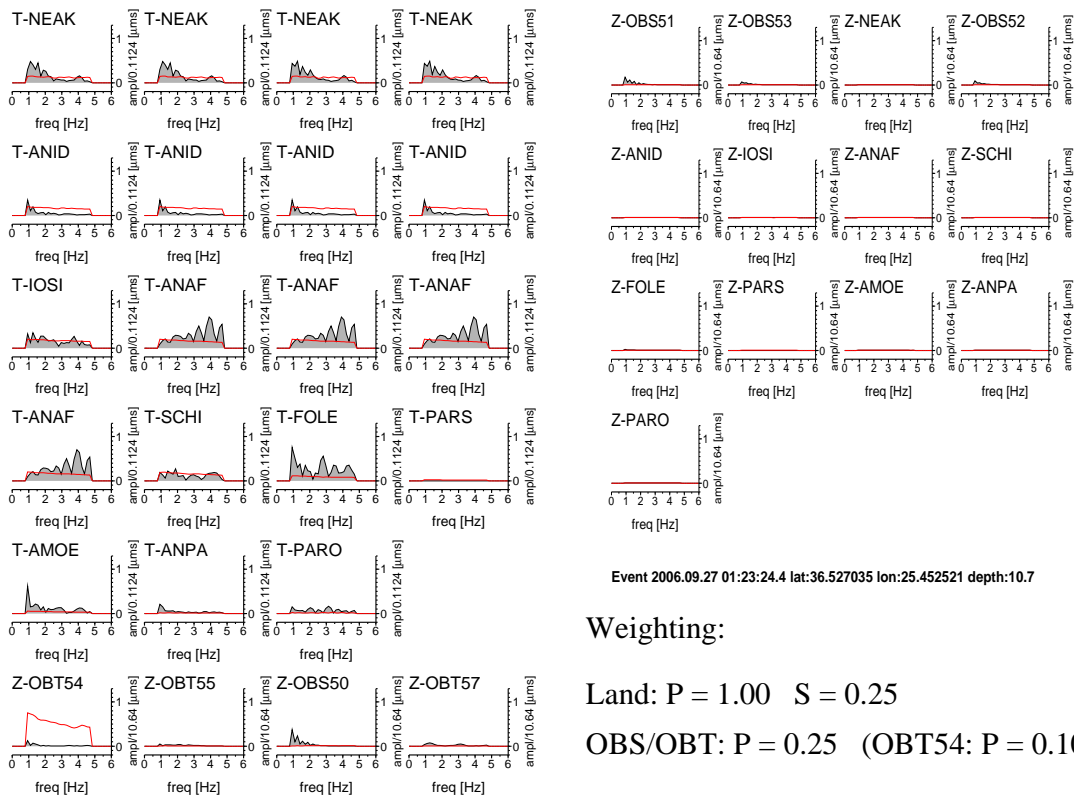
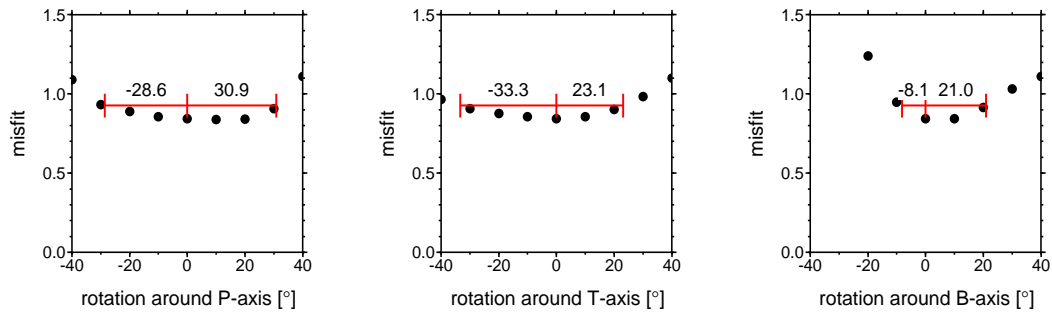
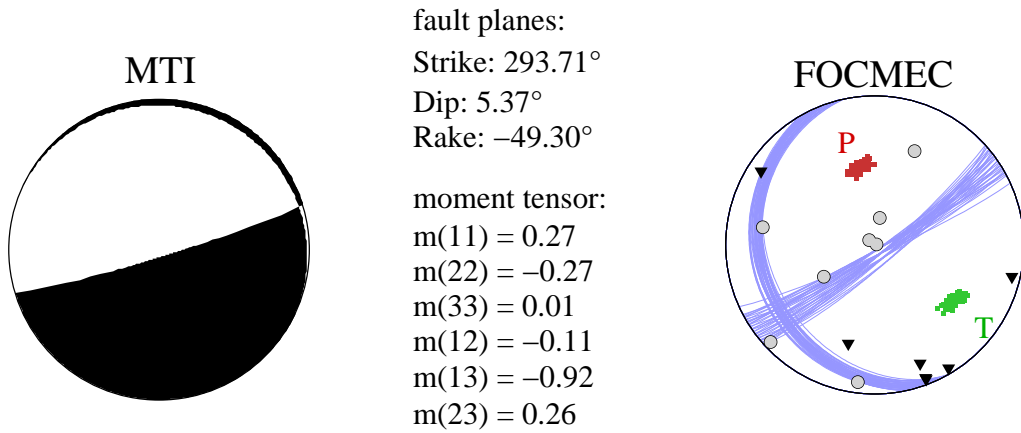


Figure E.6: Focal mechanism of MTInvers and FOCMEC of event 2006.09.27 01:23:24.4

Event: 2006/10/11 20:33:21.0 lat.: 36.537866° lon.: 25.565098° depth: 6.9km
 Gap: 87° ML = 3.7 M(0) = 0.88E+15Nm Mw = 3.9 misfit = 0.328E+00 DC = 67%

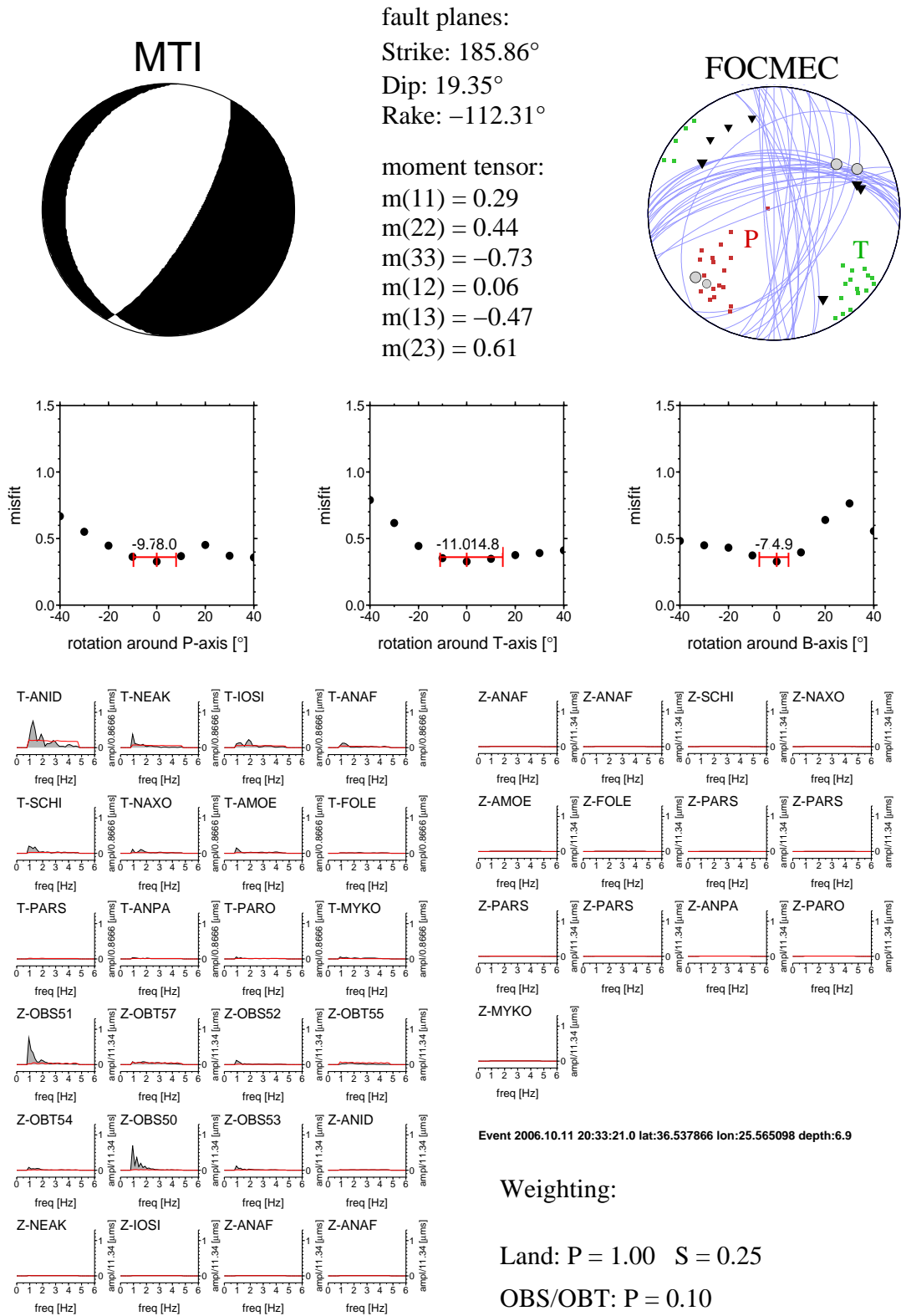
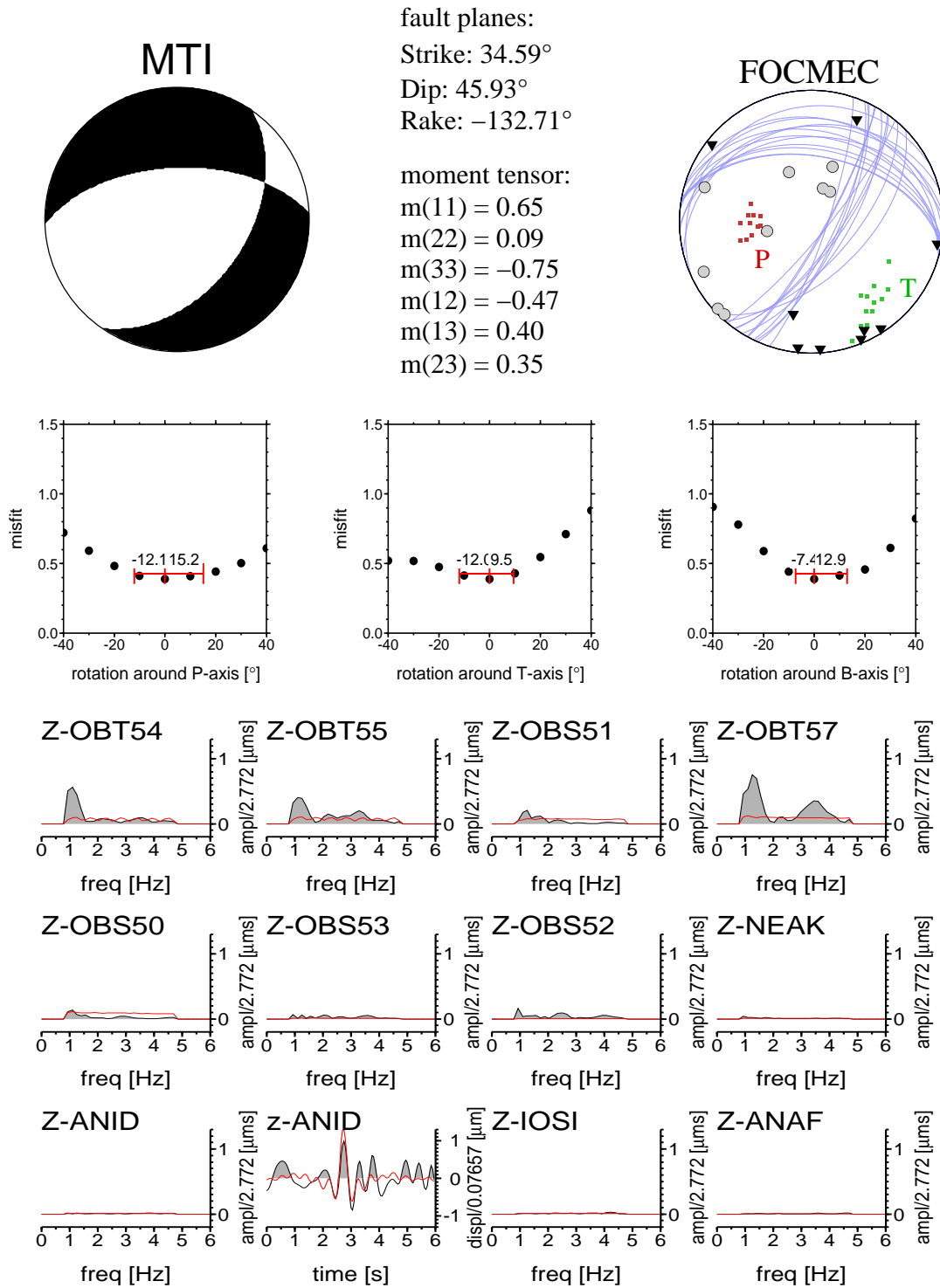


Figure E.7: Focal mechanism of MTInvers and FOCMEC of event 2006.10.11 20:33:21.0

Event: 2006/10/22 20:48:52.2 lat.: 36.540401° lon.: 25.494159° depth: 8.7km
 Gap: 68° ML = 3.8 M(0) = 0.51E+15Nm Mw = 3.7 misfit = 0.388E+00 DC = 95%



Weighting: Land: P = 1.00 S = 0.25 OBS/OBT: P = 0.25

Figure E.8: Focal mechanism of MTInvers and FOCMEC of event 2006.10.22 20:48:52.2

Event: 2006/10/22 20:50:04.2 lat.: 36.542330° lon.: 25.488088° depth: 9.0km
 Gap: 78° ML = 3.8 M(0) = 0.30E+15Nm Mw = 3.6 misfit = 0.330E+00 DC = 52%

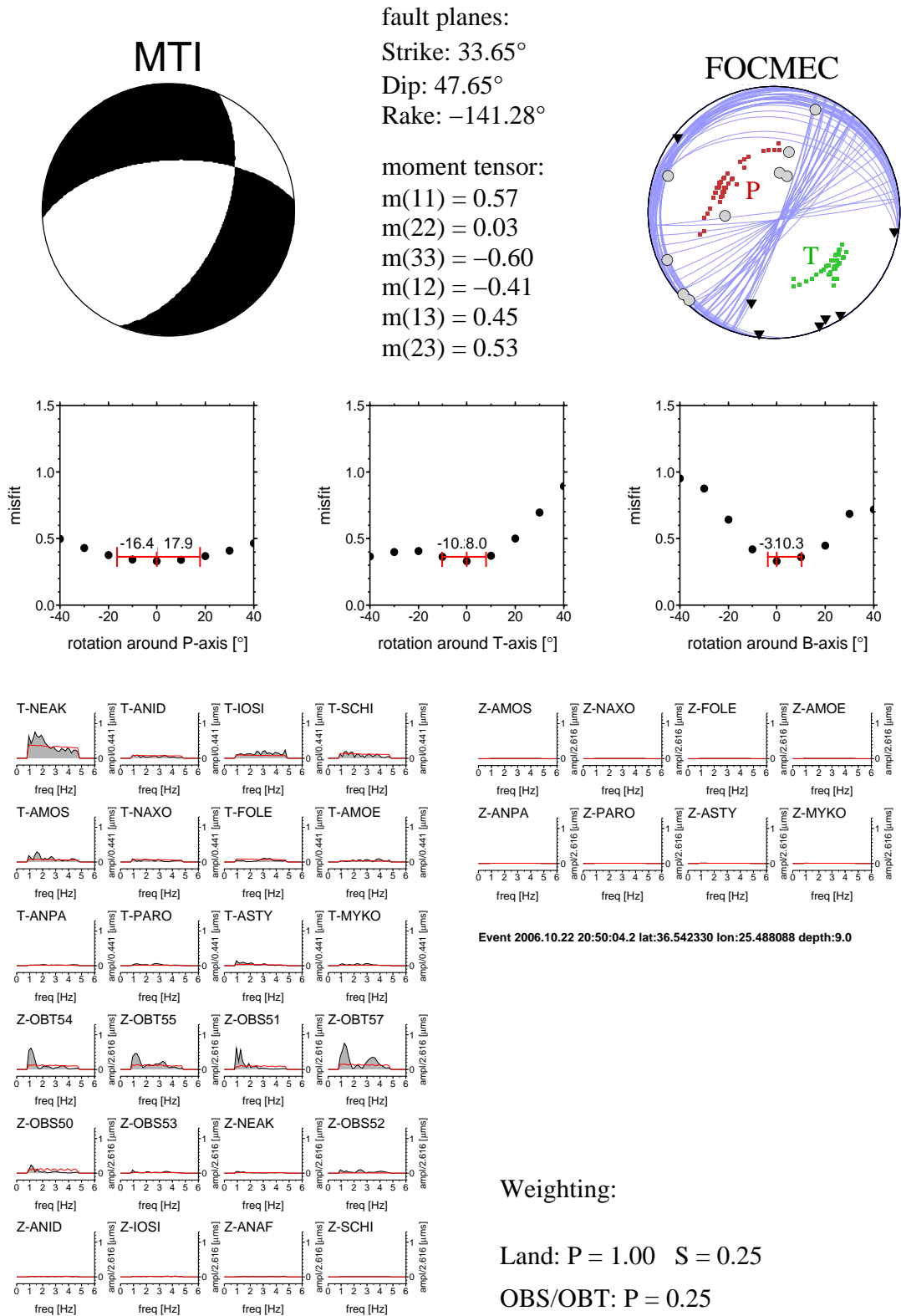
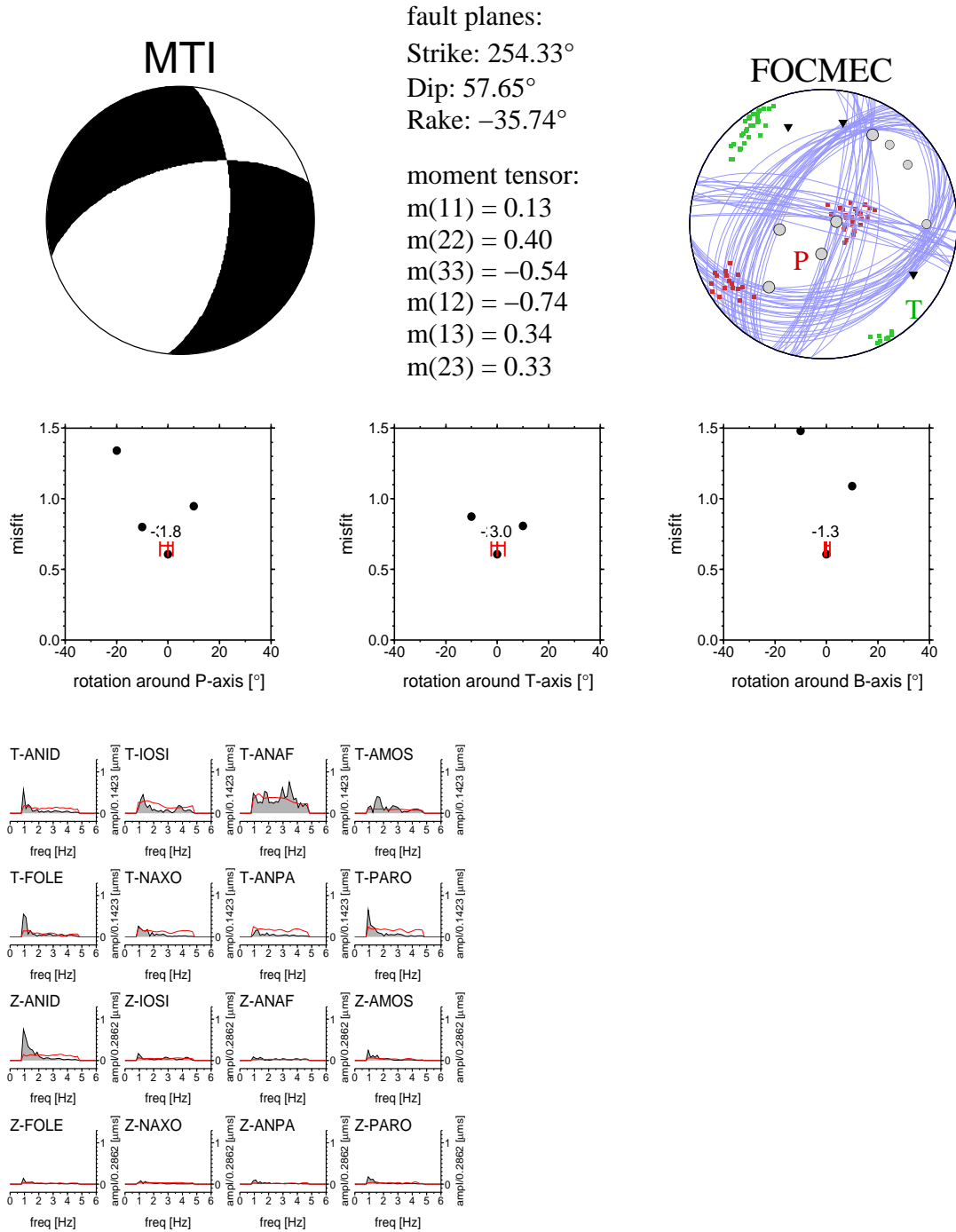


Figure E.9: Focal mechanism of MTInvers and FOCMEC of event 2006.10.22 20:50:04.2

Event: 2006/11/11 11:26:45.6 lat.: 36.509245° lon.: 25.472465° depth: 8.6km
 Gap: 61° ML = 3.5 M(0) = 0.63E+15Nm Mw = 3.8 misfit = 0.606E+00 DC = 92%



Event 2006.11.11 11:26:45.6 lat:36.509245 lon:25.472465 depth:8.6

Weighting:

Land: P = 1.00 S = 0.25

OBS/OBT: not used

Figure E.10: Focal mechanism of MTInvers and FOCMEC of event 2006.11.11 11:26:45.6

Event: 2006/11/13 08:04:24.2 lat.: 36.508219° lon.: 25.481842° depth: 6.4km
 Gap: 104° ML = 3.6 M(0) = 0.60E+15Nm Mw = 3.8 misfit = 0.408E+00 DC = 65%

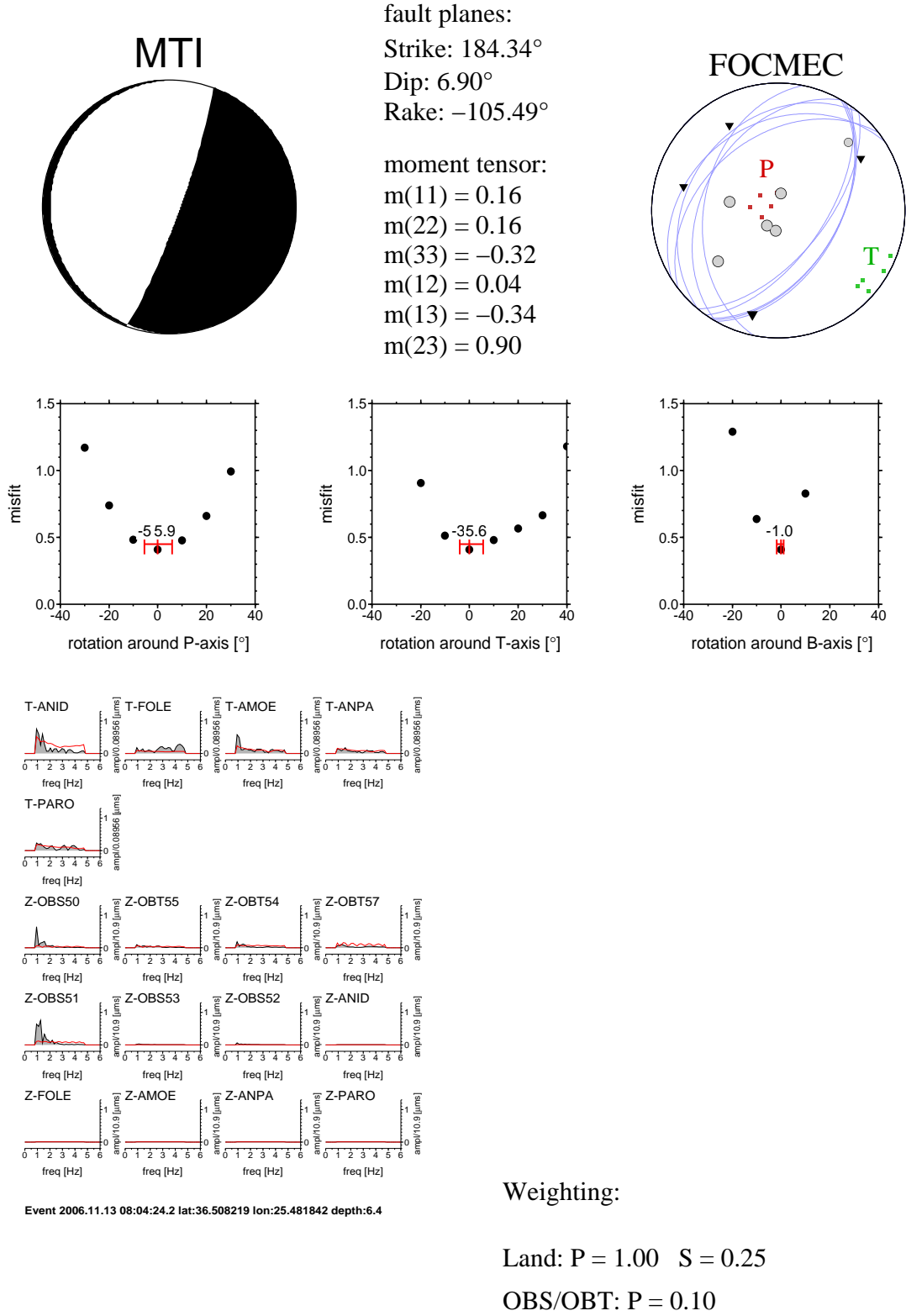


Figure E.11: Focal mechanism of MTInvers and FOCMEC of event 2006.11.13 08:04:24.2

Event: 2006/11/13 08:49:50.7 lat.: 36.508805° lon.: 25.480878° depth: 7.1km
 Gap: 80° ML = 4.0 M(0) = 0.15E+16Nm Mw = 4.1 misfit = 0.470E+00 DC = 88%

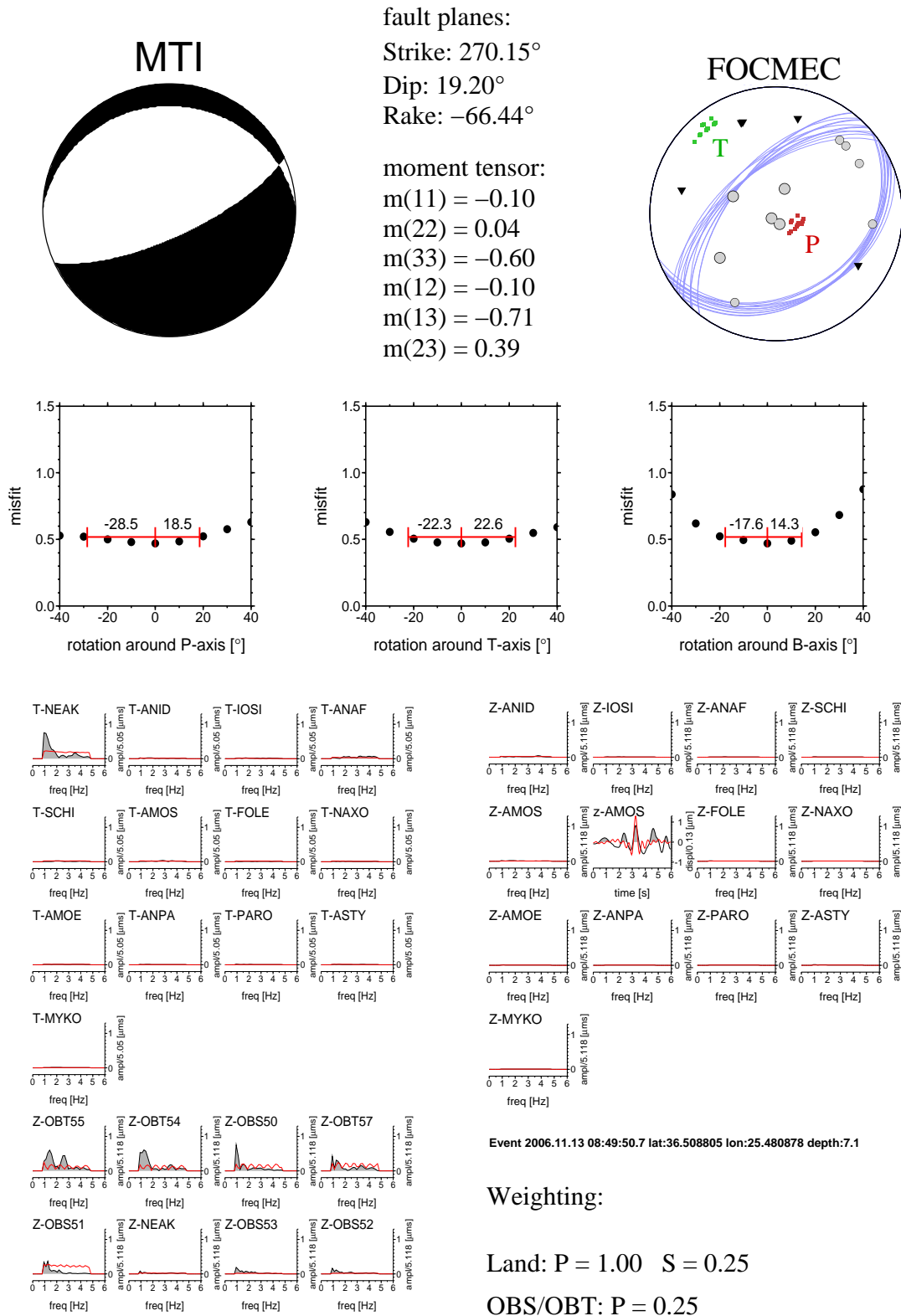
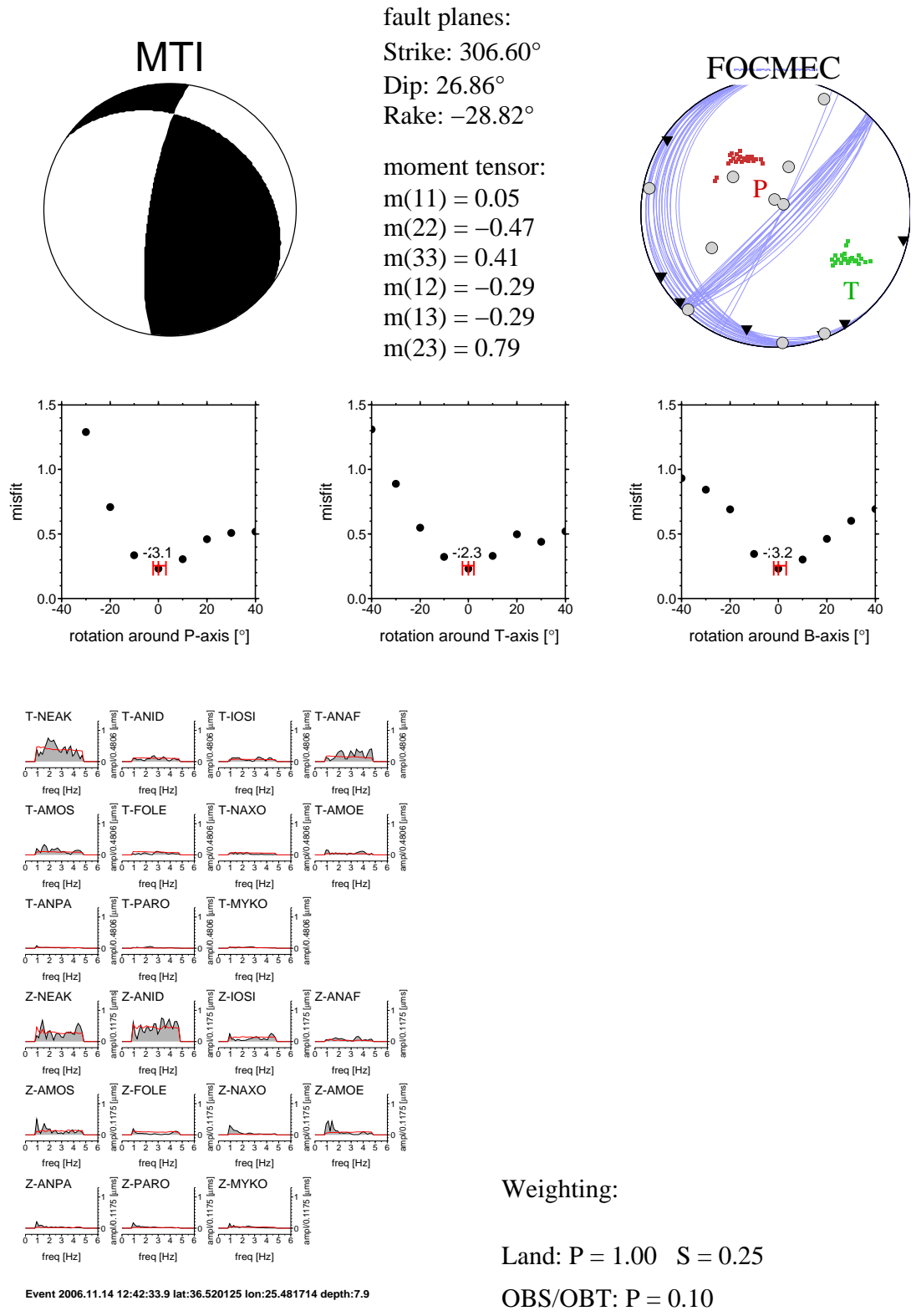


Figure E.12: Focal mechanism of MTInvers and FOCMEC of event 2006.11.13 08:49:50.7

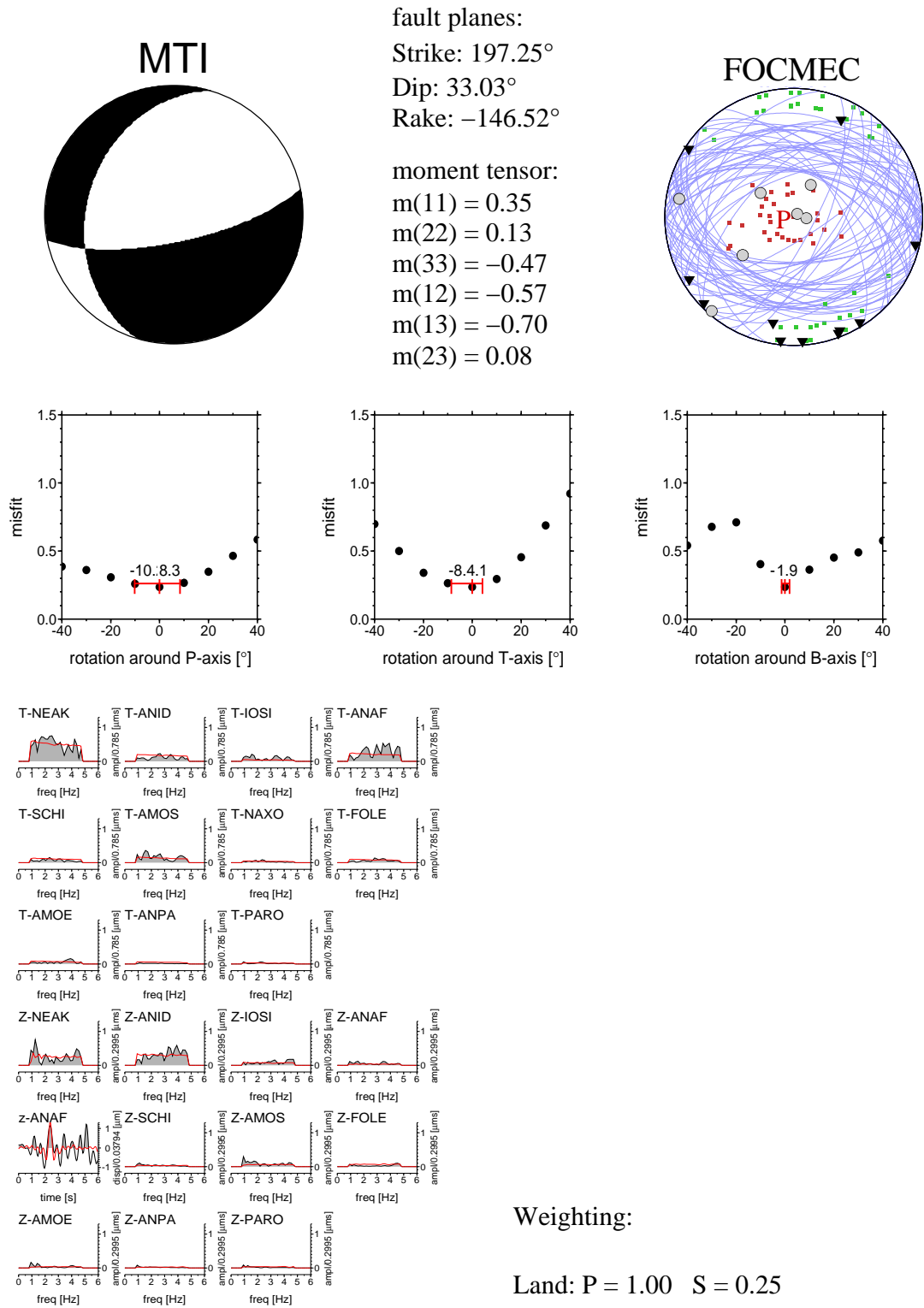
Event: 2006/11/14 12:42:33.9 lat.: 36.520125° lon.: 25.481714° depth: 7.9km
 Gap: 61° ML = 4.0 M(0) = 0.78E+15Nm Mw = 3.9 misfit = 0.231E+00 DC = 81%



Event 2006.11.14 12:42:33.9 lat.:36.520125 lon.:25.481714 depth:7.9

Figure E.13: Focal mechanism of MTInvers and FOCMEC of event 2006.11.14 12:42:33.9

Event: 2006/11/14 12:45:29.7 lat.: 36.521399° lon.: 25.484853° depth: 7.8km
 Gap: 78° ML = 4.3 M(0) = 0.45E+15Nm Mw = 3.7 misfit = 0.237E+00 DC = 73%



Weighting:

Land: P = 1.00 S = 0.25

OBS/OBT: not used

Event 2006.11.14 12:45:29.7 lat:36.521399 lon:25.484853 depth:7.8

Figure E.14: Focal mechanism of MTInvers and FOCMEC of event 2006.11.14 12:45:29.7

Event: 2006/12/06 10:24:37.9 lat.: 36.535832° lon.: 25.464870° depth: 8.5km
 Gap: 81° ML = 3.5 M(0) = 0.72E+14Nm MW=3.2 misfit = 0.642E+00 DC = 34%

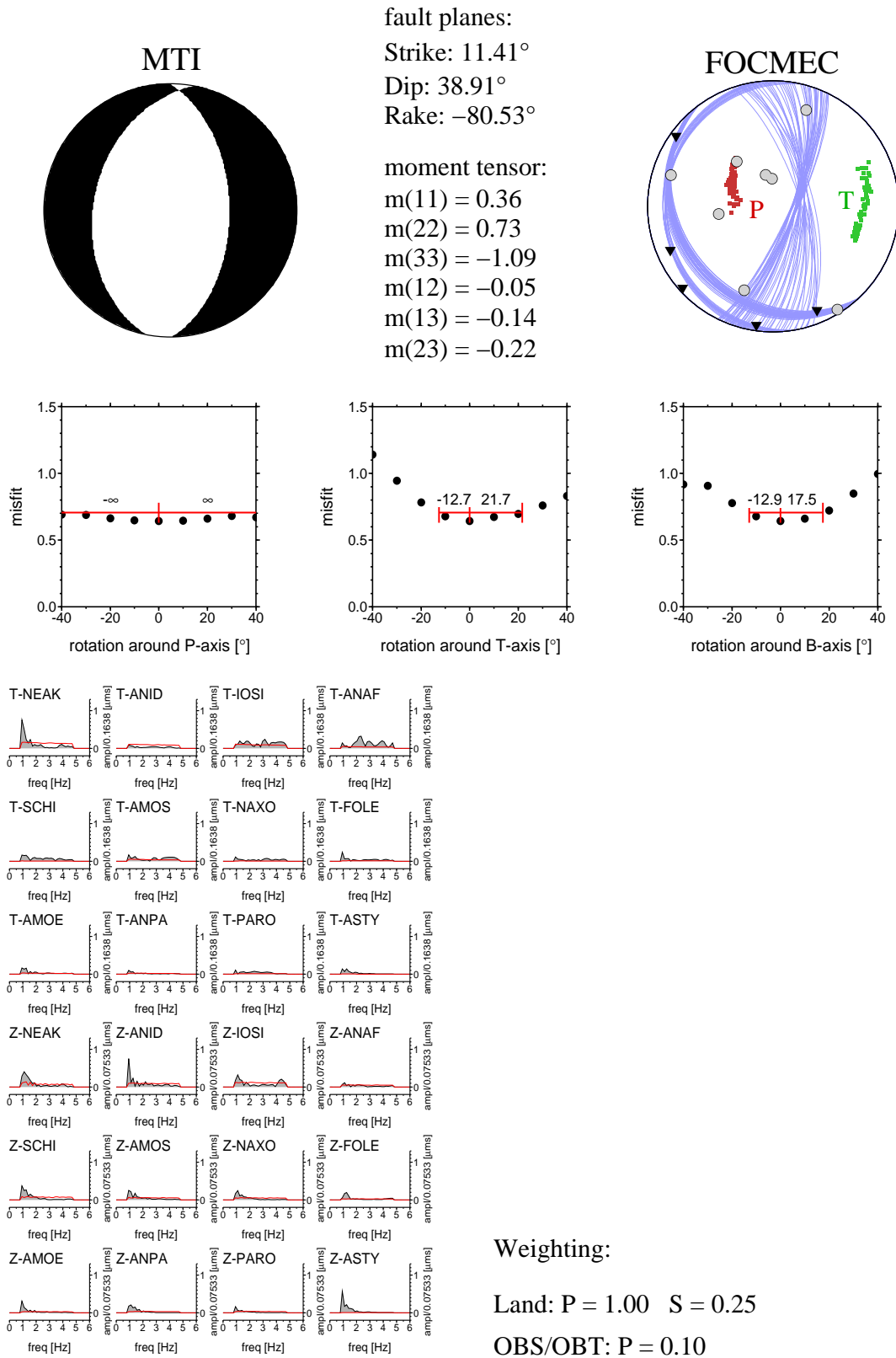


Figure E.15: Focal mechanism of MTInvers and FOCMEC of event 2006.12.06 10:24:37.9

Event: 2007/01/10 17:22:16.4 lat.: 36.655916° lon.: 25.566536° depth: 8.8km
 Gap: 62° ML = 4.0 M(0) = 0.34E+15Nm Mw = 3.6 misfit = 0.377E+00 DC = 74%

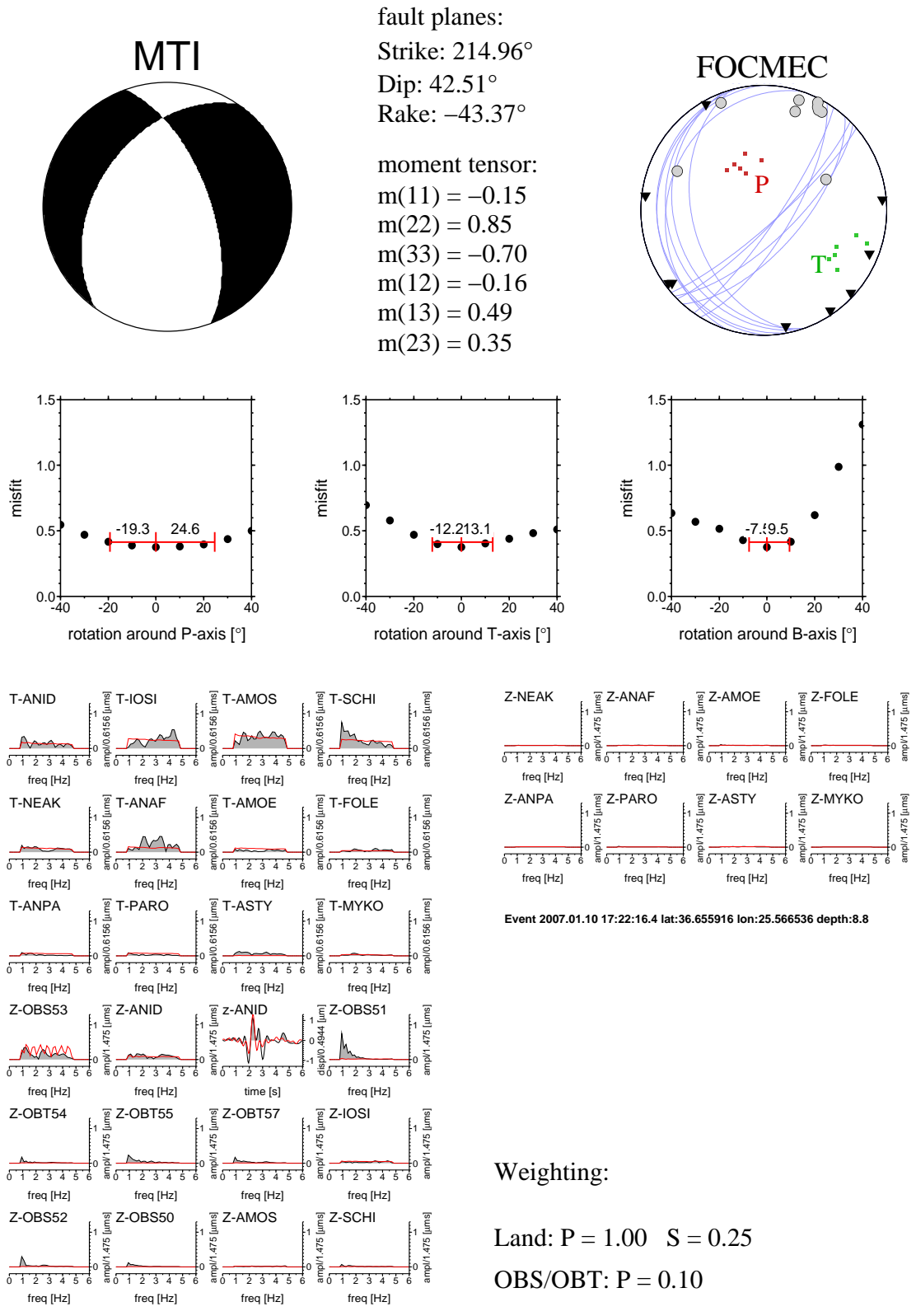


Figure E.16: Focal mechanism of MTInvers and FOCMEC of event 2007.01.10 17:22:16.4

Event: 2007/02/18 17:23:34.1 lat.: 36.531523° lon.: 25.467601° depth: 7.9km
 Gap: 81° ML = 4.5 M(0) = 0.62E+15Nm Mw = 3.8 misfit = 0.407E+00 DC = 30%

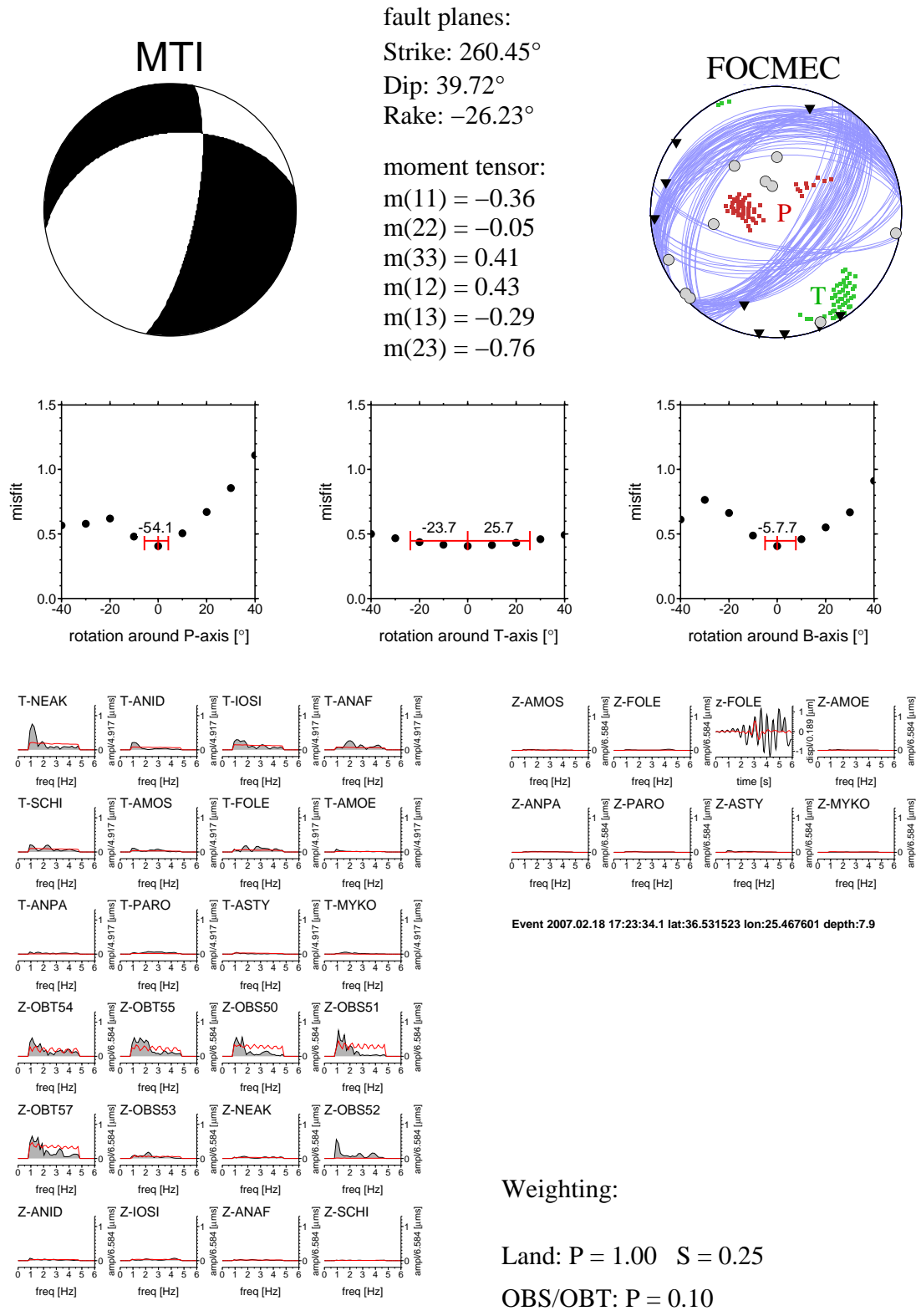


Figure E.17: Focal mechanism of MTInvers and FOCMEC of event 2007.02.18 17:23:34.1

Event: 2007/02/26 13:24:51.1 lat.: 36.610986° lon.: 25.591036° depth: 8.4km
 Gap: 67° ML = 3.5 M(0) = 0.17E+15Nm Mw = 3.4 misfit = 0.288E+00 DC = 82%

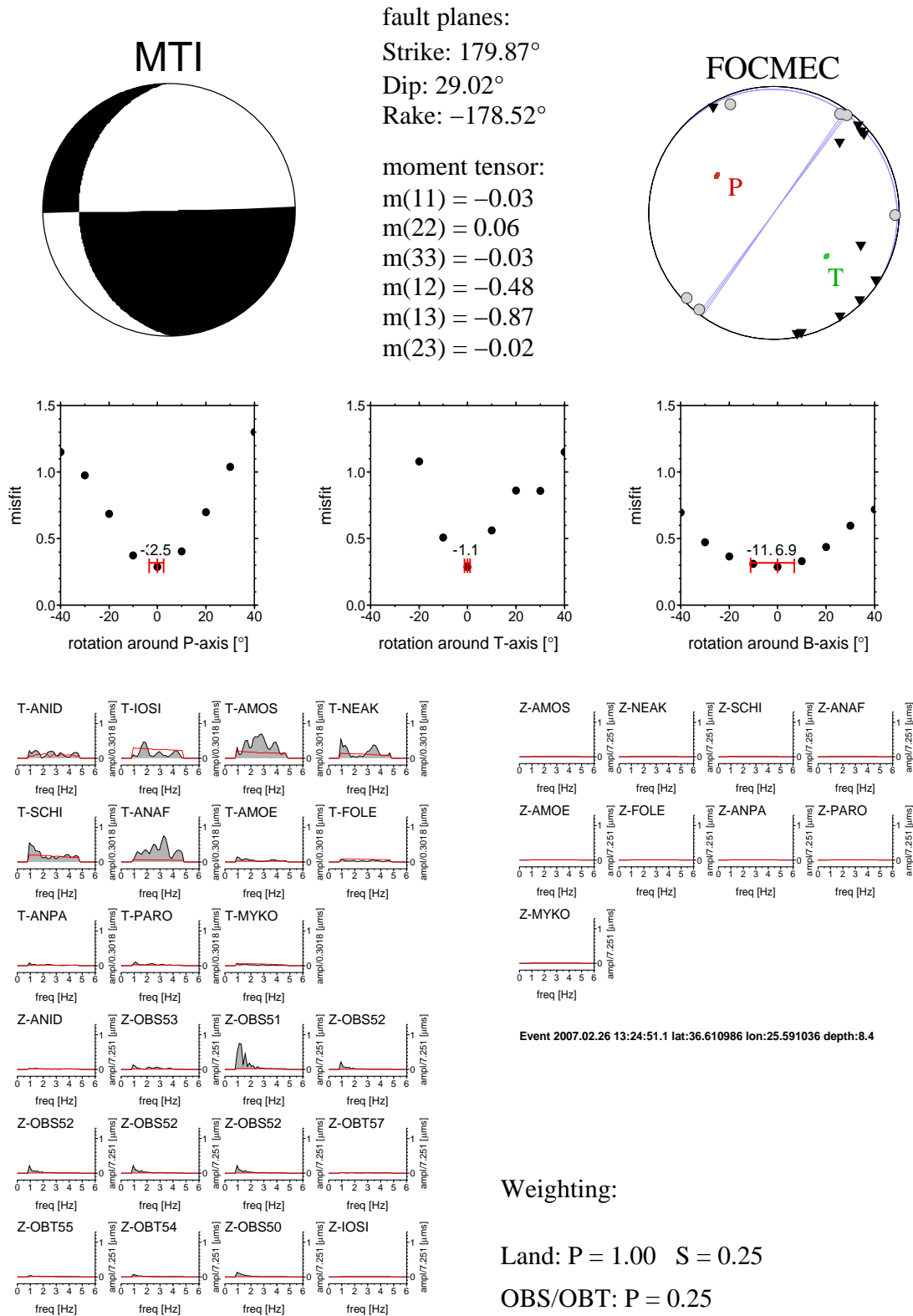


Figure E.18: Focal mechanism of MTInvers and FOCMEC of event 2007.02.26 13:24:51.1

Event: 2007/03/01 11:48:25.4 lat.: 36.517680° lon.: 25.479826° depth: 8.3km
 Gap: 73° ML = 4.1 M(0) = 0.47E+15Nm Mw = 3.7 misfit = 0.344E+00 DC = 63%

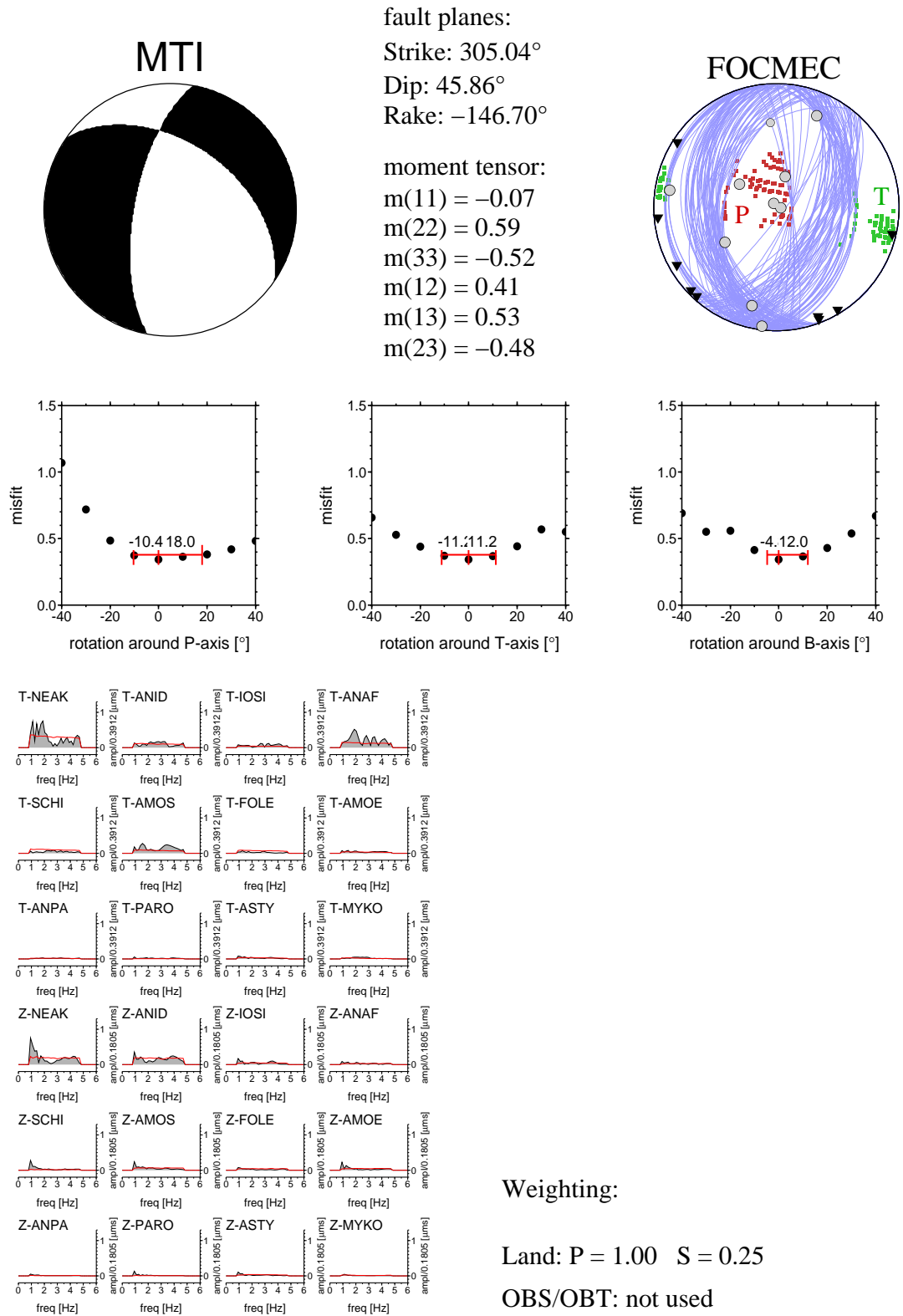
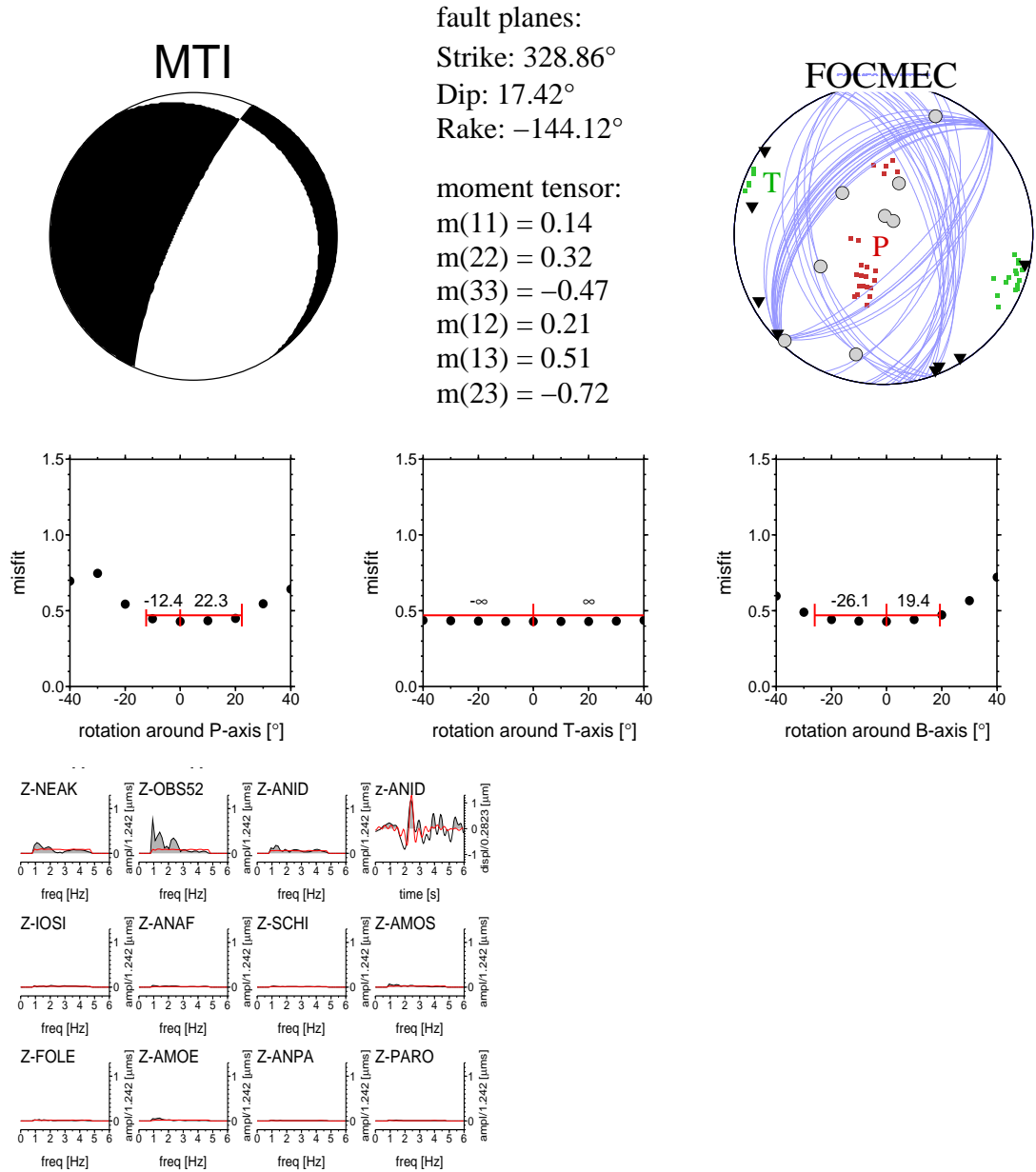


Figure E.19: Focal mechanism of MTInvers and FOCMEC of event 2007.03.01 11:48:25.4

Event: 2007/03/01 11:48:42.7 lat.: 36.519055° lon.: 25.473126° depth: 8.4km
 Gap: 69° ML = 4.4 M(0) = 0.20E+16Nm Mw = 4.1 misfit = 0.428E+00 DC = 35%



Weighting:

Land: P = 1.00 S not used

OBS/OBT: not used / OBS52: P = 0.25

Figure E.20: Focal mechanism of MTInvers and FOCMEC of event 2007.03.01 11:48:42.7

Event: 2007/03/01 11:53:41.2 lat.: 36.523071° lon.: 25.477216° depth: 7.9km
 Gap: 67° ML = 3.5 M(0) = 0.36E+15Nm Mw = 3.6 misfit = 0.559E+00 DC = 60%

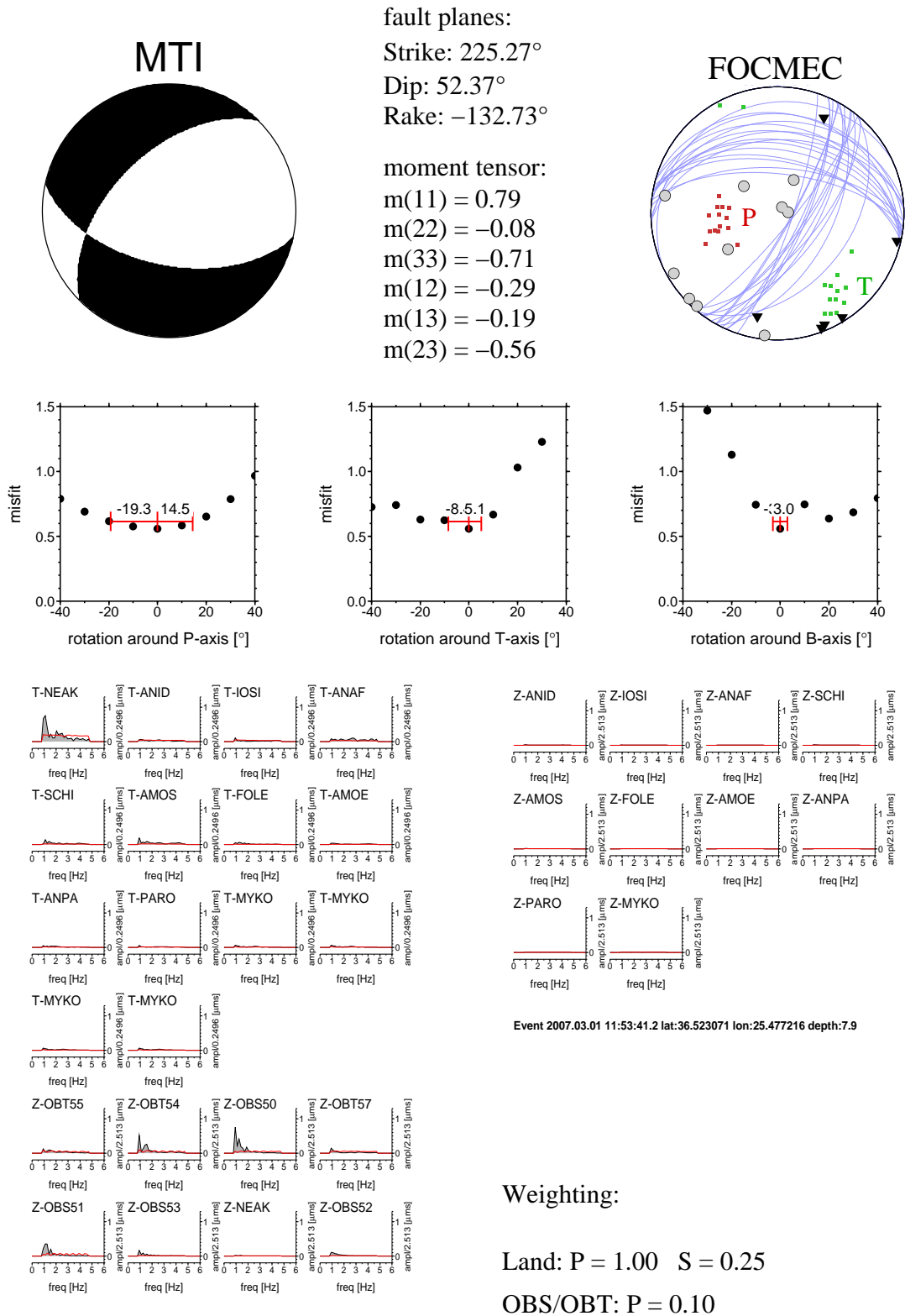
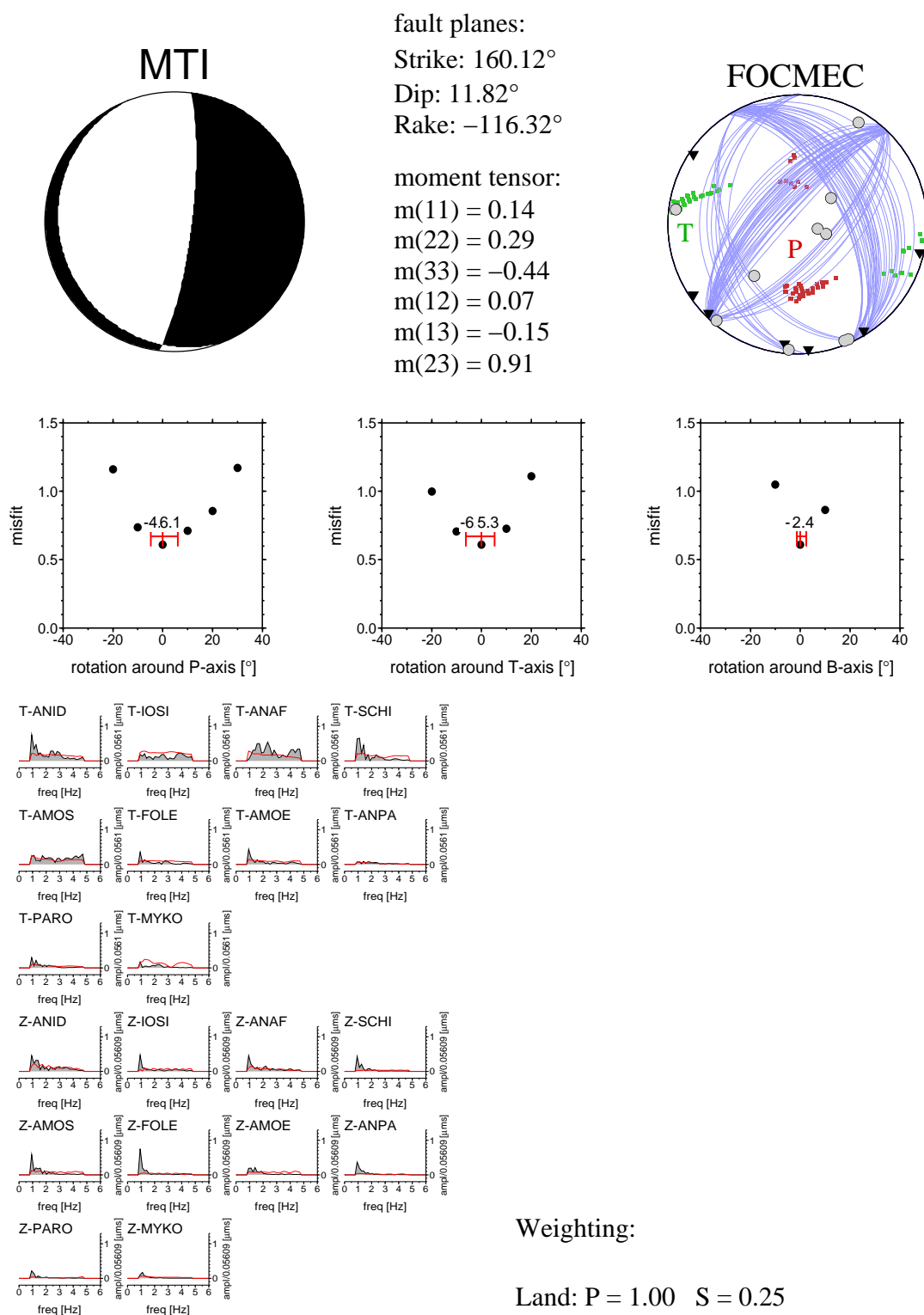


Figure E.21: Focal mechanism of MTInvers and FOCMEC of event 2007.03.01 11:53:41.2

Event: 2007/03/01 12:46:15.6 lat.: 36.510701° lon.: 25.495341° depth: 7.7km
 Gap: 78° ML = 3.5 M(0) = 0.58E+14Nm Mw = 3.2 misfit = 0.610E+00 DC = 82%



Event 2007.03.01 12:46:15.6 lat:36.510701 lon:25.495341 depth:7.7

Figure E.22: Focal mechanism of MTInvers and FOCMEC of event 2007.03.01 12:46:15.6

The following faultplane solutions of events $M_L < 3.5$ have only been inverted with MTI, since these events are on average too weak to observe 10 or more clear polarity readings to run FOCMEC. Because the inversion was run in the frequency domain, given beach balls show the most probable solution (as suggested by the stronger, crosschecked focals). The grey-white beach balls have not been checked for polarity!

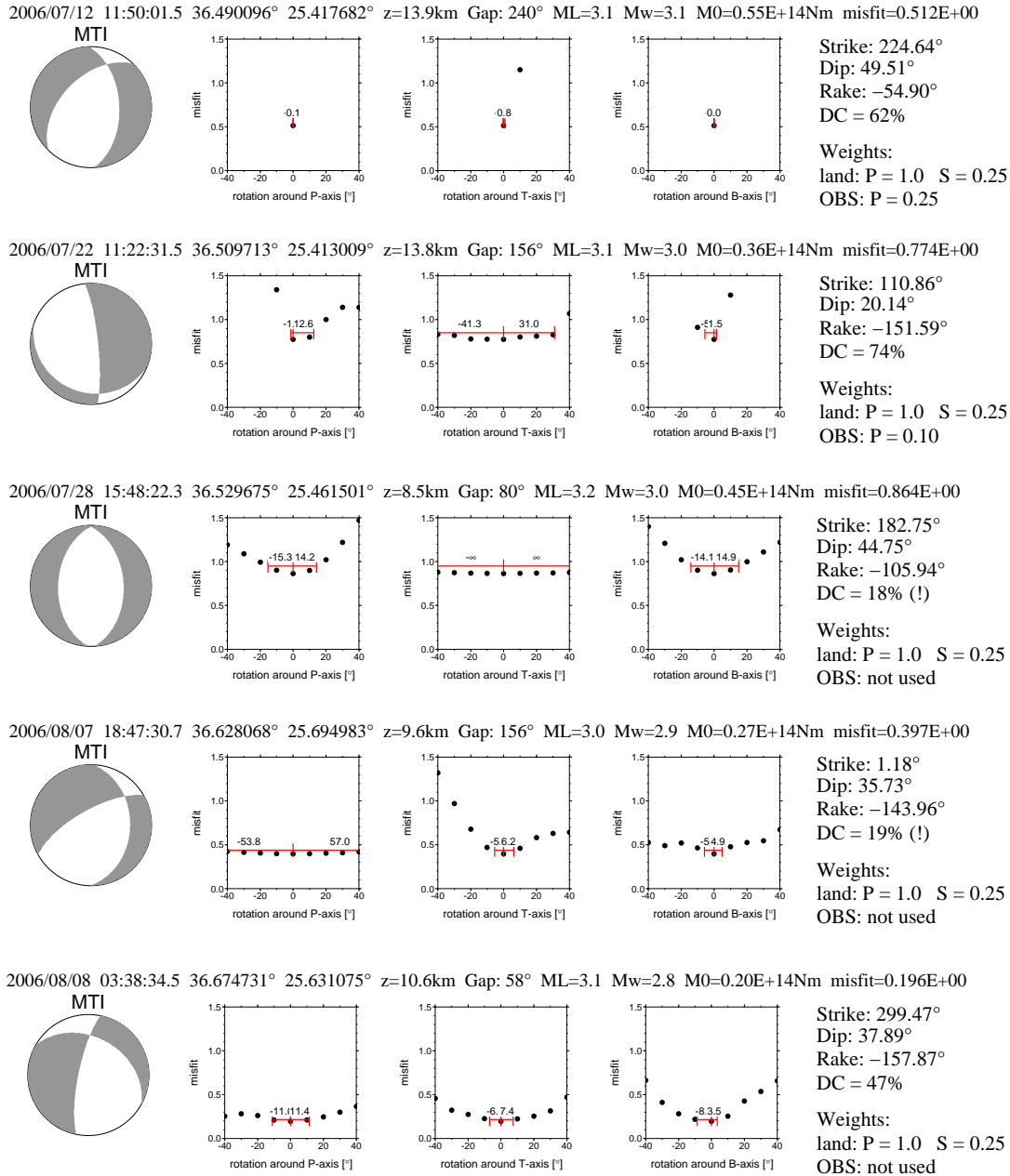
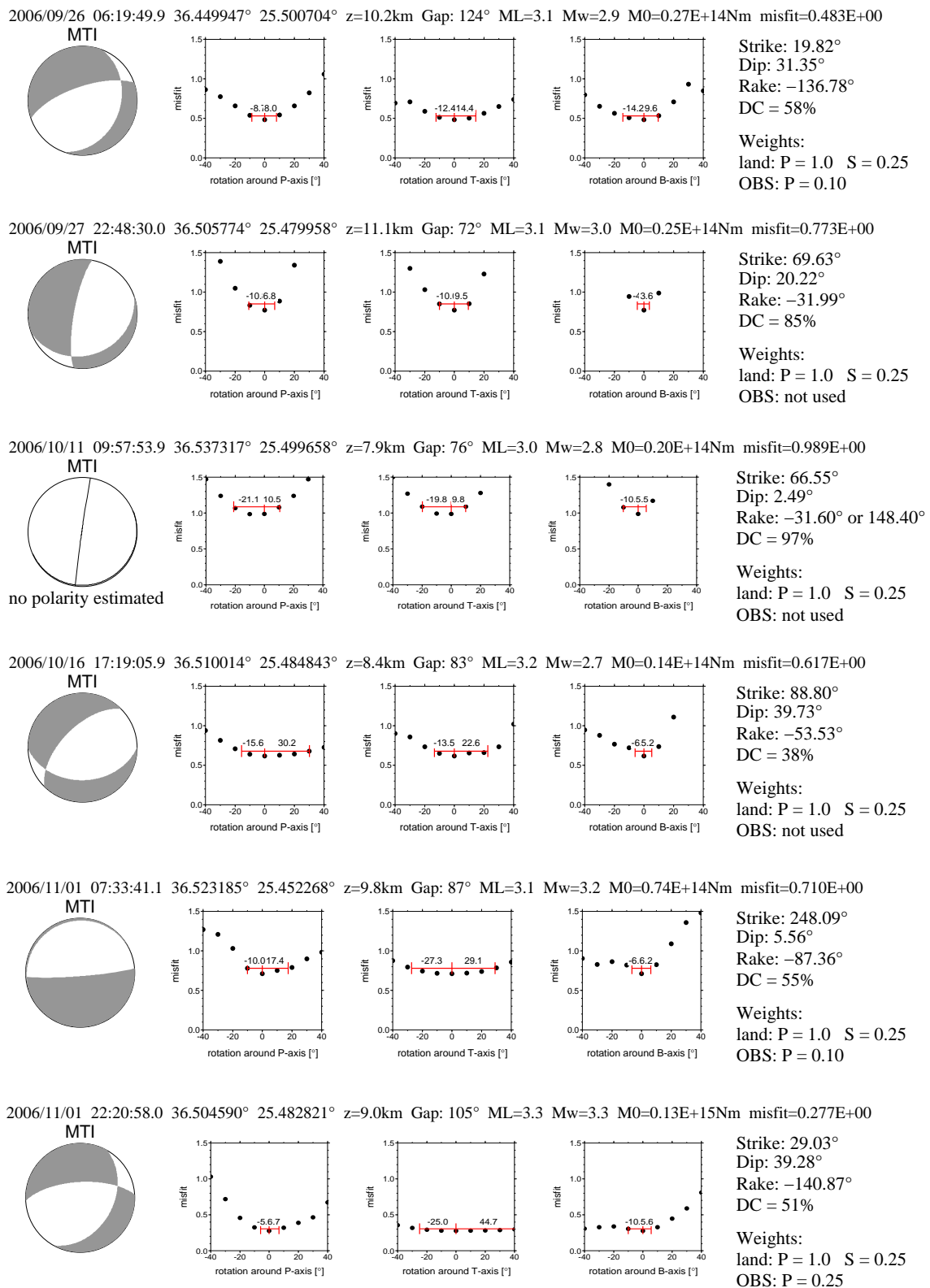
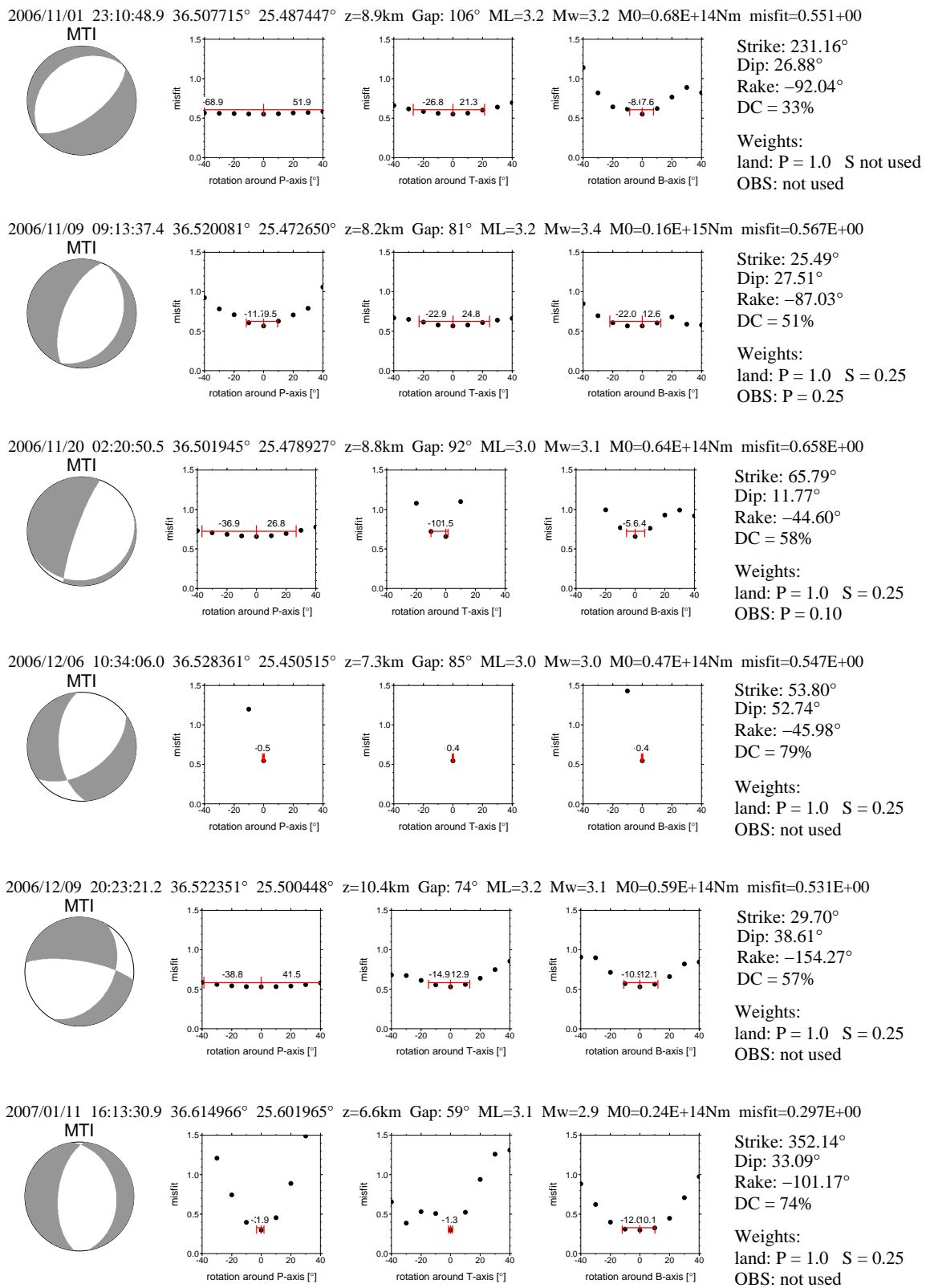
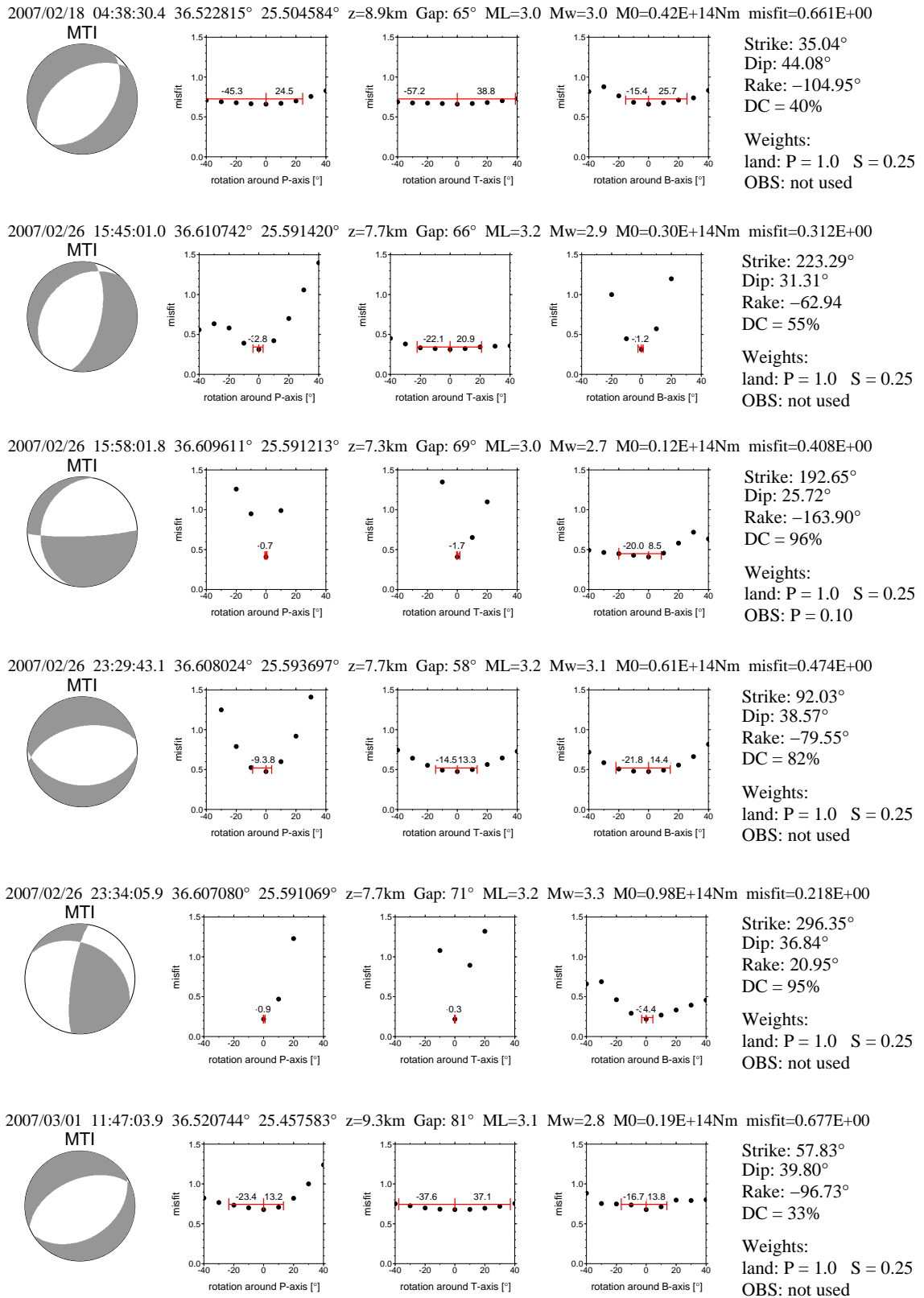


Figure E.23: Focal mechanisms of events $M_L < 3.5$ (plot 1)

Figure E.24: Focal mechanisms of events $M_L < 3.5$ (plot 2)

Figure E.25: Focal mechanisms of events $M_L < 3.5$ (plot 3)

Figure E.26: Focal mechanisms of events $M_L < 3.5$ (plot 4)

THE EGELADOS WORKING GROUP

- Ruhr-University Bochum, Germany:
Wolfgang Friederich, Thomas Meier, Uwe Casten, Monika Bischoff, Andrea Bruestle, Katja Essen, Kasper Fischer, Ludger Küperkoch, Samir Lamara, Cedric Legendre, Martina Rische, Andreas Schmidt, Markus Staackmann, Eleni Tzoumerkiotis, Sebastian Wehling
- University of Hamburg, Germany:
Torsten Dahm, Martin Hensch
- GeoForschungsZentrum Potsdam, Germany:
Rainer Kind, Forough Sodoudi
- Aristotle University of Thessaloniki, Greece:
Costas Papazachos, Iordanis Dimitriadis, Chrisanthi Ventouzi
- Istanbul Technical University, Turkey:
Tuncay Taymaz, Seda Yolsal
- National Observatory Athens, Greece:
George Stavrakakis, Christos Evangelidis, Nikolaos Melis, Panagiota Petrou, Maria Sachpazi
- Technical University of Crete (Chania), Greece:
Antonis Vafidis, Nick Andronikidis, Nikos Economou

ACKNOWLEDGEMENTS

I gladly acknowledge the following people and institutions:

- The German Research Foundation (DFG) for financial support, project Da 478/14-1 "Inspecting Columbo".
- Institute of Geophysics Hamburg: Supervisors Prof. Dr. Torsten Dahm and Prof. Dr. Matthias Hort for instructions and critical discussions; Jörg Reinhardt, Barbara Hofmann, Manuel Beitz, Sven Winter and Rolf Herber for their essential help during the Columbo Experiment; the whole rest of the institute, especially the "AG Seismologie", secretary Christel Mynarik as the good soul of the institute and my HiWis Carlos Alberto Apablaza-Sanchez, Carina Juretzek, Steffi Falk, Christian Holst, Marcel Ruhнау, Karin Landschulze, Stefan Trabs, Friederike von Schlippe and Franziska Walk.
- A special acknowledgement to our external HiWis of the Hamburg School of Applied Sciences, Peter Voss and Matthias Sell, for developing the levelling electronics of the OBT (and finishing its construction during the night before it was sent to Greece).
- Our EGELADOS project partners, especially Prof. Costas Papazachos (Aristotle University of Thessaloniki, Greece), without whose help the OBSs/OBTs would still be lying on the ground of the Aegean Sea, his former PhD students Iordanis Dimitriadis and Domenikos Vamvakaris for joining our ship cruises; Prof. Tuncay Taymaz (Istanbul Technical University, Turkey) for his participation in both cruises; Prof. Wolfgang Friederich, PD Dr. Thomas Meier, Dr. Kasper Fischer, Andrea Brüstle, Katja Esen, Monika Bischoff, Andreas Schmidt and Ludger Küperkoch (all Ruhr-University of Bochum, Germany) for the excellent cooperation between the EGELADOS and the COLUMBO projects, data supply and support.
- The GEOFON data center at the Geoforschungszentrum Potsdam (GFZ), Germany, for organising data exchange and providing their infrastructure.
- The "Leitstelle für mittelgroße Forschungsschiffe", captain Michael Schneider and the crew of RV Poseidon as well as the Hellenic Centre for Marine Research (HCMR), captain Theodoros S. Kanakaris and the crew of RV Aegaeo.
- The Black Forest Observatory in Schiltach, Thomas Forbriger, Rudolf Widmer-Schmidrig and Walter Zürn, for providing their mine and infrastructure for our OBT test measurements, as well as Erhard Wielandt (University of Stuttgart) for some inspiring discussions.
- Eleonora Rivalta, Lars Krieger, Sebastian Heimann, Simone Cesca and Florian Ziemer for (an endless amount of) critical comments.
- The Henschs of Arzheim.

REFERENCES

- Acocella, V. and Neri, M., 2009.
Dike propagation in volcanic edifices: Overview and possible developments.
Tectonophysics, vol. 471, p. 67-77.
- Aoki, Y., Segall, P., Kato, T., Cervelli, P., and Shimada, S., 1999.
Imaging magma transport during the 1997 seismic swarm of the Izu Peninsula, Japan.
Science, Vol. 286, p. 927-930.
- Battaglia, J., Ferrazzini, V., Staudacher, T., Aki, K., and Cheminée, J.-L., 1999.
Pre-eruptive migration of earthquakes at the Piton de la Fournaise volcano (Réunion Island).
Geophys. J. Int., 161, 549-558.
- Battaglia, M., Troise, C., Obrizzo, F., Pingue, F., and De Natale, G., 2006.
Evidence for fluid migration as the source of deformation at Campi Flegrei caldera (Italy).
Geophys. Res. Lett., vol 33, p. 1307-1310.
- Becker, D., Cailleau, B., Dahm, T., A., S. S., and D., K., 2009.
Stress triggering and stress memory observed from acoustic emission records in a salt mine.
submitted to Geophys. J. Int.
- Berger, W. H., 1973.
Deep-sea carbonates: Evidence for a coccolith lysocline.
Deep-Sea Research, vol. 20, p. 917-921.
- Bianco, F., Del Pezzo, E., Saccorotti, G., and Ventura, G., 2004.
The role of hydrothermal fluids in triggering the July-August 2000 seismic swarm at Campi Flegrei, Italy: evidence from seismological and mesostructural data.
Journal of Volcanology and Geothermal Research, vol. 133, p. 229-246.
- Bohnhoff, M., Makris, J., Papanikolaou, D., and Stavrakakis, G., 2001.
Crustal investigation of the Hellenic subduction zone using wide aperture seismic data.
Tectonophysics, vol. 343, p. 239-262.
- Bohnhoff, M., Rische, M., Meier, T., Becker, D., Stavrakakis, G., and Harjes, H., 2006.
Microseismic activity in the Hellenic Volcanic Arc, Greece, with emphasis on the seismotectonic setting of the Santorini-Amorgos Zone.
Tectonophysics, vol. 423 (1-4), p. 17-33.
- Bonafede, M., 1991.
Hot fluid migration: an efficient source of ground deformation: application to the 1982-1985 crisis at Campi Flegrei-Italy.
Journal of Volcanology and Geothermal Research, vol. 48, p. 187-198.

- Bonafede, M. and Mazzanti, M., 1999.
Residual gravity variations in volcanic areas: Constraints to the interpretation of uplift episodes at Campi Flegrei, Italy.
Physics and Chemistry of the Earth, vol. 24, p. 963-967.
- Cesca, S., 2005.
Inversion del tensor momento sismico de terremotos superficiales a distancias regionales.
PhD Thesis at the University of Madrid, Spain.
- Cesca, S., Braun, T., Tessmer, E., and Dahm, T., 2007.
Modelling of the April 5, 2003, Stromboli (Italy) paroxysmal eruption from the inversion of broadband seismic data.
Earth and Planetary Science Letters, 261, 164-178.
- Cox, C., Deaton, T., and Webb, S., 1984.
A Deep-Sea Differential Pressure Gauge.
Journal of Atmospheric and Oceanic Technology, vol. 1 (3), p. 237-246.
- Dahm, T., 2000.
On the shape and velocity of fluid-filled fractures in the Earth.
Geophys. J. Int., 142, 181-192.
- Dahm, T., Hainzl, S., and T., F., 2009.
Bi- and uni-directional fracture growth during hydro-fracturing: The role of driving stress gradients.
submitted to *J. of Geophys. Res.*
- Dahm, T. and Krüger, F., 1999.
Higher-degree moment tensor inversion using far-field broad-band recordings: Theory and evaluation of the method with application to the 1994 Bolivia deep earthquake.
GJI, vol. 137, p. 35-50.
- Dahm, T., Krüger, F., Essen, H.-H., and Hensch, M., 2005.
Historic microseismic data and their relation to the wave-climate in the North Atlantik.
Meteor. Z. 20 (special volume SFB 512), vol. 4 (6), p. 771-779.
- Dahm, T., Krüger, F., Stammer, K., and Yuan, X., 2004.
Moment Tensor Inversion - a practical for beginners.
ESC Young Scientist Training Course, Potsdam, Germany.
- Dahm, T. and Plenefisch, T., 2001.
A new energy-based approach in stress inversion.
pers. comm., unpublished.
- Dahm, T., Thorwart, M., Flueh, E. R., Braun, T., Herber, R., Favali, P., Beranzoli, L., D'Anna, G., Frugoni, F., and Smriglio, G., 2002.
Ocean bottom seismometers deployed in Tyrrhenian Sea.
EOS Transactions, vol. 83, p. 309.
- De Natale, G. and Pungue, F., 1993.
Ground deformations in collapsed caldera structures.
Journal of Volcanology and Geothermal Research, vol. 57, p. 19-38.

- Deane, G.-B. and Stokes, M.-D., 2002.
Scale dependence of bubble creation mechanisms in breaking waves.
Nature 418, 839-844.
- Del Pezzo, E., de Natale, G., and Zollo, A., 1984.
Space-time distribution of small earthquakes at Phlegraean Fields, south-central Italy.
Bulletin of Volcanology, vol. 47, p. 201-207.
- Dimitriadis, I., Karagianni, E., Panagiotopoulos, D., Papazachos, C., Hatzidimitriou, P., and Bohnhoff, M., 2009.
Seismicity and active tectonics at Coloumbo Reef (Aegean Sea, Greece): Monitoring an active volcano at Santorini Volcanic Center using a temporary seismic network.
Tectonophysics, vol. 465, p. 136-149.
- Dimitriadis, I. M., Panagiotopoulos, D. G., Papazachos, C. B., Hatzidimitrou, P., Karagianni, E. E., and Kane, I., 2005.
Recent activity (1994-2002) of the Santorini Volcano using data from local Seismological Network.
Developments in Volcanology, vol. 7, p. 185-203.
- Dixon, J. E., 1997.
Degassing of alkalic basalts.
American Mineralogist, vol. 82, p. 368-378.
- Dominey-Howes, D. T. M., Papadopoulos, G. A., and Dawson, A. G., 2000.
Geological and Historical Investigation of the 1650 Mt. Columbo (Thera Island) Eruption and Tsunami, Aegean Sea, Greece.
Natural Hazards, vol. 21, p. 83-96.
- Druitt, T. H., Edwards, L., Mellors, R. M., Pyle, D. M., Sparks, R. S. J., Lanphere, M., Davies, M., and Barriero, B., 1999.
Santorini Volcano.
The Geological Society of London, Memoirs vol. 19.
- Einarsson, P. and Brandsdóttir, B., 1980.
Seismological evidence for lateral magma intrusion during the July 1978 deflation of Krafla Volcano in NE-Iceland.
J. Geophys. 47, 160-165.
- Fabian, M. and Villinger, H., 2007.
The Bremen Ocean Bottom Tiltmeter (OBT) - a technical article on a new instrument to monitor deep seafloor deformation and seismicity level.
Marine Geophys. Res., vol. 28, p. 13-26.
- Fabian, M. and Villinger, H., 2008.
Long-term tilt and acceleration data from the logatchev hydrothermal vent field, mid-atlantic ridge, measured by the bremen ocean bottom tiltmeter.
Geochemistry, Geophysics, Geosystems, vol. 9, p. 7016 f.
- Fischer, T., 2003.
The August-December 2000 earthquake swarm in NW Bohemia: the first results based on automatic processing of seismograms.
J. of Geodynamics, 35, 59-81.

- Fischer, T. and Horálek, J., 2003.
Space-time distribution of earthquake swarms in the principal focal zone of the NW Bohemia/Vogtland seismoactive region: period 1985-2001.
J. of Geodynamics, 35, 125-144.
- Fox, C. G., 1990.
Evidence of active ground deformation on the mid-ocean ridge: Axial seamount, Juan de Fuca Ridge, April-June 1988.
Journal of Geophys. Res., vol. 95, p.12813-12822.
- Fox, C. G., 1999.
In situ ground deformation measurements from the summit of Axial Volcano during the 1998 volcanic episode.
Geophysical Research Letters, vol. 26, p. 3437-3440.
- Francalanci, L., Vougioukalakis, G., Perini, G., and Manetti, P., 2005.
A west-east traverse along the magmatism of the south Aegean volcanic arc in the light of volcanological, chemical and isotope data.
Developments in Volcanology, vol. 7, p. 65-111.
- Friederich, W. and Meier, T., 2008.
Temporary Seismic Broadband Network Acquired Data on Hellenic Subduction Zone.
Eos Trans. AGU, vol. 89 (40), p. 378.
- Gealey, W. K., 1988.
Plate tectonic evolution of the Mediterranean - Middle East region.
Tectonophysics, vol. 155, p. 285-306.
- Green, D. N. and Neuberg, J., 2006.
Waveform classification of volcanic low-frequency earthquake swarms and its implication at Soufrière Hills Volcano, Montserrat.
Journal of Volcanology and Geothermal Research, vol. 153, p. 51-63.
- Hanks, T. C. and Kanamori, H., 1979.
A moment magnitude scale.
Journal of Geophys. Res., vol. 84, p. 2348-2350.
- Hasegawa, H., Wetmiller, R., and Gendzwill, D., 1989.
Induced seismicity in mines in Canada – An overview.
PAGEOPH, vol. 129, p. 423-453.
- Hauksson, E., Hutton, K., Jones, L., and Given, D., 2001.
The M4.1 Bombay Beach Earthquake Swarm of 13 November 2001.
Preliminary Report of the TriNet-Network (USGS).
- Hautmann, S., Gottsmann, J., Sparks, R. S. J., Costa, A., Melnik, O., and Voight, B., 2009.
Modelling ground deformation caused by oscillating overpressure in a dyke conduit at Soufrière Hills Volcano, Montserrat.
Tectonophysics, vol. 471 (1-2), p. 87-95.
- Havskov, J. and Ottemöller, L., 2001.
SEISAN: The Earthquake Analysis Software, Version 7.2.
Institute of Solid Earth Physics, University of Bergen, Norway.

Heidbach, O., Tingay, M., Barth, A., Reinecker, J., Kurfess, D., and Müller, B., 2008.
The World Stress Map database release.
GFZ WSM release.

Heiken, G. and McCoy, F., 1984.
Caldera development during the minoan eruption, thira, cyclades, greece.
journal of Geophys. Res., vol. 89, p. 8441-8462.

Hensch, M., 2005.
Hypocenter migration of fluid-induced earthquake swarms in the Tjörnes Fracture Zone, North Iceland.
Diploma thesis at the University of Hamburg, available on request.

Hensch, M., Riedel, C., Reinhardt, J., Dahm, T., and The NICE-People, 2008.
Hypocenter migration of fluid-induced earthquake swarms in the Tjörnes Fracture Zone, North Iceland.
Tectonophysics, special volume on Plume and Ridge Interaction in Iceland, vol. 447, pp 80-94, doi:10.1016/j.tecto.2006.07.015.

Hofmann, B., 2008.
Automatic moment tensor inversion of weak, local earthquakes in south-central Chile.
Diploma Thesis at the University of Hamburg, Germany, ZMAW library.

Hort, M. and Hensch, M., 2009.
The new Hamburg Ocean-Bottom-Tiltmeter: Technical details and first experiences in practical use.
in prep.

Hübscher, C., Hensch, M., Dahm, T., Dehghani, A., Dimistriadis, I., Hort, M., and Taymaz, T., 2006.
Toward a risk assessment of Central Aegean Volcanoes.
EOS, vol. 87, No. 39, p. 401 and 407.

Jahr, T., Jentzsch, G., Gebauer, A., and Lau, T., 2008.
Deformation, seismicity and fluids: Results of the 2004/2005 water injection experiment at the KTB/Germany.
Journal of Geophys. Res., vol. 113, B11410, doi:10.1029/2008JB005610.

Jolivet, L. and Faccenna, C., 2000.
Mediterranean extension and the Africa-Eurasian collision.
Tectonics, ol. 19, no. 6, p. 1095-1106.

Jost, M. and Hermann, R., 1989.
A student's guide to and review of moment tensors.
Seismological Research Letter, vol. 60, p. 37-57.

Kahle, H., Straub, C., Reilinger, R., McClusky, S., King, R., Hurst, K., Veis, G., Kastense, K., and Cross, P., 1998.
The strain rate field in the eastern Mediterranean region, estimated by repeated GPS measurements.
Tectonophysics, vol. 294, p. 237-252.

- Kiratzí, A. and Louvari, E., 2003.
Focal mechanisms of shallow earthquakes in the Aegean Sea and the surrounding lands determined by waveform modelling: A new database.
Journal of Geodynamics, vol. 36, p. 251-274.
- Kirchdörfer, M., 1999.
Analysis and quasistatic finite element modelling of long-period impulsive events associated with explosions at Stromboli volcano.
Annali di Geofisica, vol. 42, p. 379-390.
- Knapmeyer, M., 1999.
Geometry of the Aegean Benioff zones.
Ann. Geofis. vol. 42, p. 27-38.
- Knopoff, L. and Randall, M., 1970.
The Compensated Linear Vector Dipole: A possible mechanism for deep earthquakes.
Journal of Geophysical Research, vol. 75, p. 4957-4963.
- Kühn, D. and Dahm, T., 2008.
Numerical modelling of dyke interaction and its influence on oceanic crust formation.
Tectonophysics, vol. 447, p. 53-65.
- Landschulze, K., 2009.
Auswertung gravimetrischer und magnetischer Daten über das Gebiet des Columbo-Unterseevulkans.
Diploma thesis, University of Hamburg, Germany, ZMAW library.
- Lay, T. and Wallace, T.-C., 1995.
Modern Global Seismology.
Academic Press.
- Lee, W. H. K. and Lahr, J. C., 1975.
HYPO71: A computer program for determining hypocenter, magnitude and first motion pattern of local earthquakes.
USGS Open File Report 113.
- Lupi, M., Geiger, S., Graham, C., Claesson, L., and Richter, B., 2007.
Linking fault permeability, fluid flow, and earthquake triggering in a hydrothermally active tectonic setting: Numerical simulations of the hydrodynamics in the Tjörnes Fracture Zone, Iceland.
AGU Fall Meeting Abstracts, B479.
- Martini, M., Legittimo, P. C., Piccardi, G., and Giannini, L., 1984.
Composition of hydrothermal fluids during the bradyseismic crisis which commenced at Phlegraean Fields in 1982.
Bulletin of Volcanology, vol. 47, p. 267-273.
- Maurer, H. and Deichmann, N., 1995.
Microearthquake cluster detection based on waveform similarities, with an application to the western Swiss Alps.
Geophys. J. Int. 123, 588-600.

- Meier, T., Rische, M., Endrun, B., Vafidis, A., and Harjes, H.-P., 2004.
Seismicity of the Hellenic subduction zone in the area of western and central Crete observed by temporary local seismic networks.
Tectonophysics, vol. 383, p. 149-169.
- Menke, W., 1978.
Geophysical Data Analysis: Discrete Inversion Theory.
Int. Geophys. series 45, (Academic Press, San Diego).
- Mogi, K., 1958.
Relations between the eruptions of various volcanoes and the deformations of the ground surfaces around them.
Bull. Earthquake Res. Inst. Tokyo, vol. 36, p. 99-134.
- Müller, G., 2007.
Theory of Elastic Waves.
Scientific Technical Report STR07/03, GFZ Potsdam.
- Neuberg, J. W., Tuffen, H., Collier, L., Green, D., Powell, T., and Dingwell, D., 2006.
The trigger mechanism of low-frequency earthquakes on Montserrat.
Journal of Volcanology and Geothermal Research, vol. 153, p. 37-50.
- Okada, Y., 1992.
Internal deformation due to shear and tensile faults in a half-space.
Bulletin of the Seismological Society of America, Vol. 82, No. 2, pp. 1018-1040.
- Papazachos, B. C. and Panagiotopoulos, D. G., 1993.
Normal faults associated with volcanic activity and deep rupture zones in the southern Aegean Sea.
Tectonophysics, vol. 220, p. 301-308.
- Patané, D., Chiarabba, C., Cocina, O., De Gori, P., Moretti, M., and Boschi, E., 2002.
Tomographic images and 3D earthquake locations of the seismic swarm preceding the 2001 Mt. Etna eruption: Evidence for a dyke intrusion.
Geophys. Res. Lett., vol. 29, nr. 10, 1497, 10.1029/2001/GL014391.
- Pichon, X. and Angelier, J., 1979.
The Hellenic arc and trench system: A key to the neotectonic evolution of the eastern Mediterranean area.
Tectonophysics, vol. 60, p. 1-42.
- Pollard, D. D., Delaney, P. T., Duffield, W. A., Endo, E. T., and Okamura, A. T., 1983.
Surface deformation in volcanic rift zones.
Tectonophysics, vol. 94, p. 541-584.
- Pozgay, S. H., White, R. A., Wiens, D. A., Shore, P. J., Sauter, A. W., and Kaipat, J. L., 2005.
Seismicity and tilt associated with the 2003 Anatahan eruption sequence.
Journal of Volcanology and Geothermal Research, vol. 146, p. 60-76.
- Press, F., 1965.
Displacements, strains and tilts at teleseismic distances.
J. Geophys. Res., vol. 70, p. 2395-2412.

- Reinhardt, J., 2002.
Automatisierte Kohärenz-Analyse und Relokalisierung für den Erdbebenschwarm 1997 in der Region Vogtland/NW-Böhmen.
Diploma-Thesis, University of Hamburg, Germany, ZMAW library.
- Reinhardt, J., 2007.
Inversion for local stress field inhomogenities.
PhD thesis at the University of Hamburg, Germany, ZMAW library.
- Rivalta, E., Böttinger, M., and Dahm, T., 2005.
Buoyancy-driven fracture ascent: Experiments in layered gelatine.
Journal of Volcanology and Geothermal Research, vol. 144, p. 273-285.
- Rivalta, E. and Dahm, T., 2004.
Dyke emplacement in fractured media: application to the 2000 intrusion at Izu islands, Japan.
Geophys. J. Int., 157, 283-292.
- Roman, D., Neuberg, J., and R.R.R., L., 2006.
Assessing the likelihood of eruption through analysis of VT earthquake fault-plane solutions.
Earth and Planetary Science Letters, vol. 248, p. 229-237.
- Rubin, A. M., 1992.
Dike-induced faulting and graben subsidence in volcanic rift zones.
Journal of Geophys. Res., vol. 97, p. 1839-1858.
- Rubin, A.-M. and Gillard, D., 1998a.
Dike-induced earthquakes: Theoretical considerations.
J. of Geophys. Res., vol. 103 B5, 10.017-10.030.
- Rubin, A.-M. and Gillard, D., 1998b.
A reinterpretation of seismicity associated with the January 1983 dike intrusion at Kilauea Volcano, Hawaii.
J. of Geophys. Res., vol. 103 B5, 10.003-10.015.
- Ruhnau, M., 2009.
Reflection seismic profiling at the Columbo Submarine Volcano.
Diploma thesis, University of Hamburg, in prep.
- Schweitzer, J., 2001.
HYPOSAT - An Enhanced Routine to Locate Seismic Events.
Pure and Applied Geophysics, vol. 158, p. 277-289.
- Sigurdsson, H., Carey, S., Alexandri, M., Vougioukalakis, G., Croff, K., Roman, C., Sakellariou, D., Anagnostou, C., Roustakis, G., Ioakim, C., Gogou, A., ballas, D., Misaridis, T., and Nomikou, P., 2006.
Marine Investigations of Greece's Santorini Volcanic Field.
EOS, no. 34, p. 337 and 348.
- Snoke, J.-A., Munsey, J.-W., Teague, A.-C., and Bollinger, G.-A., 1984.
A program for focal mechanism determination by combined use of polarity and SV-P amplitude ratio data.
Earthquake Notes, vol. 55, p. 3-15.

Sparks, R. S. J., 2003.

Forecasting volcanic eruptions.

Earth and Planetary Science Letters, vol. 210, p. 1-15.

Stein, S. and Wysession, M., 2003.

An introduction to Seismology, Earthquakes and Earth Structure.

Blackwell Publishin Ltd., ISBN 978-0-86542-078-6.

Steketee, J.-A., 1958.

On volterra's dislocation in a semi-infinite elastic medium.

Ca. J. Phys., vol. 36, p.192-205.

Sturkell, E., Einarsson, P., Sigmundsson, F., Geirsson, H., Ólafsson, H., Pedersen, R., de Zeeuw-van Dalfsen, E., Linde, A. T., Sacks, S. I., and Stefánsson, R., 2006.

Volcano geodesy and magma dynamics in Iceland.

Journal of Volcanology and Geothermal Research, vol. 150, p. 14-34.

Thorwart, M., 2002.

3D-stress field around a rising fluid filled batch.

EGU Nice, Poster.

Tilmann, F., Grevemeyer, I., Flueh, E., Dahm, T., and Gossler, J., 2008.

Seismicity in the outer rise offshore southern Chile: Identification of fluid effects in crust and mantle.

Earth Planet. Sci. Let.,269(1-2), 41-55, doi: 10.1016/j.epsl.2008.01.044.

Toda, S., Stein, R.-S., and Sagiya, T., 2002.

Evidence from the AD 2000 Izu islands earthquake swarm that stressing rate governs seismicity.

Nature, vol. 419, 58-61.

Tolstoy, M., Constable, S., Orcutt, J., Staudigel, H., Wyatt, F. K., and Anderson, G., 1998.

Short and long baseline tiltmeter measurements on axial seamount, Juan de Fuca Ridge.

Physics of the Earth and Planetary Interiors, vol. 108, p. 108 ff.

Ukawa, M. and Tsukahara, H., 1996.

Earthquake swarms and dike intrusions off the east coast of Izu Peninsula, central Japan.

Tectonophysics, vol. 253, p. 285-303.

Vougioukalakis, G., 1996.

Volcanic Hazard Zonation Map of Santorini.

Institute for the Study and Monitoring of the Santorini Volcano (ISMOSAV), ismosav.santorini.net.

Waldhauser, F., 2001.

hypoDD - A Programm to compute Double-Difference Hypocenter Locations.

Open File Report 01-113.

Waldhauser, F. and Ellsworth, W., 2000.

A double-difference earthquake location algorithm: Method and application to the Northern Hayward Fault, California.

BSSA, 90:1353-1368.

Wielandt, E., 2001.

Basics of the volume-source model and its application in volcano seismology.
<http://www.geophys.uni-stuttgart.de/oldwww/ew/volcano/index.html>.

Wielandt, E. and Forbriger, T., 1999.

Near-field seismic displacement and tilt associated with the explosive activity of Stromboli.
Annali di Geofisica, vol. 42, p. 407-416.

Yuan, A., 1984.

Seismicity and eruptive activity at Fuego Volcano, Guatemala: February 1975 January 1977.

Journal of Volcanology and Geothermal Research, vol. 21, p.277-296.